Dual effect of Semaphorin 4D blockade in neuroendocrine tumor malignization: from vessels to macrophages

Iratxe Zuazo Gaztelu

ADVERTIMENT. La consulta d'aquesta tesi queda condicionada a l'acceptació de les següents condicions d'ús: La difusió d'aquesta tesi per mitjà del servei TDX (**www.tdx.cat**) i a través del Dipòsit Digital de la UB (**diposit.ub.edu**) ha estat autoritzada pels titulars dels drets de propietat intel·lectual únicament per a usos privats emmarcats en activitats d'investigació i docència. No s'autoritza la seva reproducció amb finalitats de lucre ni la seva difusió i posada a disposició des d'un lloc aliè al servei TDX ni al Dipòsit Digital de la UB. No s'autoritza la presentació del seu contingut en una finestra o marc aliè a TDX o al Dipòsit Digital de la UB (framing). Aquesta reserva de drets afecta tant al resum de presentació de la tesi com als seus continguts. En la utilització o cita de parts de la tesi és obligat indicar el nom de la persona autora.

ADVERTENCIA. La consulta de esta tesis queda condicionada a la aceptación de las siguientes condiciones de uso: La difusión de esta tesis por medio del servicio TDR (**www.tdx.cat**) y a través del Repositorio Digital de la UB (**diposit.ub.edu**) ha sido autorizada por los titulares de los derechos de propiedad intelectual únicamente para usos privados enmarcados en actividades de investigación y docencia. No se autoriza su reproducción con finalidades de lucro ni su difusión y puesta a disposición desde un sitio ajeno al servicio TDR o al Repositorio Digital de la UB. No se autoriza la presentación de su contenido en una ventana o marco ajeno a TDR o al Repositorio Digital de la UB (framing). Esta reserva de derechos afecta tanto al resumen de presentación de la tesis como a sus contenidos. En la utilización o cita de partes de la tesis es obligado indicar el nombre de la persona autora.

WARNING. On having consulted this thesis you're accepting the following use conditions: Spreading this thesis by the TDX (**www.tdx.cat**) service and by the UB Digital Repository (**diposit.ub.edu**) has been authorized by the titular of the intellectual property rights only for private uses placed in investigation and teaching activities. Reproduction with lucrative aims is not authorized nor its spreading and availability from a site foreign to the TDX service or to the UB Digital Repository. Introducing its content in a window or frame foreign to the TDX service or to the UB Digital Repository is not authorized (framing). Those rights affect to the presentation summary of the thesis as well as to its contents. In the using or citation of parts of the thesis it's obliged to indicate the name of the author.

UNIVERSITAT DE BARCELONA

FACULTAT DE FARMÀCIA I CIÈNCIES DE L'ALIMENTACIÓ

PROGRAMA DE DOCTORAT EN BIOMEDICINA

DUAL EFFECT OF SEMAPHORIN 4D BLOCKADE IN NEUROENDOCRINE TUMOR MALIGNIZATION: FROM VESSELS TO MACROPHAGES

IRATXE ZUAZO GAZTELU

2018

ICO
Institut Català d'Oncologia
Hospital Duran i Reynals

Program Against
Cancer Therapeutic Resistance
ProCURE

IDIBELL
Institut d'Investigació Biomèdica de Bellvitge

UNIVERSITAT DE BARCELONA

UNIVERSITAT DE BARCELONA
FACULTAT DE FARMÀCIA I CIÈNCIES DE L'ALIMENTACIÓ
PROGRAMA DE DOCTORAT EN BIOMEDICINA

DUAL EFFECT OF SEMAPHORIN 4D BLOCKADE IN NEUROENDOCRINE TUMOR MALIGNIZATION: FROM VESSELS TO MACROPHAGES

IRATXE ZUAZO GAZTELU

2018

Memòria presentada per Iratxe Zuazo Gaztelu

per optar al grau de Doctora per la Universitat de Barcelona

Dr. Oriol Casanovas Casanovas
Director

Dr. Francesc Vinyals Canals
Tutor

Iratxe Zuazo Gaztelu
Autora

OBSERVATION

In the following pages, readers may spot some typos which will be undoubtedly overcome by their knowledge. I apologize for such inconvenience and thank you very much for your attention.

But you know, happiness can be found
even in the darkest of times,
if one only remembers to turn on the light.

Albus Dumbledore – Harry Potter III

Sabía quién era esta mañana, pero
he cambiado varias veces desde entonces.

Alicia - Alicia en el País de las Maravillas

Table of contents

Science is organized knowledge.
Wisdom is organized life.

Immanuel Kant

Table of contents

List of figures

List of tables

List of annexes

List of abbreviations

%	Percentage
ºC	Centigrade degrees
α-SMA	Alpha Smooth Muscle Actin
βTC	βeta Tumor Cell
Δ	Delta, difference
AAALAC	Association for Assessment and Accreditation of Laboratory Animal Care
Ab	Antibody
AC	Adenylate Cyclase
AML	Acute myeloid leukemia
Ang	Angiopoietin
Angptl	Angiopoietin-Like
ANOVA	Analysis of variance
APS	Ammonium persulfate
ATCC	American Type Culture Collection
BCA	Bicinchoninic acid assay
BCR	B Cell Receptor
Bcl2	B-cell Lymphoma 2
bp	Base pairs
BSA	Bovine serum albumin
c	Centi
CAF	Cancer-associated fibroblast
cAMP	Cyclic Adenosine Monophosphate
CCL	C-C motif Ligand
CD	Cluster of Differentiation
cDNA	Complementary DNA
CLL	Chronic lymphocytic leukemia
CO_2	Carbon dioxide
CRG	Centre de Regulació Genòmica
CSF1	Colony Stimulating Factor 1
CSF1R	Colony Stimulating Factor 1 Receptor
Ct	Threshold cycle
CTLA4	Cytotoxic T-Lymphocyte-Associated Protein 4
CXCL	C-X-C motif Ligand
CXCR	C-X-C motif Receptor
DAB	3,3'-Diaminobenzidine
DAPI	4',6-Diamidino-2-phenylindole dihydrochloride
DAVID	Database for Annotation, Visualization and Integrated Discovery
DC	Dendritic cell
ddH_20	Bi-distilled water
DIVAA™	Directed In Vivo Angiogenesis Assays
DMEM	Dulbeco's Modified Eagle Medium
DMSO	Dimethyl sulfoxide
DNA	Deoxyribonucleic acid
DPX	Distyrene Plasticizer Xylene
ECM	Extracellular matrix

EDTA	Ethylenediaminetetraacetic acid
EGF	Epithelial Growth Factor
EGFR	Epithelial Growth Factor Receptor
EMT	Epithelial-mesenchymal transition
ERK	Extracellular Signal-Regulated Kinase
ELISA	Enzyme-Linked Immunosorbent Assay
FBS	Fetal bovine serum
FDA	U.S. Food and Drug Administration
FDR	False discovery rate
FELASA	Federation of European Laboratory Animal Science Associations
FGF	Fibroblast Growth Factor
FGFR	Fibroblast Growth Factor Receptor
g	Acceleration of gravity
g	Gram
GAP	GTPase-activating Protein
gDNA	Genomic DNA
GEO	Gene Expression Omnibus
GLUT	Glucose Transporter
GM-CSF	Granulocyte-Macrophage Colony Stimulating Factor
GO	Gene Ontology
GPI	Glycophosphatidylinositol
GSEA	Gene Set Enrichment Analysis
GSK3β	Glycogen Synthase Kinase 3 Beta
GTP	Guanosine Triphospate
h	Hour
H_2O_2	Hydrogen peroxide
HCl	Chloridric acid
H&E	Hematoxylin and Eosin
HIF	Hypoxia-inducible Factor
HNSCC	Head and Neck Squamous Cell Carcinoma
HRP	Horseradish peroxidase
HUGO	Human Genome Organization
HUVEC	Human Umbilical Vein Endothelial Cells
IC1	Invasive carcinoma type 1
IC2	Invasive carcinoma type 2
ICF	Immunocytofluorescence
IDIBELL	Institut d’Investigació Biomèdica de Bellvitge
IFN	Interferon
Ig	Immunoglobulin
IgG	Immunoglobulin G
IHQ	Immunohistochemistry
IHF	Immunohistofluorescence
IL	Interleukin
IT	Islet/Insulinoma tumor
ITIM	Immuno-Receptor Tyrosine-based Inhibitory Motif
JAK/STAT	Janus Kinase/Signal Transducer and Activator of Transcription
Kb	Kilobase
K_D	Dissociation constant
KEGG	Kyoto Encyclopedia of Genes and Genomes
KH_2PO_4	Potassium dihydrogen phosphate

KO	Knockout
L	Liter
LC	Liquid chromatography
LPS	Lipopolysaccharide
LN	Lymph node
m	Meter or mil
m^3	Cubic meter
M	Molar
mAb	Monoclonal antibody
MAPK	Mitogen-Activated Protein Kinases
MCP	Multiple Cell Population
M-CSF	Macrophage-colony Stimulator Factor
min	Minute
MIP	Macrophage Inflammatory Protein
MLP	Metastasis-like primary tumor
MMP	Matrix Metalloproteinase
M.O.M.™	Mouse on Mouse
mRNA	Messenger ribonucleic acid
ms	mouse
MS/MS	Tandem Mass Spectrometry
MT-MMP	Membrane-type Matrix Metalloproteinase
n	Nano or population size
NaCl	Sodium chloride
Na_2HPO_4	Disodium phosphate
NET	Neuroendocrine tumor
NF-κB	Nuclear Factor Kappa-light-chain-enhancer of Activated B cells
NG2	Neural/Glial Antigen 2
NK	Natural killer
NP-40	Nonyl phenoxypolyethoxylethanol
Nrp	Neuropilin
OCT	Optimal Cutting Temperature compound
OS	Overall survival
OSCC	Oral Squamous Cell Carcinoma
p	Pico
PAGE	Polyacrylamide gel electrophoresis
PanNET	Pancreatic neuroendocrine tumor
PBS	Phosphate buffered saline
PCR	Polymerase chain reaction
PD1	Death Protein 1
PDAC	Pancreatic ductal adenocarcinoma
PDZ	Post synaptic density protein (PSD95), Drosophila disc large tumor suppressor (Dlg1) and Zonula occludens1 protein (ZO-1)
PDGF	Platelet-Derived Growth Factor
PDGFR	Platelet-Derived Growth Factor Receptor
PEBC	Programa d'Epigenètica I Biologia del Càncer
PFS	Progression-free survival
pH	Potential hydrogen
PI3K	Phosphatidylinositol 3 Kinase
PLC	Phospholipase C
PLXN	Plexin

ProCURE	Programa Contra la Resistència Terapèutica del Càncer
PSI	Plexin-Semaphorin-Integrin
qPCR	Quantitative PCR
Rb	Retinoblastoma
Rho	Ras Homolog Protein
RIP	Rat Insulin Promoter
RIP1-Tag2	Rat Insulin Promoter 1 - T antigen 2
RIPA	Radioimmunoprecipitation assay buffer
RNA	Ribonucleic acid
Ron	Recepteur d'Origine Nantais
rpm	Revolutions per minute
RT	Room temperature
RT-PCR	Real-time PCR
s	Second
SD	Standard deviation
SDS	Sodium dodecyl sulfate
SEM	Standard error of the mean
Sema	Semaphorin
SHP1	Src Homology 2 domain containing tyrosine Phosphatase 1
SLL	Small lymphocytic lymphoma
STRING	Search Tool for the Retrieval of Interacting Genes/Proteins
SV40	Simian virus 40
S4D	Semaphorin 4D
S4D+	Semaphorin 4D-expressing/positive
S4D-	Semaphorin 4D-nonexpressing/negative
t	Time
T	Tween or triton
TAE	Tris-Acetate-EDTA
Tag	T antigen
TAM	Tumor-associated macrophage
TBS	Tris-buffered saline
TEMED	Tetramethylethylenediamine
TGF	Transforming Growth Factor
TK	Tyrosine Kinase
TKI	Tyrosine Kinase Inhibitor
TLDA	TaqMan Low Density Array
TNF	Tumor Necrosis Factor
Tris	Tris (hydroxymethyl) aminomethane
TSA™	Tyramide Signal Amplification
µ	Micro
v	Speed
V	Volt
VE-cadherin	Vascular Endothelial Cadherin
VEGF	Vascular Endothelial Growth Factor
VEGFR2	VEGF Receptor 2
VEGFR3	VEGF Receptor 3
VR2	VEGFR Receptor 2
WHO	World Health Organization
Wks	Weeks
WT	Wild Type

Amino acids

F Phe, phenylalanine
L Leu, leucine
I Ile, isoleucine
M Met, methionine
S Ser, serine
P Pro, proline
T Thr, threonine
A Ala, alanine
Y Tyr, tyrosine
H his, histidine
Q Gln, glutamine
NAsn, asparragina
K Lys, lysine
D Asp, aspartic acid
E Glu, glutamic acid
C Cys, cysteine
W Trp tryptophan
R Arg, arginine
G Gly, glycine
V Val, valine

Nucleotides

A adenine T thymine G guanine C cytosine U uracil

Summary

> It is pointless to do with more
> what can be done with less.
>
> William of Ockham

Summary

Tumor progression is a complex conundrum of events that involve not only tumor cells, but also their surrounding microenvironment. Accounting to the natural dependency of tumors on angiogenesis, its therapeutic targeting remains a valid stroma-directed strategy in the fight against cancer. However, standard antiangiogenics fail to produce enduring beneficial effects due to the appearance of resistance, often as a consequence of intratumor hypoxia triggered by vessel trimming. In the case of neuroendocrine tumors (NETs), which are characterized by their low aggressiveness, high heterogeneity and vessel content, new therapeutic approaches are being explored to overcome such hurdles, where conventional therapies stumble. In this context, blockade of semaphorin 4D (Sema4D), a proangiogenic molecule with homeostatic roles in the immune system, by a monoclonal antibody (anti-Sema4D) has proved beneficial antitumor effects in the RIP1-Tag2 preclinical mouse model of pancreatic NET (PanNET). Unfortunately, the decrease in tumor burden and increase in survival of anti-Sema4D treated mice followed an increase in local invasiveness and metastasis. Contrary to the thoroughly described mechanisms governing malignization after antiangiogenic therapies, no intratumoral hypoxia was detected after Sema4D blockade.

In this doctoral thesis, aiming to decipher this novel form of resistance by which anti-Sema4D treatment acts as a double-edged sword in PanNETs, the two systems involved in Sema4D signaling were studied: the vascular and the immune system. We first described a beneficial antiangiogenic effect, characterized by structural changes in tumor vessels mediated by a pericyte-endothelial cell crosstalk. Incidentally, we found that the aggressive phenotype involved the recruitment of Sema4D-positive tumor-associated macrophages (TAMs) to the tumor ecosystem, which, after becoming activated by anti-Sema4D treatment, triggered tumor cell migration and invasion. Mechanistically, functional characterization of Sema4D-positive TAMs' secretome revealed cytokine CXCL12

to be one of the molecules involved in the proinvasive program, suggesting the implication of CXCL12/CXCR4 signaling. Comprehensive clinical validation further shed light on the implication of both macrophage-derived Sema4D and CXCR4 in the malignization steps of tumor development in PanNET patients, which undoubtedly unleashes a new range of approaches merging the immunotherapy and the antiangiogenic fields in their shared fight against cancer.

Resumen

La progresión tumoral es una intrincada sucesión de eventos que implican no solo a las células tumorales, sino también, a su microambiente circundante. Considerando la dependencia natural de los tumores por la angiogénesis, su explotación como diana dirigida contra el estroma tumoral en el tratamiento del cáncer, supone una válida estrategia terapéutica. No obstante, los antiangiogénicos estándar fracasan a la hora de producir efectos duraderos debido a la aparición de resistencia, habitualmente como consecuencia de la hipoxia intratumoral producida por la disminución del número de vasos. En el caso de los tumores neuroendocrinos (NETs), caracterizados por su agresividad, alta heterogeneidad y alto contenido vascular, donde la terapia convencional falla, están siendo explorados nuevos abordajes terapéuticos. En este contexto, el bloqueo de la semaforina 4D (Sema4D), una molécula proangiogénica con un papel homeostático en el sistema inmune, utilizando un anticuerpo monoclonal (anti-Sema4D) ha demostrado efectos antitumorales beneficiosos, en un modelo murino de cáncer de páncreas neuroendocrino (PanNET). Lamentablemente, al descenso en el volumen tumoral y al aumento en la supervivencia de los ratones tratados con anti-Sema4D les siguen un aumento en la invasión local y la metástasis. Al contrario que sucede durante los mecanismos ampliamente descritos como responsable de la malignización, no se detectó hipoxia intratumoral tras el bloqueo de la Sema4D.

Con el objetivo de descifrar esta nueva forma de resistencia, en la cual, el tratamiento anti-Sema4D actúa como un arma de doble filo en PanNETs, estudiamos los dos sistemas implicados en la señalización vía Sema4D: el sistema vascular y el inmune. Primeramente, describimos un efecto antiangiogénico beneficioso, caracterizado por un cambio estructural de los vasos tumorales, y mediado por una comunicación cruzada entre células endoteliales y pericitos. A continuación, encontramos que el fenotipo agresivo involucra el reclutamiento de

macrófagos positivos para Sema4D al ecosistema tumoral, los cuales, tras activarse por el tratamiento anti-Sema4D, potencian la migración e invasión de las células tumorales. En cuanto a su mecanismo, la caracterización funcional de los macrófagos desveló la contribución de la citoquina CXCL12 al programa proinvasivo, sugiriendo una implicación de la señalización vía CXCL12/CXCR4. Finalmente, una validación clínica integral en pacientes de PanNETs arrojó luz sobre la participación de Sema4D derivada de los macrófagos y CXCR4 en la adquisición de la malignización durante el desarrollo tumoral. En conjunto, nuestros datos reconducen el abanico de estrategias terapéuticas existentes hacia un nuevo enfoque que combina la inmunoterapia y la antiangiogénesis en la lucha común contra el cáncer.

Introduction

You cannot teach a man anything.
You can only help him discover it himself.

Galileo Galilei

1. Heterogeneity of pancreatic neuroendocrine tumors

It has been more than a century since Oberndofer coined the term carcinoid (or “karzinoide”) to first define neuroendocrine tumors (Oberndofer, 1907). Neuroendocrine tumors (NETs) comprise a spectrum of malignancies that arise from neuroendocrine cells all over the body. Even though most of them are indolent, they tend to be highly vascularized, aggressive and resistant to therapy. It has been estimated that the incidence of NETs could now reach 7 cases per 100,000 people, which reflects both improved diagnosis tools and a rue surge in the incidence of the disease (Figure 1) (Lewis et al., 2017; Yao et al., 2008).

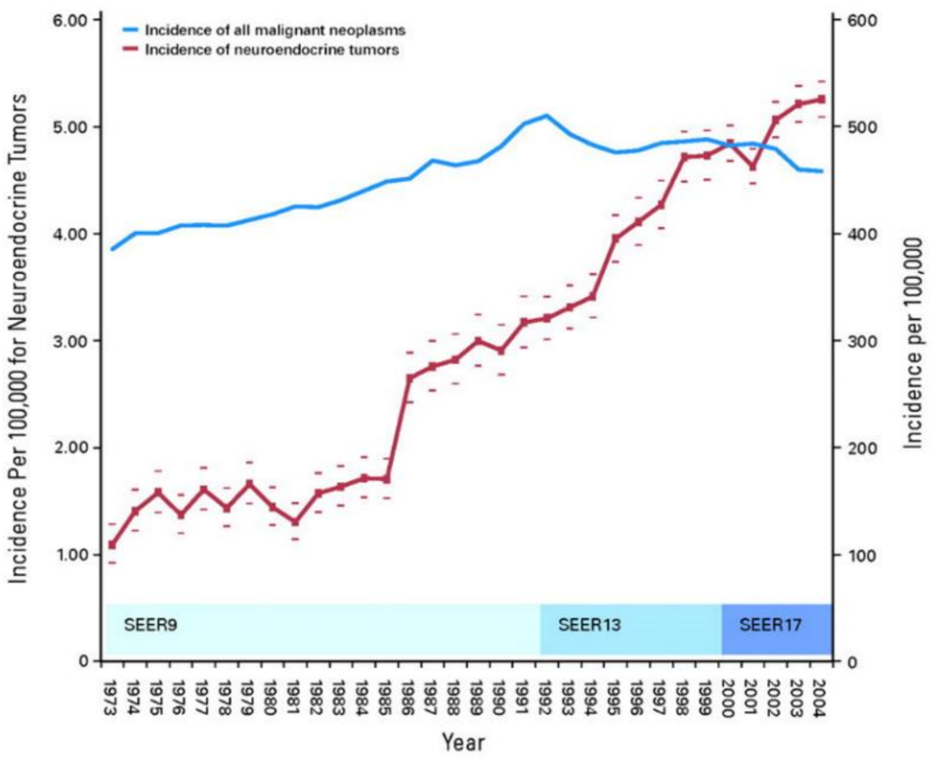

Year	Incidence (95% CI)
1973	1.09 (0.92 to 1.28)
1974	1.40 (1.22 to 1.61)
1975	1.58 (1.39 to 1.78)
1976	1.37 (1.20 to 1.56)
1977	1.61 (1.42 to 1.81)
1978	1.43 (1.27 to 1.62)
1979	1.66 (1.48 to 1.86)
1980	1.44 (1.28 to 1.63)
1981	1.30 (1.14 to 1.48)
1982	1.57 (1.40 to 1.76)
1983	1.63 (1.46 to 1.83)
1984	1.71 (1.53 to 1.91)
1985	1.70 (1.53 to 1.90)
1986	2.65 (2.42 to 2.88)
1987	2.76 (2.53 to 3.00)
1988	2.82 (2.59 to 3.06)
1989	3.00 (2.76 to 3.24)
1990	2.91 (2.68 to 3.15)
1991	3.17 (2.94 to 3.41)
1992	3.21 (3.01 to 3.41)
1993	3.31 (3.11 to 3.51)
1994	3.41 (3.21 to 3.62)
1995	3.95 (3.74 to 4.17)
1996	4.11 (3.89 to 4.33)
1997	4.27 (4.05 to 4.49)
1998	4.71 (4.49 to 4.95)
1999	4.73 (4.50 to 4.96)
2000	4.84 (4.68 to 5.01)
2001	4.63 (4.47 to 4.79)
2002	5.06 (4.90 to 5.23)
2003	5.21 (5.04 to 5.38)
2004	5.25 (5.09 to 5.42)

Figure 1 **Annual age-adjusted incidence of NETs by year (1973 to 2004).** The incidence is presented as the number of tumors per 100,000 (with 95% CIs) age-adjusted for the 2000 US standard population. Cases were selected from the Surveillance, Epidemiology, and End Results database (1973 to 2004) using International Classification of Diseases for Oncology histology codes 8150 to 8157, 8240 to 8246, and 8249. Adapted from Yao et al., 2008.

Pancreatic neuroendocrine tumors (PanNETs), traditionally diagnosed as “pancreatic islet cell” tumors, are the second most common epithelial neosplasm of the pancreas, with a pessimistic mortality rate of 60% (Scarpa et al., 2017). The incidende of PanNETs has undergone a significant increase in recent years, to a rate of nearly 1 per 100,000 (Figure 2) (Lewis et al., 2017).

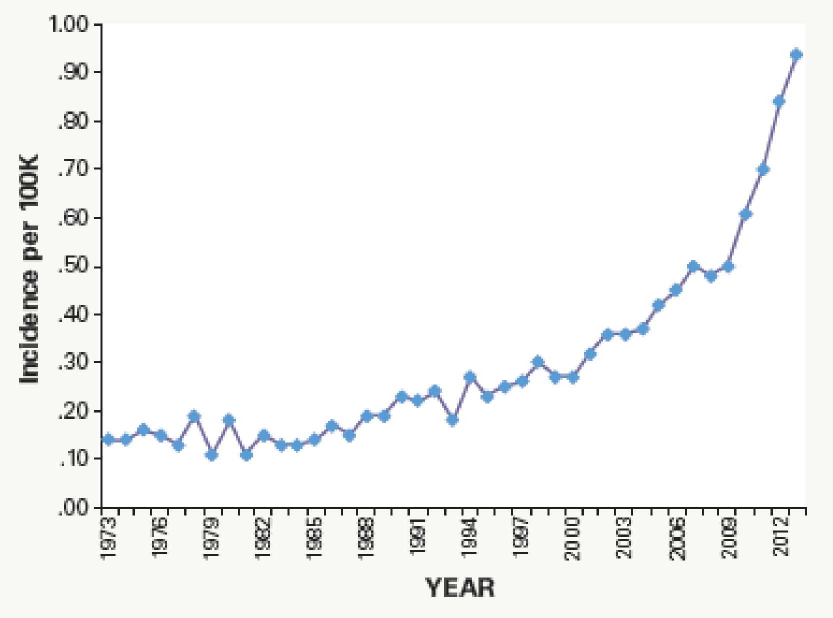

Figure 2 **Surveillance, Epidemiology and End Results (SEER) database age-adjunsted incidence of PanNETs by year of diagnosis (1973-2013).** Data from SEER Database. Figure from Lewis et al., 2017.

PanNETs can be further divided according to their ability to secrete hormones into non-functional and functional types. Functional PanNETs include insulinoma, gastrinoma and glucagonoma, among others. Non-functional PanNETs do not produce syndromes of hormonal excess, butrather cause morbidity and mortality by invading normal tissue and metastasizing (Ehehalt et al., 2009). 50-100% of PanNET cases are malignant, except for insulinoma, where only 10% of cases are. The majority of PanNETs are non-functional, and 85% will develop metastases over their lifetime. Furthermore, they account for a disproportionate number of neuroendocrine liver metastases, which are observed on presentation in an estimated 60% of patients, compared to 27% of all patients with gastroenteropancreatic NETs (Lawrence et al., 2011). Several genetic syndromes are associated with NETs (e.g. MEN1 and tuberous sclerosis); nevertheless, the majority of PanNETs are sporadic and present incidentally.

Since PanNETs are highly heterogeneous in origin, biology and progression, the World Health Organization (WHO) classification was proposed to guide their management and stratify patient prognosis. Related to their pathological grade and state of differentiation and aggressiveness, NETs are divided into three different groups: low grade (G1), intermediate grade (G2) and high-grade tumors (G3), which are mostly non-functional PanNETs (Massironi et al., 2008). The 2017 WHO classification introduced a new category of well-differentiated PanNETs with a high proliferation rate, G3 well-differentiated PanNETs (Table 1) (Lloyd et al., 2017). As depicted by the complexity of PanNET classification, the heterogeneity of PanNETs has further contributed to their limited therapeutic options.

Table 1 **2017 WHO classification of PanNETs.** NEN, neuroendocrine neoplasm; NET, neuroendocrine tumor; NEC, neuroendocrine carcinoma; WD, well differentiated; PD, poorly differentiated; HPF, high-power field. Adapted from Lloyd et al., 2017.

Classification of PanNENs	*Grades*	*Mitotic count (per 10 HPF)*	*Ki-67 index (%)*
G1 WD-PanNETs	G1 (low)	<2	<2
G2 WD-PanNETs	G2 (intermediate)	2-20	3-20
G3 WD-PanNETs	G3 (high)	>20	>20
G3 PD-PanNECs	G3 (high)	>20	>20

To date, surgery for resection of the primary and metastasized tissues is the gold standard treatment, even in some of the most advanced tumors. Beyond surgery, treatment is largely dictated by their heterogenous nature and involves a multidisciplinary approach which consists of a combination of octreotide analogs, targeted therapies and systematic chemotherapy (Lewis et al., 2017). However, many of the alternative therapeutic approaches have failed to demonstrate a long-term survival benefit (Ehehalt et al., 2009). Research on PanNETs is desperately in need for an improvement of the current therapeutic repertoire, for which preclinical model usage becomes imperative. Current and forecoming strategies to treat NETs were recently highlighted by our group (Carrasco et al., 2017).

2. Modeling PanNETs around their limitations

The rarity of PanNETs, the difficulty to access appropiate patient tissue samples, and their varying histopathology and hormone secretion patterns present challenges to researchers and clinicians. Those barriers make both animal and cell models especially useful for the investigation of the mechanisms for tumor invasion, metastasis and therapeutics. In fact, they provide invaluable insight into the natural history of the human disease, because most common animal models (mice and rats) have a relatively short life span and can be observed in large numbers. They even allow tissue retrieval at all stages of tumorigenesis, which has been essential to demonstrate that the pathogenesis of PanNETs follows distinct morphological stages of hyperplasia, dysplasia and frank PanNETs (Babu et al., 2013).

Animal models of PanNETs are murine models mainly derived from two experimental approaches. Some models are made by transgenic expression of oncogenes under the insulin or preproglucagon promoter. There are also incidental or purposed models that mimic the genetic abnormalities of human PanNETs syndromes, such as MEN1. Animal and cell models of PanNETs are thoroughly reviewed by Babu et al. (Babu et al., 2013). To date, the best described animal model of PanNET is the RIP1-Tag2 mouse, developed by Hanahan more than 30 years ago (Hanahan, 1985).

2.1. RIP1-Tag2 model: 30 years of research

The RIP1-Tag2 transgenic murine model is the par excellence animal model of pancreatic β-cell carcinogenesis, being instrumental in identifying several hallmarks of cancer, including tumor angiogenesis and invasion. In this model, PanNETs are induced by the expression of an oncogene in insulin-producing islet β cells (Figure 3A) (Hanahan, 1985). In detail, RIP1-Tag2 mice express the SV40 large T-antigen (Tag) oncogene in all their islet cells at birth, under the control of the rat insulin gene promoter (RIP). The expression of T-antigen specifically in β-cells abrogates p53 and RB tumor suppresors, eliciting the sequential development of highly vascularized tumors in the pancreatic islets over a period of 12-14 weeks (Figure 3B). Islet tumors in RIP1-Tag2 mice may finally lead to liver metastasis, as previously explained for human PanNET patients (Figure 3B).

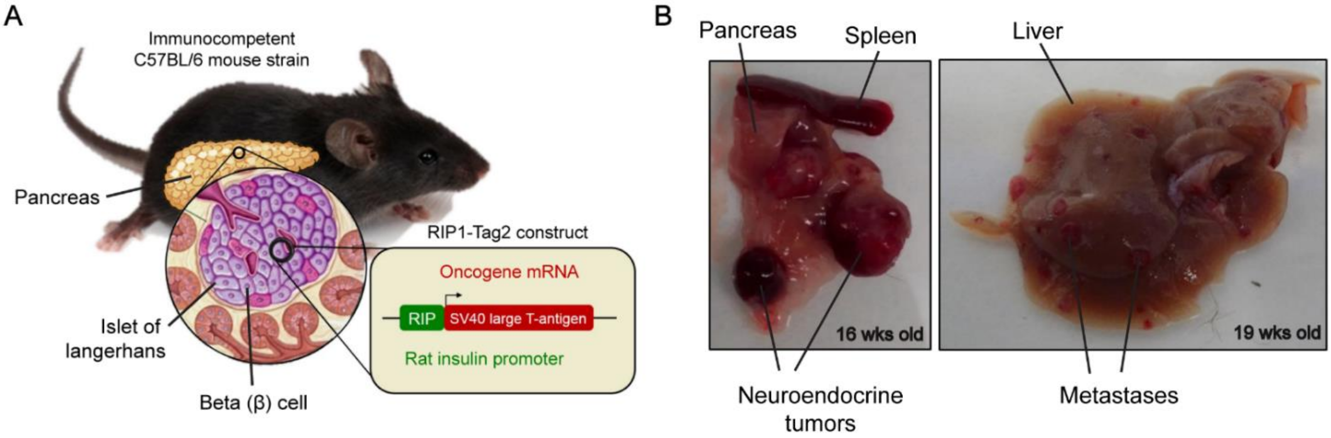

Figure 3 **Genetic and histological features of RIP1-Tag2 mouse model of PanNET. A)** RIP1-Tag2 transgenic mice are engineered to express the SV40 large T-antigen oncogene (SV40-Tag) under the rat insulin promotor (RIP), which allows the specific transformation of β-cells of the pancreas. **B)** Macroscopic images of a 16 weeks old RIP1-Tag2 mice pancreas (**left**) and a 19 weeks old RIP1-Tag2 mice liver metastases (**right**).

T-antigen hybrid oncogene is expressed in the approximately 400 pancreatic islets and elicits a highly natural, synchronous and stepwise tumorigenesis pathway (Figure 4). Hyperplastic/dysplastic islets start arising at 3 weeks of age, of which about 25% switch on angiogenic signaling by 6 to 9 weeks (Folkman et al., 1989). The switch is characterized by endothelial proliferation, vascular dilation and microhemorrhaging. This is followed by the formation of PanNET in 15-20% of the cases. At the end stage of 14-16 weeks, every mouse harbors from 2 to 10 solid tumors (Hanahan, 1985, 1988). RIP1-Tag2 mice develop PanNETs of varying malignancy, including adenomatous and invasive carcinomas (Figure 4B). Adenomatous tumors are encapsulated tumors with well-defined margins and less invasion in both surrounding exocrine pancreas, islet/insulinoma tumors (IT). Malignant RIP1-Tag2 tumors are classified according to their invasion of the adjacent tissue. Invasive carcinoma type 1 (IC1) shows focal regions of invasion with adjacent margins, with tumor cells intercalated into exocrine tissue, whereas invasive carcinoma type 2 (IC2) present widespread invasion with no evidence of margins: extensive intercalation of tumor cells into exocrine pancreas. Further morphological data to characterize the different stages of RIP1-Tag2 tumorigenesis are compiled in Lopez and Hanahan, 2002.

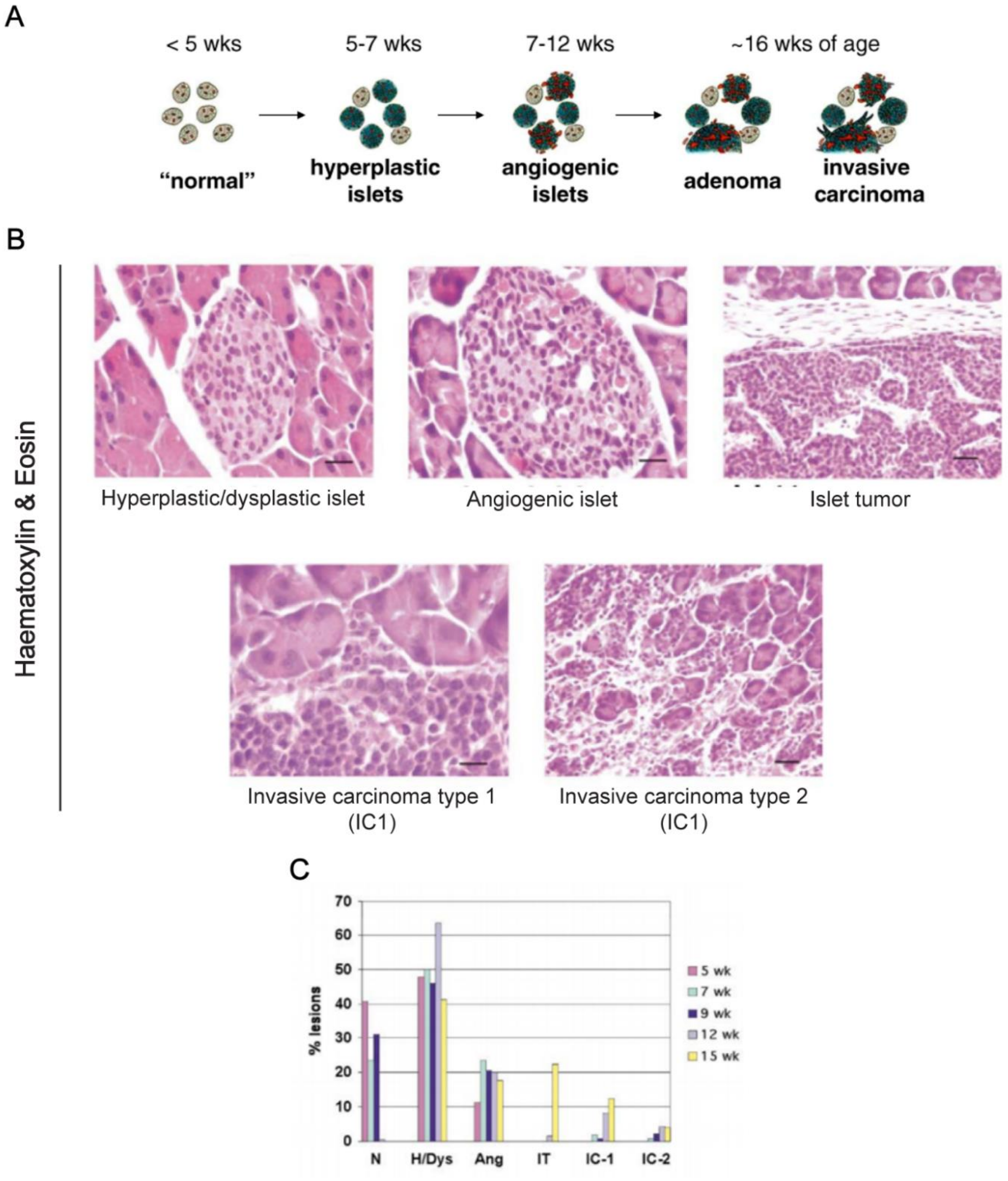

Figure 4 **Multistage cancer progression in RIP1-Tag2 mouse model. A)** Schematic representation of RIP1-Tag2 tumor progression. Modified from the *RIP1-Tag2* Manual, Hanahan laboratory, unpublished. **B)** Morphology of the distinctive stages in islet carcinogenesis. Expression of the Tag oncogene in pancreatic islets elicits four sequential stages in tumor development: normal, oncogene-expressing islets; hyperplastic islets, populated by proliferating cells; angiogenic islets, in which new blood vessel growth has

been activated; and solid tumors, which are PanNETs. Solid tumors can be classified as islet tumors (IT, encapsulated) or invasive carcinomas (IC1 or IC2). Scale bars represent 20 µm on all micrographs except the islet tumor and invasive carcinoma type 2, where the scale is 40 µm. **C)** Substantial numbers of lesions were classified at various time points in the life spans of RIP1-Tag2 mice. **B-C** were adapted from Lopez and Hanahan, 2002.

Seeking to assess the research value of RIP1-Tag2 tumors for its cognate human cancer, a genomic comparison of tumors from both human and mice samples has been recently performed (Sadanandam et al., 2015). Mouse PanNET tumors were classified into two distinctive subtypes: well-differentiated IT and poorly differentiated tumors associated with liver metastasis (MLP), which include both IC1 and IC2 subtypes. Human PanNETs were independently split into these same two subtypes, with an additional third one, specific of MEN-1 mutation-enriched subtype not present in RIP1-Tag2 mice. Interestingly, both MLP subtypes in human and mouse were similar to liver metastases regarding their transcriptome profiles and signature genes and coincided with a non-functional signature. They also expressed genes which are regulated during early pancreas development, whereas IT subtypes expressed genes specific for mature islet cells and were functional. Hence, it has been proven that the distinct molecular mechanisms behind two of the three human PanNET subtypes, IT and MLP, can be further studied using the RIP1-Tag2 model as a surrogate for both human functional and non-functional tumors (Figure 5).

In this context, when compared to the human PanNETs, the temporal and histological changes in RIP1-Tag2 model are also consistent with the multistep paradigm for tumorigenesis described in human cancers (Vogelstein and Kinzler, 1993). Besides, the synchronicity in tumor progressionmight have predicted homogeneity in histologic and genetic phenotypes, if compared to human cancers. However, interestingly, there is evidence for genetic and phenotypic heterogeneity in RIP1-Tag2 tumors, since a range of chromosomal aberrations have been observed (Hodgson et al., 2001).

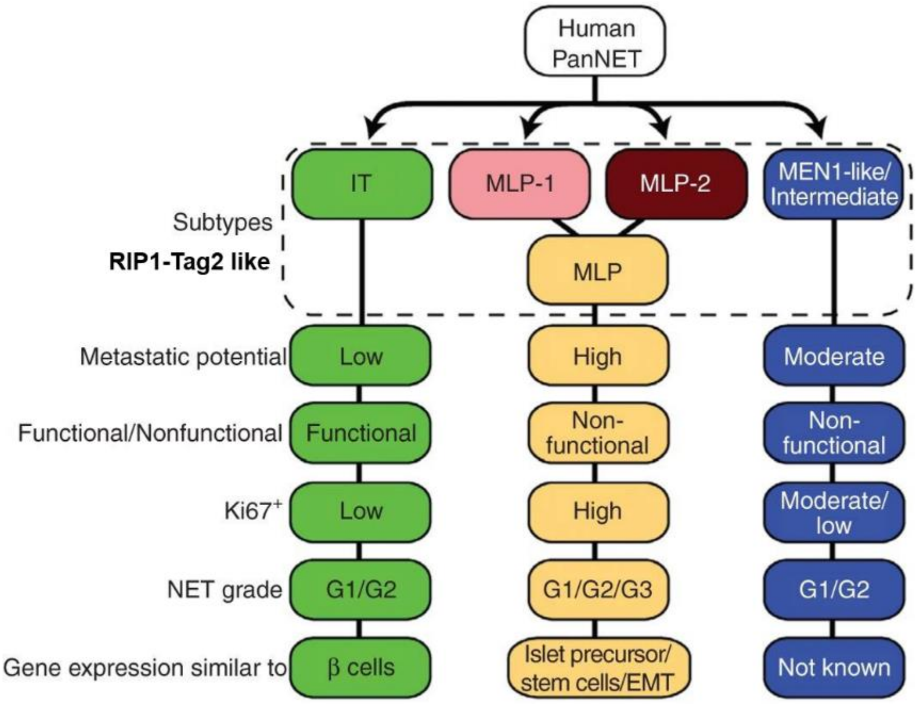

Figure 5 **PanNET tumor heterogeneity in humans has its counterpart in RIP1-Tag2 mice.** Summary of human PanNET subtypes and their characteristics. RIP1-Tag2 IT tumor subtype (including hyperplasic and encapsulated tumors) is more similar to functional low-grade G1/G2 human tumors. MLP subtypes (including invasive IC1 and IC2 tumors). Similarites in RIP1-Tag2 are inferred in the human from the concordance of transcriptomic and phenotypic data presented for mouse and human PanNET. Adapted from Sadanandam et al., 2015.

Functionally, RIP1-Tag2 model has proved to be a valuable prototype for the study of the stepwise progression of multistage tumorigenesis (Hanahan, 1988; Hanahan and Folkman, 1996). Hence, this model has revealed the angiogenic switch (Folkman et al., 1989), the importance of apoptosis attenuation (Christofori et al., 1994), and the determinants of progression towards an invasive growth phenotype (Joyce et al., 2004; Lopez and Hanahan, 2002; Perl et al., 1998). Moreover, Rip1Tag2 model has been helpful in the clinical development of targeted cancer therapies, since it allows its testing in a stage-specific manner (Bergers et al., 1999). For instance, preclinical trials of angiogenesis inhibitors targeting vascular endothelial growth factor (VEGF) signaling pathway predicted efficacy and incentivized clinical trials that led to the approval of sunitinib for the treatment of human PanNETs (Raymond et al., 2011). The role of tumor angiogenesis in RIP1-Tag2 mice is further discussed during the following sections of this Thesis.

3. Insight into angiogenic hallmarks

In order to grow beyond a limited size, all solid tissues require proper vasculature that grants oxygen, nutrients, and waste disposal. Since neoplasms are no exception to this rule, early activation of angiogenic processes is mandatory to sustain the deregulated proliferation of tumor cells (Zuazo-Gaztelu and Casanovas, 2018). Apart from serving as nutrient, oxygen, and waste transport providers, vessels also facilitate dissemination of tumor cells to distant sites, promoting metastasis. Additionally, activated endothelial cells release anti-apoptotic factors to tumor cells in a paracrine fashion. Tumor angiogenesis is thus defined as the process of blood vessel creation, penetration and growth in the tumor ecosystem, critical for the survival of solid neoplasms.

Even though PanNETs are highly heterogenous neoplasms, they share a common feature: they are highly vascular. This is a usual characteristic of endocrine glands, which have a dense vascular network that facilitates hormone secretion to the bloodstream. In the case of NETs, some studies have shown that intratumoral vessel density normally is 10-fold higher in NETs than in other neoplasms (Carrasco et al., 2017). Another of the attributes of PanNET cells is their ability to synthesize and secrete high levels of proangiogenic molecules, specially VEGF (Capdevila et al., 2014). VEGF is regarded as the canonical angiogenesis initiator due to its induction of vascular permeabilityand endothelial cell proliferation (Carmeliet, 2005; Ferrara et al., 2003).

Tumor transition from endocrine hyperplasia to neoplasia is related to the acquisition of angiogenic properties (Hanahan and Folkman, 1996), which can be blocked by the use ofantiangiogenic agents (Bergers and Benjamin, 2003). In this context, the RIP1Tag2 model has been widely used to study the sensitivity of PanNETs to different antiangiogenic drugs. In RIP1-Tag2 mice, VEGF signaling is also primarily involved in angiogenesis and tumorigenesis. VEGFA is expressed at all stages of RIP1-Tag2 tumorigenesis, which suggests that its activity is crucial for tumor progression. A beta-cell-specific VEGFA knockout resulted in islets with reduced vascularity and tumor growth, and angiogenic switch disruption (Inoue et al., 2002).

Several antiangiogenic treatments have been evaluated to prevent the angiogenic switch in premalignant lesions and restrict the rapid expansion of tumors. PanNETs show strong expression of VEGFR2 and VEGFR3 (Hansel et al., 2003). For instance, the use ofblocking antibodies to VEGFR2 demonstrated that anti-VEGFR2 markedly disrupted angiogenic switch and initial tumor growth in RIP1-Tag2 mice (Casanovas et al., 2005). PanNETs also show strong expression of platelet-derived growth factor receptors (PDGFRs) α and β, together with stem-cell factor receptor (c-kit) (Fjällskog et al., 2003, 2007). Advances in the understanding of PanNET ecosystem and biology have defined these receptors as potential targets for antiangiogenic therapies (De Dosso et al., 2013).

3.1. The angiogenic switch and intratumor hypoxia

In the absence of new vasculature, during the avascular phase, tumor growth is normally restrained to no more than 1–2 mm3. Tumors obtain nutrients and oxygen from nearby blood vessels and angiogenic processes are not observed. The avascular tumors reach a stable state characterized by a balance between proliferation and apoptosis. To grow beyond the restricted size and sustain unlimited proliferation, tumors require their vascular network to be extended. This transition from this avascular state to the angiogenic phase is commonly known as “angiogenic switch” and, in PanNETs, it occurs early during tumor progression (Figure 6) (Hanahan and Folkman, 1996).

The angiogenic switch depends on a dynamic balance between positive (proangiogenic) and negative (antiangiogenic) factors controlling vascular homeostasis (Hanahan and Folkman, 1996). Under physiological conditions, this balance is shifted towards negative regulation of angiogenic processes, thus maintaining the quiescence of the vasculature. Once tumor progression is started, when RIP1-Tag2 mice develop hyperplastic islets, the loss of tumor suppressor genes and oncogene upregulation revert this balance. During the first steps of tumorigenesis, high levels of strong angiogenic inducers, such as VEGF and FGF, are released to the tumor ecosystem. Other proangiogenic molecules upregulated for the engagement of tumor angiogenesis are PDGF, EGF, TGF-β, FGF, semaphorins, MMPs, and angiopoietins (Zuazo-Gaztelu and Casanovas, 2018).

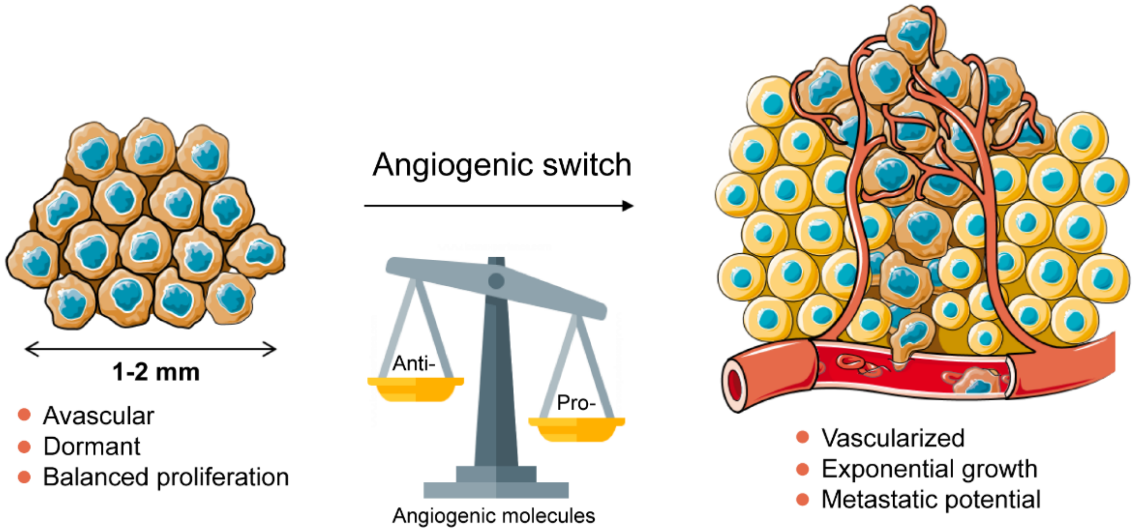

Figure 6 **Angiogenic switch.** Early during tumor progression, malignant cells switch on the angiogenic program to grow beyond a restricted size of 1-2 mm^3. An increase in proangiogenic molecules produces a shift on the angiogenic regulation which increases vascularization, growth and metastatic potential of the tumor.

Lack of oxygen inside the tumor occurs as an inevitable consequence of the rapid expansion of the tumor mass. Neoplasms have been generally described as highly hypoxic structures, bearing distorted and abnormal vascular networks, inefficient in oxygen transportation (Vaupel, 2004). Hypoxia is known to upregulate proangiogenic inducers and endothelial–pericyte destabilizing molecules (Ang-2) and downregulate inhibitors. Furthermore, mobilization of bone marrow-derived precursor cells and recruitment of immune cells to the tumor ecosystem is also positively controlled by hypoxia (Blouw et al., 2003).

4. Targeting the vessels for PanNET treatment: Antiangiogenic therapy in NETs

Due to the limitations of conventional drugs, which are not selective enough and produce severe side effects, vascular inhibitory targeting was proposed as a new approach to fight against tumor growth in PanNET patients. Although the rationale of using angiogenesis inhibitors as anticancer drugs was received with skepticism among researchers when first presented by Folkman in the 70s, it soon startled an active research in the field, with the identification of several angiogenic inhibitors and subsequent clinical trials (Sherwood et al., 1971). This promising strategy leads to tumor cell death by the lack of oxygen and nutrient deprivation as a consequence of blood vessels. In this context, growth factors, their receptors and subsequent signaling cascades involved in vascular homeostasis are promising targets in angiogenesis inhibition. Importantly, many drugs have been developed and tested in well-differentiated NETs to block angiogenic growth factors and their receptors. Some of them, such as bevacizumab and sunitinib, have been already approved by the US Food and Drug Administration (FDA) for the treatment of some of these tumor types (Capozzi et al., 2016).

Taking into account the abundance of mechanisms involved in tumor angiogenesis, blood vessel formationcan be inhibited at many different levels (Zuazo-Gaztelu and Casanovas, 2018). The main effects of angiogenic inhibitors can be classified according to their effects on: inhibition, regression, or normalization of tumor blood vessels. PanNET-derived tumor cells can deregulate the tyrosine kinase (TK) activity, thereby affecting many aspects of cellular function and confering advantages to cancer cells regarding proliferation, angiogenesis and invasiveness. Tyrosin kinase inhibitors (TKIs) are small molecules with the ability to interact with the highly conserved kinase domains shared by different VEGFRs, as well as PDGF receptors, FGF receptors (FGFRs), EGF receptors (EGFR), Raf kinases and c-kit (a receptor of the pluripotent cell growth factor or stem cell factor), hence blocking the receptor activation (Krause and Van Etten, 2005). TKIs can also be antibodies that bind to growth factors and prevent ligand-receptor binding. Since TK receptors are expressed both in tumor and vascular cells, TK inhibitors (TKIs) are regarded as a useful drugging strategy for their potentially dual effect.

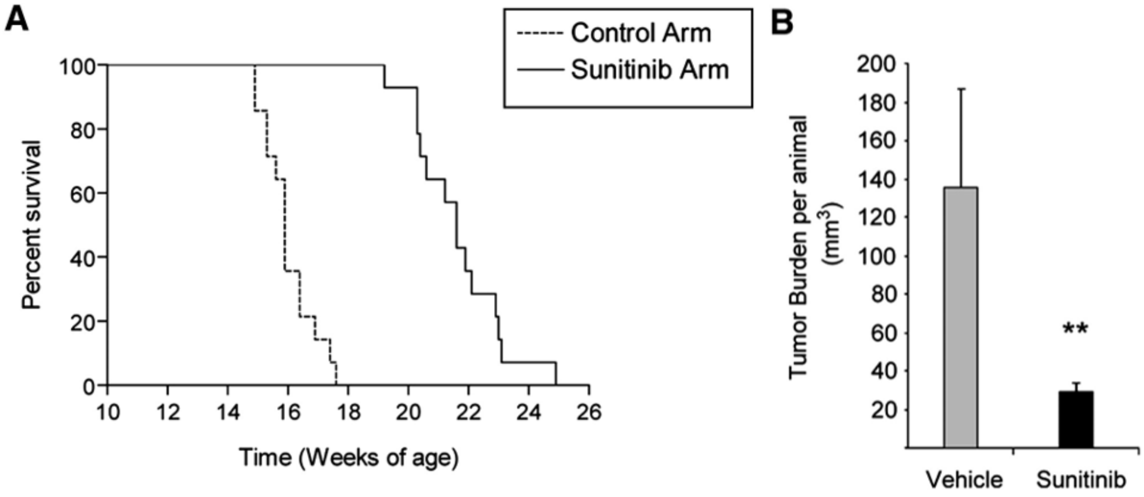

Figure 7 **Increased life span and tumor reduction in sunitinib-Treated RIP1-Tag2 animals. A)** Kaplan-Meier survival curves in tumor-bearing RIP1-Tag2 mice (12 weeks) treated continuously with vehicle control or sunitinib starting at 12 weeks. While vehicle-treated mice showed a median life span of 15.2 weeks, mice receiving continuous sunitinib treatment demonstrated a survival benefit of 7 additional weeks. **B)** Total tumor burden analysis in 5-week treatment trials with sunitinib or vehicle control starting therapy at 10 weeks of age. **p < 0.01 by Mann-Whitney test. Error bars indicate ± SEM. Modified from (Pàez-Ribes et al., 2009).

Sunitinib malate (Sutent®, Pfizer) inhibits VEGFR2-3, PDGFRα-β and c-kit (Faivre et al., 2007; Mendel et al., 2003) and delays tumor growth in RIP1-Tag2 mice by reducing endothelial cell density and pericyte coverage of tumor vessels (Pàez-Ribes et al., 2009; Pietras and Hanahan, 2005; Yao et al., 2006). On the basis of these findings, a phase 3 clinical trial of sunitinib was performed to assess its effectivity in patients with advanced PanNETs (Raymond et al., 2011). Median progression-free survival in the sunitinib group was 11.4 months, as compared with 5.5 monts in the placebo group. Improvement in overall survival and the objective response rate (9% versus 0% in the placebo group) were also observed. Those findings were of particular importance due to the limited number of effective treatment options for advanced disease. The ClinicalTrials.gov identifier was NCT00428597.

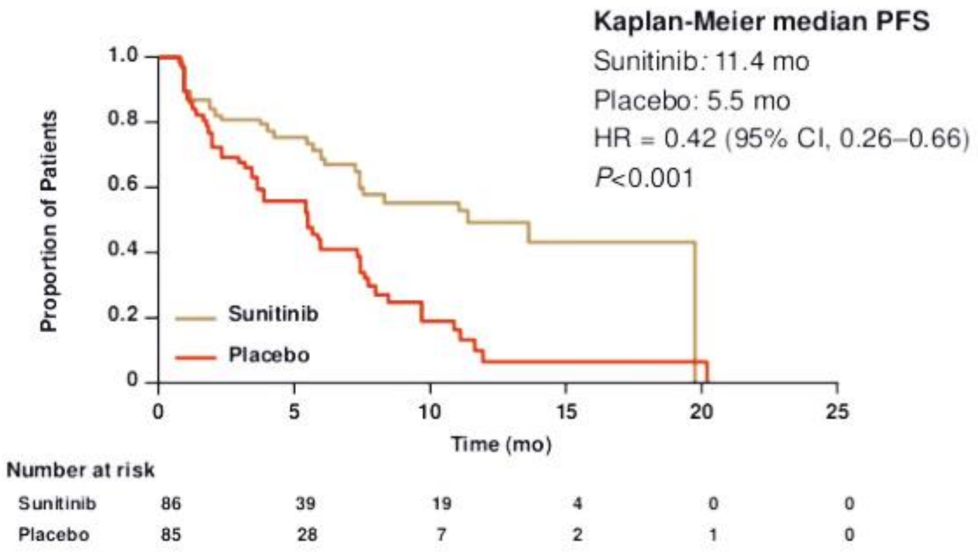

Figure 8 **Kaplan-Meier Analysis of Progression-free Survival in Sunitinib Vs. placebo treated advanced PanNET patients.** Among 171 (86 patients who received sunitinib and 85 patients who received placebo), the median progression-free survival was 11.4 months in the sunitinib group versus 5.5 monts in the placebo group. Modified from (Raymond et al., 2011)

5. Resistance to standard antiangiogenic therapy

Even though many angiogenesis inhibitors have been described, only some of them have been approved and used in the clinic. Furthermore, the clinical benefit of antiangiogenic drugs remains limited due to the acquisition of drug resistance by stromal cells, so they need to be improved to guarantee patient's long-term response. As a result, antiangiogenics produce a progression delay with a period of clinical benefit, rather than providing enduring efficacy in tumor shrinkage or dormancy (Bergers and Hanahan, 2008).

An example of therapy failure was observed in a preclinical study using the RIP1-Tag2 model. The initial efficacy of antiangiogenic therapy in vivo was then followed by the acquisition of resistance, as demonstrated by tumor revascularization, regrowth and invasiveness (Casanovas et al., 2005). Using RIP-Tag2 mice, our group has recently described not only an appearance of phenotypic resistance to antiangiogenic therapies, but also an increase of the invasive phenotype in tumors under anti-VEGF treatment (Figure 9) (Pàez-Ribes et al., 2009).

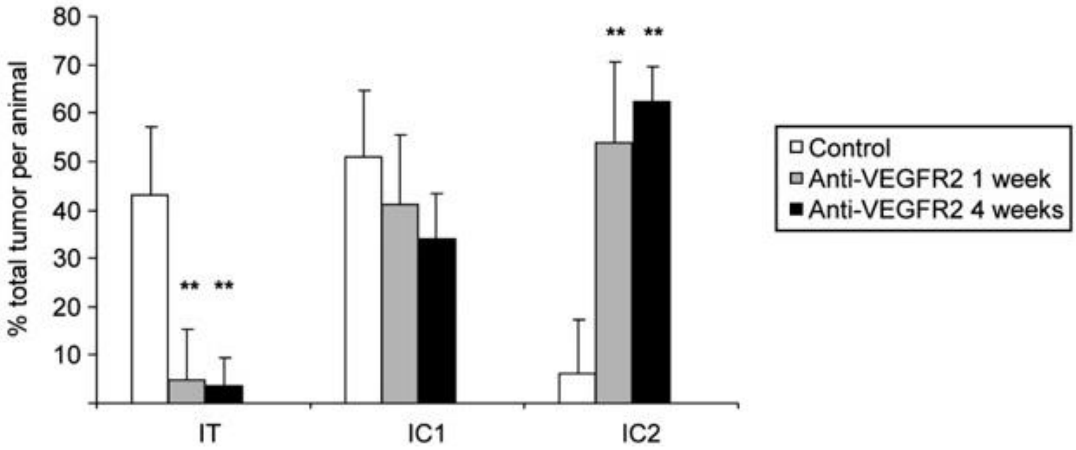

Figure 9 **Increased invasive phenotype after anti-VEGFR2 therapy.** Quantification of histological analysis tumor invasiveness represented as the percentage of encapsulated islet tumors (IT), microinvasive carcinomas (IC1), and fully invasive carcinomas (IC2) for control and anti-VEGFR2 antibody (DC101)-treated RIP1-Tag2 mice. Both anti-VEGFR2 treatments show a statistically significant decrease in the percentage of IT and a significant increase in IC2 tumors (**p < 0.01 by Kruskal-Wallis test). Modified from Pàez-Ribes et al., 2009.

Among the effects that could be identified after short-term treatment (2 weeks treatment), we described tumor cells invasion into blood and lymphatic vessels, which consequently led to an increase in the incidence of lymphatic and hepatic metastases (Figure 10). These features are related to tumor malignization after antiangiogenic therapy is supplied.

As a consequence of vessel trimming after angiogenic inhibitors, an increased hypoxic environment develops inside the tumor (Figure 11). Even though cancer cells can endure hypoxic conditions (Fraisl et al., 2009), growing evidence indicates that tumor cells escape from this environment to better nourished locations, using hypoxia as a positive stimulus for invasion (Pennacchietti et al., 2003). In fact, it has been reported that there is a strong correlation between tumor hypoxia, increased invasion, metastasis and poor patient outcome (Schindl et al., 2002; Semenza, 2002; Zhong et al., 1999)

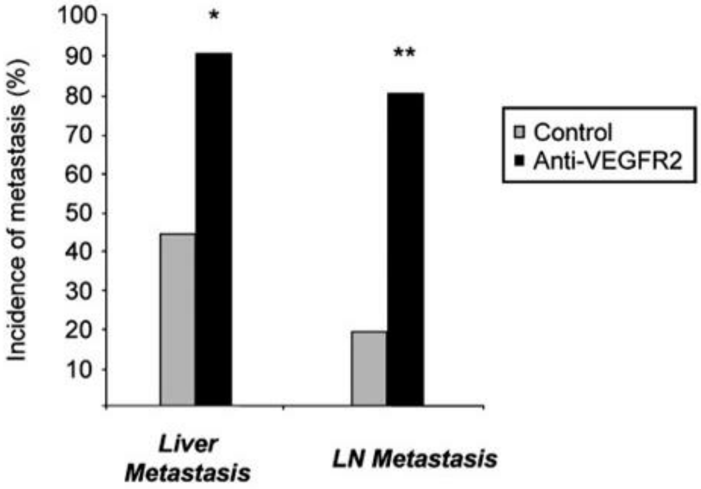

Treatment:	Yes	No		Yes	No	
Anti-VEGFR2	9 (90%)	1 (10%)	*10*	8 (80%)	2 (20%)	*10*
Control	7 (44%)	9 (56%)	*16*	3 (19%)	13 (81%)	*16*
	16	*10*	***26***	*11*	*15*	***26***

χ^2, $p < 0.05$ χ^2, $p < 0.01$

Figure 10 **Increased incidence of lymph node and liver metastasis in Anti-VEGFR2-treated animals.** Histological analysis of lymph node (LN) and liver metastasis (Met) in RIP1-Tag2 animals treated with anti-VEGFR2 for 10 days starting at 10 weeks of age and then left untreated until 16 weeks of age. **Top:** Quantification of the incidence of animals with microscopic liver micrometastasis and macroscopic LN metastasis in the control (gray bars) and anti-VEGFR2-treated (black bars) treatment arms. **Bottom:** contingency table relating the number and percentage of animals in each treatment/metastasis case. Treated animals show a statistically significant increase in the incidence of liver micrometastasis and LN metastasis by the chi-square test (*p < 0.05; **p < 0.01). Modified from Pàez-Ribes et al., 2009.

A key mediator of cellular responses to low oxygen is the hypoxia inducible factor-1 (HIF-1), a transcription factor also described as an activator of c-Met, a protein involved in the increase of aggressiveness and invasiveness of hypoxic cells ((Pennacchietti et al., 2003). VEGF inhibitors have been reported as positive regulators of HIF-1-induced c-Met expression that leads to an invasive cellular program and promotes metastases (Bottaro and Liotta, 2003; You et al., 2011). In order to avoid the latter appearance of resistance due to increased hypoxia levels, new strategies are being developed, aimed at targeting other players of tumor angiogenesis alone or combined with traditional targets such as VEGF.

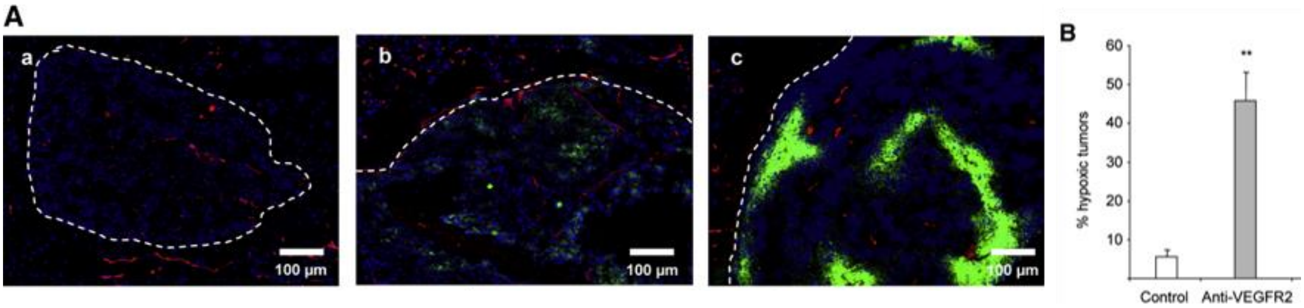

Figure 11 **Antiangiogenic treatment also provokes hypoxia in tumors. A)** Hypoxia in islet tumors was detected by immunofluorescence staining of pimonidazole adducts in sections of pancreas from control untreated animals (Aa) and animals receiving short-term (Ab) or long-term (Ac) anti-VEGFR2 treatment. **B)** Quantification of the incidence of hypoxic tumors was performed in long-term anti-VEGFR2-treated animals and plotted as the percentage of pimonidazole-positive tumors per animal compared to control animals. $^{**}p < 0.01$ by Mann-Whitney test. Error bars indicate ± SEM. Modified from Pàez-Ribes et al., 2009.

6. Semaphorins as alternative targets for antiangiogenic therapies

The semaphorin family was initially characterized for its axon guidance properties, but they have subsequently been implicated also in the regulation of organ formation, immune responses, angiogenesis and a wide range of additional physiological, developmental and pathological functions. Recent research has given insight into the role of semaphorins in tumor progression (Neufeld et al., 2016).

6.1. The semaphorin family

Members of the semaphorin family are divided into 8 subclasses, of which subclasses 1 and 2 contain invertebrate semaphorins, while subclasses 3-7 contain 22 vertebrate counterparts. Subclass 8 contains viral semaphorins. Currently used unified semaphorin nomenclature was adopted in the late nineties, in which “sema” is followed by the subclass number and by alphabetic designation within each subclass (Goodman et al., 1999). The main characteristic of semaphorins is the presence of a ~ 500 aminoacids long Sema domain located close to the N-terminal region, which is also present in semaphorin receptors of the plexin family. They also have a plexin-semaphorin-integrin (PSI) domain, located downstream of the sema domain. Sema domain is essential for the activity of semaphorins and plays a role in the determination of the receptor binding specificity (Feiner et al., 1997). Sema domains from different semaphorin types reveal a seven-bladed β-propeller topology, as seen by X-ray crystallography studies (Love et al., 2003).

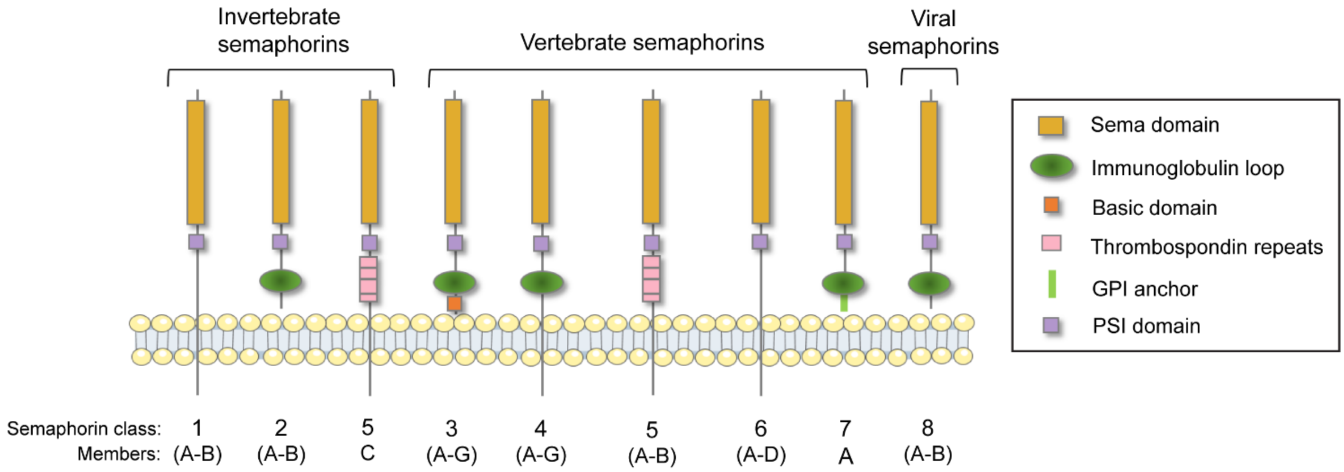

Figure 12 **Structure of semaphorins and their receptors. A)** The structural elements of semaphorin subclasses are shown. All feature the signature N-terminal sema domain. A conserved stretch of amino-acid residues near the C-terminal of the sema domain bears homology to the N-terminal of β-integrins and is designated as the PSI domain. Class-3 semaphorins are distinguished by a conserved basic domain at their c-termini. Class 4–7 semaphorins are membrane-anchored. Class 5 semaphorins are distinguished by thrombospondin repeats. All the vertebrate semaphorins except for the class-5 and 6 semaphorins also contain an immunoglobulin like domain. Adapted from Neufeld et al., 2016.

Class-specific structural motifs characterize different semaphorin subclasses (Figure 12). Hence, the vertabrate semaphorins belonging to classes 3, 4 and 7 contain immunoglobulin-like domains, whereas class-5 semaphorins contain thrombospondin repeats. Class-3 semaphorins contain a basic domain and are the only vertebrate semaphorin produced as secreted proteins. The rest of vertebrate proteins are membrane-anchored or transmembrane proteins that can be processed into soluble forms by proteolytic cleavage (Figure 12). Some membrane-anchored semaphorins, such as Sema4D, may function as signal transducing proteins (Witherden et al., 2012). Moreover, the active forms of several semaphorins are homodimeric, suggesting that all active semaphorins can form homodimers.

6.2. Semaphorin receptors

6.2.1. Plexins

Most semaphorins are able to bind one or several members of the plexin gene family (Hota and Buck, 2012), which comprises 9 receptorsdivided into 4 groups, consisting of 4 type-A plexins, 3 type-B plexins, and single C and D plexins (Alto and Terman, 2017). Some binding partner examples include: Plexin-B1 and Sema4D, PlexinB3 and Sema5A, PlexinA1 and Sema6D/Sema5A-B (Figure 13).

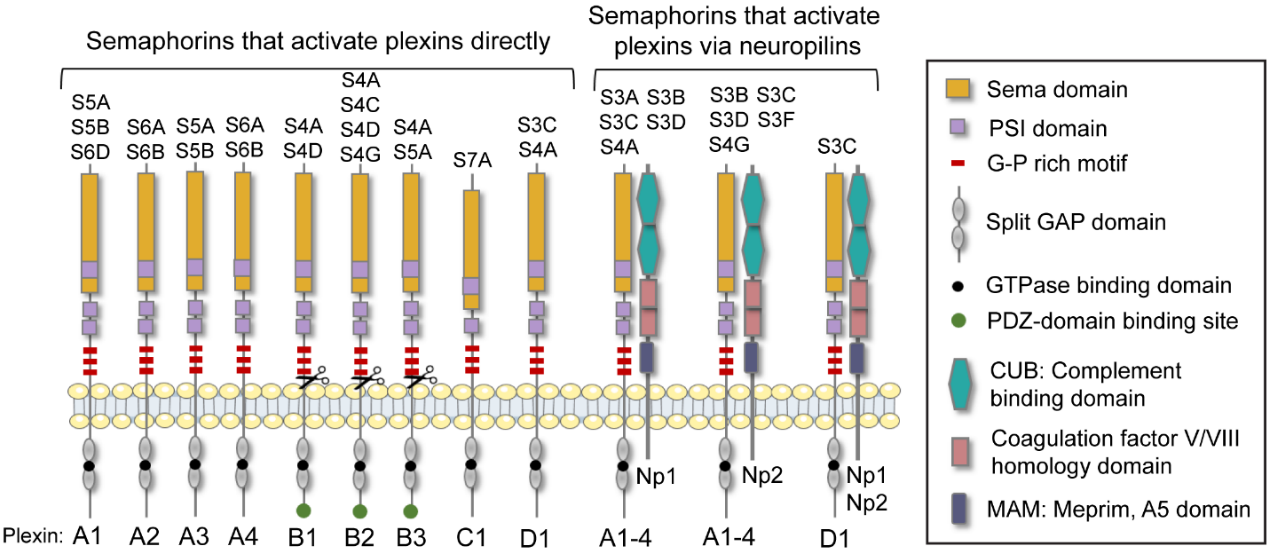

Figure 13 **Interaction of vertebrate semaphorins with their neuropilins and plexin receptors.** Different semaphorins are described using a 3-letter code in which the S stands for semaphorin, the number designates the subfamily, and the following letter designates the specific subfamily member. For instance, s3a stands for sema3A. The specific interactions between individual semaphorins and either single plexins or specific neuropilins are shown. Adapted from Neufeld et al., 2016.

The extracellular domains of all plexins contain a sema domain that serves as an auto-inhibitory domain in the non-activated, basal state of the receptor. The intracellular domain contains a split cytoplasmic SP (sex-plexin) domain and a putative tyrosine phosphorylation sites, but no tyrosine kinase domain. Those intracellular parts also are characterized by the presence of a GTPase activating (GAP) domain, which is highly conserved throughout the family (Negishi et al., 2005a).

Plexins have also been found to form complexes with other receptors such as TK receptors, activating them "in-trans" upon binding of specific semaphorins such as Sema4D and Sema6D (Swiercz et al., 2008). Activation of plexin signaling by semaphorins such as Sema4D activates the GAP domain of Sema4D receptor PlexinB1, inducing the inactivation of R-ras. This results in the subsequent inactivation of β1-integrin, which eventually reduces cell-adhesion (Negishi et al., 2005b). Moreover, Sema4D also activates various intracellular tyrosine-kinases, and inactivates small GTPases such as Rho (Franco and Tamagnone, 2008; Püschel, 2007). To date, even though many efforts have been made to describe semaphorin-plexin interactions, semaphorin-induced signaling is far from being comprehensively understood.

6.2.2. Neuropilins

6 out of the 7 class-3 semaphorins do not bind to plexins directly but instead bind one or both of the 2 receptors of the neuropilin (Nrp) receptor family (Figure 13) (Neufeld et al., 2016). Neuropilins then subsequently associate with type-A or type-D plexins to transduce class-3 semaphorin signaling. Neuropilins are best described as "scaffold receptors", since they bind and modulate activity of diverse types of receptors but do not transduce signals independently. Interestingly, neuropilins can also bind several types of growth factors such as VEGF, bFGF and HGF. In this context, neuropilin-1 functions as an amplifier that enhances VEGF proangiogenic signaling mediated by VEGFR-2 receptor (Soker et al., 1998).

6.2.3. Other semaphorin receptors

Some semaphorins bind to other types of receptors besides plexins and neuropilins. Sema4D, for instance, is able to bind to the lymphocyte receptor CD72 (Kumanogoh et al., 2000), whereas Sema4A also signals through Tim-2 receptor, a member of T-cell Ig domain expressed on activated T cells (Kumanogoh et al., 2002a).

6.3. Semaphorins as regulators of tumor progression

During tumor progression, semaphorins can act by directly influencing the behaviour of tumor cells, or indirectly, by modulating angiogenesis (Figure 14) (Carrasco et al., 2017). Additionally, depending on their post-translational modifications, they can have ambivalent roles in tumor progression. For instance, while Sema4A, 4B, 3E and 3F act as negative regulators of tumor angiogenesis (Klagsbrun et al., 2002; Schwarz et al., 2004), Sema3C-D and 5A promote tumor angiogenesis (Banu et al., 2006; Basile et al., 2004; Miyato et al., 2012; Sadanandam et al., 2010a). Semaphorins are highlighted as alternative antiangiogenic targets which, if adequately inhibited or activated, could potentially impair tumor growth (Capparuccia and Tamagnone, 2009; Pircher et al., 2014; Rehman and Tamagnone, 2013).

More than 10 years ago, Hanahan and Weingerg gathered the pleiotropic changes occurring during tumor progression into six hallmarks shared by most types of tumors (Hanahan and Weinberg, 2000). Ten years later, tradicional hallmarks were updated to include new additionally important acquired characteristics of tumor cells (Hanahan and Weinberg, 2011). Semaphorin signaling appears to regulate at least seven of such hallmarks: sustained proliferation, apoptosis evasion, oxidative stress regulation, angiogenesis activation, activation of invasion and metastasis, pro-tumorigenic inflammation and immune surveillance evasion (Figure 14) (Rehman and Tamagnone, 2013).

Another important Sema3 molecule with a potent antiangiogenic activity is Sema3F. It has been shown to suppress tumor angiogenesis and metastasis in several cancer mouse models (Kessler et al., 2004). Similarly to Sema3A, Sema3F acts as a vascular normalizing agent, blocking peritumoral vessel sprouting, tumor cell adhesion and migration. Moreover, it has also been described as a metastasis suppressor in different animal models (Bielenberg et al., 2006). Sema3E is also involved in the regulation of tumor angiogenesis and cancer progression. In fact, its re-expression in a xenograft melanoma model strongly reduces metastasis formation (Roodink et al., 2008). Finally, Sema3B, in addition to its direct antitumor effect, can also acts as an angiogenic inhibitor (Varshavsky et al., 2008). These findings further corroborate that the aberrant vasculature in tumors is a direct consequence of an imbalance between the pro- and antiangiogenic factors. Therefore, the restoration of this equilibrium in tumors by re-expressing Sema3A, E and F, is crucial for tumor vasculature normalization and, consequently, tumor growth control.

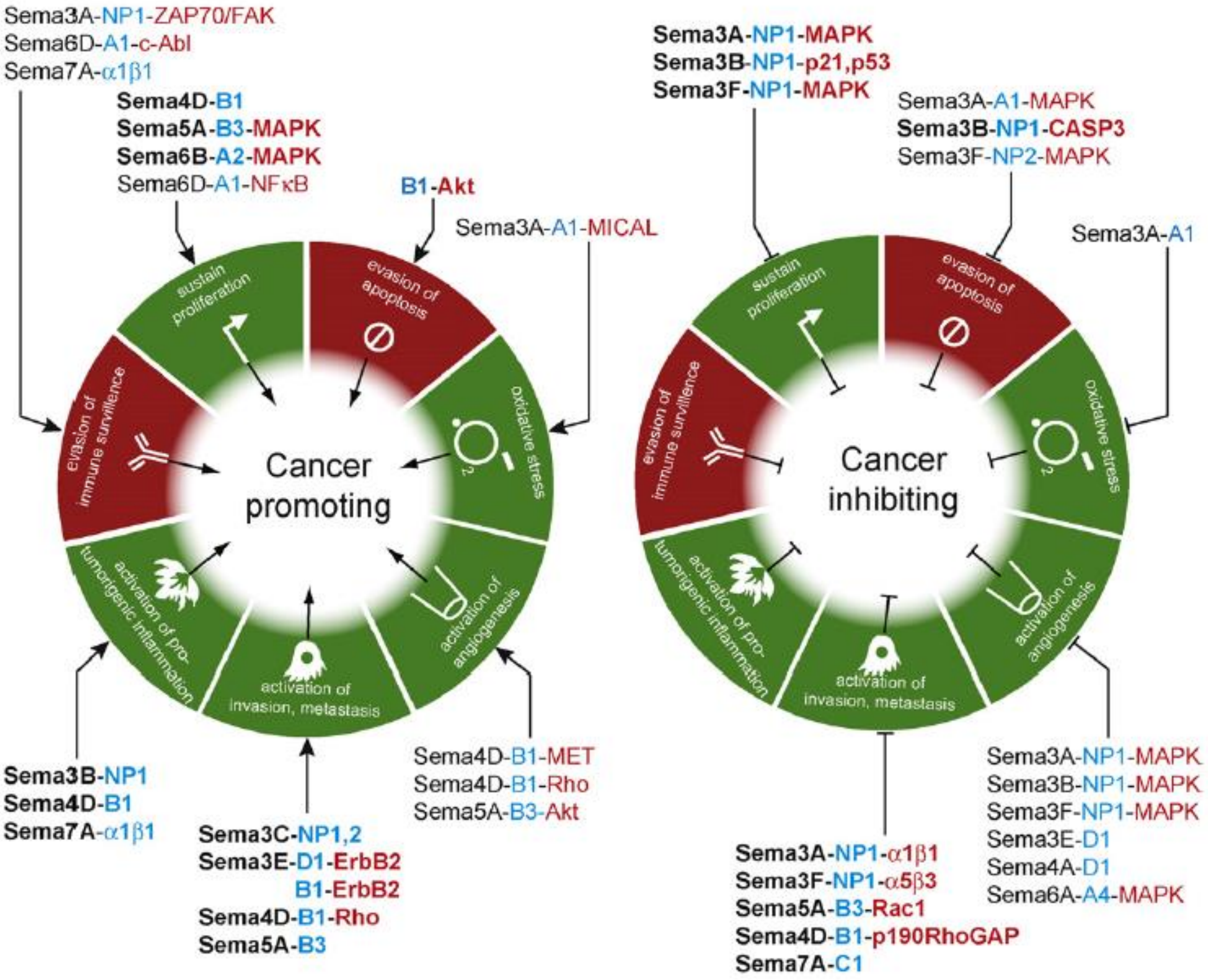

Figure 14 **Semaphorin signaling contributes to seven hallmarks of cancer.** Semaphorins (black) can either promote (left) or inhibit (right) cancer progression upon interaction of plexin/neuropilin receptors (blue) with intracelular signaling mediators (red). Bold items relate to observations in tumor cell lines or experimental tumor models. Extracted from Rehman and Tamagnone, 2013.

6.3.1. Semaphorins engaging tumor angiogenesis

Apart from their beneficial role as tumor angiogenesis inhibitors, it has been shown that some semaphorins also contribute to trigger tumorigenesis and metastasis (Figure 14) (Basile et al., 2004, 2006; Wang et al., 2015). The most studied proangiogenic semaphorins are Sema4D (described in the following sections), which promotes tumor angiogenesis by inducing endothelial cell proliferation, adhesion and migration, and Sema3C, whose expression in some types of cancer has been correlated with tumor progression (Banu et al., 2006; Galani et al., 2002; Herman and Meadows, 2007). Sema3C promotes tumor migration and is highly expressed in metastatic tumor cells. Semaphorin 3C also promotes endothelial cell proliferation, migration and tube formation.

Another proangiogenic molecule is Sema5A, a transmembrane semaphorin which binds to PlexinB3, thereby increasing angiogenesis, tumor growth, invasion and metastasis (Pan et al., 2010; Sadanandam et al., 2010a), and is a putative metastatic marker for pancreatic cancer (Sadanandam et al., 2007). It has been demonstrated that Sema5A, as a proangiogenic molecule, can regulate several processes during angiogenesis, such as endothelial cell proliferation, survival and migration, and sprouting of blood vessels (Sadanandam et al., 2010b). In fact, it has been shown that secreted Sema5A enhances invasiveness and metastasis of tumor cells via ERK phosphorylation, while proliferation of endothelial cells is promoted through upregulation of angiogenic factors (Sadanandam et al., 2012). To sum up, the Semaphorin family members are essential regulators of the tumor microenvironment, since their expression is often altered in tumor samples compared to normal tissues. Importantly, the expression of certain inhibitory semaphorins is decreased in some aggressive tumor cells, supporting the idea that they work as tumor suppressing genes. In contrast, proangiogenic and tumorigenic semaphorins are upregulated during malignant processes, which suggests that their inhibition could be a potential therapeutic approach.

7. Semaphorin 4D

Semaphorin 4D was first discovered more than twenty years ago expressed on human normal lymphocytes, where it increased their activation, (Bougeret et al., 1992). Apart from the profound physiological effects of interactions between Sema4D and its receptors on the immune and nervous systems, increasing evidence has demonstated their role in organ development, autoimmune and bone disease, and specially human cancer (Wu et al., 2016). In this Thesis, the focus will be placed on the contribution of Sema4D to tumor progression and angiogenesis.

Semaphorin 4D (Sema4D), also known as CD100, was originally shown to be either a 150 KDa membrane-bound molecule or a 120 KDa soluble molecule. The latter originates as a consequence of a proteolytic cleavage (Basile et al., 2007b). Because of its distinctive structure, it was later classified as a member of class 4 semaphorin family (Figure 15) (Kolodkin et al., 1993). Sema4D consists of an NH_2-terminal signal peptide followed by a sema domain, an Ig domain of the C_2 type, a hydrophobic transmembrane region and a cytoplasmic tail. As previously stated, its crystalization has revealed a conserved seven-blade β-propeller structure (Love et al., 2003). Its murine counterpart shows an 88% aminoacid identity with the human Sema4D (Furuyama et al., 1996). The cytoplasmic portion of Sema4D presents a tyrosine and multiple serine/threonine sites for phosphorylation (Delaire et al., 1998). It is expressed on the cell surface as a monomer (150 KDa) and a disulfide-linked homodimer (300 KDa) (Figure 15), even though the homodimer is the dominant form (Wu et al., 2016).

Sema4D also exists in a soluble 120 KDa form, which is released from cell surface by different cell types under inflammatory and neoplasic conditions (Basile et al., 2007b). The membrane type 1 metalloprotease (MT1-MMP), also known as MMP14, is involved in the cleavage of Sema4D. Besides, release of Sema4D from the surface of T lymphocytes is regulated by proteolysis (Elhabazi et al., 2001). It is postulated that the special bioactivity of soluble Sema4D might partly differ from that of the membrane-bound form. On the cell surface, Sema4D is associated with protein tyrosine phosphatase for CD45 activity potentiation, which is critical in T cell activation (Herold et al., 1996).

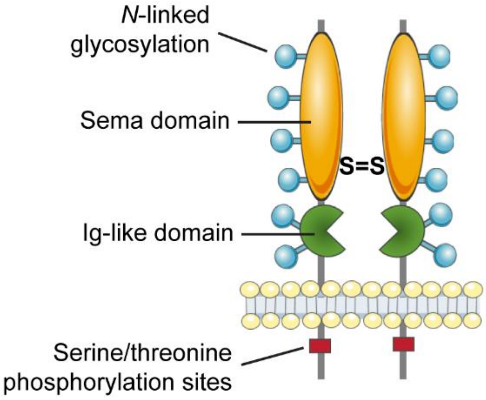

Figure 15 **Structure of Semaphorin 4D.** A disulfide-linked homodimer of Semaphorin 4D (Sema4D) is depicted. The extracellular part of Sema4D protein is composed by Sema and Immunoglobulin-like (Ig-like) domains, which have multiple N-linked glycosylation sites. The intracellular domain of Sema4D contains a single tyrosine and multiple serine/threonine sites for phosphorylation.

7.1. Expression and function of Sema4D receptors

In order to better understand the role of Sema4D, it is neccesary to analyze the expression and distribution of Sema4D receptors. Sema4D activity is mediated by its binding to three different affinity receptors: PlexinB1, PlexinB2 and CD72. The high affinity receptor PlexinB1 and intermediate affinity receptor PlexinB2 are both widely expressed (Malik et al., 2014). On the contrary, the low affinity CD72 is mainly expressed by hematopoietic cells.

PlexinB1 is a 2135 aminoacid long glycoprotein firstly identified in the nervous system, where it fulfilled axon guidance functions. PlexinB1 mRNA transcripts have been found in multiple tissues, including the digestive system, thyroid, prostate, trachea and fetal kidney (Malik et al., 2014). Slightly lower expression of PlexinB1 was detected in fetal brain, lung, female reproductive system and liver. Main sources of PlexinB1 have been described to be epithelial (Basile et al., 2004; Chabbert-de Ponnat et al., 2005; Fazzari et al., 2007). On the cell surface, PlexinB1 exists both in monomeric and heterodimeric forms (Suzuki et al., 2008; Tong et al., 2009). While there are not any mutated or truncated forms described for Sema4D, PlexinB1 is expressed in two truncated forms and three isoforms (Artigiani et al., 2003; Malik et al., 2014; Wu et al., 2016). PlexinB2 is a transmembrane protein composed of 1838 aminoacids. Similarly to PlexinB1, PlexinB2 contains an intracellular domain with a PDZ motif, which interacts with the PDZ domain of Rho molecules (Figure 16) (Malik et al., 2014).

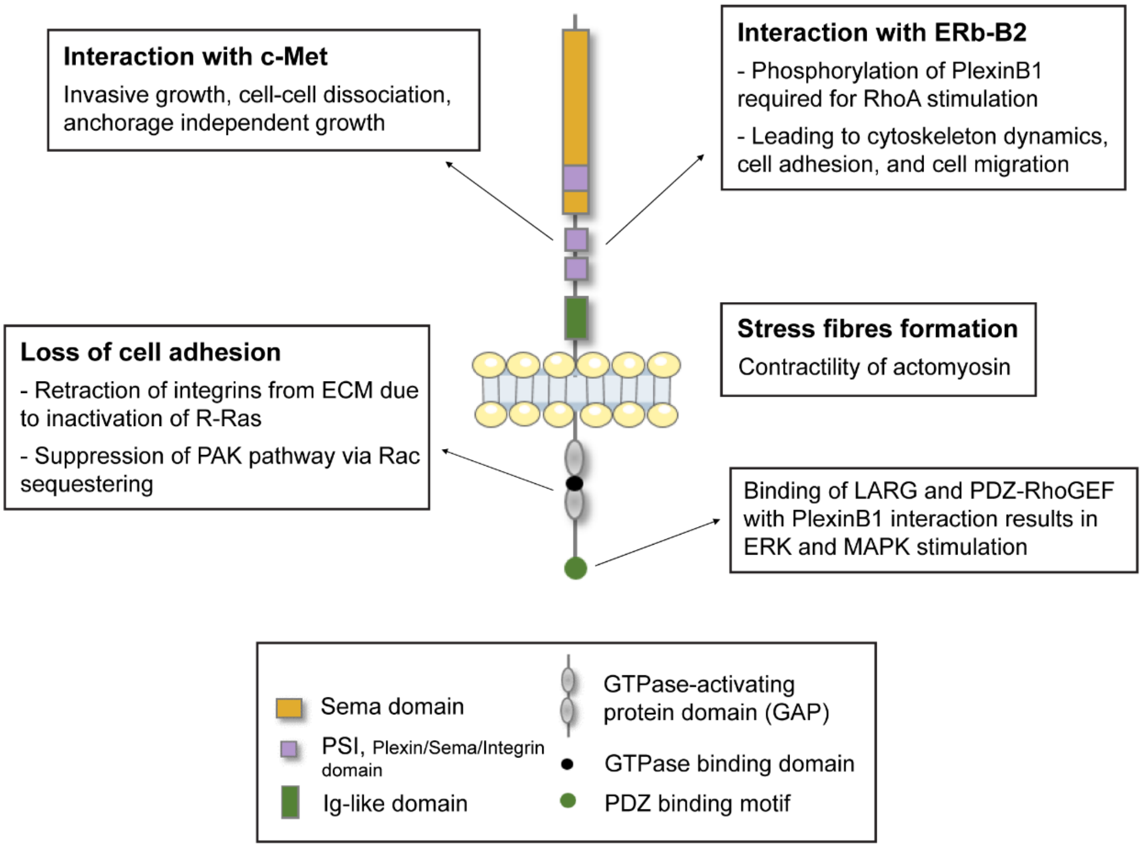

Figure 16 **PlexinB1 structure and interactions.** Schematic representation of PlexinB1 structures, its main functions regarding interactions with other membrane receptors. Adapted from Malik et al., 2014.

Since Sema4D and PlexinB1 and B2 share structural homology with TK receptors c-Met and Erb-B2, PlexinB1 activation by Sema4D has been described to transactivate them (Figure 16 and Figure 17) (Conrotto et al., 2004; Soong et al., 2012). In this context, PlexinB1 transactivates c-Met and promotes invasiveness and angiogenesis of tumor cells by binding Sema4D (Malik et al., 2014; Stevens et al., 2010; Yap et al., 2011). Another similar study showed that Ron, a scatter factor receptor similar to Met, is also able to couple with PlexinB1 and transduce Sema4D signals, promoting an invasive response (Figure 17) (Conrotto et al., 2004). In the immune system, Deaglio et al. have shown that PlexinB1 expression was detected on dendritic cells and activated T cells in the lymphoid tissue. In this context, Sema4D/PlexinB1 signaling was important for normal and malignant (chronic lymphocytic leukemia) B-cell proliferation and survival (Deaglio et al., 2005). Regarding PlexinB2, it is present in epithelial cells of the mouse colon and skin keratynocyes. The Sema4D/PlexinB2 interaction is required for keratinocyte and colon epithelium healing during epidermitis and colitis through effective T cell function (Meehan et al., 2014).

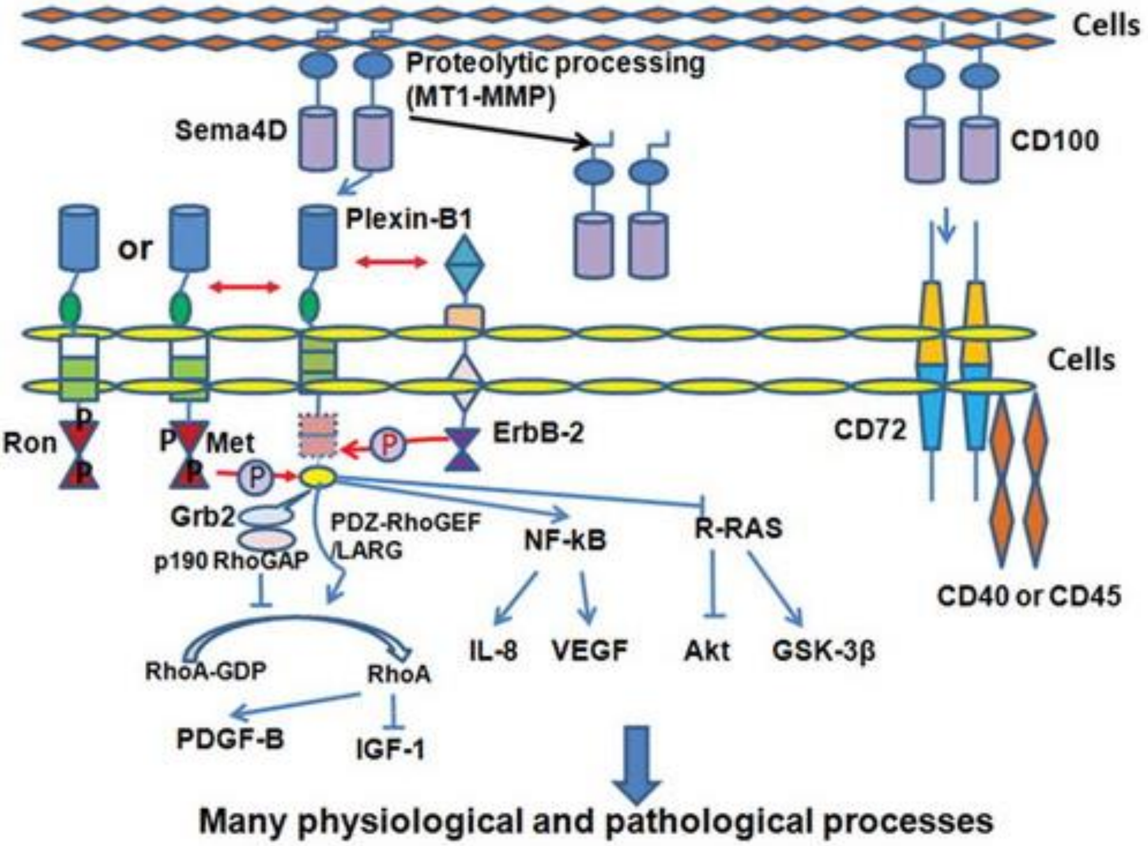

Figure 17 **Sema4D mediated cell signaling in physiological and pathological processes.** Sema4D/PlexinB1 or CD72 interactions play critical roles in organ development, immune response and homeostasis. Sema4D interaction with PlexinB1 can transactivate ErbB-2, Ron or c-Met, leading to the triggering of multiple signaling pathways such as Rho-dependent, NF-kB and Akt. Sema4D (or CD100) also binds to CD72 in immune cells. From Wu et al., 2016.

CD72 is a 45 KDa type II transmembrane protein that belongs to the calcium-dependent C type lectin superfamily. It is a major lymphocyte receptor for Sema4D (Delaire et al., 1998; Kumanogoh et al., 2000; Suzuki et al., 2008). Inside the intracytoplasmatic domain, CD72 harbors two immune-receptor tyrosine-based inhibition motifs (ITIMs) (Parnes and Pan, 2000). One of these ITIMs is able to recruit Src homology 2 domain-containing tyrosine phosphatase, SHP-1 (Figure 18). Conversely, CD72 is expressed by various immune, inflammatory and epithelial cells, although its expression is mainly restricted to antigen presenting cells, such as B cells, DCs and macrophages (Chabbert-de Ponnat et al., 2005; Delaire et al., 1998; Kumanogoh et al., 2000; Suzuki et al., 2008). However, a small fraction of activated T cells was found to also express CD72 (Suzuki et al., 2008).

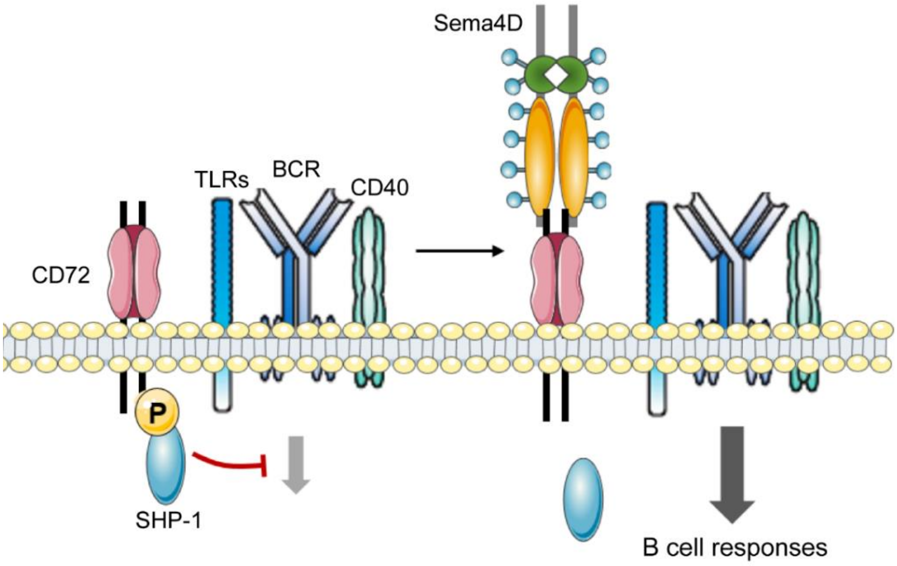

Figure 18 **Sema4D/CD72 signaling in the immune system.** Schematic representation of Sema4D mediated activation of B cell homeostasis. In lymphocytes, Sema4D binding to CD72 impairs SHP-1 phosphorylation, activating B cell responses.

On the cell surface, CD72 is expressed as a homodimer (Figure 18 and Figure 17) (Chabbert-de Ponnat et al., 2005; Delaire et al., 1998). The binding of Sema4D to CD72 causes its dephosphorylation followed by a dissociation of SHP-1 from CD72. Kumanogoh et al. have reported that Sema4D regulates the sensitivity of B-cell receptor (BCR) by preventing its association with CD72, required for proper B-cell homeostasis (Kumanogoh et al., 2005). Since CD72 functions as a negative regulator of BCR/CD40 signaling in B cells and DCs, Sema4D binding enhances immune cell activation and maintains homeostasis (Figure 18) (Suzuki et al., 2008).

7.2. Role of Semaphorin 4D in the tumor microenvironment

The simplistic view of a tumor as a conundrum of just mutant cells engaged in clonal expansion is currently evolving into a more holistic approach where tumors are regarded as organ-like structures (Bissell and Radisky, 2001; Radisky et al., 2001). For neoplastic cell expansion and growth, the ability to handle the surrounding stroma in order to create a favorable ecosystem becomes imperative (Liotta and Kohn, 2001). The insight into the dynamic action of the tumor ecosystem has improved exponentially over the last years, regarding the stroma as an integral part of tumor initiation, progression, and malignization. As such, therapeutic targeting of stroma-related processes is on the rise. Sema4D and its receptor are widely expressed both by stromal and tumor cells (Worzfeld and Offermanns, 2014). In this context, the direct and indirect effects of Sema4D over tumor cell proliferation, immune activation, tumor angiogenesis promotion and invasion are being explored, together with the potential drugability of Sema4D to revert tumor progression (Figure 19) (Wu et al., 2016).

7.2.1. Semaphorin 4D and tumor angiogenesis

As previously explained for PanNETs, tumor progression and metastasis highly rely on the ability of cancer cells to initiate angiogenesis. Sema4D is overexpressed in some angiogenic-rich malignancies such as head and neck squamous cell carcinomas (HNSCCs) and primary tumors of epithelial ovarian cancers (Basile et al., 2006; Chen et al., 2013).

Basile et al. have described that class 4 semaphorins positively regulate tumor angiogenesis as they induce blood vessel growth and endothelial cell homing during vessel development (Basile et al., 2004). In addition to well-established growth factors and inflammatory mediators such as VEGF, the role of Sema4D in tumor angiogenesis has also been highlighted (Zhou et al., 2012b). Tumor-derived Sema4D acts through PlexinB1 receptor in endothelial cells to promote angiogenesis in a RhoA and Akt-dependent manner (Figure 19) (Sierra et al., 2008;

Zhou et al., 2014). PlexinB1 also has been described to bind c-Met receptor and, upon Sema4D binding, proangiogenic response is engaged (Conrotto et al., 2005; Swiercz et al., 2008). When Sema4D is absent, maturation of tumor vessels is impaired, as demonstrated by Sema4D knockout mice (Sierra et al., 2008). Sema4D upregulation has been linked to NK-kB activation in vessels of the tumor stroma, which promotes angiogenesis by the production of the downstream target IL8 (Yang et al., 2011).

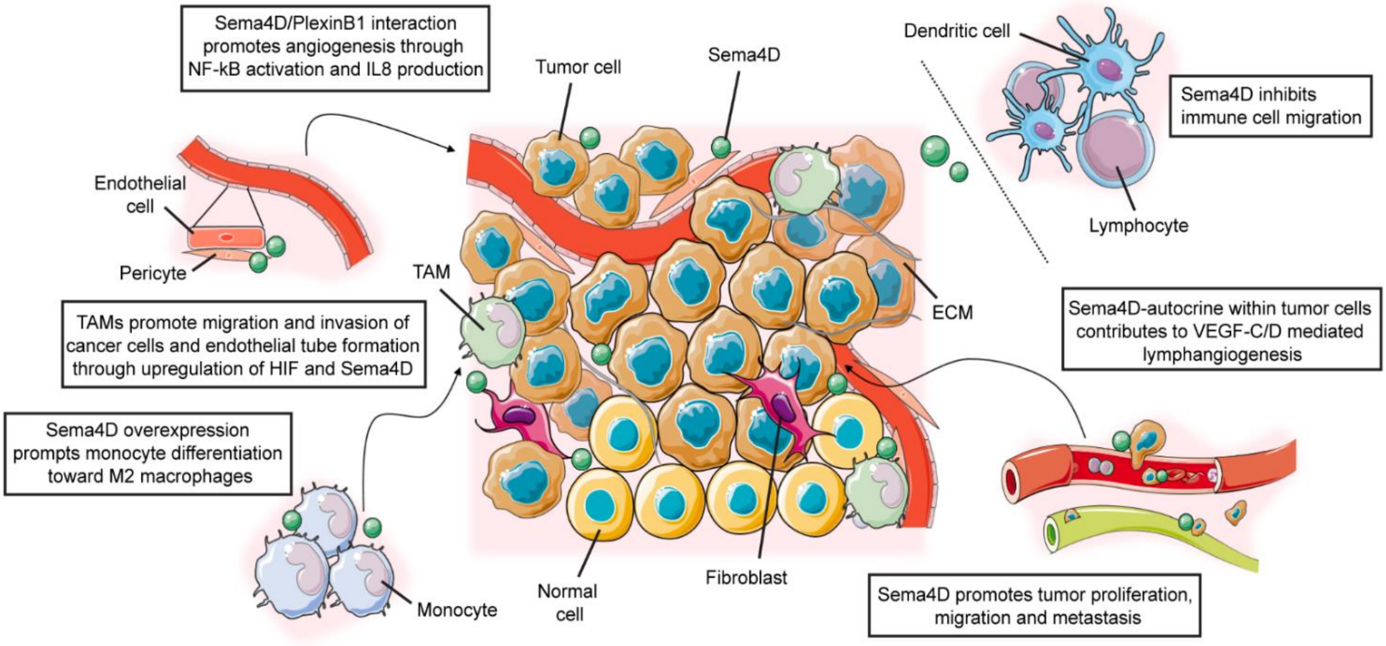

Figure 19 **Role of Semaphorin 4D in the tumor microenvironment.** Sema4D is involved in tumor angiogenesis, tumor-associated macrophage activation and tumor invasiveness. Adapted from Wu et al., 2016.

In HNSCCs, Sema4D provides a link between axon guidance cues and tumor-induced angiogenesis, which is a previously undescribed function (Basile et al., 2006). In these tumors, Sema4D appeared to be highly upregulated in invading islands of transformed epithelial cells, but not in normal and non-invasive dysplastic epithelium. When shed from tumor cells, Sema4D stimulates endothelial cell migration. These effects were abolished by Sema4D silencing, blocking antibodies and Sema4D knockdown, which dramatically reduced the size and vascularity of HNSCC tumor xenografts. Moreover, Sema4D is able to induce the expression of platelet-derived growth factor-B (PDGFB) and angiopoietin-like protein 4 (ANGPTL-

4) from endothelial cells in a PlexinB1/Rho-dependent manner, thus influencing proliferation and differentiation of pericytes and vascular permeability (Zhou et al., 2014). These results indicate that Sema4D upregulation is a frequently used strategy to promote tumor angiogenesis in certain tumor models, highlighting its possible therapeutic targeting for antiangiogenic treatment.

One of the key factors for tumor angiogenesis promotion is hypoxia, which induces the release of angiogenic molecules from tumor cells and attracts endothelial and inflammatory cells. Recruited endothelial cells migrate toward hypoxic areas, whereas inflammatory cells secrete molecules that intensify the angiogenic stimuli. When endothelial cells are engaged, perivascular cells stabilize nascent vessels and guarantee appropriate blood flow (Yang et al., 2011; Zhou et al., 2014). During hypoxic conditions, when a malignancy outgrows its blood supply, tumor cells activate the hypoxia-inducible factor (HIF) family of transcriptional regulators. Evidence emerging through xenograft models, the use of interference RNA, *in vitro* and *in vivo* angiogenesis assays have demonstrated that Sema4D expression is also under the control of HIF (Figure 19). In oral squamous cell carcinoma (OSCC), HIF-stimulated Sema4D cooperates with VEGF to promote tumor growth and vascularity (Zhou et al., 2012c).

In ovarian primary tumors, the overexpression of Sema4D correlated to low differentiation, platinum resistance and refractoriness (Chen et al., 2013). Moreover, the expression of Sema4D in ovarian cancer cell lines and their supernatants was found to be higher than in human primary cultured normal ovarian cells. Hence, Sema4D expression could be used as an independent indicator of overall survival and progression-free survival for those patients and might be used as a predictive tool for early disease detection.

In cervical cancer, Liu et al. have shown that Sema4D expression is higher in metastatic samples than in non-metastatic ones (Liu et al., 2014). The increased Sema4D expression was associated with VEGF-C/-D and lymphatic invasion (Figure 19). Autocrine Sema4D within tumor cells also contributed to enhanced invasion and tumor progression through the increased motility of cervical cancer cells, after RhoA, MAPK and Akt activation.

7.2.2. Tumor-associated macrophages (TAMs)

Nearly 150 years have passed since Virchow first described the presence of inflammatory leukocytes in tumor tissues and proposed that the “lymphoreticular infiltrate” in the tumor reflects the origin of chronic inflammation at the tumor site (Mantovani et al., 1992). Increasing evidence suggests now that cancer-associated inflammation supports tumor growth and progression (Figure 20) (Crusz and Balkwill, 2015; Szebeni et al., 2017). In the tumor ecosystem, inflammatory cells and molecules influence nearly every aspect of tumor progression, including metastasis. Hence, cancer-associated inflammation emerges as the seventh feature of the Hallmarks of Cancer (Hanahan and Weinberg, 2011). Many inflammatory molecules have recently been identified to originate from stromal cells recruited to the tumor microenvironment (Figure 20). Reports have recently noted the close correlation between inflammatory infiltration of the tumor stroma and high vascularity (as reviewed in Zuazo-Gaztelu and Casanovas, 2018).

From all the immune cell types infiltrating tumor stroma, tumor-associated macrophages (TAMs) represent up to 50% of the tumor mass (Kim and Bae, 2016). Macrophages are highly heterogeneous cells with high plasticity and with a wide spectrum of activation states, ranging from the classically activated M1 to the alternatively activated M2 macrophages (Figure 21) (Sica et al., 2015). In cancer, macrophages act as a double-edged sword, since they can exert both anti- and protumoral functions (Franklin and Li, 2016). Nevertheless, bad prognosis associated with high TAM intra-tumoral content has been reported in 80% of tumor cases (Laoui et al., 2014) as a consequence of tumor specific immune response inhibition, angiogenesis promotion and tumor cell dissemination (Figure 20) (Biswas et al., 2013; Caronni et al., 2015; Franklin et al., 2014). Identification of new molecular targets for TAM inhibition is under the scope of research nowadays (Szebeni et al., 2017).

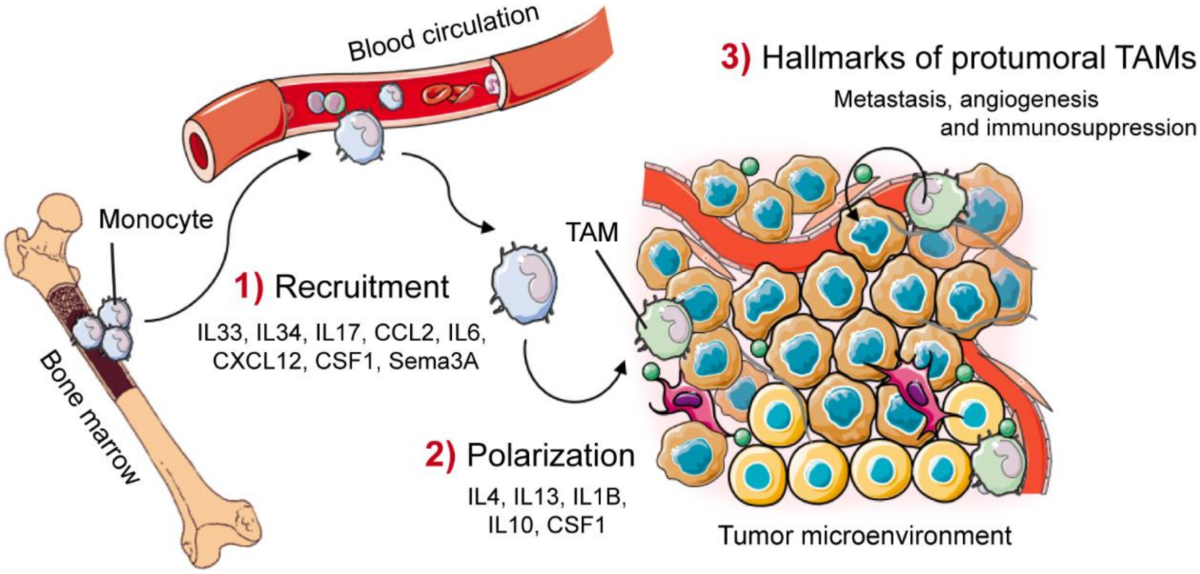

Figure 20 **Tumor-associated macrophages (TAMs) are the major inflammatory component of the tumor microenvironment, supporting tumor growth and progression.** In response to several chemokines and cytokines (IL33, IL34, IL17, CXCL12, CCL2…) released by malignant or tumor stromal cells, monocytes are recruited from the bone marrow to blood circulation. Infiltrating monocytes are polarized into TAMs in response to molecules such as IL4 and IL13. TAMs in the tumor microenvironment exert several protumoral functions such as immunosuppression, angiogenesis, and metastasis.

7.2.2.1. Classical M1 and M2 activation of macrophages

M1 activation leads to classical proinflammatory and antitumoral M1 activation of macrophages and occurs upon recognition of pathogen-associated molecular patterns (e.g. interaction with Toll like receptor and C-type lectin). As a result, pro-inflammatory cytokines (IL-12, TNF-α among others) are produced (Figure 21) (Porta et al., 2015). Local signals in the tumor ecosystem such as IL4, IL6, IL10 and CSF1 polarize macrophages into alternative, protumoral M2-like cells (Caronni et al., 2015). Importantly, different tumor types from different stages and tumor tissue regions are characterized by the presence of highly heterogeneous macrophage populations (Laoui et al., 2014).

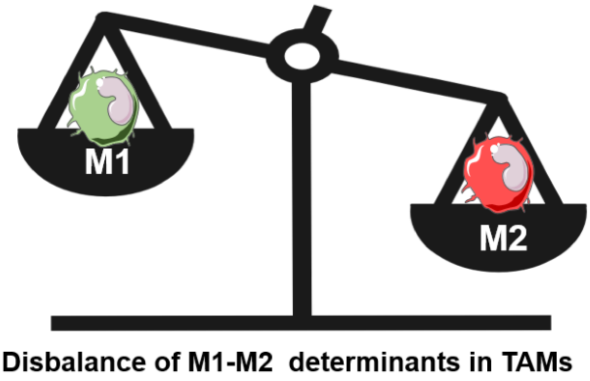

Signal transduction molecules	TSC2, SOCS3, Notch	mTOR, SHIP1, PDL-1, CD164, CD206, TRAF-2
Soluble mediators (cytokines, growth factors)	IL12, TNFα, Gas6, CXCL9, CXCL10, CXCL11	IL1, IL4, IL6, IL10, IL33, IL34, TGFβ, CSF1, CXCL12, CCL2, CCL17, CCL18

Figure 21 **The polarization of TAMs is skewed to alternative activation due to different stimuli.** M1 polarization promotes the expression of proinflammatory cytokines and chemokines, whereas M2 macrophages show an anti-inflammatory phenotype. Some of the different signal transduction molecules and soluble mediators used to classify macrophages regarding their phenotype are listed. Adapted from Szebeni et al., 2017.

A series of chemoattractants such as CCL2 and CXCL12 engage the recruitment of TAMs to the tumor site, and their differentiation towards an M2 phenotype. Cells from the tumor ecosystem produce hematopoietic growth factors (CSF1, GM-CSF and IL34) which increase the expansion of the macrophage lineage (Lauoi, 2014). For instance, inhibition of CSF1 signaling (also known as M-CSF), the primary regulator of tissue macrophage differentiation, dampens macrophage infiltration and decreases mammary tumor growth (Aharinejad et al., 2004). Interestingly, overexpression of Sema4D in ovarian cancer has been correlated with higher M2 macrophage count (Figure 19). In their model, soluble Sema4D addition engages monocyte maturation towards a M2 phenotype (Chen et al., 2013).

7.2.2.2. Role of Sema4D-positive TAMs

Within the tumor stroma, TAMs have been demonstrated to be the main cells producing Sema4D. Stromal-derived Sema4D is critical for tumor angiogenesis and blood vessel maturation (Figure 19) (Sierra et al., 2008). In breast cancer models, Sema4D is a key modulator of the complex interactions between tumor cells and their microenvironment (Basile et al., 2006; Evans et al., 2015). Sema4D inhibits cell migration, which can be interpreted as a means of prolonging cell-cell contact in a physiologic immune response (Figure 19) (Chabbert-de Ponnat et al., 2005). This highlights a novel function of immune cells involved in the inflammatory response of tumors, independent of angiogenesis. Furthermore, TAMs promote migration and invasion of colon cancer cells and endothelial tube formation through HIF and Sema4D upregulation (Figure 19) (Mu et al., 2014). Both proteins are closely related to lymphatic metastasis in aggressive stages of colon cancer.

7.3. Sema4D as a prognostic biomarker and a therapeutic target

Research in recent years has brought cumulative evidence regarding the roles of Sema4D/PlexinB1 interaction in tumor progression from both *in vitro* and *in vivo* studies (Malik et al., 2014; Wu et al., 2016). Clinical studies have also provided further insight into the significance of Sema4D expression in human tumors (Table 2). Indeed, notable correlations have been established between the clinical stages and the expression of Sema4D in different cancers (Table 3).

Table 2 **Pathological role of Sema4D and its receptors in various human cancers.** Adapted from Wu et al., 2016.

Cancer type	*Finding*	*Prognosis*
Soft tissue sarcoma	A higher expression of Sema4D was correlated with higher mitotic counts, cellularity, and a higher necrosis ratio and Ki67 index	A poorer overall survival and a disease-free survival with higher Sema4D expression
B-cell chronic lymphocyte leukemia	Sema4D expressing B cells show better viability and a higher proliferative rate	
Colorectal carcinoma	HIF1α and Sema4D expression was closely correlated with histological tumor type, TNM stage, and lymphatic metastasis	Sema4D as a prognostic indicator

Non-small cell lung cancer	Sema4D promotes tumor proliferation, migration and metastasis by influencing Akt protein phosphorylation	Sema4D as a reliable tool for early prediction of poor prognosis
Cervical cancer	Autocrine Sema4D contributes to enhanced invasion and tumor progression by inducing activation of RhoA, MAPK, and Akt	
PDAC	Overexpression of Sema4D and PlexinB1 in tumor-infiltrating lymphocytes was significantly correlated with lymph node and distant metastasis, and poor prognosis. Sema4D potentiates the invasiveness of pancreatic cancer cells by inducing RhoA activation and MAPK and Akt phosphorylation	Metastasis and poor prognosis with overexpression of Sema4D

Sema4D is highly expressed in some human tumors, such as soft tissue sarcoma (Ch'ng et al., 2007), colorectal carcinoma (Mu et al., 2014), cervical cancer (Liu et al., 2014), pancreatic ductal adenocarcinoma (Kato et al., 2011) and neurotropic malignancies (Binmadi et al., 2012). In soft tissue sarcoma, a higher expression of Sema4D correlated with higher mitotic counts, cellularity, necrosis ratio and Ki-67 index. This suggested a proliferative advantage in tumors with higher Sema4D expression, and is associated with poorer OS and disease-free survival (Ch'ng et al., 2007). Similarly, via PlexinB1 activation, Sema4D-expressing CD38^{+} B-cell leukemic cells show better viability and a higher proliferative rate (Deaglio et al., 2005).

Table 3 **Correlations of the clinical stages with the expressions of Sema4D and PlexinB1.** Adapted from Wu et al., 2016.

Cancer type	*Sema4D expression, n%*				*p. value*
	I-II		III-IV		
Ovarian cancer	37.5		74.4		0.003
Pancreatic cancer	Low	High	Low	High	0.002
	90.4	74.5	9.6	25.5	
Non-small cell lung cancer	48.4		82.8		0.005

Colorectal carcinoma	43		70		0.017
Cervical cancer	I a	I b	II a	II b	0.021
	10.9	73.2	69.9	46	

Similarly, in PDAC patients, cancer tissue cells expressing Sema4D were first found to be tumor-infiltrating lymphocytes. Overexpression of Sema4D by immune cells significantly correlated with clinical events such as lymph node and distant metastases (Kato et al., 2011). In this model, Sema4D potentiates the invasiveness of pancreatic cancer cells by inducing RhoA activation and MAPK and Akt phosphorylation. Remarkably, there is no information about the relevance of Sema4D in either neuroendocrine tumors or in PanNETs.

Altogether, research in the Sema4D field has underlined its potential role as a prognostic biomarker and as a therapeutic target in certain cancer patients. Deciphering the complex mechanisms involving Sema4D-dependent interplay between tumor and stromal cells will be required to validate it as a competent therapeutic option.

8. Ongoing clinical trial with anti-Sema4D antibody

Taking into account the role of Sema4D in tumor progression, immune system and central nervous system, there is a strong rationale for its therapeutic exploitation. Theoretically, neutralization of Sema4D would inhibit tumor growth and invasion by affecting tumor, endothelial and immune cells. To this aim, a humanized anti-Sema4D antibody (VX15/2503, isotype IgG4) was generated from a mouse anti-Sema4D antibody (mAb 67-2, isotype IgG1) by the biotechnological company Vaccinex Inc. in Rochester (Fisher et al., 2016). Briefly, Sema4D KO mice were immunized with Sema4D and the lead mouse anti-Sema4D monoclonal antibody was selected (Figure 22). This antibody was later humanized and optimized to generate a highly specific anti-human Sema4D. Affinity, defined as the equilibrium dissociation constant (K_D), for native, cell-associated human Sema4D for both antibodies was 0.45 nM. They also recognized mouse-derived Sema4D within the nM range.

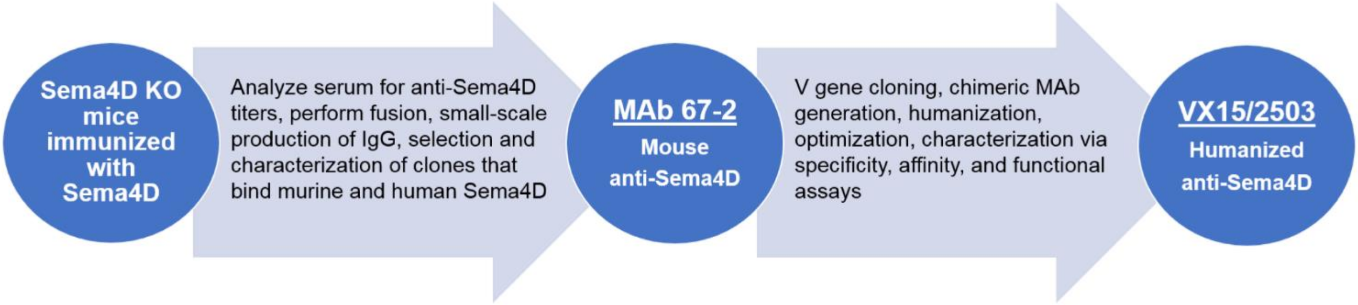

Figure 22 **Generation of mouse anti-Sema4D (mAB 67-2) and humanized anti-Sema4D (VX15/2503).** mAb 67-2 was selected as the lead mouse anti-Sema4D monoclonal antibody after Sema4D KO mice immunization. The selected antibody was humanized and optimized to generate VX15/2503. Adapted from Fisher et al., 2016.

It was also functionally demonstrated that those antibodies can block the interaction of Sema4D with any of its receptors (Fisher et al., 2016). The epitope mapping of both antibodies demonstrated that the discontinuous epitope was comprised by three aminoacid sequences in human Sema4D (Figure 23). All three sequences are part of the SEMA domain of the protein, in a conformational epitope. Detailed analysis of the epitope suggests that VX15/2503 interferes with Sema4D-receptor interactions by both binding the Sema4D homodimerization domain and by sterically interfering with the PlexinB1 binding site (Figure 23).

Anti-Sema4D treatment has demonstrated to be efficacious in ameliorating disease in several animal models of oncology (Evans et al., 2015), multiple sclerosis (Smith et al., 2015) and Huntington's disease (Southwell et al., 2015). The first-in-human study of anti-Sema4D VX15/2503 for the treatment of advanced refractory solid tumors showed promising results (Patnaik et al., 2016). Among the 42 patients with colon, breast, pancreas, abdomen or lung primary tumors included in the study, 19 patients (45.2%) exhibited no evidence of disease progression for at least 8 weeks and 8 (19%) showed a similar absence of disease progression for at least 16 weeks. Interestingly, there was a correlation between immune cell levels at baseline and progression-free survival, which is consistent with an immune-mediated mechanism of action. The therapy was well tolerated at all evaluated doses and demonstrated expected pharmacodynamic properties, successfully completing the Phase I clinical trial. The ClinicalTrials.gov identifier was NCT01313065. Currently, Vaccinex is further evaluating the safety and efficacy of anti-Sema4D VX15/2503 in four different oncology studies, which include a broader type of tumors and combination regimens with approved immunotherapies.

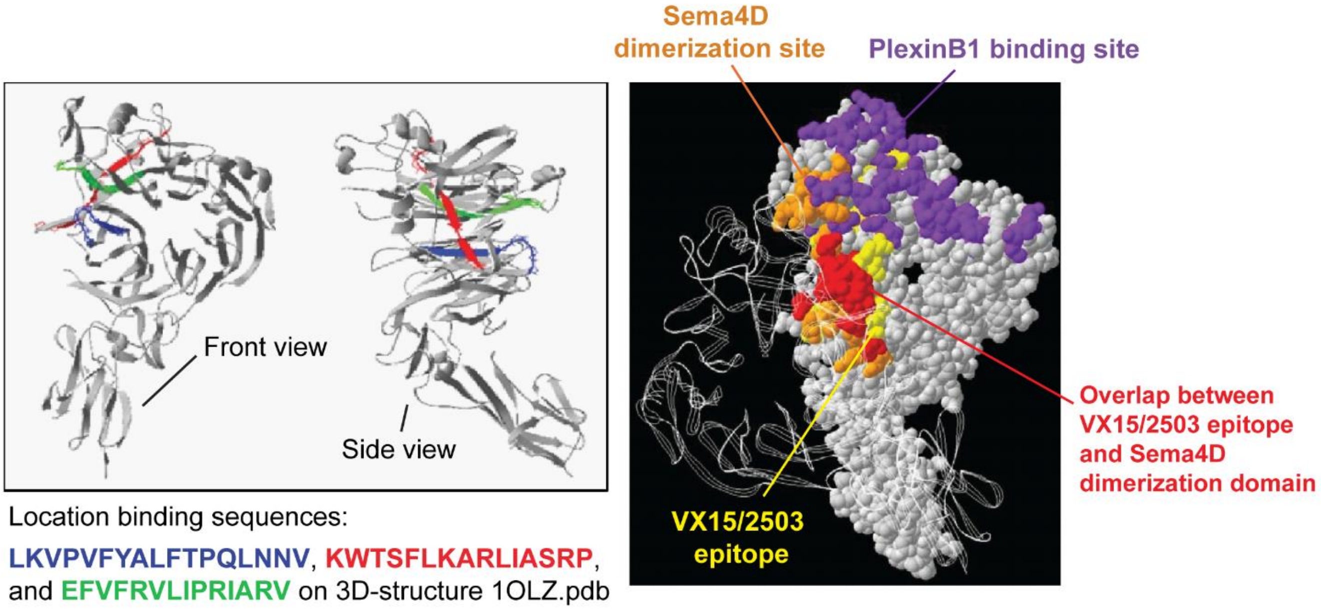

Figure 23 **Epitope mapping of anti-Sema4D:Sema4D interaction.** A) Three aminoacid sequences putatively comprise the discontinuous epitope in anti-Sema4D VX15/2503 and mAb 67-2 antibodies. B) A combination ribbon/space-filling structural diagram of a Sema4D dimer that shows the VX15/2503 epitope overlapping the dimerization and plexin-binding domains. Adapted from Fisher et al., 2016.

9. Previous results from the group

With the aim of extending our previous knowledge regarding the acquisition of a more aggressive phenotype after blocking VEGF signaling pathway (Paez-Ribes et al., 2009), our group decided to focus on the inhibition of the alternative angiogenic Sema4D. To assess the effects of Sema4D blockade, RIP1-Tag2 mice were treated with the mouse antibody anti-Sema4D from Vaccinex: mAb 67-2 (Martín-Mitjana, 2014; Pàez-Ribes, 2010).

9.1. Inhibition of Sema4D exerts an antitumor and prosurvival effect that is followed by increased invasiveness and metastasis

RIP1-Tag2 mice were either treated with anti-Sema4D (Vaccinex) or with a blocking monoclonal antibody anti-VEGFR2 (DC101, own production from hybridoma). Results obtained with Anti-VEGFR2 treated mice served as a gold standard for the effects of traditional antiangiogenic treatments in the RIP1-Tag2 model, and were thoroughly described in the literature (Casanovas et al., 2005; Pàez-Ribes et al., 2009). Anti-Sema4D treatment during 4 weeks (long treatment) produced a decrease in the tumor volume similar to the one observed in the anti-VEGFR2 treatment (Figure 24A). This decrease was associated with an extension of lifespan in both differently treated mice (Figure 24B), highlighting a beneficial effect of anti-Sema4D treatment.

Previous published data from our group showed that anti-VEGFR2 treatment produced an increase in local invasion (Paez-Ribes et al., 2009). Similarly, a detailed study of anti-Sema4D treated tumors demonstrated an increase in the number of highly invasive tumors after long treatment (Figure 24C). While highly invasive tumors presented wide fronts of invasion encroaching upon the adjacent acinar tissue, the majority of control tumors were predominantly encapsulated or microinvasive, following the classification criteria by Lopez and Hanahan (Lopez and Hanahan, 2002).

One of the main consequences of an increase in local invasion involves the rise in tumor dissemination and metastasis, as described during the blockade of the VEGF pathway (Ebos et al., 2009; Paez-Ribes et al., 2009). As expected, incidence of lymphatic nodule (LN) and liver metastasis doubled in treated groups, irrespective of whether it was anti-VEGFR2 or anti-Sema4D treated (Figure 24D-E).

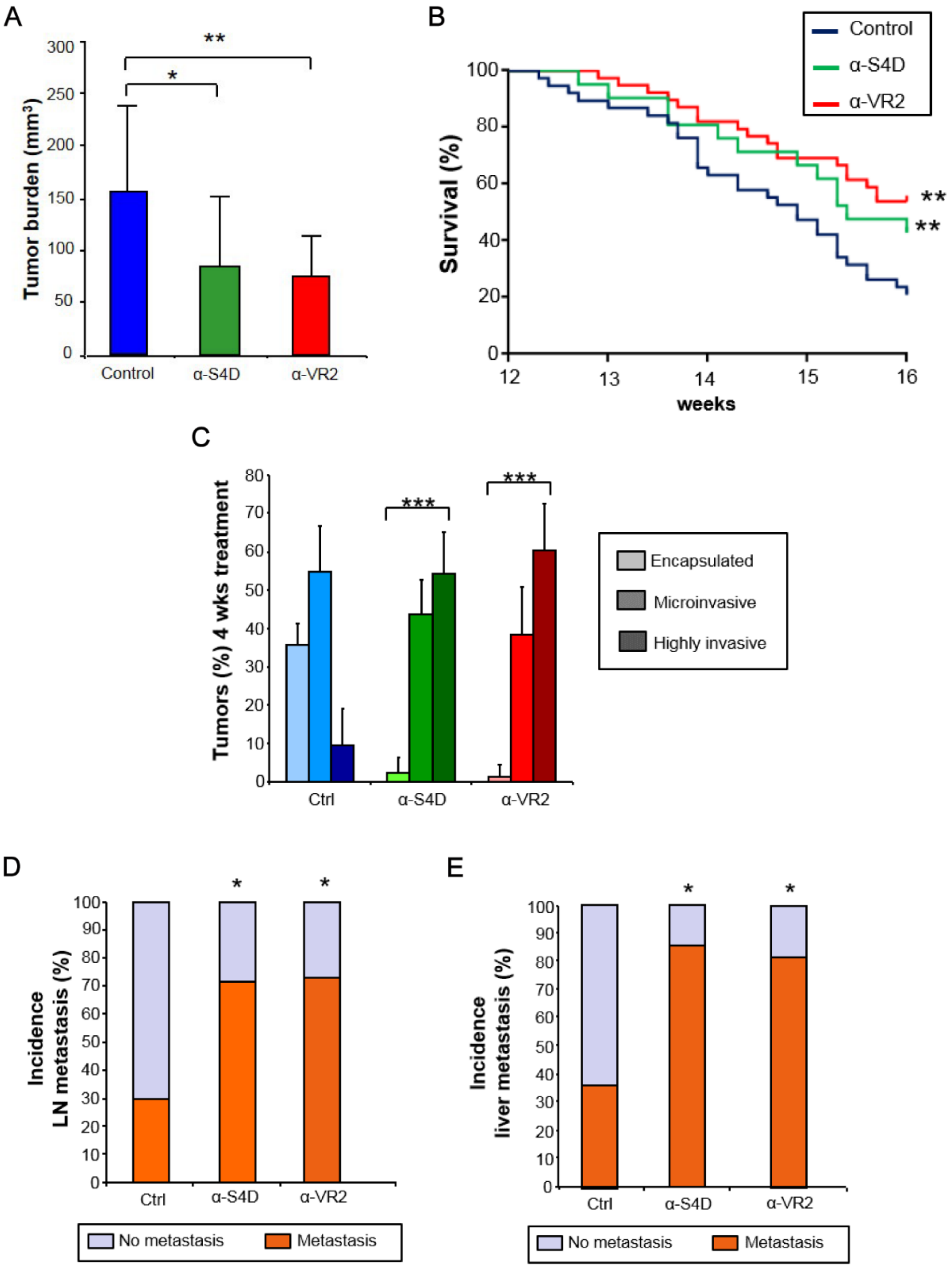

Figure 24 **Sema4D blockade demonstrates antitumor effects and extends survival, while increasing local invasion and distant metastases. A)** Tumor volume from control and 4 weeks-long anti-Sema4D (α-S4D) and anti-VEGFR2 (α-VR2) treated animals was macroscopically determined. At least 10 animals were analyzed per group. *p < 0.05 and **p < 0.01 by Mann-Whitney test. Error bars indicate ± SD. **B)** Kaplan-Meier survival curves show a statistically significant increase in lifespan after anti-VEGFR2 and anti-Sema4D treatment compared to control mice. At least 20 animals were analyzed per group. *p < 0.001 by Log-rank test. **C)** Quantification of tumor invasiveness per animal after long (4 weeks) treatment with anti-Sema4D and anti-VEGFR2. Percentage of non-invasive tumors (encapsulated), microinvasive tumors and highly invasive tumors is shown per condition. At least 5 sections per animal and

5 animals per condition were analyzed per group. **$p < 0.01$, ***$p < 0.001$ by Fisher exact probability test. Error bars indicate ± SD. **D-E)** Percentage of lymph node (**D**) or liver (**E**) metastasis in control and 4 weeks-long anti-Sema4D or anti-VEGFR2 treated RIP1-Tag2 mice. At least 10 animals per condition were analyzed per group. Each animal was scored for presence/absence of metastasis in 5 tissue sections per animal. *$p < 0.05$ by Chi-square test. Adapted from Pàez-Ribes, 2010.

Overall, these first evidences demonstrated that anti-Sema4D treatment had a beneficial anti-tumor effect followed by the acquisition of an adaptive resistance, similar to the one produced with traditional VEGF signaling inhibitors (Ebos et al., 2009; Paez-Ribes et al., 2009). This acquired resistance is characterized by an increase in local invasiveness and the presence of distant metastasis.

9.2. Sema4D is highly expressed in immune-like cells and weakly in tumor cells

The presence of target Sema4D was assessed and it was found to be expressed by all tumor cells in the RIP1-Tag2 tumor stroma (Figure 25). Interestingly, the membrane of scattered cells showed a high expression of Sema4D, following a pattern compatible with immune cells (Figure 25, pointed with white arrows). These findings were consistent with previously published literature regarding Sema4D expression (Basile et al., 2006; Sierra et al., 2008).

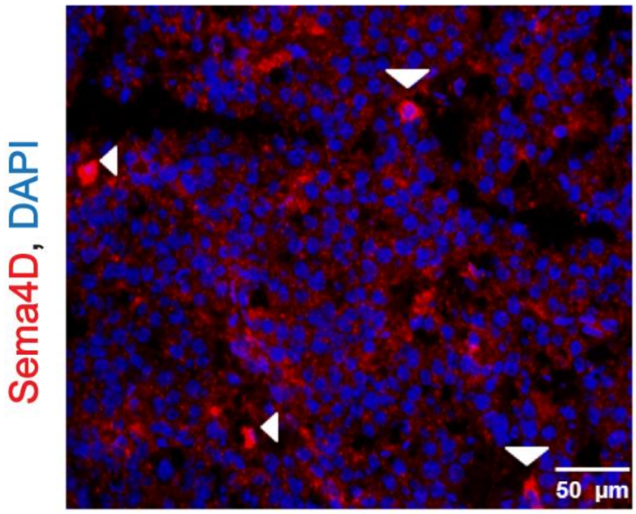

Figure 25 Sema4D is highly expressed in scattered cells and lesser in tumor cells from RIP1-Tag2 tumor stroma. A) Immunohistofluorescence analysis of Sema4D (in

red) expression in RIP1-Tag2 control tumors. DAPI (blue) is used to counterstain for cell nuclei. Adapted from Martín-Mitjana, 2014.

9.3. Absence of retrograde effect of Sema4D

The membrane-bound Sema4D is able to signal bidirectionally due to the presence of phosphorylation sites in the cytoplasmic region of the protein. Nevertheless, a retrograde effect of Sema4D as the main responsible for the invasive phenotype was discarded, since no changes in adhesion or disadhesion and proliferation of βTC4 tumor cells derived from RIP1-Tag2 mice were observed after inhibiting tumor-derived Sema4D (Figure 26). Therefore, although Sema4D is expressed in tumor cells, it seems appears to be functionally irrelevant in an autocrine manner.

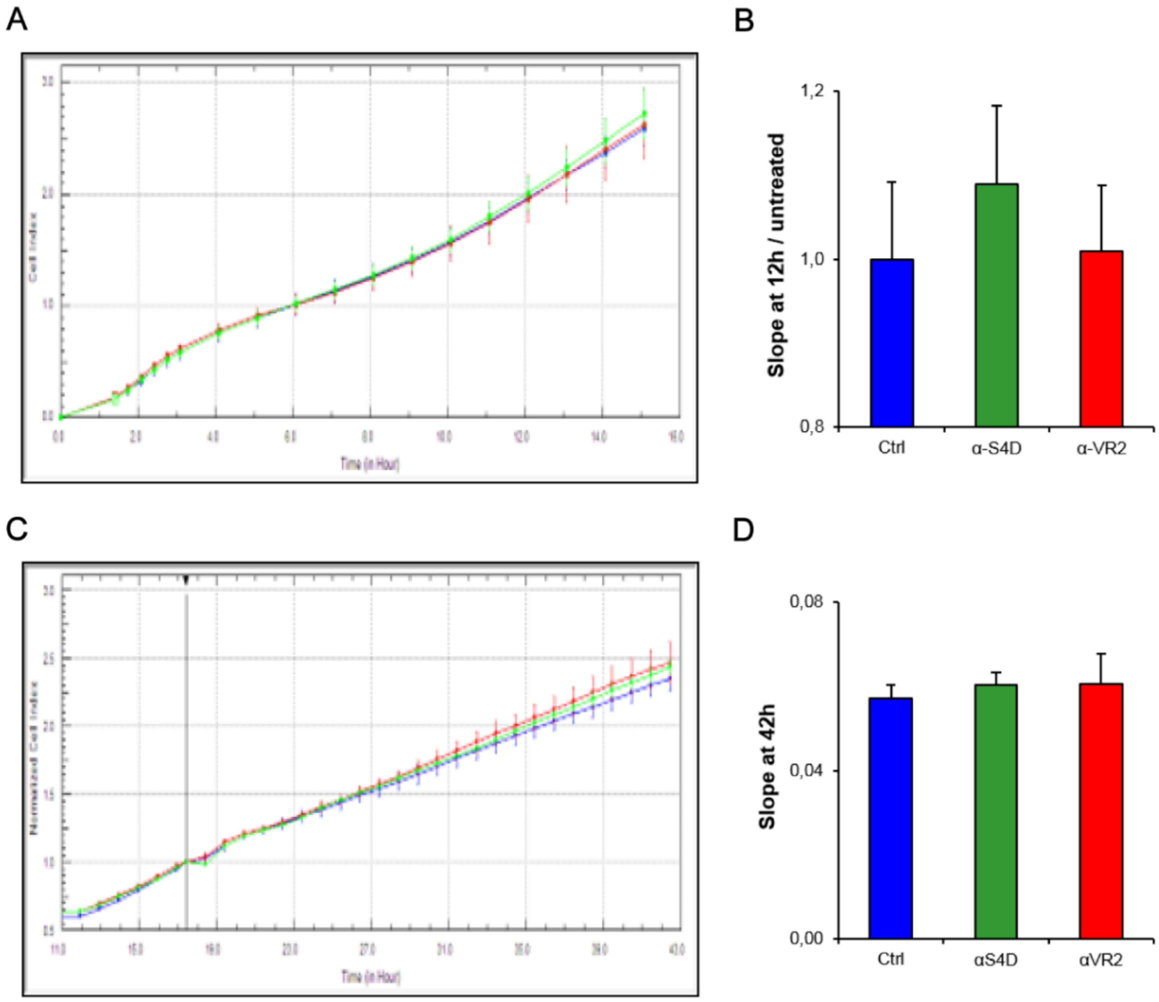

Figure 26 **No retrograde effect is observed in βTC4 cells after anti-Sema4D treatment. A)** Graphic of the βTC4 Cell Index in untreated (blue line), treated with

anti-VEGFR2 (red line) or with anti-Sema4D (green line) cells at 0 hours. **B)** Boxplot of the slopes at 12 hours normalized by untreated slopes for the 3 experimental groups. **C)** Graphic of the Normalized Cell Index of βTC4 cells in untreated (red line), treated with anti-VEGFR2 (green line) or with anti-Sema4D (blue line) cells at 17 hours. D) Boxplot of the slopes at 42 hours for the 3 experimental groups. All data were obtained using XCELLigence System. Error bars indicate ± SD. Adapted from Martín-Mitjana, 2014.

9.4. Anti-Sema4D treatment alters vascular structure in the absence of vessel trimming and intratumor hypoxia

As a first approach to decipher the antitumor and proinvasive mechanism of anti-Sema4D treatment, a molecular analysis of angiogenesis-related gene expression was performed in anti-Sema4D and anti-VEGFR2 treated tumors (Table 4). Expression of some genes such as *Angpt1*, *Angpt2* and *Pdgfra* and *Pdgfrb* showed an abrupt increase, validating anti-Sema4D action upon tumor angiogenesis.

Table 4 **Some angiogenesis related genes are changed after anti-SEMA4D and anti-VEGFR2 treatment.** TaqMan Low Density Array (TLDA) analysis for a angiogenesis related gene expression after anti-Sema4D and anti-VEGFR2 long-term treated tumors. A selection of the most upregulated genes after anti-Sema4D treatment is shown. Results are shown as mean ± SD. Adapted from Martín-Mitjana, 2014.

Gene	Anti-Sema4D	Anti-VEGFR2
Angpt1	4.26 ± 0.31	0.89 ± 0.4
Angpt2	0.42 ± 0.23	0.58 ± 0.42
Angpt4	4.13 ± 0.72	0.17 ± 0.09
Pdgfra	2.02 ± 0.19	0.73 ± 0.52
Pdgfrb	1.82 ± 0.4	0.44 ± 0.18
Pdgfa	0.48 ± 0.37	1.46 ± 0.87
Pdgfb	0.83 ± 0.12	0.3 ± 0.33

In order to characterize the antiangiogenic effect, tumor vascularization parameters of different treatment groups were analyzed (Figure 27). Microvessel density quantification revealed a significant reduction in the number of vessels after anti-VEGFR2 therapy. Surprisingly, there was no vascular trimming effect with anti-

Sema4D treatment (Figure 27A). In absence of vascular trimming, other vascular parameters were analyzed to assess the potential alteration of tumor vasculature after anti-Sema4D addition. Similar to anti-VEGFR2, but more modestly, Anti-Sema4D treatment showed a significant reduction in the number of endothelial cell nuclei (Figure 27B). Moreover, vascular integrity was detected by quantifying erythrocyte microhemorrhaging out of the vessels and into the tumor parenchyma (Figure 27C). After long anti-Sema4D treatment, the percentage of macroscopic hemorrhagic tumors was significantly reduced. The reduction was even stronger with anti-VEGFR2 treatment, suggesting that, since anti-Sema4D did not reduce vessel density but rather affected their structure and integrity, its effect was more modest. Contrarily, no differences were observed neither in the plasticity of the basement membrane, nor in cell-cell junctions (data not shown). Altogether, these results indicate that even though anti-Sema4D does not modify mean vessel density, it alters vascular structure at endothelial cell levels, which suggests a direct vascular antiangiogenic effect of Sema4D blockade.

Since interactions between endothelial cells and pericytes in the vessel wells are central processes in the regulation of vascular formation, stabilization, remodeling and function (von Tell et al., 2006), pericyte coverage of the vessel structures was assessed in the different treatment groups (Figure 27D). Anti-Sema4D treatment produced an increase in pericytes positive for Desmin and NG2 markes, together with a decrease in the number of α-SMA positive cells. These findings suggests that Sema4D drives a switch towards a more immature pericyte phenotype, as previously stated (Miller et al., 1995).

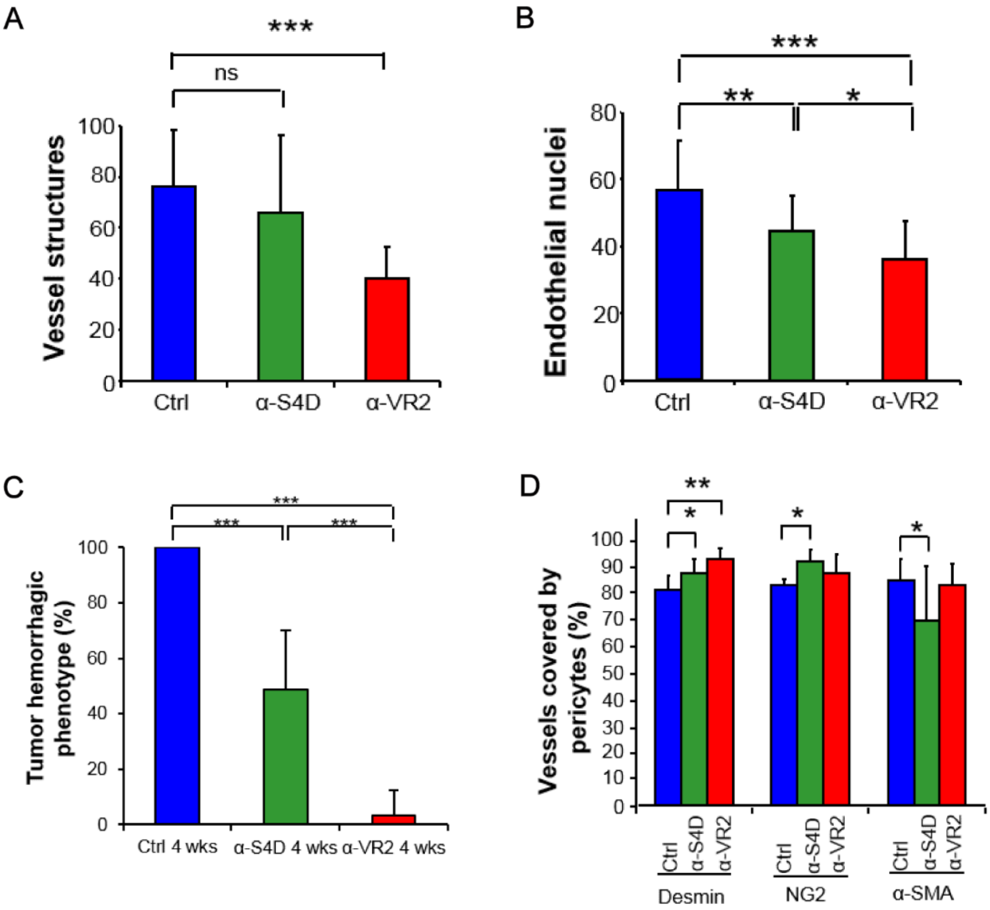

Figure 27 **No changes in the number of vessel structures after anti-Sema4D therapy.** **A)** Quantification of vessel structures by counting the number of CD31-positive endothelial cells per field of viable RIP1-Tag2 control, anti-Sema4D (α-S4D) and anti-VEGFR2 (α-VR2) tumors. At least 5 tumors were analyzed per group. **B)** Quantification of the number of endothelial cells nuclei positively stained by the endothelial restricted transcription factor ERG per field of viable tumor At least 13 tumors were analyzed per group. **C)** Quantification of the percentage of hemorrhagic tumors after anti-Sema4D 4 weeks long treatment. At least 8 animals were analyzed per group. **D)** Quantification of the percentage of vascular structures covered by different pericyte markers per field of viable tumor normalized by the total number of vessel structures. In the case of Desmin, at least 6 tumors, 5 for NG2 and 13 for α-SMA were analyzed per group $^*p < 0.05$, $^{**}p < 0.01$ $^{***}p < 0.001$ by Mann-Whitney test. Error bars indicate ± SD. Adapted from Martín-Mitjana, 2014.

As previously explained, our group had described that one of the mechanisms of tumor resistance and malignization after antiangiogenic therapies involves intratumor hypoxia (Pàez-Ribes et al., 2009). After anti-Sema4D therapy, results regarding local invasion and metastasis, even in the absence of vascular trimming, were comparable to the ones produced with anti-VEGFR2 treatment. It was reasonable to think that the same mechanism of resistance would be engaged when Sema4D was blocked. To check this hypothesis, intratumoral hypoxia was assessed in anti-Sema4D treated tumors (Figure 28). Strikingly, no intratumor hypoxia was found in any of the treatment regimens of anti-Sema4D (Figure 28B).

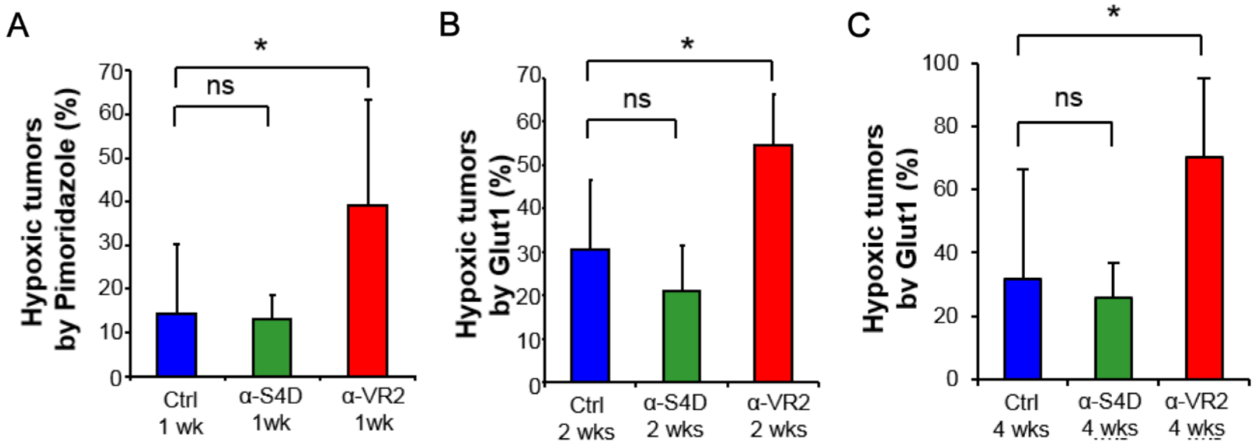

Figure 28 **Antiangiogenic treatment with anti-Sema4D does not increase intratumor hypoxia.** Quantification of the incidence of hypoxic tumors after anti-Sema4D and anti-VEGFR2 1 week (**A**), 2 weeks (**B**) and 4 weeks (**C**) long treatments compared to controls by staining of pimonidazole or Glut 1 adducts. At least 132 tumors were analyzed per group. *p < 0.05 by Mann-Whitney test. Error bars indicate ± SD. Adapted from Martín-Mitjana, 2014.

10. Premise

The field of tumor angiogenesis has reached maturation over the past decades, with regulation mechanisms being thoroughly described and antiangiogenic therapies effectively introduced in the clinic. However, therapies targeting angiogenesis have not proven enduring efficacy and new targets are currently under research. This is the case for Sema4D, a multifunctional neural molecule that is overexpressed in different tumors. With beneficial results in a variety of tumor types, the effectivity of anti-Sema4D treatment remains to be proved in other angiogenic tumors such as NETs. With that aim, using the preclinical RIP1-Tag2 mouse model of PanNETs, our group conducted a study on the effects of Sema4D blockade.

In summary, previous data from our group have demonstrated a beneficial anti-tumor effect of anti-Sema4D therapy in RIP1-Tag2 mice, as depicted by the decrease in tumor burden and increased lifespan. Sadly, these beneficial effects gave way to an increase in local invasion and distant metastasis, an effect already described during traditional VEGF blocking antiangiogenic therapy (Casanovas et al., 2005; Pàez-Ribes et al., 2009). Importantly, in absence of vascular trimming, a partial antiangiogenic effect of anti-Sema4D was observed regarding vessel structure. This effect could explain the beneficial outcome of the therapy. However, further research is needed to decipher the precise antiangiogenic role of anti-Sema4D. Surprisingly, no intratumor hypoxia was observed after Sema4D blockade, which contradicts the previously described hypoxia-mediated malignization after antiangiogenic therapy (Pàez-Ribes et al., 2009). The hypoxia-independent mechanism involved in Semaphorin 4D-mediated malignization has not yet been described.

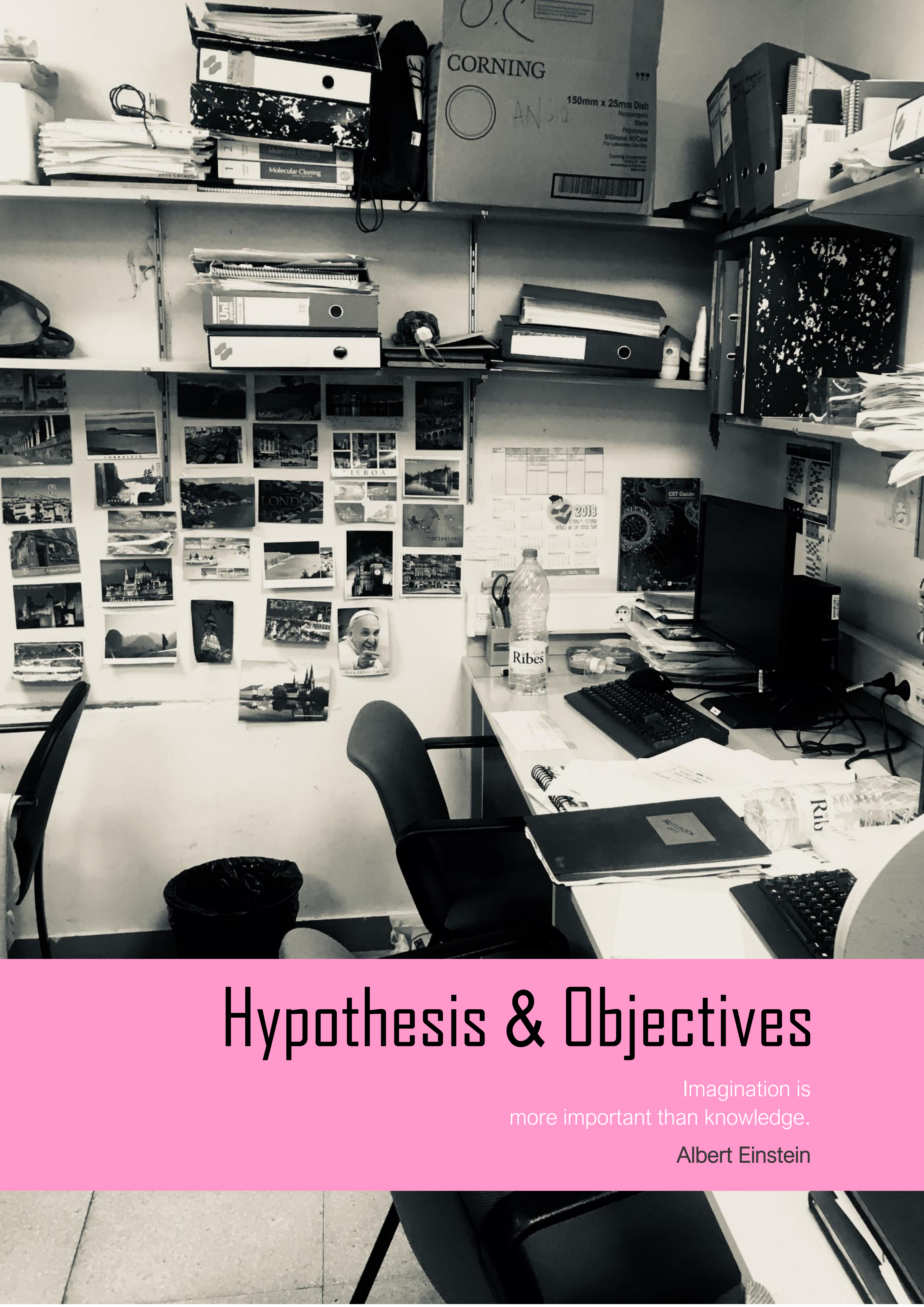

Hypothesis & Objectives

Imagination is
more important than knowledge.

Albert Einstein

1. Hypothesis

Anti-Sema4D treatment effectively decreased tumor burden and increased RIP1-Tag2 mice lifespan, while producing an increase in local invasiveness and distant metastasis in the absence of hypoxia. Changes in vessel structures and decrease in hemorrhagic phenotype occurred in the absence of vessel trimming. We hypothesize that anti-Sema4D therapy is directly altering endothelial cell and pericyte biology, producing the moderate anti-angiogenic effects observed in treated mice. Moreover, data regarding Sema4D expression in RIP1-Tag2 revealed that scattered cells, phenotypically compatible with immune cell infiltrates, highly expressed Sema4D. Since immune-derived Sema4D has been linked with pro-tumorigenic effects, we propose that immune cells, such as tumor-associated macrophages, in the tumor stroma of the RIP1-Tag2 mice are the main contributors to tumor progression.

Overall, we hypothesize that Sema4D inhibition produces a dual action in the RIP1-Tag2 model of PanNETs. On the one hand, it could trigger a switch in the immune phenotype that potentiates tumor cell invasion. On the other hand, blockade of Sema4D produces an antitumor effect that might be directed by its antiangiogenic action upon vascular cells.

2. Objectives

This Doctoral Thesis aims at evaluating the effect of pharmacological inhibition of Sema4D over the tumor stroma of RIP1-Tag2 mouse model, focusing on the mechanisms underlying both its anti-angiogenic and its pro-invasive effects. Specifically our objectives are:

1) *Elucidate the complexity of Sema4D signaling system in the RIP1-Tag2 mouse model tumor ecosystem*

In order to understand the effect of anti-Sema4D therapy, we will first study the expression of the target Sema4D and its receptors PlexinB1 and CD72 in the tumor stroma of RIP1-Tag2 mice.

2) *Decipher the anti-angiogenic and anti-tumor effects of anti-Sema4D in the RIP1-Tag2 mice*

We will focus in the biology of endothelial cells and pericytes in response to anti-Sema4D, placing special emphasis in describing the change in pericyte coverage and the absence of vessel trimming.

3) *Dissect the mechanism underlying tumor malignization after anti-Sema4D treatment in the RIP1-Tag2 mice*

We will functionally validate the implication of macrophages in tumor malignization. For that, molecular changes in macrophage biology and their interaction with tumor cells after anti-Sema4D will be studied.

4) *Validate the functional link described in RIP1-Tag2 tumor malignization after Sema4D blockade in a clinical series of PanNET patients*

Materials & Methods

> An experiment is a question
> which Science poses to Nature.
> A measurement is the recording
> of Nature's answer.
>
> Max Planck

1. *In vivo* experiments

1.1. Animal experimentation

1.1.1. Ethics statement

The use of animals complied with the institutional and European legislation concerning vivisection, the use of genetically modified organisms, animal care and welfare (European Directive 2010/63/UE adopted by the European Parliament and the Council of the EU on September 22, 2010). Both RIP1-Tag2 transgenic and wild type (WT) mice from the B57/BL6 strain were maintained in Specific Pathogen Free (SPF) conditions at the Institut d'Investigació Biomèdica (IDIBELL) animal facility (AAALAC accreditation number 1155). Animals were allowed food and water *ad libitum*, maintained at constant temperature of 20-22 ºC in ventilated racks and manipulated in vertical laminar flow hoods. In accordance with FELASA (Federation of European Laboratory Animal Science Associations) procedure, mice were routinely screened for pathogens. The experimental protocols for anti-Sema4D treatment administration and sacrifice by cervical dislocation were approved by the Institutional Committee for Animal Care and Use (P-3863).

1.1.2. RIP1-Tag2 animal model and genotyping

The generation and characterization of the transgenic RIP1-Tag2 mice have been previously described (Hanahan, 1985) and are further detailed in the previous section of this Thesis. In order to avoid the severe hyperglycemia that some RIP1-Tag2 animals may suffer as a consequence of the insulinoma burden, sucrose (Merck) was added to the water at 5% when animals reached 12 weeks of age.

Since RIP1-Tag2 female mice were sterile, RIP1-Tag2 heterozygous males were backcrossed with WT females in order to perpetuate the RIP1-Tag2 lineage. Pups were weaned at 3 weeks of age, sexed and identified in the ears. DNA extraction for the genotyping of the pups was carried out from tail biopsies that were immersed in digestion solution (EDTA, pH 8; 1% SDS; 2 mg/mL proteinase K) and incubated at 65ºC during 4-12 hours. Inactivation of proteinase K was done by incubating the samples at 95º for 10 minutes. A PCR was then performed using two pairs of primers (Invitrogen) at 2.5 pmol/µl: one pair spanning the T-antigen gene and another pair for the endogenous control β2-globulin (Table 5). The design of the primers guarantees that a 300 bp or a 600 bp DNA fragment is obtained when wild type or RIP1-Tag2 alleles are amplified, respectively. The PCR was run under the conditions depicted in Figure 29.

Table 5 **List of primers used for RIP1-Tag2 mice genotyping.** Sequence of the pair of oligos designed against T-antigen (Tag) and the endogenous control β2 globulin used in the PCR to genotype RIP1-Tag2 mice.

Gene	Forward (5’-3’)	Reverse (5’-3’)
Tag	GCTCAAAGTTCAGCCTGTCC	GGTGGGTTAAAGGAGCATGA
β2 globulin	ATTCACCCCCACTGAGACTG	TGGAGGAAGCTCAGGAAAGA

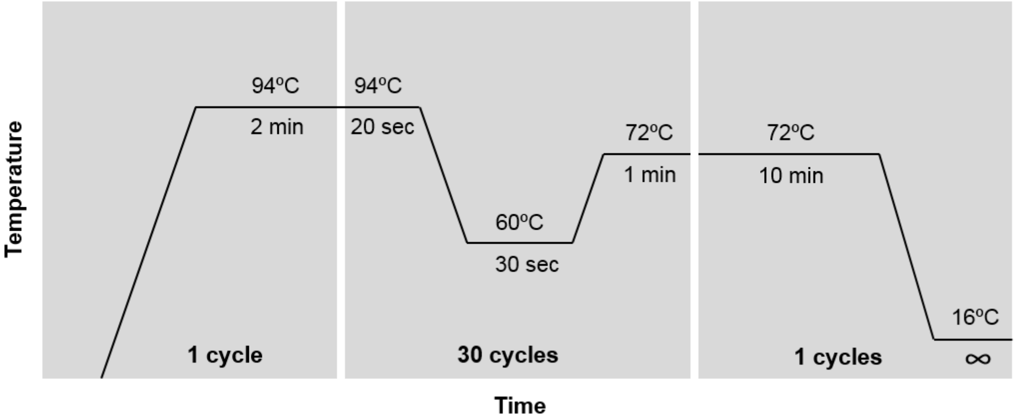

Figure 29 **Termal cycling temperature profile for RIP1-Tag2 genotyping.**

Samples were then run in a 2% agarose gel stained with the cyanine dye SYBR Safe® (Life Technologies) in order to visualize the DNA fragments. Samples with double band pattern would correspond to heterozygous transgenic RIP-Tag2 mice, whereas those showing a single band would represent a wild type genotype (Figure 30). A DNA ladder 100 bp (Niborlab), and negative (water) and positive controls were also included in order to ensure the quality of the PCR reaction.

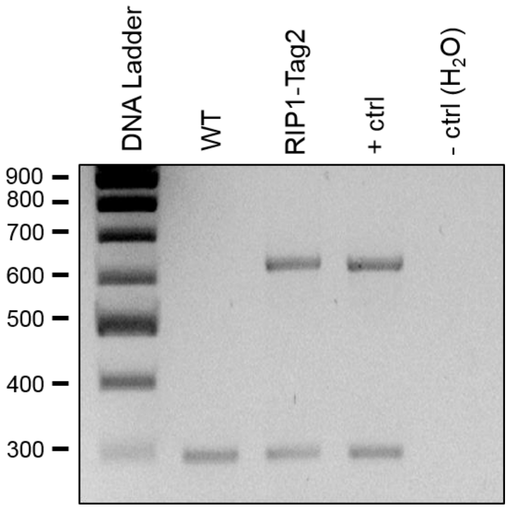

Figure 30 **Agarose gel of a PCR to genotype RIP1-Tag2 mice.** A single band pattern corresponding to β2-globulin gene amplification can be observed for WT mice. An extra band, corresponding to T-antigen amplification, represents RIP1-Tag2 mice. No bands are observed in the negative control (water).

1.1.3. Treatment administration

The administration of the antiangiogenic therapy against Sema4D was started at 12 weeks of age, when the RIP1-Tag2 murine model is described to develop tumors (Hanahan, 1985). A group of ten RIP1-Tag2 mice was treated with anti-Semaphorin 4D (anti-Sema4D) murine progenitor of the VX15/2503 monoclonal antibody (Mab67) (Vaccinex). The antibody was administered at a final concentration of 1 mg/animal once a week through intraperitoneal injection using 25G needles (BD Microlance). As previously stated (Martín-Mitjana, 2014; Pàez-Ribes, 2010), the antiangiogenic and invasive effect was better observed in RIP1-Tag2 tumors after the long treatment of anti-Sema4D. In order to recapitulate this same phenotype, we decided to treat the animals for 4 weeks. As an isotype control, we treated another group of four RIP1-Tag2 mice with ChromPure murine whole IgG1 (Jackson Immuno Research Laboratories) under the same concentration and timing conditions. An additional untreated group of animals at 16 weeks of age was also added as control for the study.

1.2. βTC4 pancreatic neuroendocrine tumor cell line

Cell line βTC4 was derived from RIP1-Tag2 mouse pancreatic tumors as previously described (Efrat et al., 1988). Briefly, pancreatic insulinomas were removed from transgenic animals and excised from the acinar pancreas in DMEM. Tumor β-cells were mechanically disrupted from the tumor capsule and plated at high confluence in 12-well plates in the presence of DMEM containing high serum concentration (15% horse serum and 2.5% FBS, respectively) and 25 mmol/L glucose. When cells reached 50% confluency, they were transferred to 100 mm plates by dissociation by 0.05% trypsin/0.5 mM EDTA. After a few passages, cells were stabilized and subcultured approximately every 5-7 days and fed twice a week. For subculture, trypsin usage should be avoided, as cells are easily detached by slight pipetting and do not need any aggressive enzymatic treatment. βTC4 cells are able to grow up to about 60-70% of confluence, after which increased cell mortality is noted. Additionally, since the cells do not proliferate well below a 20% of confluence, cloning remains challenging.

1.2.1. βTC4 cell maintenance and handling

βTC4 cells were grown in Dulbecco's Modified Eagle Medium (DMEM) from Lonza, enriched with 15% of fetal bovine serum (FBS) (Gibco), previously inactivated by heating at 56ºC for 30 minutes and supplemented with 50U/ml of penicillin, 50µg/ml of streptomycin sulfate, 2mM of L-glutamine, 1% pyruvate and 1% non-essential aminoacids (all from Life Technologies). Where indicated, for some experiments, serum-deprived (0% FBS) or low percentage serum (5% FBS) DMEM was equally prepared. Cells were maintained in a humidified atmosphere of 37ºC, 5% CO_2, and were either counted, handled, frozen or thawed following the standard protocol depicted in the *in vitro* section in this chapter (page 83). Given that this primary cell line is not immortalized, βTC4 cells are described to maintain the features of differentiated β pancreatic cells for about 50 passages in culture. They are capable of producing both proinsulin I and II, and successfully drive their maturation into insulin in a way comparable to normal β-cells. During subsequent passages, so as to discard undifferentiation events, βTC4 phenotype was authenticated by insulin expression assessment by immunocytofluorescence, as described below.

1.2.2. βTC4 cell treatments

To evaluate the direct effect of anti-Sema4D treatment over neuroendocrine tumor cells alone, c-met activity was assayed. Hence, βTC4 cells were treated with 10 µg/ml of anti-Sema4D (Abnova, clon 3B4), 10 µg/ml of isotype control mouse IgG1 (ms IgG1) (Invitrogen) or 40 ng/µl of hepatocyte growth factor (HGF) (R&D systems) during 30 mins prior to protein extraction. A549 cells equally treated with HGF were used as a positive control.

1.3. Tumor and organ collection

After four weeks of therapy, when mice reached 16 weeks of age, they were sacrificed by cervical dislocation. In sterile conditions, RIP1-Tag2 neuroendocrine tumors from the three treatment groups were excised together with the pancreas and the spleen.

On one hand, out of all tumor samples with their surrounding organs, three were randomly chosen and embedded in OCT (Tissue-Tek® Sakura), oriented in the mold and immediately frozen in dry ice. On the other hand, two more samples were individually placed in petri dishes in the presence of 4 mL DMEM 1% penicillin/streptomycin. Acinar pancreas, fat and adjacent non-tumor tissue was carefully removed from the neuroendocrine round tumors with the help of a blade. Clean tumors were rapidly placed in dry ice and, together with ready-to-cut OCT samples, stored at -80ºC until use. The spleen was carefully separated, collected and stored at -80ºC until use to serve as positive control of some experiments.

Remaining samples were rinsed in PBS (0.15 M NaCl, 0.9 mM Na2HPO4 and 0.1 mM KH2PO4), after which they were included into a cassette for paraffin embedding and fixed in tamponed paraformaldehyde 4% overnight (o/n). After fixation, cassettes were rinsed in tap water to eliminate excess of fixative and subjected to a dehydration process as depicted in Table 6. Finally, samples were embedded in paraffin at 65ºC, oriented in the mold and left to solidify at 4ºC in a cold plate. Ready-to-cut paraffin blocks were finally stored at RT until use.

Table 6 **Dehydration steps for paraffin-embedding.**

Step	Time
Ethanol 70%	60 minutes
Ethanol 96%	60 minutes
Ethanol 96%	60 minutes
Ethanol 96%	Overnight
Ethanol 100%	60 minutes
Ethanol 100%	90 minutes
Ethanol 100%	90 minutes
Xylene	90 minutes
Paraffin (65ºC)	Overnight

Additionally, kidney and brain tissues from the untreated group of RIP1-Tag2 mice were also collected and either snap-frozen, paraffin or OCT-embedded, to serve as positive controls for the experiments described hereinafter.

1.4. Molecular analysis

1.4.1. RNA detection by RT-PCR

1.4.1.1. RNA extraction of tumor samples and organs

RNA was extracted from RIP1-Tag2 tumors and organs stored at -80ºC using the RNeasy Plus kit (Qiagen) following the manufacturer's instructions. Briefly, the frozen tissue was pieced with a blade and disrupted in the instructed amount of RLT buffer in presence of 1:100 of β-mercaptoethanol by using a tissue glass homogenizer. All the homogenization process was carried out on ice to avoid RNA degradation. Before continuing with RNA extraction, a gDNA Eliminator spin column (supplied in the kit) was used to remove contaminating genomic DNA. After completing the workflow, the resulting RNA was quantified with the spectrophotometer NanoDrop TM1000 (Thermo Scientific).

Additionally, 500 ng of RNA were loaded in a 1% of agarose gel, using 1 Kb Plus DNA ladder (Invitrogen) as a molecular weight marker, in order to assess the quality of the extracted RNA. When gDNA contamination was found, an additional treatment with DNAse was performed, using DNA-free^{TM} DNA removal kit (ThermoFisher Scientific) following manufacturer's instructions.

1.4.1.2. Obtaining cDNA from mRNA by Reverse Transcription

Reverse transcription (RT) was performed with random primers using 2 μg of total RNA from each sample for complementary DNA synthesis by High Capacity RNA to cDNA Master Mix Kit (Applied Biosystems) following the Manufacturer's instructions. The obtained cDNA was stored at -20ºC until use.

1.4.1.3. Real-Time quantitative PCR (qRT-PCR)

RNA expression was determined with a LightCycler® 480 Real Time PCR system (Roche), using Taqman® Technology (Applied Biosystems). The PCR reaction was prepared in 384 well plates with 25 ng of cDNA, 10 μL of Taqman® Universal PCR Master Mix (Applied Biosystems), 0.5 μL specific Taqman probe (Table 7) and ddH$_2$O in a final volume of 10 μL for each sample in duplicate. Quantitative PCR reaction was then performed as depicted in Figure 31. Results were analyzed with LightCycler® 480 Software 1.5 (Roche). The number of cycles required for the fluorescent signal to cross the threshold (Ct) for each gene was normalized with the Ct of the housekeeping gene *Hprt1*. ΔCt was then converted to RNA expression following this equation:

$$RNA\ expression\ of\ gene\ A = 2^{-\Delta Ct} = 2^{-(Ctgene\ A - Ct\ housekeeping\ gene)}$$

Table 7 **Mouse specific probes used in Taqman system quantitative PCR.**

Gene	Dye-Label	Reference
Sema4d	FAM^{TM}-MGB	Mm00443147_m1
Plxnb1	FAM^{TM}-MGB	Mm00555359_m1
Cd72	FAM^{TM}-MGB	Mm00514270_m1
Cxcl12	FAM^{TM}-MGB	Mm00445553_m1
Cxcr4	FAM^{TM}-MGB	Mm01292123_m1
Ackr3 (Cxcr7)	FAM^{TM}-MGB	Mm00432610_m1
Adgre1 (F4/80)	FAM^{TM}-MGB	Mm00802529_m1
Il12b	FAM^{TM}-MGB	Mm01288989_m1
Nos2	FAM^{TM}-MGB	Mm00440502_m1
Mrc1 (CD206)	FAM^{TM}-MGB	Mm01329362_m1
Arg1	FAM^{TM}-MGB	Mm00475988_m1
Hprt1	FAM^{TM}-MGB	Mm01545399_m1
Actb	FAM^{TM}-MGB	Mm02619580_g1

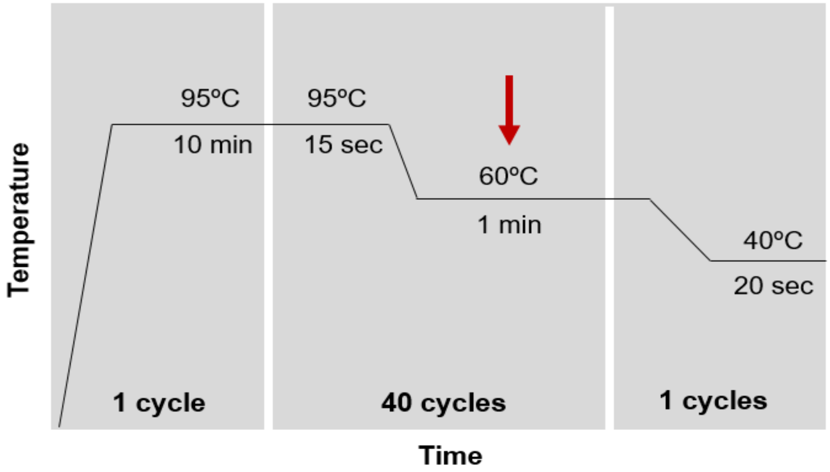

Figure 31 **Termal cycling temperature profile for Taqman RT-PCR.** Fluorescent signal was read out at 60ºC (red arrow).

1.4.2. Protein detection by Western Blotting

1.4.2.1. Preparation of protein lysates from tissues

Protein was extracted from RIP1-Tag2 tumors and organs stored at -80ºC. Briefly, the frozen tissue was pieced with a blade and disrupted in RIPA lysis buffer (Table 8) using a tissue glass homogenizer. All the homogenization process was carried out on ice to avoid protein degradation. The lysate was transferred to a 1.5 ml Eppendorf, gently mixed and incubated on ice for 5 min. After 30-40 min of incubation with rotation at 4ºC, the lysate was centrifuged at maximum speed for 15 min at 4ºC. Supernatants were collected and stored at -20ºC until use.

Table 8 RIPA lysis buffer composition for protein extraction.

PBS	Diluent
NP-40	1%
SDS	0.1%
Sodium deoxycholate	0.5%
NaF	50 mM
β-glycerolphosphate	40 mM
Na_3VO_4	0.2 mM
PMSF	0.1 mM
Pepstatin A	1 µM
Aproptin	4 µg/mL
Leupeptin	1 µg/mL
Benzamidina	0.1 µg/µL

1.4.2.2. Quantification of the protein extracts

For protein quantification, the colorimetric Pierce™ BCA Protein Assay Kit (Thermo Scientific) was used. For each measurement, a standard curve of protein concentration was prepared with Bovine Serum Albumin (BSA) ranging from 0 to 2 mg/ml. The reaction was prepared by mixing BCA working solutions A-B at 50:1 v/v. 190 µl of this mix was added to 10 µl of 1:10 prediluted query samples or BSA standards into a 96-well plate. The plate was incubated at 37ºC and absorbance was finally measured by spectrophotometry (Power Wave XS, BIO-TEK) at 560 nm wavelength, using KCJr Win software. Unknown protein concentration was calculated by extrapolation in the BSA standard curve.

Once quantified, each lysate was boiled in loading Laemmli buffer (Table 9) at a final concentration of 1:4 for 5min at 95°C, in order to reduce and denature the samples and obtain 40 µg/µl concentrated protein samples. After sample boiling, they were spun and stored at -20ºC until use.

Table 9 **Laemmli buffer composition.**

TRIS-HCl pH 6.8	300 mM
SDS	12%
Glicerol	60%
DTT	600 mM
Bromophenol blue	0.6%
β-mercaptoethanol	12%

1.4.2.3. Western Blotting

Protein separation according to their molecular weight was done with denaturalizing sodium dodecyl sulfate poly-acrylamide gels (SDS-PAGE: SDS-PolyAcrilamide Gel Electrophoresis). Poly-acrylamide gels consisted of two different parts: the stacking and the resolving fraction. The first one was always prepared at the same acrylamide concentration (4%), as it functions to gather proteins. In contrast, the resolving one was prepared at different concentrations, ranging from 7.5-12% depending on the molecular weight of the proteins of study, functioning as a sorter for these proteins by their size (after denaturalization). Gels were prepared using 1.5 mm width glass plates (Bio-Rad) and 10 or 15 well combs, with a mixture of H_20, acrylamide-bisacrylamide, Tris-HCl with 0,4% SDS (1.5 Mm, pH 8.8 for stacking and 0,5 Mm, 6.8 for resolving), APS and TEMED. Once the gel was ready, it was assembled into the gel holder and immersed into the electrophoresis chamber, which was filled with running buffer (Table 10**, left**). Samples were loaded into the gel, together with a molecular weight standard (Page Ruler^{TM} prestained, Thermo Scientific) so as to know the molecular weight of the proteins of interest. Separation was carried out at a constant voltage of 120 V, during 1.5 hours, at RT.

After electrophoresis, proteins in the acrylamide gel were transferred to a nitrocellulose membrane (Immobilon-P, Merck Millipore), previously activated in methanol as stated by the manufacturer. Then, together with the membrane, Whatman paper was soaked in transfer buffer (Table 10**, right**) for 5 minutes, and the “transfer sandwich” was assembled as follows (from bottom to top): Sponge – 2 Whatman papers – acrylamide gel – membrane – 2 Whatman papers – sponge. A 90 V constant voltage was applied for 2 hours, at 4ºC.

Table 10 **Running (left) and transfer (right) buffer composition.**

Running buffer	
TRIS-HCl pH 8.3	25 mM
Glycine	192 mM
SDS	0.1%

Transfer buffer	
TRIS-HCl pH 8.3	25 mM
Glycine	192 mM
Methanol	20% (v/v)

For desired protein blotting, the transferred membrane was blocked in 5% skimmed milk (Nestle ®) in TBS (Tris 150 Mm and NaCl 150 mM) – Tween 01% (TTBS) during 1 hour in agitation at RT to prevent unspecific binding of the antibodies. After blocking, the membrane was incubated with the primary antibody against the protein of interest (see antibodies and conditions in Table 11), diluted in 1% skimmed milk in TTBS, o/n in motion at 4ºC. As housekeeping control, membranes were cut and incubated with an antibody against α-tubulin. The membrane was then washed thrice during 10 minutes in TTBS, and subsequently incubated with the HRP-linked secondary antibodies anti-rabbit IgG (1:5000) or anti-mouse IgG (1:2500) (GE Healthcare), diluted 1:5000 or 1:2500 respectively in 1% skimmed milk in TTBS, during 1h in agitation at RT. The membrane was again washed thrice during 10 minutes in TTBS. Finally, blots were developed with Amersham ECL Select$^{\text{TM}}$ western blotting detection reagent (GE Healthcare Life Sciences), according to manufacturer’s instructions. Signals on blots were detected with ChemiDoc Touch System (Bio-Rad), whereas densitometric analysis of protein band intensity was performed using Image Lab software (Bio-Rad).

Table 11 Primary antibodies used for Western blotting.

Primary antibody	Host	Dilution	Manufacturer	Catalogue nº
c-met	mouse	1:100	Santa Cruz Biotec.	sc-8057 clone B2
Phospho c-met	rabbit	1:750	Cell signaling	3077
α-tubulin	mouse	1:2000	Invitrogen	32-2500

1.4.3. Protein detection by Enzyme-linked immunosorbent assay (ELISA)

Two ELISAs for high sensitivity detection of PDGF-BB (MBB00 Quantikine ELISA kit, R&D systems) and CXCL12 (MCX120 Quantikine ELISA kit, R&D systems) were performed under the manufacturer's instructions, in untreated and anti-Sema4D treated frozen tumors. Since protein extracting RIPA buffer contains detergents such as SDS and NP-40 that interfere with antibody-antigen interactions in the ELISA, we decided to extract protein directly in PBS, in absence of detergents as depicted in Table 12. Next steps for protein extraction and quantification were identical to the ones previously detailed for Western blot (page 70 and 71).

For the ELISA, standards and samples (without dilution) were loaded in duplicate and any PDGF-BB or CXCL12 present was bound by the immobilized antibody on each 96 well plate. After washing away unbound substances, an enzyme-linked polyclonal antibody specific for these two proteins was added to the wells of each plate. Following a wash to remove any unbound antibody-enzyme reagent, a substrate solution was added to the wells and color developed in proportion to the amount of PDGF-BB or CXCL12 bound in the initial step. The color development was stopped with the Stop Solution and the intensity of the color was measured 30 minutes later as absorbance at 450 nm in the Power Wave XS spectrophotometer (BIO-TEK), using KCJr Win software. Expression of the proteins of interest was calculated by extrapolation in the standard curve and normalized by the total amount of loaded protein.

Table 12 Lysis buffer composition for protein extraction for ELISA.

PBS	Diluent
NaF	50 mM
β-glycerolphosphate	40 mM
Na_3VO_4	0.2 mM
PMSF	0.1 mM
Pepstatin A	1 µM
Aproptin	4 µg/mL
Leupeptin	1 µg/mL
Benzamidina	0.1 µg/µL

1.5. Histological analysis

1.5.1. Immunohistochemistry (IHC) in paraffin embedded sections

Paraffin-embedded RIP1-Tag2 untreated, ms IgG1 and anti-Sema4D treated samples were cut into 5 µm-thick sections using a microtome and placed in poly-L-lysine pretreated slides. For poly-L-lysing, slides were previously incubated for 10 minutes with 1:2 poly-L-Lysine (Sigma) in ddH_2O and left to air-dry at 37ºC o/n. A pre-deparaffination step was carried out in order to optimize the immunohistochemistry by placing the slides at 65ºC o/n. Next, paraffin was removed and samples were rehydrated. To this aim, sample slides were placed in pre-heated xylene at 65ºC for 20 minutes and then soaked in subsequent alcohols as indicated in Table 13.

After rehydration, samples were rinsed for 5 minutes with distilled water and then boiled in a solution containing citric acid (0.38 mg/mL) and sodium citrate (2.45 mg/mL) at pH 6, for antigen retrieval, during 5-10 minutes. Samples were then left immersed in this solution for 20 minutes at RT, and they were afterwards rinsed for 5 minutes in distilled water. In favor of minimizing the background, endogenous peroxidases were blocked by submerging the slides twice in 6% hydrogen peroxide for 10 minutes. After rinsing the samples in distilled water during 5 minutes, cell membrane permeabilization was achieved through immersion in PBS – Triton 0.1% (TPBS) during 10 minutes. Thereafter, samples were blocked with 100 µl of 1:5 serum from the species (usually goat) used to generate the secondary antibody, in PBS during 1 hour in humidity at RT. Slides were ultimately incubated o/n with 100 µl of primary antibody (Table 14) diluted in blocking solution at 4ºC in a wet chamber. Slides incubated with blocking solution, in absence of primary antibody, served as a specificity control.

Table 13 Hydration steps for IHC.

Step	Time
Xylene	10 minutes
Xylene	10 minutes
Xylene	10 minutes
Xylene	10 minutes
Ethanol 100%	5 minutes
Ethanol 100%	5 minutes
Ethanol 100%	5 minutes
Ethanol 96%	5 minutes
Ethanol 96%	5 minutes
Ethanol 96%	5 minutes
Ethanol 70%	5 minutes
Ethanol 50%	5 minutes

On the following day, slides were tempered for 20-30 minutes and washed thrice with TPBS for 5 minutes. Incubation with 100 µl of secondary anti-mouse or anti-rabbit peroxidase-conjugated antibodies (Envision^{+} system-HRP, Dako) for 1 hour at RT in a humid chamber. Afterwards, samples were washed thrice with TPBS for 5 minutes and peroxidase reaction was developed by covering each section with the chromogenic substrate DAB^{+} (Envision Kit, Dako), from 30 seconds to 10 minutes, depending on the antibody and the samples used. When a brown precipitate appeared, the reaction was stopped by soaking the slides in tap water for 10 minutes.

Table 14 Primary antibodies used for immunohistochemistry in paraffin.

Primary antibody	Host	Dilution	Manufacturer	Catalogue nº
CXCR4	rabbit	1:750	Sigma	C8352
CXCL12	mouse	1:20	R&D systems	MAB350

Last steps included counterstaining with haematoxylin 0,1% (Merck) in ethanol 96º for 20 seconds followed by a dehydration procedure, as indicated in Table 15. Slides were finally mounted using DPX (Merck) and tissues were visualized in a Nikon eclipse 80i microscope with the appropriate filters. Representative images were taken with a Nikon DS-Ri1 digital camera and using NIS-Elements BR 3.2 (64-bit) software. Images were edited with ImageJ software and quantifications were manually performed as explained in each of the experiments in the Results section. Tumors were classified depending on their tumor front invasiveness. Those with over 30% adjacent tissue invasion were classified as invasive, whereas the rest were regarded as non-invasive.

Table 15 Dehydration steps for IHC.

Step	Time
Ethanol 70%	5 minutes
Ethanol 96%	5 minutes
Ethanol 96%	5 minutes
Ethanol 96%	5 minutes
Ethanol 100%	5 minutes
Ethanol 100%	5 minutes
Ethanol 100%	5 minutes
Xylene	10 minutes
Xylene	10 minutes
Xylene	10 minutes

1.5.2. Haematoxylin-Eosin staining in paraffin-embedded sections

In order to visualize the morphology of the invasive front, formaldehyde-fixed and paraffin-embedded samples were used due to their preserved morphology, which allows the study of tissue architecture. Paraffin-embedded RIP1-Tag2 untreated, and anti-Sema4D treated samples were cut, predeparaffinized and rehydrated as explained in page 75. Slides were finally mounted using DPX (Merck) and tissues were visualized in a Nikon eclipse 80i microscope with the appropriate filters. Representative images were taken with a Nikon DS-Ri1 digital camera and using NIS-Elements BR 3.2 (64-bit) software.

Slides were submerged in haematoxylin 0,1% (Merck) in ethanol 96º for 10 minutes and rinsed in tap water for excess elimination. Afterwards, slides were submerged in HCl 1% until tissue color shifted to red, following submersion in ammonia water solution (200 ml of distilled H_2O + 1 ml of ammonia 30%) until it turned bluish. Sections were finally counterstained with eosin (2.5 g of eosin in 1L of ethanol 50%) for 10 minutes. Slides were finally mounted using DPX (Merck) and tissues were visualized in a Nikon eclipse 80i microscope with the appropriate filters. Representative images were taken with a Nikon DS-Ri1 digital camera and using NIS-Elements BR 3.2 (64-bit) software.

1.5.3. Immunohistofluorescence in OCT- or paraffin-embedded sections

1.5.3.1. OCT-embedded samples

OCT-embedded RIP1-Tag2 untreated, ms IgG1 and anti-Sema4D treated samples were cut into 5 µm-thick sections using a cryostat, cooled at -20ºC, and placed in poly-L-lysine pretreated slides. For poly-L-lysing, slides were previously incubated for 10 minutes with 1:2 poly-L-Lysine (Sigma) in ddH_2O and left to air-dry at 37ºC o/n. Slides were fixed by immersion in precooled acetone (-20ºC), at 4ºC for 10 minutes. Then, slides were set to air-dry and washed in PBS for 5 minutes.

Aiming to block unspecific binding of the secondary antibody, tissues were blocked with 100 µl goat serum at 4% in PBS per section at RT for 1 hour. Slides were ultimately incubated o/n with 100 µl of primary antibody (Table 16) diluted in blocking solution, at 4ºC in a wet chamber. Combinations of one, two or three primary antibodies were used, as described in the Results section. Slides incubated with blocking solution, in absence of primary antibody, served as a specificity control for secondary antibodies.

Table 16 **Primary antibodies used for immunohistofluorescence.**

Primary antibody	Host	Dilution	Manufacturer	Catalogue nº
Insulin	guinea pig	1:50	Dako	A0564
F4/80	rat	1:50	AbD Serotec	MCA497R
Semaphorin 4D	rabbit	1:1000	Vaccinex	G3256
CD31	rat	1:50	BD Biosciences	550274
Desmin	rabbit	1:150	Abcam	ab15200
NG2	rabbit	1:50	Millipore	AB5320
α-SMA	rabbit	1:100	Thermo Scientific	RB-9010
Plexin B1	mouse	1:50	Santa Cruz Biotec.	sc-28372
CD72	rabbit	1:100	Cloud-clone Corp.	PAB261Mu01
CD19	rat	1:25	BD Pharmingen	550284
CD3e	hamster	1:10	BD Pharmingen	550275

After washing thrice with PBS, slides were incubated with secondary antibodies from Invitrogen (Table 17) at 1:200, at RT for 1 hour, in a wet chamber protected from light. Finally, slides were washed in PBS thrice to remove the unbound secondary antibody. Cell nuclei were counterstained with DAPI 1:3000 (Sigma) for 10 minutes at RT and sections were finally mounted with coverslips in Fluoromount® Aqueous Mounting Medium (Sigma) and stored at 4ºC until use. Double-stained tissues were visualized in a Nikon eclipse 80i microscope with the appropriate filters, whereas triple-stained tissues were analyzed in a Leica TCS SP5 confocal microscope. Representative images were taken with a Nikon DS-Ri1 digital camera and using NIS-Elements BR 3.2 (64-bit) software. Confocal images were obtained using LAS X software. Images were finally edited with ImageJ software and quantifications were manually performed as explained in each of the experiments in the Results section.

Table 17 **Secondary antibodies used for immunohistofluorescence.**

Secondary antibody	Host	Fluorochrome
Anti-mouse	goat	Alexa Fluor 488
Anti-mouse	goat	Alexa Fluor 546
Anti-rat	goat	Alexa Fluor 488
Anti-rat	goat	Alexa Fluor 546
Anti-rabbit	goat	Alexa Fluor 488
Anti-rabbit	goat	Alexa Fluor 546
Anti-rabbit	goat	Cy5
Anti-hamster	goat	Alexa Fluor 488
Anti-guinea pig	goat	Alexa Fluor 647

For detection of Sema4D or Plexin B1, modifications were made to the standard procedure as explained below:

- *Tyramide Signal Amplification (TSA^{TM}) for Sema4D staining*

For Sema4D detection, a 568 TSA^{TM} Kit (Life Technologies), was used. TSA^{TM} is an enzyme-mediated detection method that uses the catalytic activity of horseradish peroxidase (HRP) to generate high density labelling of a target protein. Instead of using a fluorochrome-labelled secondary antibody for Sema4D detection, slides were incubated with 100 µl secondary anti-rabbit peroxidase-conjugated antibody (Envision^{+} system-HRP, Dako) for 1 hour at RT in a humid chamber. After subsequent washes in PBS, tyramide amplification step was carried out as described by the manufacturer, during 10 minutes at RT. Slides were counterstained with DAPI, mounted and visualized as previously explained.

- *Mouse on Mouse (M.O.M.™) for PlexinB1 staining*

In order to avoid the unspecificity of mouse primary antibodies on mouse tissues, M.O.M.™ Immunodetection Kit (Vector Laboratories) was used for PlexinB1 detection. The kit includes a proprietary mouse Ig Blocking Reagent to significantly reduce undesired binding of the secondary antibody to endogenous tissue immunoglobulins. Briefly, blocking step was performed during 1h in working solution of M.O.M.™ Mouse IgG Blocking, followed by an incubation with M.O.M.™ Diluent. Primary antibodies were then added, diluted in M.O.M.™ Diluent to the appropriate concentration, o/n at 4ºC. Secondary antibody incubation, counterstaining, mounting and visualization were carried out as previously explained.

1.5.3.2. Paraffin-embedded samples

In order to perform a simultaneous and discriminable detection of CD72 and pericyte markers (Desmin, NG2 and α-SMA) using antibodies produced in the same host, we designed a protocol based on tyramide probe amplification, using 488 TSA™ Kit (Life Technologies).

Paraffin-embedded RIP1-Tag2 untreated, ms IgG1 and anti-Sema4D treated samples were cut, predeparaffinized and rehydrated as explained in page 75. Similarly, endogenous peroxidase inactivation, antigen retrieval and blocking were performed as previously described. Slides were ultimately incubated 1 hour with 100 µl per section of primary rabbit anti -Desmin, -NG2 and -α-SMA antibodies (combined and separately) diluted 1:50 in blocking solution, at RT. After washing, 100 µl secondary anti-rabbit peroxidase-conjugated antibody (Envision+ system-HRP, Dako) was applied for 1 hour at RT in a humid chamber. Slides were washed and tyramide amplification step was carried out as described by the manufacturer for 10 minutes at RT. In order to stop tyramide binding reaction, a microwave treatment which consisted of 5 minutes of boiling samples in citrate solution pH 6, was performed. Samples were washed and primary rabbit anti-CD72 antibody was applied at a 1:50 dilution in blocking solution, o/n at 4ºC in a humid chamber.

Afterwards, samples were washed thrice with PBS and secondary goat anti-rabbit Alexa 488 antibody was added 1:200 in blocking solution. Sudan black staining was further performed by incubating samples with 01% Sudan Black in 70% ethanol in order to avoid paraffin autofluorescence,. Finally, sections were washed, counterstained with DAPI, mounted and visualized as previously explained for OCT-embedded samples (page 78).

1.5.4. In situ zymography for MMPs detection

In situ zymography has been performed in frozen sections from control and anti-Sema4D treated RIP1-Tag2 tumors in order to detect MMP-9 activity in the tumor milieu. To this aim, DQ gelatin (EnzCheck^{TM} Gelatinase/Collagenase Assay Kit, Molecular Probes) was used according to the manufacturer's instructions, together with rat anti-mouse F4/80 antibody (MCA497R, AbD Serotec) at 1:50 in PBS. Briefly, OCT preserved samples at -80ºC were cut into 5 μm-thick sections and fixed by immersion in precooled acetone (-20ºC), at 4ºC for 10 minutes. Then, slides were left to air dry and washed in PBS during 5 minutes. Tissues were blocked with 4% goat serum in TPBS at RT for 20 minutes to avoid unspecific binding of the secondary antibody.

Protected from light, 100 μl of DQ^{TM} gelatin 1/500 in PBS were subsequently applied at RT for 2 hours. DQ^{TM} gelatin is a fluorescein conjugate gelatin so heavily labeled with fluorescein that the fluorescence is quenched. This substrate is efficiently digested by most gelatinases and collagenases to yield highly fluorescent peptides. The increase in fluorescence is proportional to proteolytic activity. Slides were then washed in PBS and primary rat anti-F4/80 and secondary antibodies were applied as described in page 78. Finally, slides were washed in PBS thrice to remove the unbound secondary antibody. Cell nuclei were counterstained with DAPI 1:3000 during 10 minutes at RT and sections were finally mounted with coverslips in Fluoromount® Aqueous Mounting Medium (Sigma) and stored at 4ºC until use. Tissues were visualized in a Nikon eclipse 80i microscope with the appropriate filters. Representative images were taken with a Nikon DS-Ri1 digital camera and using NIS-Elements BR 3.2 (64-bit) software. Images were edited with ImageJ software.

2. *In vitro* experiments

2.1. 2D culture

2.1.1. Cell lines and culture conditions

All cell lines were obtained and authenticated by STR profiling by the ATCC. RAW 264.7 (RAW) murine macrophage cells were kindly provided by Dr. E. Ballestar (Programa d'Epigenètica I Biologia del Càncer, Barcelona). Jurkat and A549 cells were generously donated by Dr. Alemany (ProCURE, ICO-IDIBELL, L'Hospitalet).

Cell line origin, type and culture conditions are detailed in Table 18. DMEM (Lonza) media was enriched with 10% fetal bovine serum (FBS) (Gibco), previously inactivated by heating at 56ºC for 30 minutes, and supplemented with 50U/ml of penicillin, 50µg/ml of streptomycin sulfate, 2mM of L-glutamine, 1% pyruvate and 1% non-essential aminoacids (all from Life Technologies). Where indicated, for some experiments, serum-deprived (0% FBS) DMEM media was equally prepared. Cells were maintained in a humidified atmosphere of 37ºC, 5% CO_2. All cell lines needed to be split at sub-confluent cultures (70-80%), every 2-3 days, according to ATCC indications.

Table 18 Used cell lines and their features.

Cell line	Organism	Tissue origin	Cell type	Culture media	Culture properties
RAW 264.7	Mouse	Leukemia	Macrophage	DMEM	Adherent
A549	Human	Lung carcinoma	Lung epithelial	DMEM	Adherent

2.1.2. Cell viability and counting by trypan blue

Analysis of cell viability and counting was performed manually by trypan blue (Sigma) dying exclusion. At the desired times of treatment, RAW cells were scrapped cautiously using a cell scraper (Sarstedt), while A549 cells were detached by incubation with pre-warmed 1% Trypsin (Gibco) in PBS for 2 minutes at 37ºC. Trypsin was inactivated by addition of fresh media supplemented with FBS. Cell suspensions were then centrifuged for 5 minutes at 1000 rpm. Cell pellet was resuspended with fresh full media and 10 µl were mixed with 90 µl of trypan blue. Viable and non-viable (blue stained) cells were counted in a Neubauer chamber, counting eight squares/condition, in duplicates. Regarding viability, results were expressed as percentage of viable and non-viable cells. Only when viable cell percentage was greater than 95%, experiments were performed with such cells. Cell concentration was calculated with the following equation:

$$Concentration\left(\frac{cells}{ml}\right) = Mean\ viable\ cells\ per\ quadrant\ x\ dilution\ factor\left(\frac{1}{10}\right) x\ 10^4$$

2.1.3. Cell freezing and cryopreservation

When cells reached 90-100% confluence, they were trypsinized or scraped, collected and centrifuged as explained in the previous subsection. Cell pellet was resuspended in 2 ml of cold freezing medium containing FBS and 10% DMSO (Sigma). The suspension was then distributed into two cryotubes and placed in a container filled with 2-propanol for its freezing at -80ºC for a minimum of 24 hours. Finally, cryotubes were stored in a liquid nitrogen tank for long term conservation.

For cell thawing, cells were quickly transported in dry ice from liquid nitrogen to a water bath at 37ºC. When liquified, cells were diluted in prewarmed media and centrifuged at 1000 rpm for 5 minutes. The pellet was resuspended in fresh media and plated into the desired plate, usually a p100 plate, in order to optimize their recovery.

2.2. 3D culture

2.2.1. βTC4 spheroid handling

During the *in vitro* 2D culture of βTC4 neuroendocrine tumor cell line, when overconfluence was achieved, arousing of spherical cellular aggregates was observed Figure 32. Formation of these tight compact aggregates, termed "βTC4 spheroids", occurs spontaneously as a consequence of cell-cell contact domination over cell-substrate interactions. βTC4 spheroids exist in a variety of sizes and can be partitioned from the cellular monolayer by employing cell strainers of varying pore size.

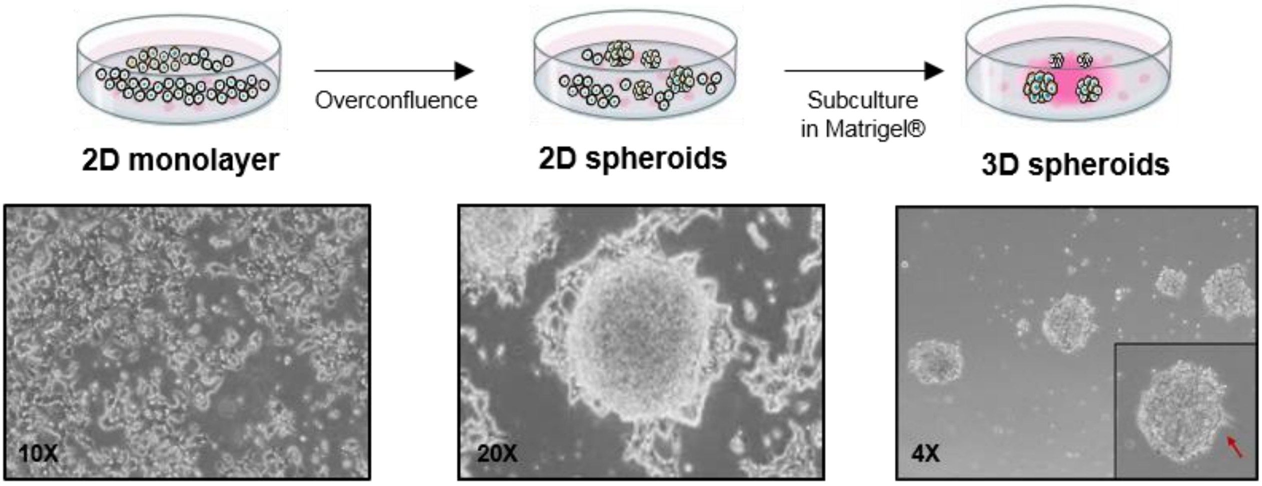

Figure 32 **Spontaneous formation of βTC4 spheroids and 3D culture in Matrigel®.** Overconfluence of βTC4 cells induces the spontaneous formation of spherical cellular aggregates termed βTC4 spheroids in 2D culture conditions. Subsequent culture of βTC4 spheroids in Matrigel® allows the establishment of a 3D tumor model. Images were acquired using an inverted microscope, employing the indicated magnification. A typical invasive strand is pointed by a red arrow.

For spheroid subculture and maintenance, a βTC4 overconfluent p100 plate is firstly cautiously washed with PBS, resuspended in βTC4 media (composition detailed in page 66) and filtered using a 40 μm nylon cell strainer (Falcon Corning). Then, the spheroids retained in the cell strainer are collected and cultured in a new p100 plate for spheroid expansion.

A 3D model of βTC4 spheroids was established by using Matrigel® matrix Growth Factor Reduced (Matrigel® GFR, Corning) so as to better mimic the in vivo conditions in RIP1-Tag2 tumors (Figure 32). Matrigel® GFR is primarily composed by laminin, followed by collagen IV and heparan sulfate proteoglycans. Thus, it effectively mimics the extracellular matrix of most tumors. With regard to 3D model generation, a βTC4 overconfluent p100 plate is equally handled, using a 70 µm nylon cell strainer (Falcon Corning) to exclude smaller spheroids. Retained spheroids are collected in a 15 ml Falcon tube and allowed for physical decantation for 2-4 minutes. Spheroids at the bottom are placed in an Eppendorf, diluted 1:10 in fresh βTC4 media, and they are ready to use.

When growing the isolated spheroids within a 3D matrix, the manufacturer's instructions regarding the "Thick Gel Method" were followed. Briefly, 30 µl of cool liquid Matrigel® were placed in each well of a 24 well plate. 5 µl of previously filtered spheroids were added to the gel in a drop and were gently mixed, avoiding bubble formation. Using an inverted microscope (Leica DMi1), spheroids were manually counted. If confluence was over 30-40 spheroids per Matrigel® drop, filtrated spheroids were further diluted until desired concentration was reached. The 24 well plate was incubated at 37ºC for 30 minutes for Matrigel® solidification. Finally, 1 ml of βTC4 media was added to each well and renewed every 3-4 days.

2.2.2. Freezing and cryopreservation

Spheroid freezing and cryopreservation is performed as previously described for 2D cells (page 84). After thawing, spheroids are first left to expand during 2 weeks prior to any experiment.

2.3. Molecular analysis

2.3.1. RNA detection by RT-PCR

When cells reached the desired confluence, they were detached and collected as explained in the previous section. After 5 minute centrifugation at 1000 rpm, cell pellet was washed with PBS and recentrifuged. The resulting pellet was directly stored at - 80ºC until RNA extraction was performed. All the procedures regarding RNA extraction, cDNA obtention and Taqman® RT-PCR were carried out as previously detailed in page 68.

2.3.2. Protein detection by Western Blotting

When RAW and A549 adherent cells reached the desired confluence, they were placed on ice. Culture medium was removed and dishes were washed twice with PBS. 400 µl of cold RIPA lysis buffer (Table 8) were added per p100 plate. Plates were incubated for 15 minutes in agitation at 4ºC. Consequently, cell plates were placed on ice and generously scraped using a cell scraper (Sarstedt). Cell lysates from both types of cells were collected and centrifuged at 14000 rpm during 15 minutes at 4ºC. Supernatants were stored at -20ºC until use. Quantification and protein detection by Western Blotting was done following the indications and using the antibodies described in the previous sections (page 70). For CD206 detection, a mouse anti-CD206 (AB8918, Abcam) was used at 1:10 dilution.

2.3.3. Protein detection by immunocytofluorescence

For protein detection by immunocytofluorescence, round glass coverslips (VWR) were deposited into 24 well plates with sterile tweezers and following UV sterilization of the plate for 2 hours. Adherent cells were seeded onto the coverslips and left to grow in 500 µl of the corresponding cell media until they reached 60-80% confluence. At that point, cell media was removed and cells were washed twice in PBS. Fixation was carried out with cool paraformaldehyde 4% for 10-15 minutes. Once fixed, cells were washed twice with PBS during 5 minutes in agitation at RT, after which they were permeabilized for 15 minutes with TPBS. This step is optional, as it enables antibodies to pass through the lipid cell membranes when intracellular antigen detection is required. In order to avoid unspecific binding of the secondary antibody, blocking was performed using goat serum diluted 1:5 in PBS, in drops of 30-40 µl/coverslip, during 30 mins at RT. Parafilm was used for flipping the coverslips over the drops. Next, antibody against the desired antigen was equally applied at the corresponding dilution in blocking solution (Table 19) for 1 hour at RT.

Table 19 Primary antibodies used for immunocytofluorescence.

Primary antibody	Host	Dilution	Manufacturer	Catalogue nº
F4/80	rat	1:50	AbD Serotec	MCA497R
Semaphorin 4D	mouse	1:50	Abnova	H00010507-M01 Clone 3B4
Plexin B1	mouse	1:50	Santa Cruz Biotec.	sc-28372
CD72	rabbit	1:50	Cloud-clone Corp.	PAB261Mu01
Insulin	guinea pig	1:50	Dako	A0564

Coverslips were then washed twice in PBS for 10 minutes in agitation at RT. For fluorescence detection, fluorescent-conjugated secondary antibody against the species used to generate the primary antibody was used (Table 20) at 1:200 in blocking solution, for 1 hour at RT. After washing the cells with PBS twice, drops of 30-40 µl/coverslip of 1:3000 of DAPI (Sigma) were added for nuclear DNA staining. All incubations were performed in a humidity chamber. Finally, cells were washed twice in PBS for 10 minutes in agitation and mounted using Fluoromount™ Aqueous Mounting Medium (Sigma) for visualization. Cells were visualized in a Nikon eclipse 80i microscope with the appropriate filters. Representative images were taken with a Nikon DS-Ri1 digital camera and using NIS-Elements BR 3.2 (64-bit) software. Images were edited with ImageJ software.

Table 20 Secondary antibodies used for immunocytofluorescence.

Secondary antibody	Host	Fluorochrome
Anti-mouse	goat	Alexa Fluor 546
Anti-rabbit	goat	Alexa Fluor 546
Anti-rat	goat	Alexa Fluor 546
Anti-guinea pig	goat	Alexa Fluor 546

2.4. Macrophage conditioned media

2.4.1. Conditioned media production and treatments

In order to obtain conditioned media, 9x10^5 RAW cells were seeded in 6 well plates and left to grow. When they reached 60-70% confluence, cell medium was removed and 1 ml of serum-free DMEM was added, together with 10 µg/ml anti-Sema4D or 10 µg/ml ms IgG1 (Invitrogen), in triplicates (Figure 33). An IgG1-treated condition was generated as a control of the putative noise produced by antibody addition to immune cells. Both anti-Sema4D antibodies from Vaccinex and Abnova were similarly used. Cells were incubated during 24h in a humidified atmosphere of 37ºC, 5% CO_2. Thereafter, conditioned media were collected and, as a control of direct anti-Sema4D effect upon tumor cells, 10 µg/ml anti-Sema4D or 10 µl/ml of ms IgG1 (Invitrogen) were added to untreated conditioned media, generating the “added” conditions (Figure 33). Conditioned media were then filtered with a syringe filter with a PES membrane of 0.22 µm (TRP) and stored at -20ºC until use. For long term storage, conditioned media were placed at -80ºC. Cells were also harvested as previously explained in page 86 for further RNA or protein analysis.

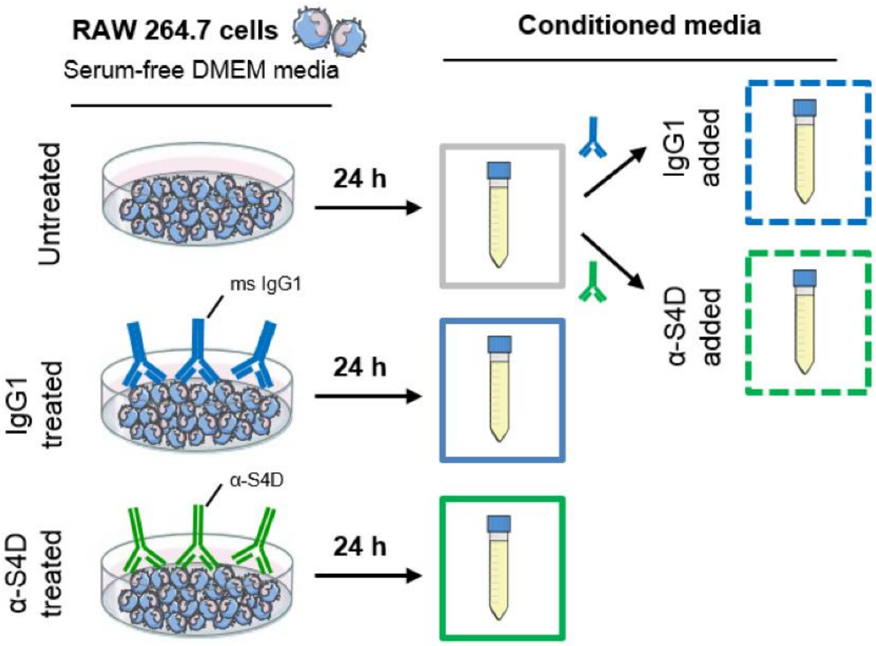

Figure 33 **Macrophage conditioned media production.** $9x10^5$ RAW macrophage cells are expanded in normal conditions until they are 60-70% confluent. The growth media is then exchanged with serum-free media containing 10 µg/ml anti-Sema4D or 10 µg/ml ms IgG1 (Invitrogen), and left for 24 h in a CO_2 incubator. Conditioned media are collected and 10 µg/ml anti-Sema4D or 10 µg/ml ms IgG1 (Invitrogen) are added to untreated conditioned media to generate "added" control conditions. Conditioned media from all treatment conditions are then filtered with a syringe filter with a PES membrane of 0.22 µm (TRP) and stored at -20ºC until use.

2.4.2. Proteomic analysis of conditioned media

In order to analyze the secretome of RAW macrophages under different treatments, a shotgun proteomic approach was designed. Previously collected 4 ml of conditioned media for each treatment were first concentrated using a Vivaspin 2 KDa molecular mass cut-off spin column (Sartorius), at 3000 g, for 4:30 hours at 4ºC. Protein was finally concentrated in 150-200 µl total volume. 20 µl of each protein concentrate, together with 150 µl of flow through, were mixed with 5 µl of WB loading buffer and subjected to electrophoresis in a 9% SDS-PAGE gel. Gel was stained with 0.1% Coomassie blue (10% isopropanol, 10% glacial acetic acid, 1g Coomassie blue in 800 ml of distilled water), during 30 minutes. Gel was then destained o/n in destaining solution (5 ml acetic acid and 12,5 ml of 2-propanol in 32,5 ml of distilled water). After washing in water, protein content was qualitatively visualized.

The shotgun proteomic analysis of the triplicated samples of untreated, anti-Sema4D (Vaccinex) added, anti-Sema4D treated and ms IgG1 (Invitrogen) treated RAW concentrated conditioned media was performed by the Proteomics Platform in the Centre de Regulació Genòmica (CRG) (Barcelona), following standard procedures. Briefly, the mass spectrometric analysis (LC-MS/MS) was done according to previously published protocols (Perkins et al., 1999; Rappsilber et al., 2007). Proteins were first filtered by a FDR score of 0.05. Proteins were annotated with their corresponding HUGO gene symbol using DAVID (Dennis et al., 2003) bioinformatic tool.

2.4.2.1. Bioinformatic analysis by GSEA

Filtered proteomic data was subjected to a Gene Set Enrichment Analysis (GSEA). GSEA is a computational method that determines whether an a priori defined set of genes (or proteins) shows statistically significant and concordant differences between two biological states previously defined and reviewed in the literature (Subramanian et al., 2005). The GSEA analysis tool was run using default values for all parameters, using Signal2Noise metric for ranking genes, phenotype permutation type and excluding comparison with gene sets smaller than 5 and bigger than 500 genes. The GSEA analysis used pathway annotations from the Kyoto Encyclopedia of Genes and Genomes (KEGG) (Kanehisa et al., 2012), and Gene Ontology (GO). Results were represented as statistically significant pathways enriched in anti-Sema4D treated conditions with respect to REST phenotype, which included control untreated, anti-Sema4D added and IgG1 treated samples.

2.4.2.2. Bioinformatic analysis of secretome by STRING

Starting with the proteomic data, only proteins with a peptide count higher than two units were used for the bioinformatic Search Tool for the Retrieval of Interacting Genes/Proteins (STRING) analysis (Szklarczyk et al., 2015). After comparing anti-Sema4D and ms IgG1 treated samples, enriched proteins that showed a p. value lower than 0.05 by Mann-Whitney test were selected in the form of fold-change for the bioinformatic analysis. Secreted proteins were further selected according to subcellular localization information in UniProt database (Bateman et al., 2017). STRING analysis was run using default values for all parameters. Focus was placed on results regarding pathways related to molecular functions or biological processes that showed statistical significance.

2.4.3. Macrophage profile estimation

Starting with the proteomic data, only proteins with a peptide count higher than two units were used. After comparing anti-Sema4D and ms IgG1 treated samples, enriched and depleted proteins that showed a p. value lower than 0.05 by Mann-Whitney test were selected in the form of fold-change for the bioinformatic macrophage profile estimation. Data for gene expression profiles of different experiments that analyzed varyingly differentiated macrophages (monocytes, bone-marrow derived macrophages, tissue macrophages and M1 or M2 type macrophages) were taken from the corresponding publications and from the Gene Expression Omnibus (GEO) references GSE5099 and GSE68817. In order to determine which of the macrophage types best fitted with proteomic data, supervised (enriched and depleted genes) and unsupervised (enriched genes) heatmaps analysing GEO dataset gene expression of proteomic derived data were performed in collaboration with Luis Palomero from ProCURE (ICO-IDIBELL, L’Hospitalet). Data were normalized using z-score and Ward’s method was used for the clustering. Spearman correlation was calculated for the expression of each gene of the proteomic analysis rank.

2.4.4. Mouse cytokine array

For a more specific analysis of the secretome of RAW macrophages, ELISA-based AAM-CYT-1000 murine cytokine array (RayBiotech) was run. Four independent samples of anti-Sema4D treatment, added and IgG1 treated conditioned media were assayed without previous concentration and following the manufacturer's instructions. Signals on blots were detected with ChemiDoc Touch System (Bio-Rad), whereas densitometric analysis of spot intensity was performed using Image Lab software (Bio-Rad). Results for each cytokine were expressed as the average of the four independent conditioned media samples of the intensity for each treatment condition. The intensity is calculated as the Adjusted Volume (the background-adjusted volume given by Image Lab) for each treatment condition divided by the average Adjusted Volume of the three treatment conditions.

2.4.5. ELISA

An ELISA for high sensitivity detection of CXCL12 (MCX120 Quantikine ELISA kit, R&D systems) was performed following the manufacturer's instructions, in untreated, ms IgG1 and anti-Sema4D treated RAW conditioned media. Standards and samples (without dilution) were loaded in duplicate. Next steps of the ELISA were carried out as previously detailed in page 74.

2.5. *In vitro* motility assays

2.5.1. Migration assays

2.5.1.1. Wound healing assay

For wound healing migration assays, 2-well culture silicone inserts (Ibidi®) with a defined cell-free gap were used. Inserts were stacked separately in wells of a 12 well plate o/n, at 37ºC. Next, $2x10^4$ βTC4 cells were seeded in each compartment of the insert, in a final volume of 70 µl. The outer area of the insert was filled with 500 µl additional βTC4 media. When cells reached 60-70% confluence, the inner media was discarded and RAW cells were seeded onto βTC4 cells at a 1:100 ratio, in a final volume of 70 µl of untreated, 10ug/ml ms IgG1 (Invitrogen) or 10ug/ml anti-Sema4D treated media (Vaccinex). βTC4 monoculture was used as a negative control. When the co-culture reached confluence, inserts were gently removed by using sterile tweezers, leaving an empty line between the two cell fronts. The used well was filled with 500 µl cell free media untreated or treated with 10ug/ml ms IgG1 (Invitrogen) or 10ug/ml anti-Sema4D (Vacinex). Cells were refed at the third day. Pictures of the wound closure were taken during 7 days, every 24 hours, using and inverted microscope (Leica DMi1). Opened area was quantified with Image J software for each time-point. For result interpretation, using the slope of each of the equations that relate area with time for each condition, migration speed ($v_{migration}$) was calculated.

2.5.1.2. Transwell migration assay

In order to assess directional migration of RAW cells in response to anti-Sema4D, a transwell migration assay was performed with RAW cells (Figure 34A). Briefly, 10^5 RAW cells were seeded onto the 6.5 mm inserts with an 8 µm polycarbonate membrane of the Costar Transwell® Permeable Supports (Corning), in the presence of 100 µl of 0% FBS complete DMEM media. Meanwhile, 600 µl of 10% FBS complete DMEM media were added in the bottom compartment to act as a chemoattractant. 10 µg/ml anti-Sema4D or 10 µg/ml ms IgG1 (Invitrogen) were added both to the top and the bottom chambers. Both anti-Sema4D antibodies from Vaccinex and Abnova (clon 3B4) were similarly tested. All control and experimental groups were performed in parallel and in duplicate. The transwells were incubated for 24h at 37ºC in a humidified atmosphere with 5% CO_2.

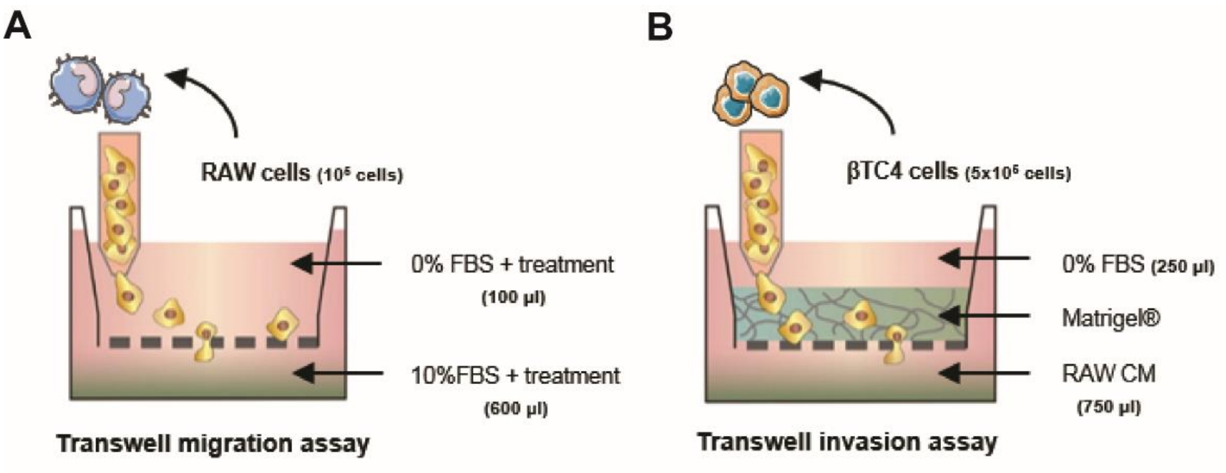

Figure 34 **Schematic representation of transwell migration and invasion assays. A)** For transwell migration assays, RAW cells were seeded onto of the porous membrane and subjected to a serum gradient in the presence of different stimuli, including anti-Sema4D and IgG1 treatment. **B)** For transwell invasion assays, βTC4 cells were seeded onto of the Matrigel® coated porous membrane and subjected to a chemoattractant gradient produced by the presence of RAW conditioned media. Final volumes and cell quantities are indicated. Adapted from Katt et al., 2016.

For the quantification of the migrated cells, the bottom surface of the membrane was first wiped with a cotton swab to remove non-migrated cells, and fixed for 2 minutes in methanol. Then, the upper chamber was washed with PBS and stained with haematoxylin for 90 seconds. After membrane removal for the insert using a blade, it was mounted on a microscope slide. Pictures of 20-30 representative fields for each membrane were taken using Nikon 80i microscope at 20X magnification. Migrated stained cells were manually counted and represented as the total number of migrated cells per field for each condition.

2.5.2. Invasion assays

2.5.2.1. Transwell Matrigel® invasion assay

- *Effect of RAW conditioned media*

For the study of the invasive capability of βTC4 cells in response to conditioned media of RAW cells, a transwell invasion assay was performed (Figure 34B). Briefly, 250 µl of serum deprived 5x10^5 βTC4 cells were placed onto the BD BioCoat Matrigel Invasion Chamber (Corning). At the bottom of the well, 750 µl of pre-warmed conditioned media from RAW cells differentially stimulated (page 89) were added. Aiming to rule out a direct effect of the treatment upon βTC4 cells, in the untreated conditioned media, 10 µg/ml of anti-Sema4D or 10 µg/ml ms IgG1 (Invitrogen) were added. Both anti-Sema4D antibodies from Vaccinex and Abnova (clon 3B4) were similarly tested. All control and experimental groups were performed in parallel and in duplicate. The transwells were incubated 48h at 37ºC in a humidified atmosphere with 5% CO_2. Cell fixation, staining and counting were performed as explained above for the transwell migration assay.

- *Effect of SDF1/CXCR4 signaling axis*

For the study of the invasive capability of βTC4 cells in response to recombinant SDF1 or its inhibitor, a transwell invasion assay was equally performed. Briefly, 250 µl of serum-deprived $5x10^5$ βTC4 cells were placed onto the BD BioCoat Matrigel Invasion Chamber (Corning). At the bottom of the well, 750 µl of 5% FBS complete DMEM media or conditioned RAW media (page 89) were added. The chemoattractant effect of SDF1 was assessed by adding 100 ng/ml of mouse recombinant SDF1 (Peprotech) on the lower chamber. At the same time, the inhibitory effect was studied by adding 1 µg/ml of CXCR4 inhibitor, AMD3100 (Tocris), to the upper compartment of the transwell. All control and experimental groups were performed in parallel and in duplicate. The transwells were incubated 48h at 37ºC in a humidified atmosphere with 5% CO_2. Cell fixation, staining and counting were performed as explained above for the transwell migration assay.

2.5.2.2. 3D invasion and viability assay

In order to assess the invasive capability of neuroendocrine cells in a similar but not as complicated setting as the *in vivo* RIP1-Tag2 approach, a 3D invasion assay based on βTC4 spheroid culture was designed. Spheroids were embedded in Matrigel® as previously described in page 85 in the presence of RAW conditioned media, previously treated with 10 µg/ml of anti-Sema4D (Vaccinex) or 10 µg/ml ms IgG1 (Invitrogen). βTC4 culture media was used as control. Shape was monitored and total number of invasive strands per spheroid was quantified during seven days using an inverted microscope (Leica DMi1). Disruption of the architectural structure of the spheroid and darker regions imaged in brightfield were counted as necrotic areas, as reviewed in literature (Zanoni et al., 2015). Invasive ability was calculated as the number of strands per invasive spheroid for each time point and treatment.

3. *In silico* studies on patient PanNET-derived samples

3.1. Extraction of data from a clinical dataset of patients

Human mRNA transcriptomes from a core independent clinical gene expression dataset of PanNET patients described by Missiaglia et al. were used for further analysis (GEO Omnibus reference GSE73338) (Missiaglia et al., 2009; Sadanandam et al., 2015). As previously described, the data set primarily contains 97 samples that include non-functional PanNETs, functional insulinomas, associated metastases, normal pancreatic tissues and normal pancreatic islet samples (Missiaglia et al., 2009; Sadanandam et al., 2015). We compared *Sema4D*, *Cxcl12* and *Cxcr4* expression among normal pancreatic islet samples (n=4), non-functional samples (n=63), which were termed primary tumors, and the associated metastases of some of these primary tumors (n=7). Looking to further study the malignization process, primary non-functional samples were divided into non-malignant or malignant, according to the clinical history of the patients (Sadanandam et al., 2015). Malignant tumors were termed after primary tumors that had undergone a synchronous metastasis at the time of sample collection.

3.2. *In silico* microdissection

For the estimation of immune and stromal cell population counts in patient samples, the Multiple Cell Population-counter method was applied as previously described (Becht et al., 2016). For data visualization, an unsupervised heatmap of MCP data was created together with Sema4D expression for primary and metastases samples performed in collaboration with Luis Palomero from ProCURE (ICO-IDIBELL). Data were normalized using z-score and Ward's method was used for the clustering. Pearson correlation was calculated for the expression of each gene and annotated in a dot-plot fashion.

4. Statistical analysis

Experiments were carried out at least 2-3 independent times with at least 2 technical replicates. Results are presented as mean ±SD for in vivo assays and mean ±SEM for in vitro. Data were statistically analyzed with GraphPad Prism v6 software to determine significance between groups in all experiments. For most cases, due to the small sample size and the fact that not all the data presented a normal distribution, a suitable non-parametric test was used. For continuous variables following non-Gaussian distribution, Mann-Whitney test was used for unpaired analysis, whereas Wilcoxon test defined paired samples' statistics. For correlation analyses, Pearson or Spearman correlation was calculated. Results are provided as P value, where * $p<0.05$, ** $p<0.005$, *** $p<0.001$ are considered significant. More information is given in the figure legends.

5. Figure design

Graphic elements from Servier Medical Art according to a Creative Commons Attribution 3.0 Unported License guidelines 3.0 were used in figures designed by the author of this thesis. Simplification and color changes were made to the original cartoons. https://creativecommons.org/licenses/by/3.0/

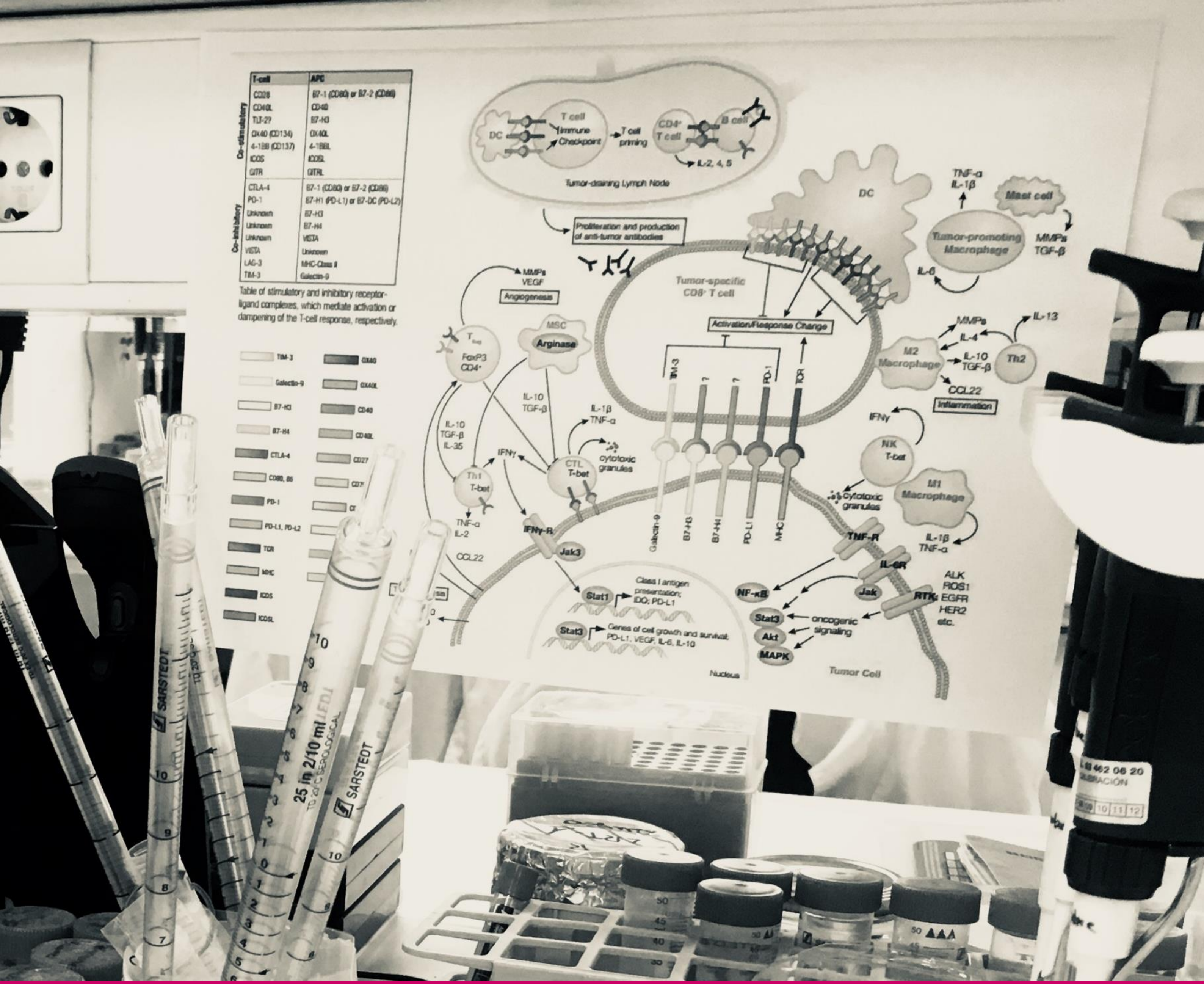

Results

Nothing in life is to be feared,
it is only to be understood.
Now is the time to understand more,
so that we may fear less.

Marie Curie

1. Semaphorin 4D signaling system in the RIP1-Tag2 mouse model tumor ecosystem

Treatment with anti-Sema4D has demonstrated a dual action in the RIP1-Tag2 mouse model of PanNETs. A beneficial modest antiangiogenic effect followed an unexpectedly high increase in malignant invasiveness and metastasis, which occurred in the absence of hypoxia. This thesis will examine the mechanisms that underpin Semaphorin 4D blockade, starting with the description of the main players in the receptor-ligand system of Sema4D signaling in our tumor model.

1.1. Expression of Sema4D

There is a large number of published studies that describe Sema4D expression by immune infiltrating cells and tumor cells inside the tumor ecosystem (reviewed in Wu et al., 2016). In accordance with these findings, previous results from our group showed high expression of Sema4D in scattered immune cells along the tumor mass, together with a rather dim expression in tumor cells.

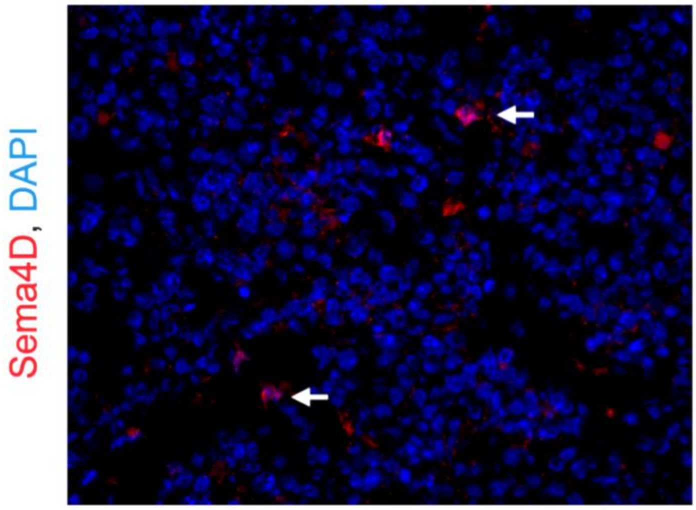

Figure 35 **Sema4D is highly expressed in scattered cells of the tumor stroma of RIP1-Tag2 tumor stroma.** Immunohistofluorescence analysis of Sema4D (in red) expression in in RIP1-Tag2 control tumors. DAPI (blue) is used to counterstain for cell nuclei. A representative field from at least 10 tumors of five control untreated RIP1-Tag2 mice is shown. Images were taken at 40X magnification.

We further confirmed this observation by immunofluorescence staining of Sema4D in RIP1-Tag2 tumors (Figure 35). While faint Sema4D expression was observed throughout the tumor mass, some disseminated cells exhibited distinct expression. Sema4D expression was not restricted to the membrane of Sema4D positive cells, but it was also located in their cytoplasm.

1.2. Expression of PlexinB1

1.2.1. PlexinB1 is not expressed in pericytes

We checked the expression of PlexinB1, the high affinity receptor for Sema4D, in the tumor stroma of the RIP1-Tag2 mouse model. Taking into account the antiangiogenic effect observed after anti-Sema4D treatment, we hypothesized that PlexinB1 should be expressed in the vascular fraction of the tumor stroma. Previous data from our lab reported alterations in the profile of different subtypes of pericytes after anti-Sema4D treatment. Since those modifications occurred without any changes in the number of vessels, we sought to first check PlexinB1 expression in pericytes of the tumor ecosystem.

Pericytes are defined as microvascular periendothelial mesenchymal cells that appear to be ubiquitously present in blood microvessels, but not in lymphatic capillaries (Kelly-Goss et al., 2014). Besides, pericytes are present on >97% of vessels in RIP-Tag2 tumors (Morikawa et al., 2002). Since tumor pericytes are loosely associated with endothelial cells, their identification according to morphologic criteria is complicated. Thus, these cells are commonly identified by immunohistochemical techniques, using specific markers of different subsets of tumor pericytes such as desmin, NG2 and α-SMA. Desmin is an intracellular intermediate filament protein that marks the cytoskeleton of a subset of these cells (Bergers and Song, 2005). NG2 is an integral membrane chondroitin sulfate proteoglycan involved in pericyte recruitment to tumor vasculature. Besides, NG2 marks vessels undergoing remodeling and its expression decreases as the vessels mature and become stable and quiescent (Miller et al., 1995). α-SMA, alpha-smooth muscle actin, is a structural protein which is not expressed in quiescent pericytes but commonly upregulated in tumor angiogenesis, tissue fibrosis and inflammation (Gerhardt and Betsholtz, 2003). The presence of PlexinB1 in different NG2, desmin or α-SMA pericytes was assessed by double immunostaining sections of pancreatic tissue from RIP-Tag2 mice with each one of those makers and with an anti-PlexinB1 antibody (Figure 36).

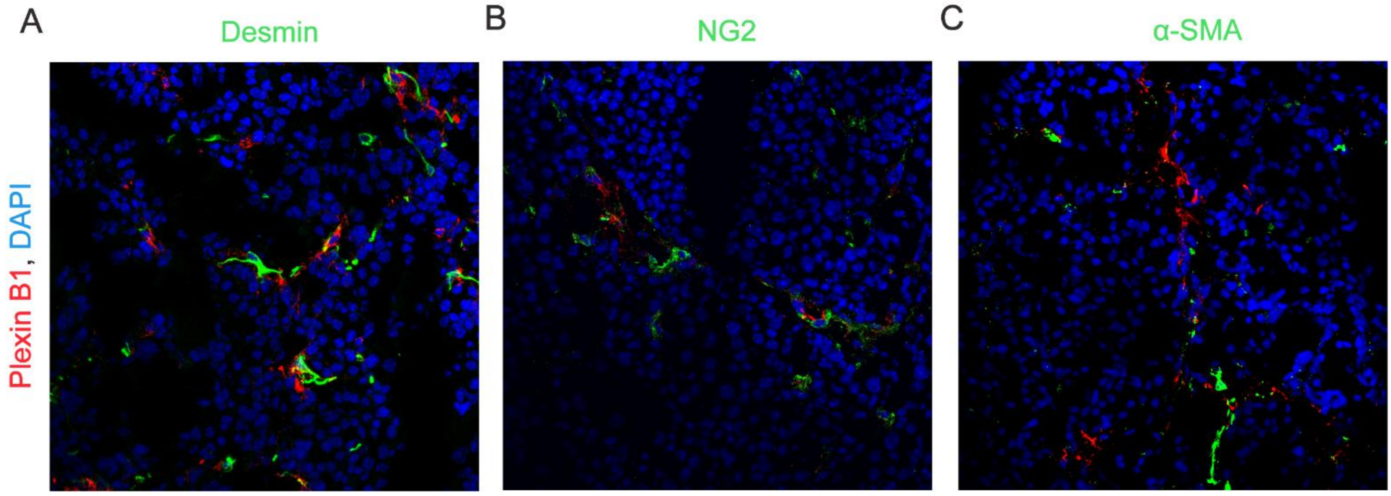

Figure 36 **PlexinB1 is not expressed in desmin, NG2 or α-SMA positive pericytes from RIP1-Tag2 tumor stroma.** Immunohistofluorescence analysis of PlexinB1 (in red) expression in **A)** Desmin, **B)** NG2 and **C)** α-SMA (in green) markers of pericyte subsets, in RIP1-Tag2 control tumors. DAPI (blue) is used to counterstain for cell nuclei. A representative field from at least 10 tumors of five control untreated RIP1-Tag2 mice is shown. Images were taken at 40X magnification.

As it is shown in Figure 36A, B and C, no costaining of any of the pericyte markers with PlexinB1 receptor is observed inside the pancreatic neuroendocrine tumors. For instance, desmin positive pericytes, marked in green, are shown to surround PlexinB1 positive structures, marked in red (Figure 36A). PlexinB1 positive structures are located between cell nuclei (counterstained with DAPI, in blue), in a shape that recalls that of vessel structures, suggesting that PlexinB1 is expressed in other vascular cells, such as endothelial cells. At the same time, NG2 and α-SMA are expressed in capillaries inside the tumors (Figure 36B and C, marked in green) whereas Plexin B1 is, in this case, surrounding these structures. No determinant colocalization is observed in any of the stainings. Closer inspection of the immunofluorescence assays shows a higher amount of Desmin positive pericytes if compared to the NG2 or α-SMA positive fraction. Taken together, these results indicate that Desmin, NG2 or α-SMA positive pericytes do not express PlexinB1 receptor for the angiogenic Sema4D on their membranes.

1.2.2. PlexinB1 is expressed in a subset of endothelial cells

Aiming to check that PlexinB1 was certainly expressed in the endothelial cells of these vascular structures of pancreatic RIP1-Tag2 tumors and not in the perivascular compartment, we costained PlexinB1 with CD31. CD31, also known as Platelet Endothelial Cell Adhesion Molecule (PECAM-1), is a protein mainly expressed in tight junctions of endothelial cells, for which it is used to demonstrate presence of these cells (Liu and Shi, 2012). A subset of CD31 positive structures costained with PlexinB1, thus indicating that endothelial cells express the high affinity receptor for Sema4D (Figure 37, pointed with a white arrow) as previously described (Basile et al., 2004).

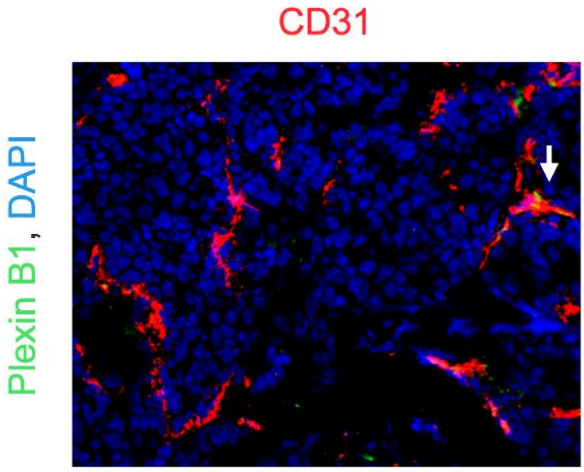

Figure 37 **PlexinB1 is expressed in a subset of endothelial cells from RIP1-Tag2 tumor stroma.** Immunohistofluorescence analysis of PlexinB1 (in green) expression in CD31 positive endothelial cells (in red), in RIP1-Tag2 control tumors. DAPI (blue) is used to counterstain for cell nuclei. White arrow marks a Plexin B1 positive vessel. A representative field from at least 10 tumors of five control untreated RIP1-Tag2 mice is shown. Images were taken at 40X magnification.

1.2.3. PlexinB1 is expressed in a subset of macrophages

Other authors have also described leukocytes positive for PlexinB1 expression in other animal models (Basile et al., 2004). In order to test whether

PlexinB1 is expressed in immune infiltrates, we performed an immunofluorescence assay over pancreatic tissue from control RIP1-Tag2 mice costaining PlexinB1 with F4/80, CD19 and CD3e markers (Figure 38). F4/80 is a cell surface glycoprotein expressed by macrophages during their maturation and activation. It is used as a murine macrophage marker since it is expressed on a wide range of mature tissue macrophages including Kupffer cells, Langerhans and microglia (Austyn and Gordon, 1981). CD19 is a membrane protein expressed on follicular dendritic cells and B cells from early recognizable B-lineage cells during development, accordingly being used as a B cell marker. CD3e is one of the subunits of the CD3 T cell co-receptor protein complex associated with T cell activation, hence being used as a T cell marker.

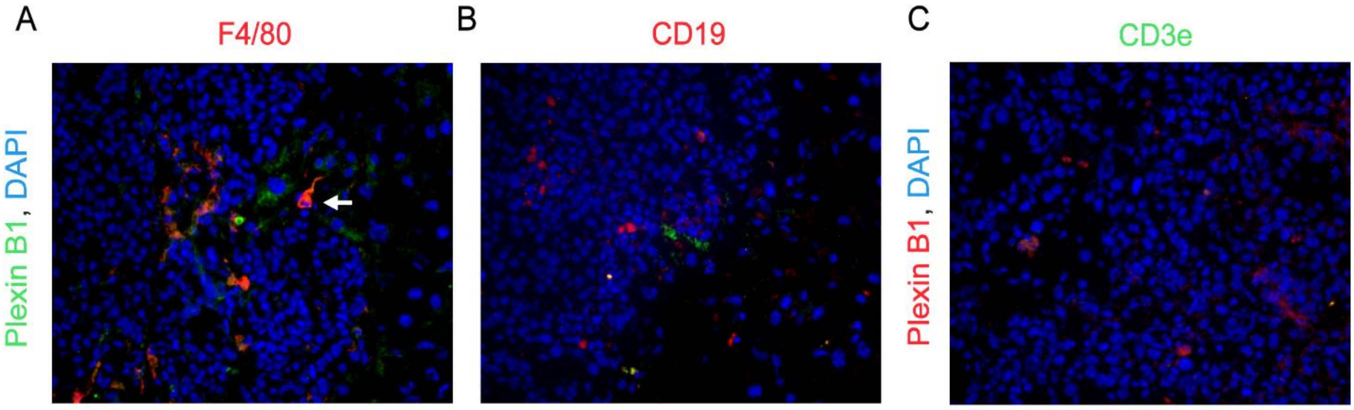

Figure 38 Plexin B1 is expressed in a subset of macrophages, but not in B or T lymphocytes. Immunohistofluorescence analysis of PlexinB1 (in green) expression in **A)** macrophages (F4/80 positive, in red), **B)** B lymphocytes (CD19 positive, in red) and **C)** T lymphocytes (CD3e positive, in green), in RIP1-Tag2 control tumors. DAPI (blue) is used to counterstain for cell nuclei. White arrow marks a Plexin B1 positive macrophage. A representative field from at least 10 tumors of five control untreated RIP1-Tag2 mice is shown. Images were taken at 40X magnification.

Only a proportion of the F4/80 positive cells colocalized with PlexinB1 receptor (Figure 38A, pointed with a white arrow), whereas none of the CD19 or CD3e positive cells were positive for Plexin B1 (Figure 38B and C). Intriguingly, the highest amount of infiltrating macrophages (F4/80 positive cells) was found in the peritumoral area (Figure 38A). Moreover, no T cells (CD3e positive cells) were found within the intratumoral or peritumoral area of the tissues (Figure 38C). These results indicate that only a fraction of the PlexinB1 positive single cells are F4/80 positive macrophages.

1.3. Expression of CD72

1.3.1. CD72 is not expressed in the vascular system

After discarding Plexin B1 expression in pericytes, we checked whether the alteration in their vessel coverage after anti-Sema4D treatment occurred as a consequence of Sema4D/CD72 signaling blockade. To this aim, we performed immunofluorescence costaining of CD72 with a pan-pericyte, which contained antibodies against Desmin, NG2 and α-SMA. There was no costaining of both proteins, thus ruling out the expression of CD72 on the membrane of this subset of perivascular cells (Figure 39A). We also checked whether CD72 was expressed in endothelial cells of the RIP1-Tag2 tumor stroma, obtaining a negative result (Figure 39B). Interestingly, we found that some scattered round-shaped cells marked strongly positive for CD72 (Figure 39B, pointed with a white arrow).

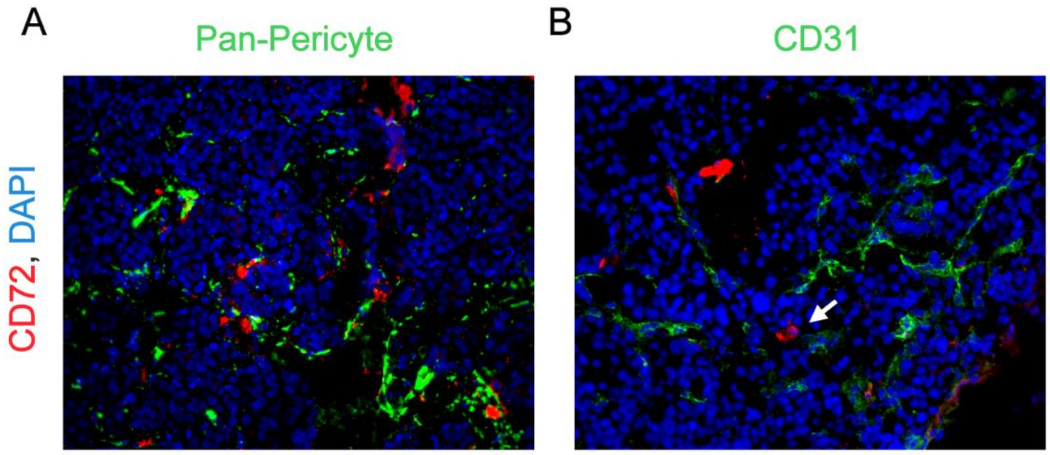

Figure 39 **CD72 is not expressed in pericytes nor in endothelial cells.** Immunohistofluorescence analysis of CD72 (in red) expression in **A)** pericytes (Pan-Pericyte positive staining, which includes Desmin, NG2 and α-SMA markers, in green), **B)** endothelial cells (CD31 positive, in green), in RIP1-Tag2 control tumors. DAPI (blue) is used to counterstain for cell nuclei. White arrow marks a CD72 positive cell with an immune cell phenotype. A representative field from at least 10 tumors of

five control untreated RIP1-Tag2 mice is shown. Images were taken at 40X magnification.

1.3.2. CD72 is expressed in macrophages

A great deal of previous research has described that CD72 is expressed in cells of the immune system infiltrated in the tumor stroma (Gordon, 1994; Kumanogoh et al., 2000, 2002b; Robinson et al., 1997). In order to confirm that the scattered CD72 positive cells found in Figure 39 are immune cells, we performed an immunofluorescence of CD72 together with F4/80 macrophage marker. As can be seen in Figure 40, some macrophages of the RIP1-Tag2 tumor stroma are positive for CD72 (pointed with a white arrow).

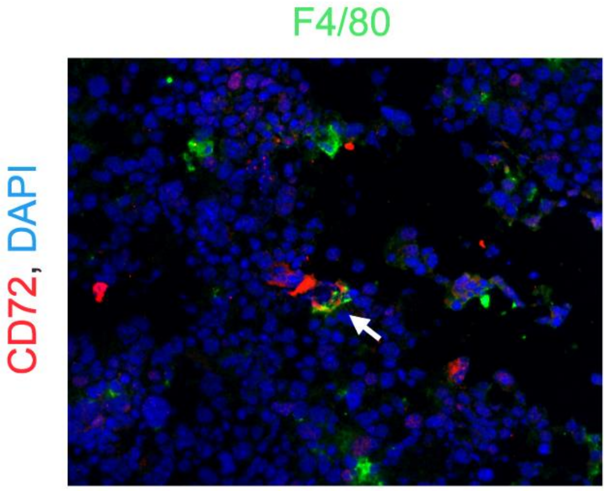

Figure 40 **CD72 is expressed in a subset of macrophages.** Immunohistofluorescence analysis of CD72 (in red) expression in macrophages (F4/80 positive, in green) in RIP1-Tag2 control tumors. DAPI (blue) is used to counterstain for cell nuclei. White arrow marks a CD72 positive macrophage. A representative field from at least 10 tumors of five control untreated RIP1-Tag2 mice is shown. Images were taken at 40X magnification.

Overall, our study regarding the principal effectors of Sema4D signaling network in the RIP1-Tag2 tumor stroma reveals that the ligand, Sema4D, is highly expressed by macrophages and less by tumor cells, as previously reported. Surprisingly, the high affinity Plexin B1 receptor and the low affinity CD72 receptor were not expressed by pericytes. Whereas Plexin B1 was found expressed in some endothelial cells, CD72 was located in the membrane of F4/80$^+$ macrophages.

2. Antiangiogenic mechanism of Semaphorin 4D blockade

Contrarily to canonical antiangiogenics such as anti-VEGFR2, anti-Sema4D produces a change in the number of endothelial cell nuclei and pericyte coverage in the absence of vessel trimming. Considering those results and the previously described location of the Sema4D/PlexinB1 receptor-ligand system in RIP1-Tag2 vascular stroma, we sought to further examine the atypical antiangiogenic mechanism of this therapy.

2.1. Anti-Sema4D treatment increases the number of Plexin B1 positive vessels

Since our results indicate that PlexinB1, the receptor with the highest affinity for Sema4D, is expressed in a subset of endothelial cells (Figure 37), we hypothesized that they may undergo phenotypic changes after anti-Sema4D therapy. To prove this hypothesis, an immunofluorescence assay of PlexinB1 and CD31 was performed in control and treated RIP-Tag2 mice (Figure 41).

When RIP-Tag2 mice were treated with α-Sema4D, an increase in the number of PlexinB1 positive vessel structures could be discerned, as it is seen in Figure 41A, where the amount of colocalization is particularly higher in the case of the animal from the α-Sema4D treated group. Consistent with previous studies from our group, only a 33% ± 16 of the total manually counted vessel structures expressed Plexin B1 in control mice (Figure 41B). Surprisingly, there is a significant increase of up to a 63% ± 15 in the number of PlexinB1 positive vessels after Sema4D treatment (Figure 41B). Similar results were obtained when Image J MacBiophotonics Colocalization Analysis tools were used (data not shown).

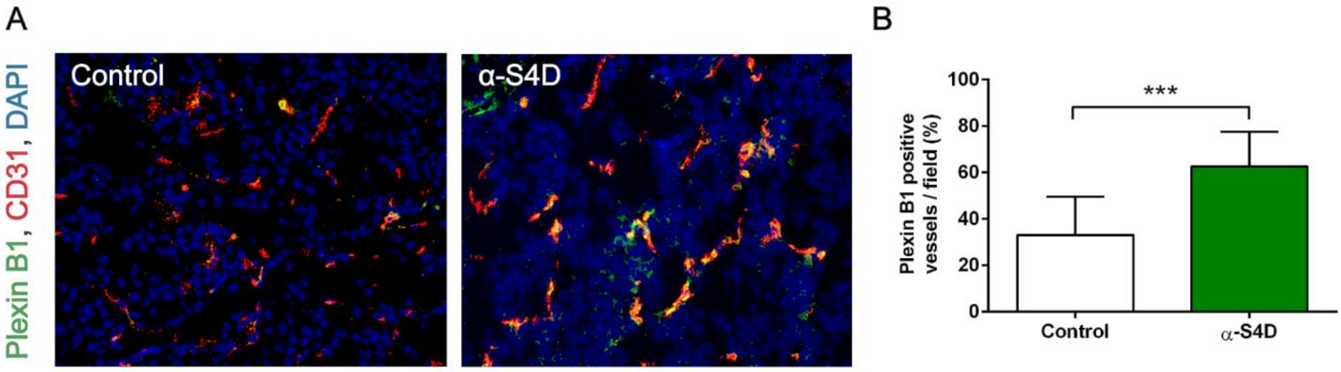

Figure 41 **Increase in PlexinB1 positive vessels after anti-Sema4D therapy. A)** Immunohistofluorescence analysis of PlexinB1 (in green) expression in CD31 positive endothelial cells (in red) in control and anti-Sema4D (α-S4D) treated RIP1-Tag2 tumors. DAPI (blue) is used to counterstain for cell nuclei. A representative field from at least 10 tumors of five RIP1-Tag2 mice for each condition is shown. Images were taken at 40X magnification. **B)** Quantification of the percentage of PlexinB1 positive microvessel structures (CD31 positive) per field for each condition. At least 10 tumors were analyzed per group. ***$p < 0.001$ by Mann-Whitney test. Error bars indicate ± SD.

Besides, previous results had stated that no decrease in the number of vessels was observed after anti-Sema4D therapy. We checked the number of vessels in each condition and no differences were noted (data not shown). Similar negative results were obtained when we manually examined tumor sections for phenotypic differences in vessel size and structure after anti-Sema4D therapy. Taken together, these findings indicate that α-Sema4D treatment upregulates PlexinB1 expression in the endothelial cells of the RIP-Tag2 tumor vasculature, in the absence of changes in vessel shape or amount. Surprisingly, when we analyzed the RNA expression in whole RIP1-Tag2 control and anti-Sema4D treated mice, we found no increase of PlexinB1 expression at the transcriptional level (Figure 42).

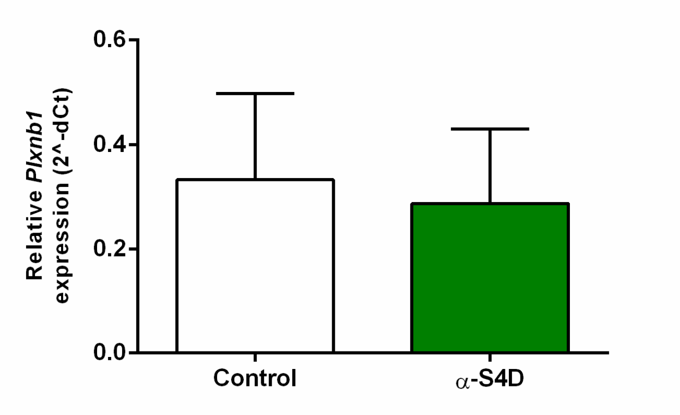

Figure 42 **Anti-Sema4D treatment does not alter Plexin B1 expression at the transcriptional level.** qRT-PCR analysis of *Plxnb1* gene in control and anti-Sema4D (α-S4D) treated RIP1-Tag2 tumors. Relative expression to *Hprt1* gene. At least 5 tumors were analyzed per group. No significant difference is found by Mann-Whitney test. Error bars indicate ± SD.

2.2. Plexin B1 increase does not correlate with alterations in pericyte coverage

Our previous data indicate that anti-Sema4D treatment does not modify mean vessel density, but it does alter vascular structure at endothelial and pericyte cell level, suggesting a direct vascular antiangiogenic effect of Sema4D blockade via Plexin B1 receptor in endothelial cells. As described before, previous data from our group found that pericytes positive for Desmin and NG2 were increased after anti-Sema4D treatment, whereas the number of α-SMA positive pericytes was decreased. Since pericytes do not harbor any of the receptors for Sema4D, we hypothesize an indirect action of anti-Sema4D upon pericytes via a crosstalk mechanism governed by Plexin B1 receptor activation in endothelial cells.

In order to decipher the underlying mechanism, we checked whether the changes in pericyte coverage occurred in PlexinB1 positive vessels. With that aim, we stained RIP1-Tag2 control and anti-Sema4D treated tumors with pan-pericyte, CD31 and Plexin B1 (Figure 43A, top). In order to better visualize plexin B1 positive vessels that were covered by pericytes, we removed DAPI for manual quantification. Although a slight increase is observed in anti-Sema4D treated samples, no significant differences in pericyte coverage between the PlexinB1 positive or negative endothelial cells were observed (Figure 43B).

Since the previous pericyte analyses of our group were carried out focusing on each pericyte marker individually, we sought to reproduce this last experiment using Desmin pericyte marker, which stains most of the pericytes in the RIP1-Tag2 tumor stroma. We stained control and anti-Sema4D treated tumors with desmin, CD31 and Plexin B1 and equally examined vessel coverage (Figure 44A). As previously described, we noted an increase in the number of vessels covered by Desmin pericytes (Figure 44A). However, we found that this increase was related to Plexin B1 negative vessels, rather than to positive ones (Figure 44C-D). These results are somewhat counterintuitive, as they may indicate that pericyte coverage is independent from the expression of PlexnB1 in endothelial cells.

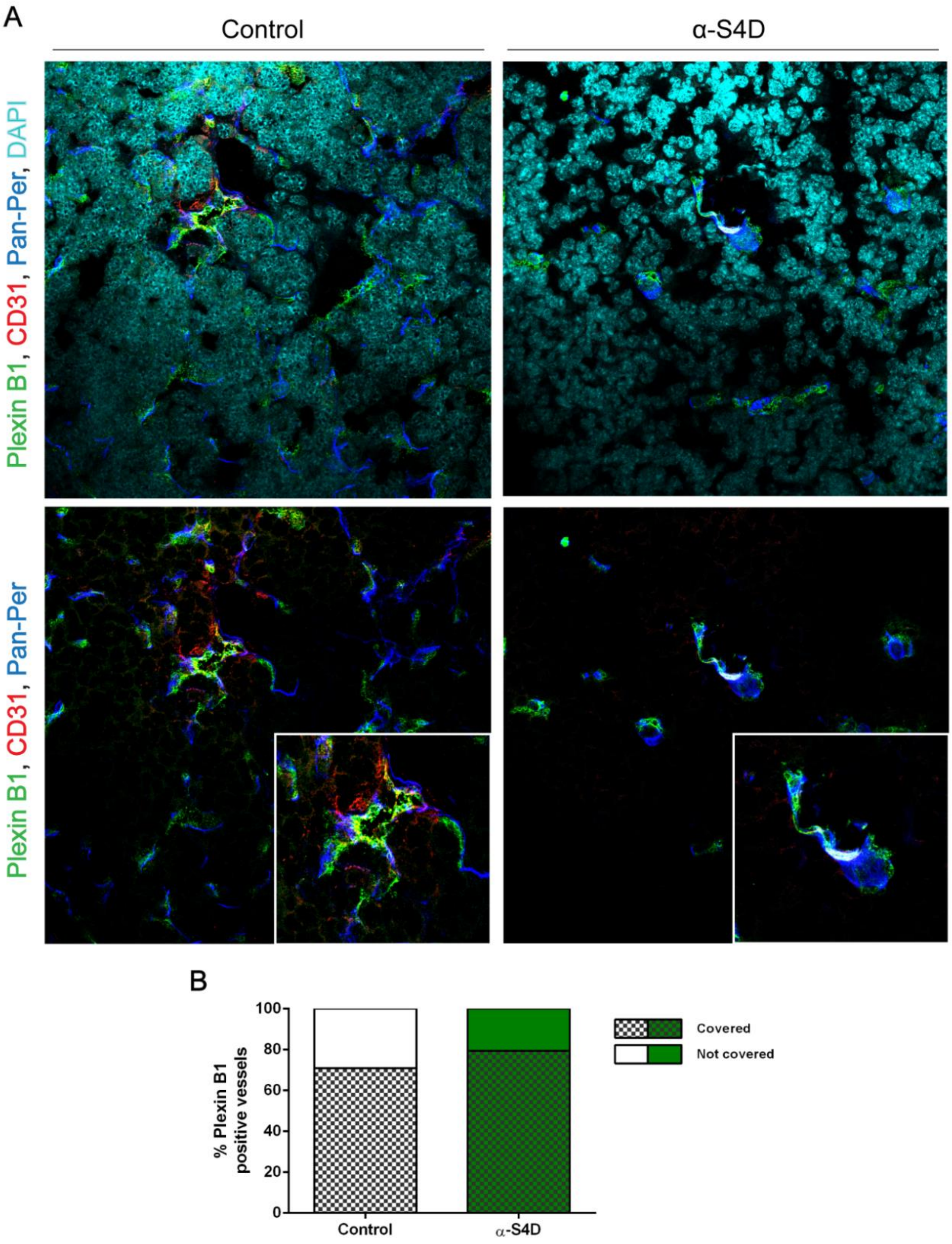

Figure 43 **PlexinB1 positive vessels do not alter their pericyte coverage in response to anti-Sema4D treatment. A)** Immunohistofluorescence analysis of the pericyte coverage (in blue) of PlexinB1 (in red) positive endothelial cells (in green) in control and anti-Sema4D (α-S4D) treated RIP1-Tag2 tumors. In the top panel, DAPI (in cyan) is used to counterstain for cell nuclei. Pan-pericyte (Pan-per) includes Desmin, NG2 and α-SMA pericyte subset. Representative fields from at least 10 tumors of five RIP1-Tag2 mice for each condition are shown. Images were taken at 63X magnification. **B)** Quantification of the percentage of covered and not-covered PlexinB1 positive microvessel structures (CD31 positive) per field for each condition. To quantify pericyte coverage, vessel structures with one or more points that

intersect with pericyte markers were counted as positive. Vessels positive for Plexin B1 marker that intersect with pericyte markers were counted as Plexin B1 positive vessels covered by pericytes. At least 10 tumors were analyzed per group. No significant difference is found by Two-way ANOVA test.

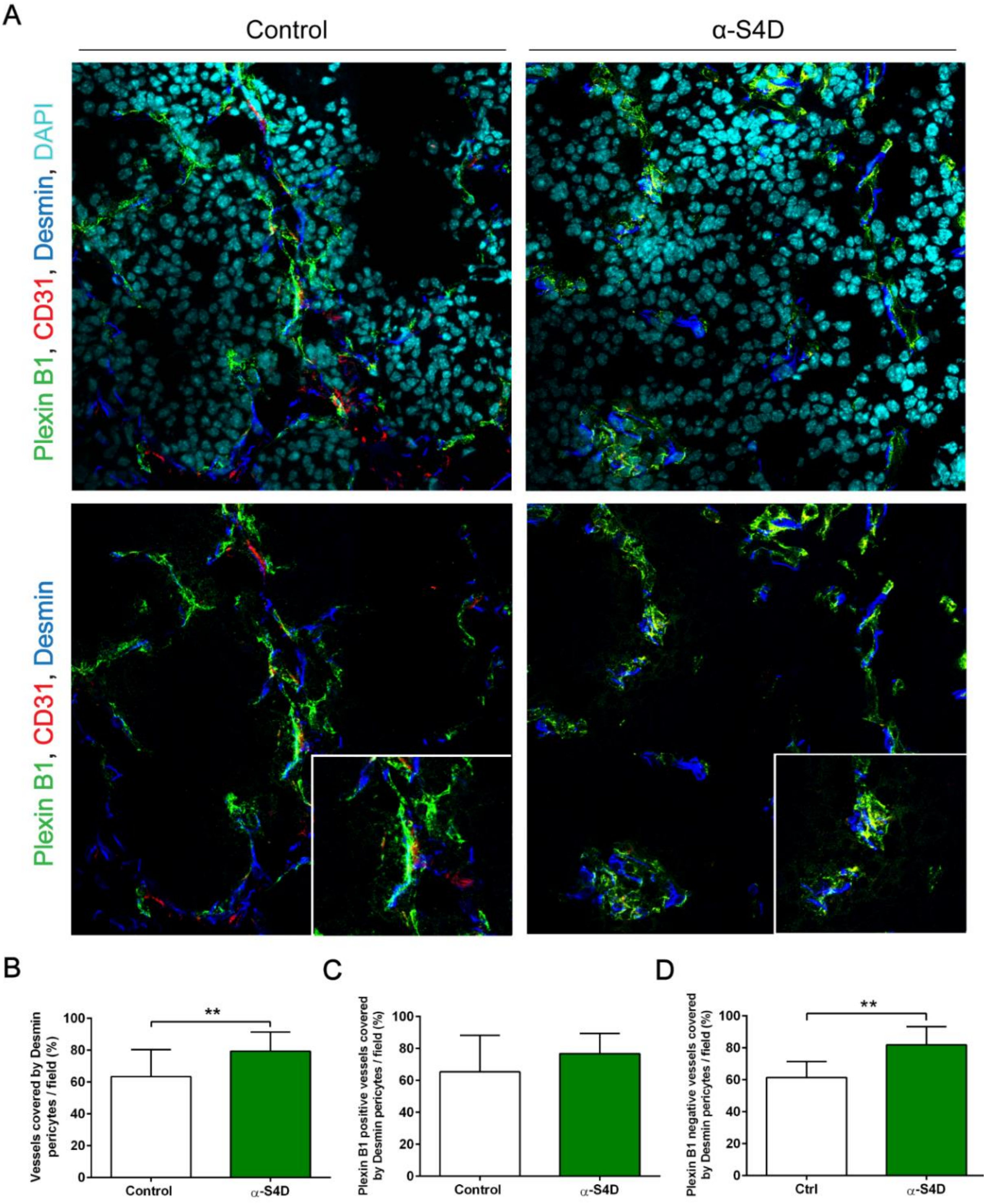

Figure 44 **PlexinB1 positive vessels do not alter their Desmin positive pericyte coverage in response to anti-Sema4D treatment. A)** Immunohistofluorescence analysis of Desmin positive pericyte coverage (in blue) of PlexinB1 (in red) positive endothelial cells (in green) in control and anti-Sema4D (α-S4D) treated RIP1-Tag2

tumors. In the top panel, DAPI (in cyan) is used to counterstain for cell nuclei. For PlexinB1, CD31 and Pan-pericyte co-staining visualization, images without DAPI were analysed (bottom panel). A 2X zoom is done in the microvessel areas for better visualization (white square). Representative fields from at least 10 tumors of five RIP1-Tag2 mice for each condition are shown. Images were taken at 63X magnification. **B)** Quantification of the percentage of covered and non-covered PlexinB1 positive microvessel structures (CD31 positive) per field for each condition. To quantify pericyte coverage, vessel structures with one or more points that intersect with Desmin pericyte marker were counted as positive. Vessels positive for Plexin B1 marker that intersect with pericyte markers were counted as Plexin B1 positive vessels covered by Desmin expressing pericytes. At least 10 tumors were analyzed per group. $^{**}p < 0.01$ by Mann-Whitney test. Error bars indicate ± SD.

2.3. Pericyte-endothelial crosstalk is partly driven by PDGF signaling

Several studies have explored different crosstalk mechanisms between endothelial cells and pericytes (Geevarghese and Herman, 2014). Among them, experiments by Zhou et al. demonstrated a crosstalk where Sema4D treatment of endothelial cells elicits the production of PDGF-BB and promotes differentiation of mesenchymal stem cells into pericytes (Zhou et al., 2014). Based on this work, we examined PDGF-BB expression in control and anti-Sema4D treated tumors. As expected, ELISA assay of PDGF-BB showed a slight decrease in PDGF-BB levels after Sema4D blockade when compared to control tumors (Figure 45). This result was further validated with a previously performed Taqman® analysis of angiogenesis related genes, in which a decrease in PDGFB levels, corresponding to 0,83 ±0,12 of relative expression compared to control, was also observed (Table 4). Therefore, PDGF-BB could be one of the molecules altering the crosstalk between endothelial cells and pericytes.

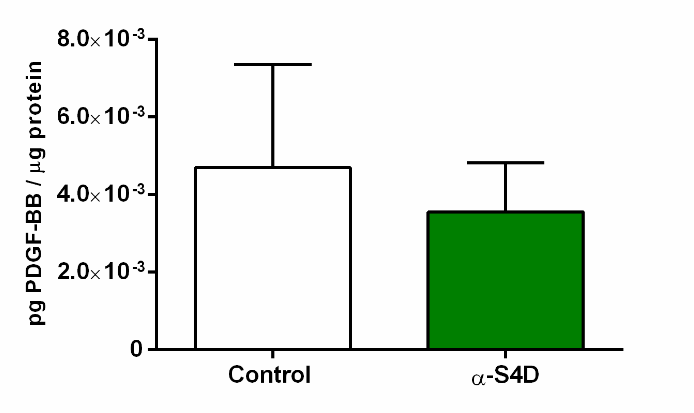

Figure 45 **Anti-Sema4D treatment slightly decreases PDGF-BB expression at protein level.** ELISA analysis of PDGF-BB protein in control and anti-Sema4D (α-S4D) treated RIP1-Tag2 tumors. At least 3 tumors were analyzed per group. No significant difference is found by Mann-Whitney test. Error bars indicate ± SD.

As for the antiangiogenic mechanism after Semaphorin 4D functional blockade, we have demonstrated that the change in pericyte coverage is spatially independent from Plexin B1 expressing vessels. Besides, a crosstalk mechanism depending on PDGF-BB release from PlexinB1 positive vessels could be one of the mechanisms altering pericyte behavior.

3. Malignization mechanism of Sema4D blockade

3.1. Lack of direct effect of Sema4D in tumor cells via c-met

To date, the best described mechanism for tumor aggressiveness after antiangiogenic inhibition in RIP1-Tag2 tumors involves hypoxia and c-met activation (Sennino et al., 2012; You et al., 2011). As previously explained in the Introduction section, the malignization process following Sema4D blockade does not involve hypoxia. However, the behavior of c-met under anti-Sema4D treatment conditions has not been explored. C-met is upregulated in many human cancers and contributes to tumor growth, angiogenesis, invasiveness and metastasis (Mo and Liu, 2017).

In order to check whether malignization after Sema4D blockade was driven by c-met, we first studied if its expression was upregulated under treatment conditions (Figure 46A). RNA analysis of untreated and anti-Sema4D treated tumors revealed there were no changes in c-met transcriptional activity. We then assayed the presence of its precursor protein and its active form, phosphorylated c-met, by western blotting. We observed no expression of the precursor and lack of activation of c-met signaling pathway, both in the untreated and the anti-Sema4D treated conditions (Figure 46B). Overall, these data suggest that malignization effects in RIP1-Tag2 mice are restricted to an indirect effect of Sema4D blockade over tumor cells, rather than to a direct action of the proangiogenic molecule inhibition upon tumor cell derived c-met.

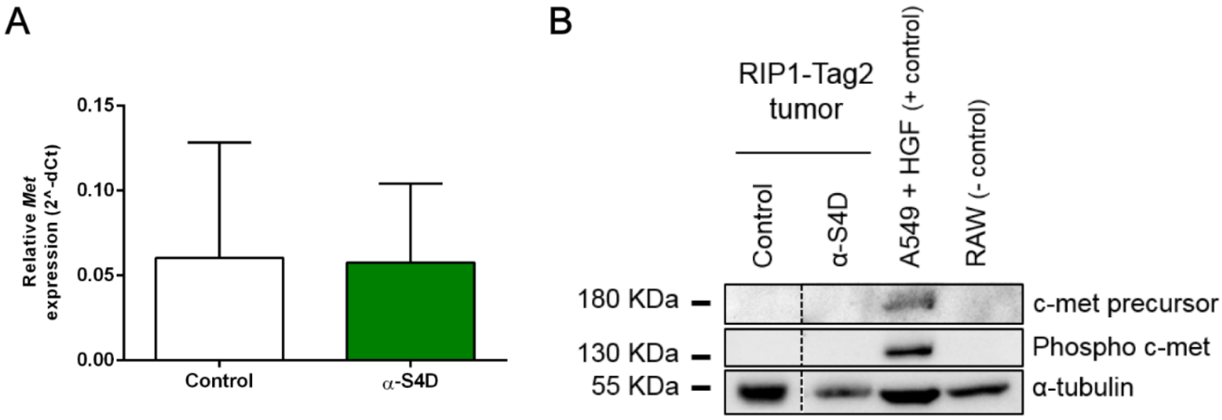

Figure 46 **Anti-Sema4D treatment does not alter c-Met expression nor its activation. A)** qRT-PCR analysis of *Met* gene in control and anti-Sema4D (α-S4D) treated RIP1-Tag2 tumors. Relative expression to *Hprt1* gene. At least 5 tumors were analyzed per group. No significant difference is found by Mann-Whitney test. Error bars indicate ± SD. **B)** Western blot analysis of the active form of c-Met protein (phospho c-met) in control and α-S4D treated RIP1-Tag2 tumors. α-tubulin protein is used as a housekeeping control. Representative image of at least 3 samples per condition. Lysate from A549 cells treated with HGF in equal conditions was used as a positive control for c-met phosphorylation. RAW cell line was used as a negative control.

3.2. Increase in the intratumoral Sema4D positive macrophage population

After discarding a direct effect of anti-Sema4D over tumor cell invasion, we sought to find which cells of the tumor ecosystem were indirectly mediating the malignization process. A study by Sierra et al. demonstrated that tumor-associated macrophages (TAMs) were the main Sema4D-producing cells within the tumor stroma (Sierra et al., 2008). In their setting, TAM-derived Sema4D expression was critical for tumor angiogenesis and progression. As explained in the Introduction section, previous results from our group described an infiltrate of macrophages that express Sema4D in the tumor stroma. Apart from confirming these findings (Figure 35), we found a subset of F4/80$^+$ macrophages also expressing both Sema4D receptors PlexinB1 and CD72 (Figure 38 and Figure 40). We hypothesize that Sema4D positive TAMs could also harbor a protumoral role in our RIP1-Tag2 setting.

With the aim of deciphering the role of these inflammatory cells and their contribution to the malignant phenotype of RIP-Tag2 mice after anti-Sema4D therapy, an immunofluorescence assay of F4/80 marker was performed over control and treated RIP-Tag2 mice (Figure 47). From now on, since our focus is placed on macrophages, sensitive to antibody stimuli via FcγR (Weiskopf and Weissman, 2015), isotype controls (treated with mouse IgG1) will be included to guarantee Sema4D-derived specific effects.

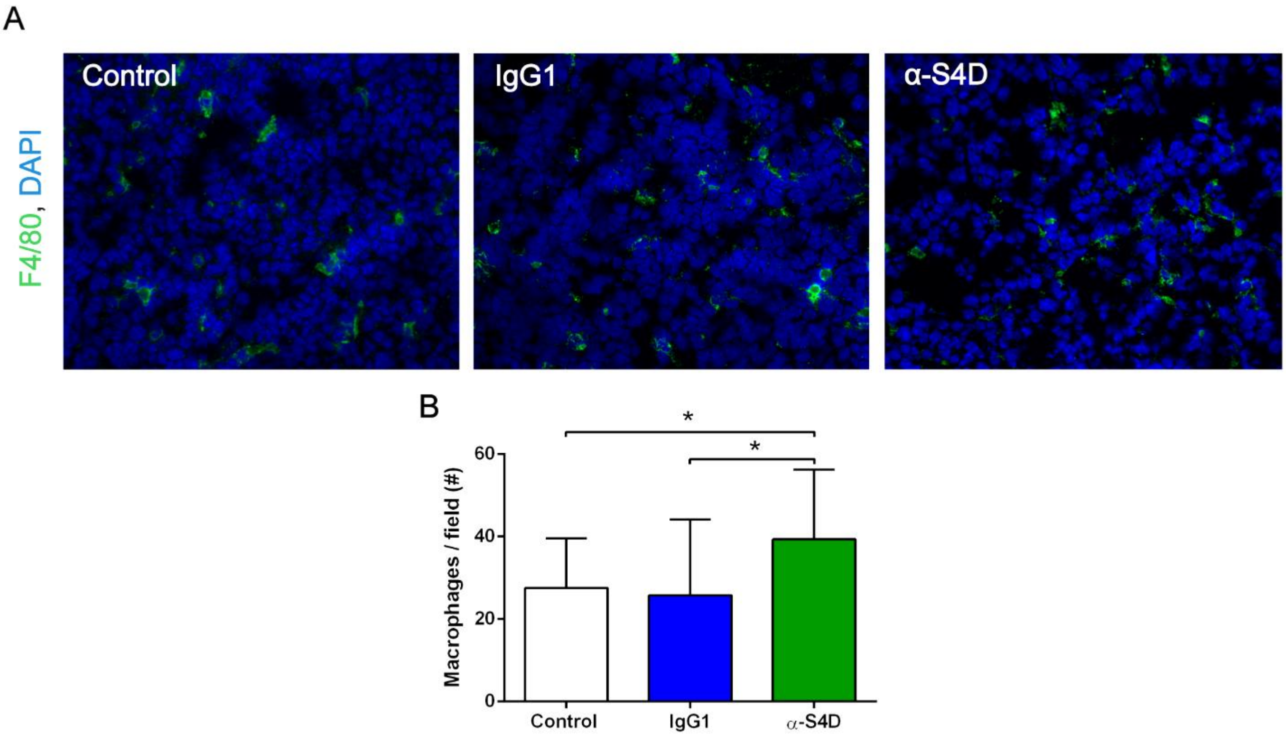

Figure 47 **Increase in the number of infiltrating macrophages after anti-Sema4D therapy. A)** Immunohistofluorescence analysis of infiltrating F4/80$^+$ macrophages (in green) in control, IgG1 treated and anti-Sema4D (α-S4D) treated RIP1-Tag2 tumors. Representative fields from at least 18 tumors of three RIP1-Tag2 mice for each condition are shown. Images were taken at 40X magnification. **B)** Quantification of the number (#) of intratumoral F4/80$^+$ macrophages per field for each condition. At least 18 tumors were analyzed per group. $*p < 0.05$ by Mann-Whitney test. Error bars indicate ± SD.

When RIP1-Tag2 mice were treated with anti-Sema4D, an increase in the number of F4/80 positive infiltrated macrophages could be visually noted (Figure 47A). A thorough analysis revealed an increase from 25.8 ± 10.9 to 39.3 ± 3.9 average macrophages per field when anti-Sema4D therapy was supplied (Figure 47B). Importantly, IgG1 treated mice did not show an increase in tumor-infiltrating macrophages, suggesting a specific effect of anti-Sema4D over TAM infiltration.

This result also validated the use of IgG1 as negative control for anti-Sema4D treatment in the next experiments.

In order to characterize tumor-infiltrating macrophages, we next checked their Sema4D expression levels. An immunofluorescence analysis of Sema4D and F4/80 in RIP1-Tag2 control, anti-Sema4D and IgG1 treated tumors revealed that the number and percentage of Sema4D-positive macrophages increased after anti-Sema4D treatment (Figure 48A-B). In fact, the mean number of Sema4D positive intratumoral macrophages increased more than ten times in anti-Sema4D treated tumors (24.67 ±11.18 macrophages), when compared to IgG1 treated samples (2.24 ±3.66 macrophages). The number of Sema4D-negative macrophages remained invariable after the therapy (Figure 48B). Overall, the percentage of Sema4D positive macrophages inside the tumor ecosystem increased significantly, growing from 11% to 65% of total macrophages (Figure 48C).

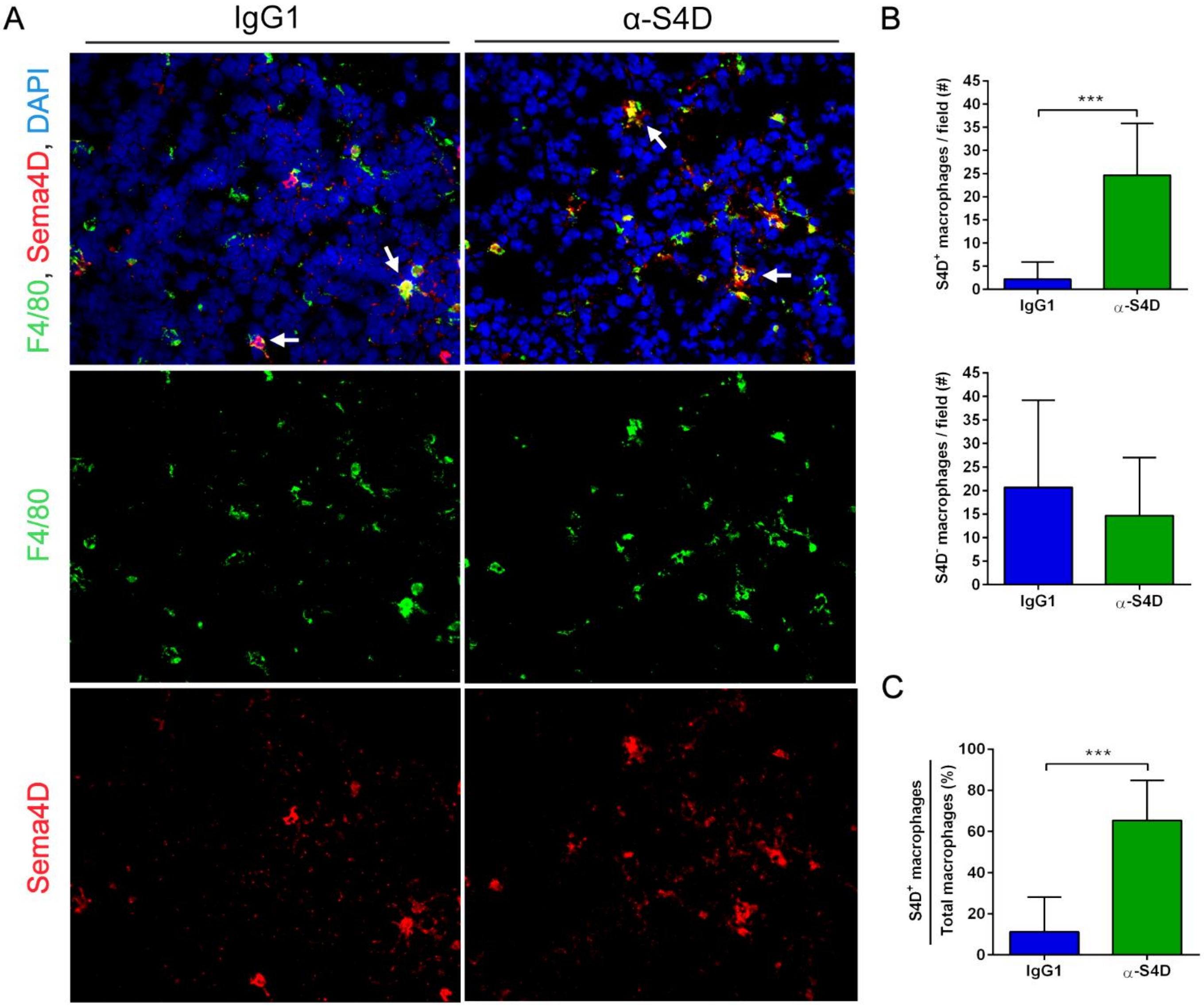

Figure 48 **Anti-Sema4D treatment increases the number of infiltrating Sema4D positive macrophages.** Immunohistofluorescence analysis of infiltrating Sema4D positive ($S4D^+$, in red) and negative ($S4D^-$) $F4/80^+$ macrophages (in green) in IgG1 treated and anti-Sema4D (α-S4D) treated RIP1-Tag2 tumors. White arrows mark some $S4D^+$ macrophages. Representative fields from at least 18 tumors of three RIP1-Tag2 mice for each condition are shown. Images were taken at 40X magnification. **B)** Quantification of the number (#) of intratumoral $S4D^+$ (top) and $S4D^-$ $F4/80^+$ (bottom) macrophages per field for each condition. **C)** Percentage of intratumoral $S4D^+$ macrophages per total number of macrophages. At least 18 tumors were analyzed per group. IgG1 treated mice were used as controls. ***$p < 0.001$ by Mann-Whitney test. Error bars indicate ± SD.

Moreover, we confirmed by RNA analysis that both *Sema4D* and *Adgre1* (F4/80) expression followed a clear upward trend in RIP1-Tag2 tumors after the therapy (Figure 49). In conjunction, these data demonstrated that, *in vivo*, there was a change in the number and phenotype of TAMs after anti-Sema4D treatment.

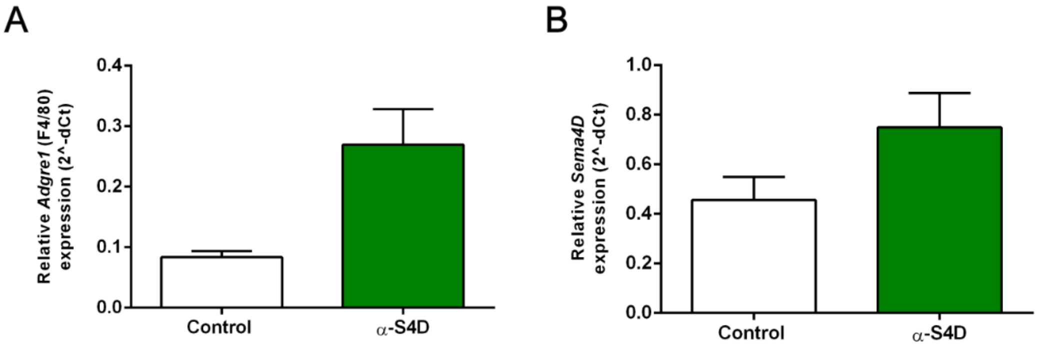

Figure 49 **Anti-Sema4D treatment increases F4/80 and Sema4D expression at the transcriptional level.** qRT-PCR analysis of **A)** *Adgre1* (F4/80) and **B)** *Sema4D* genes in control and anti-Sema4D (α-S4D) treated RIP1-Tag2 tumors. Relative expression to *Hprt1* gene. At least 5 tumors were analyzed per group. No significant difference is found by Mann-Whitney test. Error bars indicate ± SD.

3.3. Macrophages *in vitro* increase their migration capacity

Once we described the increase in the number of macrophages and the change in their phenotype after blocking Sema4D, we aimed at functionally validating its consequences. In this line, we chose an *in vitro* system based on RAW 264.7 (from now on RAW) murine macrophage cell line. First, we proved that RAW cells mimicked the phenotype of the tumor-infiltrating macrophages in the RIP1-Tag2 tumor ecosystem. RAW cells were positive for F4/80, Sema4D and CD72 and negative for PlexinB1 by RNA expression analysis (Figure 50A). At the protein level, by immunocytofluorescence assay, nearly 100% of RAW cells stained positive for Sema4D and CD72, whereas almost half of them could be considered F4/80 positive (Figure 50B). Some RAW cells showed faint PlexinB1 expression, which localized in a specific part of the cell membrane. The same protein localization pattern could be observed for Sema4D, while CD72 and F4/80 appeared homogeneously distributed throughout all the cell membrane. If compared to TAMs *in vivo*, RAW cells mostly imitate them, especially regarding Sema4D and CD72 expression, which is crucial for the next experimental approaches.

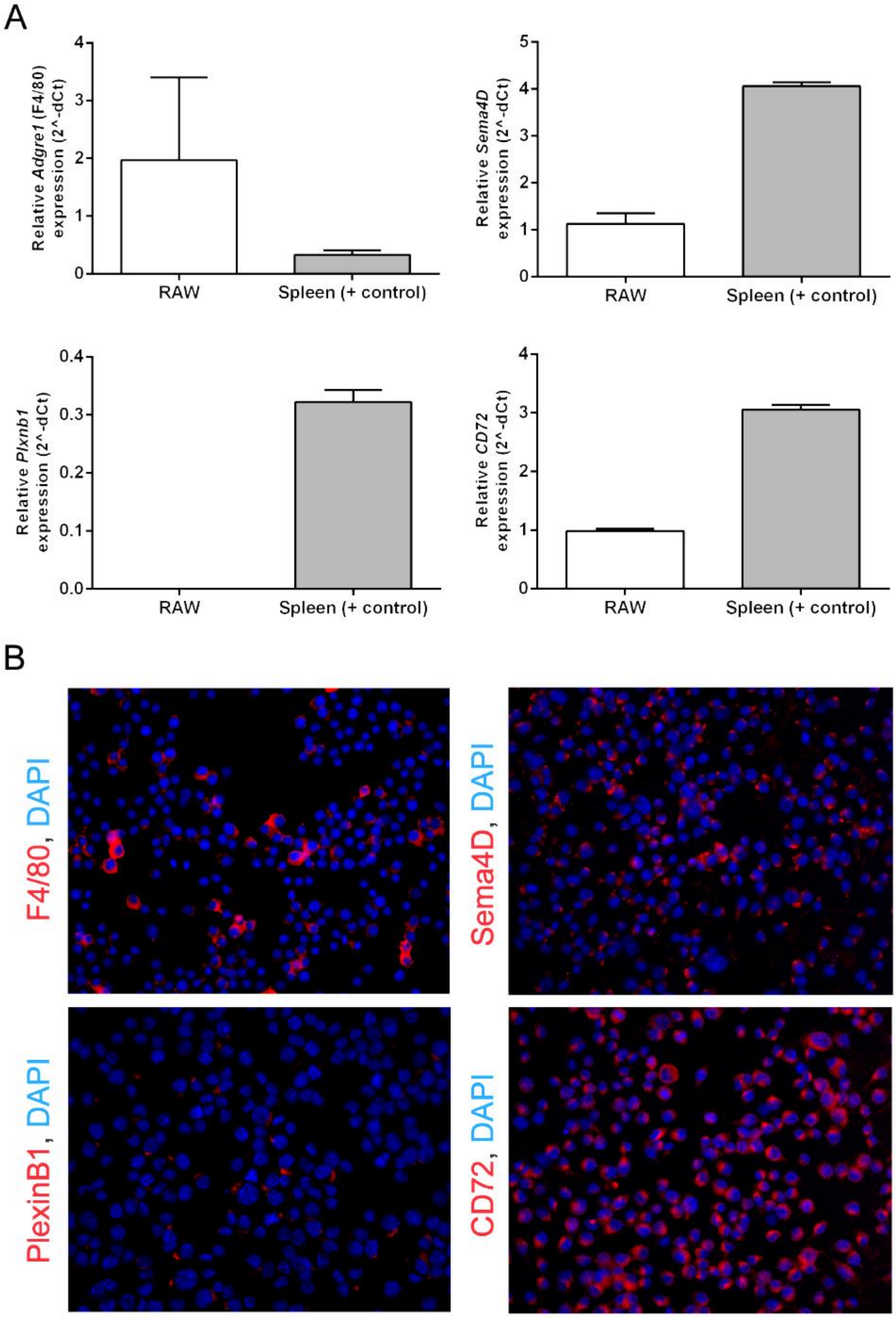

Figure 50 **RAW macrophages mostly reproduce the expression profile of the tumor-associated macrophages of the RIP1-Tag2 tumor stroma. A)** qRT-PCR analysis of *Adgre1* (F4/80), *Sema4D*, *Plxnb1* and *CD72* genes in RAW macrophages. Murine spleen is used as a positive control. Relative expression to *Hprt1* gene. At least 3 samples were analyzed per group. Error bars indicate ± SEM. **B)** Immunocytofluorescence analysis of F4/80, Sema4D, PlexinB1 and CD72 (in red)

protein expression in RAW macrophages. Representative fields from at least 3 slides of RAW cells. Images were taken at 40X magnification.

Next, we determined whether the migratory properties of RAW cells were modified after anti-Sema4D treatment *in vitro*. As shown in Figure 51, there was an increase in migration of inflammatory cells after Sema4D inhibition. In fact, anti-Sema4D treatment produced a nearly 50% increase of the number of migratory cells when compared to the untreated control (Figure 51B). Treatment with IgG1 isotype also produced a modest increase of RAW migratory capacity. These results correlate with previous studies (Chabbert-de Ponnat et al., 2005; Delaire et al., 2001; Oinuma et al., 2006; Toguchi et al., 2009) and support the idea that Sema4D could act as a cell migration inhibitory molecule. Moreover, we performed the same experiment, using another Sema4D-blocking antibody (Abnova, clone 3B4) (Luque et al., 2013), obtaining similar results (data not shown). These data support the idea that the effects after anti-Sema4D addition are Sema4D specific and might involve macrophage activity.

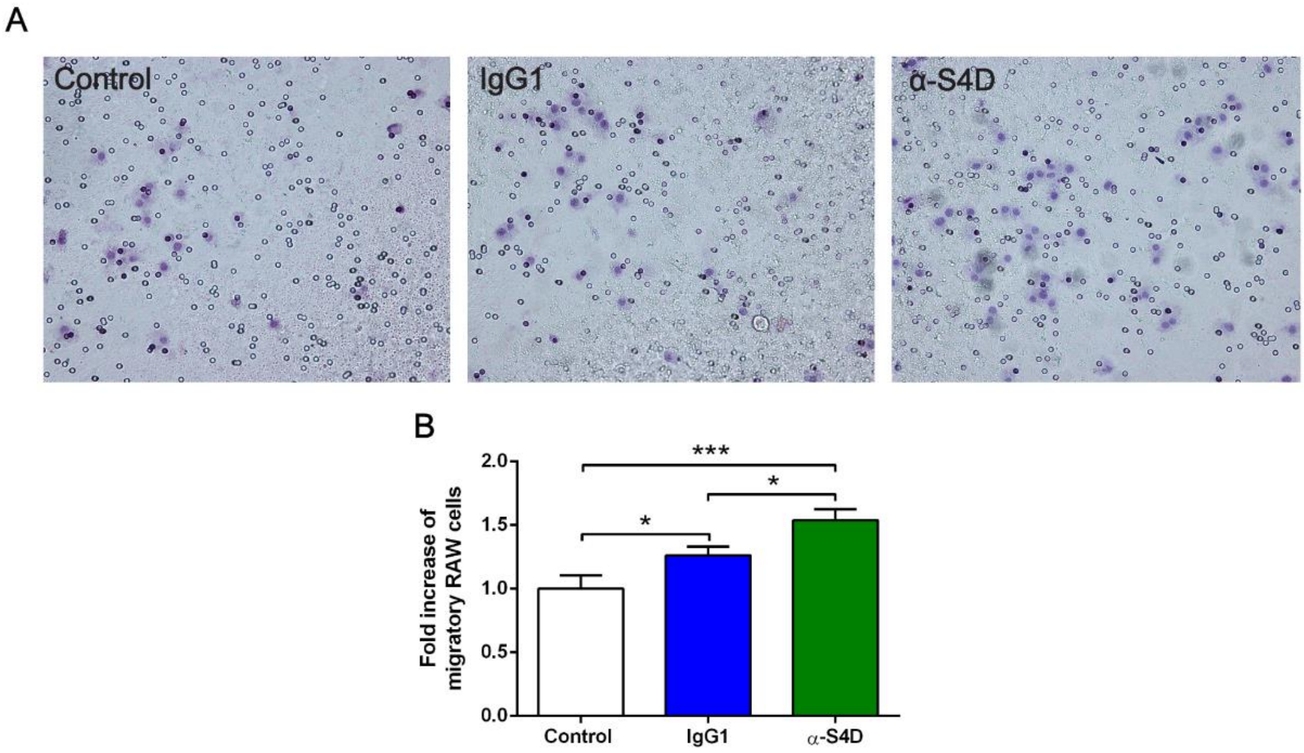

Figure 51 **Anti-Sema4D treatment increases in vitro macrophage migration capacity. A)** Transwell migration assay of RAW macrophages in presence of 10 µg/µl of anti-Sema4D or IgG1. Untreated RAW cells are used as control. Representative fields from at least 20 fields for each condition of five independent experiments. Images were taken at 20X magnification. **B)** Fold

increase of the number of migrated RAW cells per field after IgG1 or α-S4D treatment. Quantification of the migrated haematoxylin stained cells from at least 20 fields for each condition taken at 20X. Control untreated RAW cells were used for normalization. $^{*}p < 0.05$ and $^{***}p < 0.001$ by Mann-Whitney test. Error bars indicate ± SEM.

3.4. Secretome analysis by proteomics reveals changes in macrophage migration, activation and proliferation

Most macrophage activity is mediated by cytokines and chemokines that act in autocrine fashion and paracrine fashion, upon other macrophages or even upon other cells from the tumor ecosystem. Aiming to delve into macrophage study, we performed a mass spectrometric analysis (LC-MS/MS) of secreted proteins (secretome) composing RAW conditioned media previously stimulated with anti-Sema4D. Concentration of RAW conditioned media was needed prior to the proteomic analysis. Apart from using anti-Sema4D treated conditioned media, we assayed untreated, anti-Sema4D added, IgG added, and IgG treated conditions to serve as controls. While the untreated conditioned media provides the basal effect of macrophages, the isotype IgG control is important to discern the inflammatory activity due to antibody addition from the specific Sema4D blocking effect. Finally, two added conditions were introduced in the study to further discard a direct effect of the antibodies that would not need RAW cell activation.

After concentrating the conditioned media, as expected, a consensus is observed regarding heavy chain molecular weight in all samples containing antibodies (Figure 52). However, IgG1 treated conditioned media shows a slightly smaller molecular weight of its light chains. While the heavy chain is the protein portion that determines antibody isotype, being the same in all cases, the light chain fraction is where specificity towards a certain antigen resides. Anti-Sema4D antibody obviously has a higher molecular mass than IgG isotype control, producing a different band pattern in the Coomassie gel. This proves that basal and isotype controls are necessary when working with immune cells and functional antibodies.

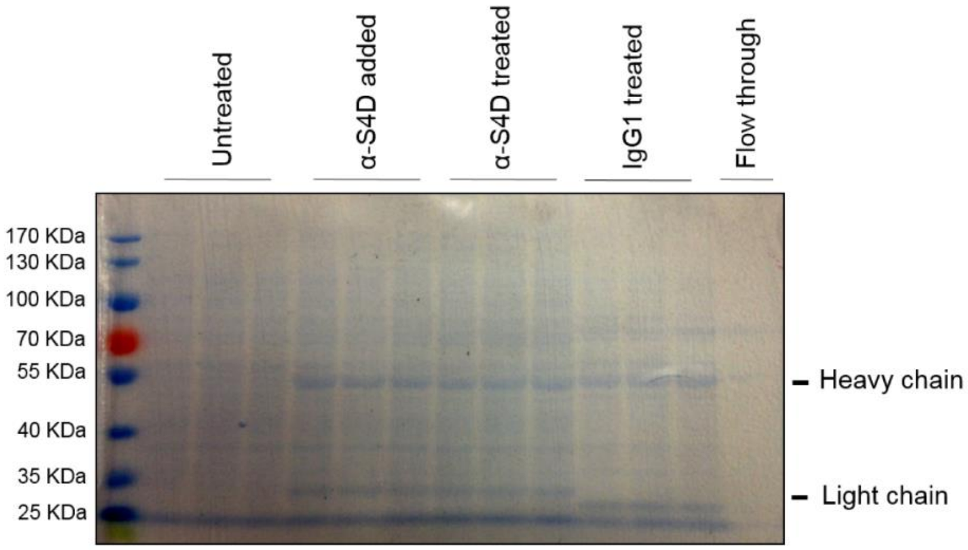

Figure 52 **Coomassie staining of concentrated RAW conditioned media.** Conditioned media from untreated control, anti-Sema4D (α-S4D) added, anti-Sema4D (α-S4D) treated and IgG1 treated RAW cells in triplicate were concentrated using a 2 KDa concentrator and electrophoretically separated. Protein was visualized using Coomassie staining. Heavy and light chains of the IgG antibody are visualized in the α-S4D added, (α-S4D treated and IgG1 treated conditions. Flow through of one IgG1 treated sample was loaded as a negative control of the concentration process.

The proteomic data consisted of 1138 proteins, filtered by 5% of FDR score. We first eliminated proteins that did not have a murine origin and those that were barely represented. The filtered list of 1085 proteins was then converted to a gene symbol list, their human homologs were found and a whole GSEA analysis was performed (Subramanian et al., 2005). For the GSEA analysis, we compared the expression of genes in the anti-Sema4D treated samples to all control conditions. We obtained a ranked list of 1075 genes (Annex 1) together with the enrichment plots.

The most interesting results regarding activated molecular pathways and functions that were statistically significant were manually selected and are shown in Figure 53. The analysis revealed an anti-Sema4D-dependent statistical enrichment in proteins related to important macrophage functions: cell migration, cell projection, cytoskeleton and RAC1 pathway (grouped in migration); DNA replication and cell cycle (grouped in proliferation); FCγR mediated phagocytosis and immunological synapse (grouped in activation). Taken together, the analysis of the secretome by proteomic profiling suggests a direct effect of Sema4D upon macrophage activity, specially affecting their migration, proliferation and activation.

Upregulated genes in the enriched gene sets were manually annotated (Figure 54). Interestingly, some of the top-score genes in the enrichment plots of the GSEA analysis possess shared functions among the three different phenotypes designed in Figure 53. For instance, ARPC2, ARPC5, MYH9 and SYK share functions in activation and migration, whereas LMNB1 is related both to migration and proliferation. These results remark the importance and plasticity of a particular set of genes to control important cellular functions.

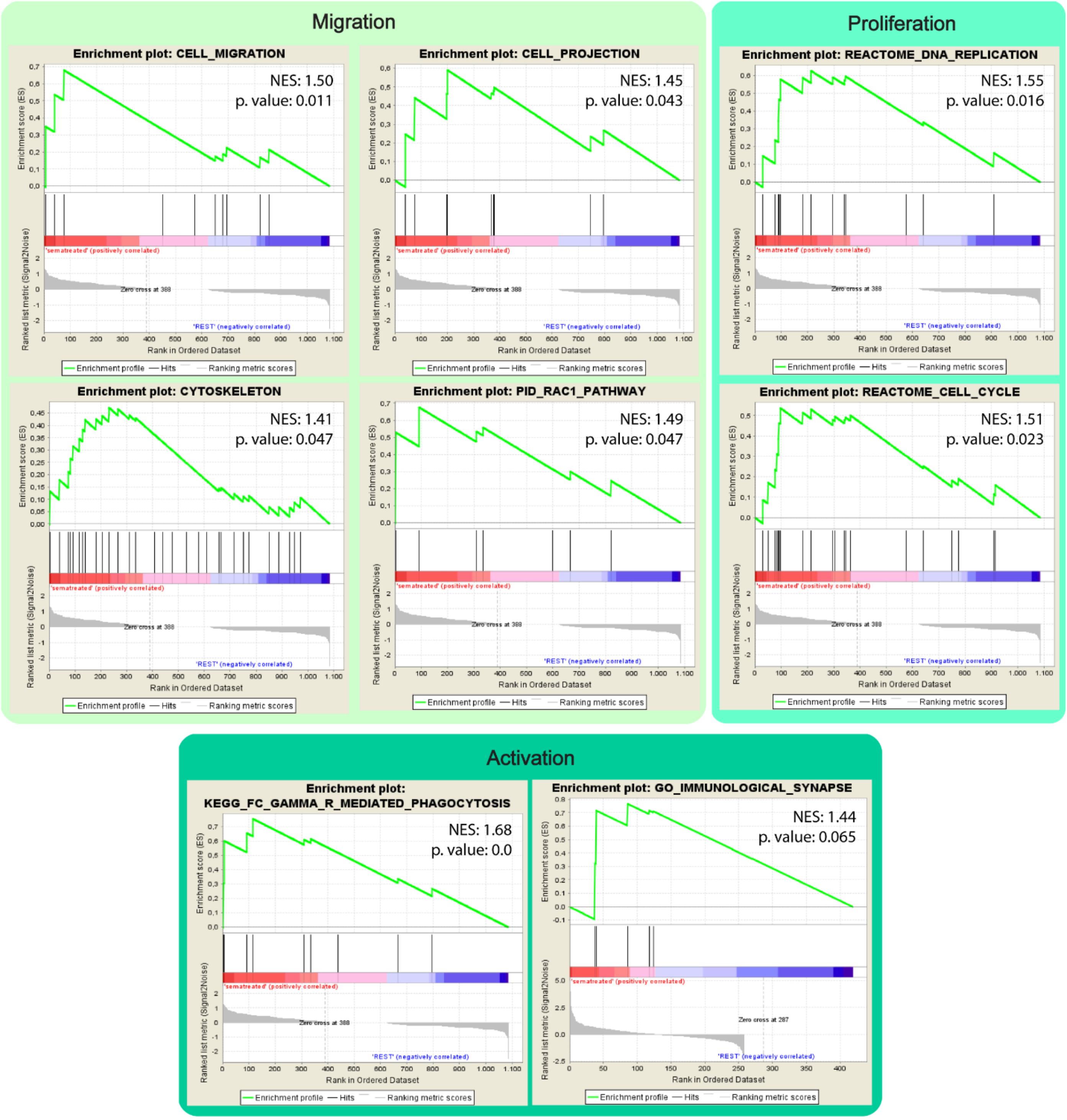

Figure 53 **Analysis of anti-Sema4D treated macrophage conditioned media reveals enrichment in molecular pathways related to migration, proliferation and activation.** A GSEA analysis of the proteomic data obtained from anti-Sema4D treated RAW macrophage conditioned media was performed, using untreated, IgG1 treated and anti-Sema4D added RAW conditioned media as controls for comparison. Representative enrichment plots were further classified according to the molecular function as follows: Migration includes enrichment in cell migration, cell projection, cytoskeleton and RAC1 pathway (**Top left**); proliferation includes enrichment in DNA replication and cell cycle (**Top right**); activation includes enrichment in FCγR mediated phagocytosis and immunological synapse (**Bottom**). The top portion of each enrichment plot

shows the enrichment scores (ES) for each gene, whereas the middle portion shows where the members of the gene set appear in the ranked list of genes. The bottom portion of the plot shows the value of the ranking metric moving down the list of ranked genes. Inside each plot, the normalized enrichment score (NES) and the p. value for that feature are depicted. GSEA analysis was performed in November 2015.

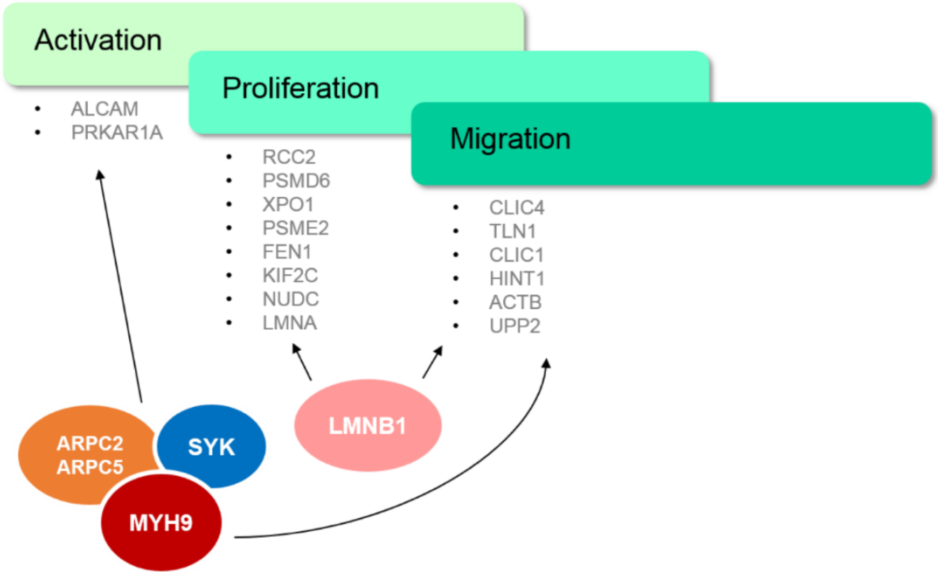

Figure 54 **Some of the genes enriched in anti-Sem4D treated macrophage conditioned media share molecular functions related to cell activation, proliferation and migration.** List of enriched genes obtained from the upregulated gene sets regarding activation, proliferation and migration phenotypes from the GSEA analysis of anti-Sema4D treated RAW conditioned media. Untreated, IgG1 treated and anti-Sema4D added RAW conditioned media were used as controls. ARPC2, ARPC5, MYH9 and SYK share functions in activation and migration, whereas LMNB1 is related both to migration and proliferation. GSEA analysis was performed in November 2015.

With the aim of further characterizing the secretome of anti-Sem4D treated macrophages, we decided to perform a more restricted analysis. Our previous experiments have validated the use of IgG1 treated samples as a good basal control condition for the antibody addition effect on inflammatory cells. For simplification, we decided to focus only on proteins present in anti-Sema4D and IgG1 treated samples that bare a peptide count higher than 2 for each sample. We obtained a list of 391 proteins (Annex 2). Strikingly, most proteins (nearly 89%) were not secreted according to UniProt database (Bateman et al., 2017).

We selected the 45 secreted proteins (Annex 3) and performed a STRING analysis with the 24 proteins that were upregulated in the anti-Sema4D treated condition according to their fold change (Figure 55) (Szklarczyk et al., 2015). Nearly 55% of the proteins, 13 out of 24, showed interconnections with other secreted proteins in the list, indicating shared functions between them. Besides, some interesting molecular pathways involved with macrophage activation showed statistical significance by FDR score (Figure 55). Anti-Sema4D treatment demonstrates a role in IL4 response, cytokine activity, receptor binding and negative regulation of cell death. Importantly, at least 3 or 4 proteins of the list were involved in each of the enriched pathways.

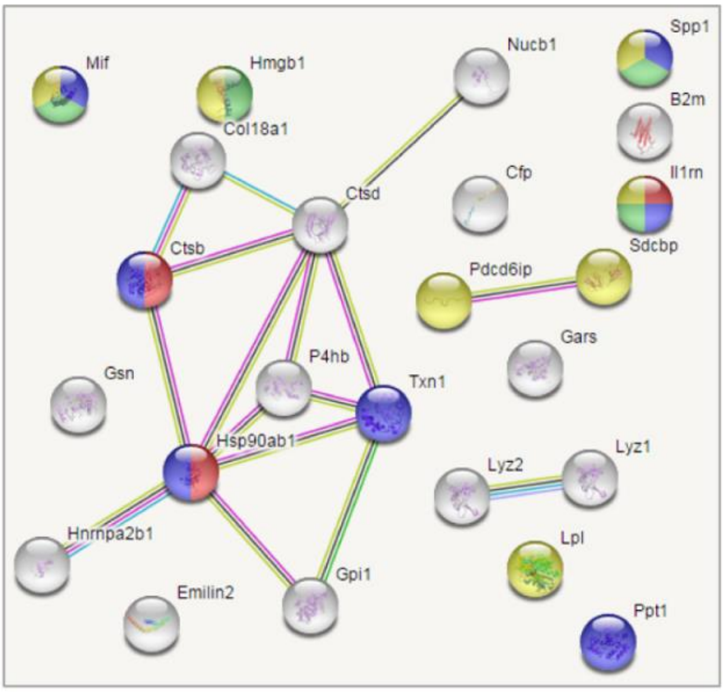

Biological process / Molecular Function(GO)			
Pathway description	*Count in gene set*	*FDR*	
Response to Interleukin-4	3	0.0117	🔴
Negative regulation of cell death	7	0.0152	🔵
Cytokine activity	4	0.0153	🟢
Receptor binding	7	0.045	🟡

Figure 55 **Analysis of anti-Sema4D treated macrophage secretome reveals enrichment in proteins related to macrophage activation.** STRING analysis of the secreted proteins from the proteomic data obtained from anti-Sema4D treated RAW macrophage conditioned media was performed. The analysis included 24 proteins upregulated in the anti-Sema4D condition, using IgG1 treated RAW conditioned media as control. 13 proteins showed interconnections (**Top**). Representative pathways that showed statistical significance by FDR score according to the analysis

by biological process or molecular function (GO) are listed, together with the protein count in the gene set (**Bottom**).

3.5. Macrophage characterization

The proteomic analysis of the macrophage derived conditioned media gave us a wide perspective of what processes macrophages underwent when treated with anti-Sema4D. However, in order to understand their behavior and effect in the tumor ecosystem, we needed to better characterize their phenotype after the treatment. Interestingly, the STRING analysis revealed an increase in IL4 response after anti-Sema4D treatment. IL4 is an interleukin traditionally used in the laboratory to induce the alternative activation of monocytes, also known as the M2 antiinflamatory or the wound-healing macrophage phenotype (Mosser and Edwards, 2008). M2 macrophages are best known for their role in tumor progression. As described in the Introduction section, several membrane proteins help classify macrophages according to their M1 or M2 phenotype (Jablonski et al., 2015). Among them, probably the best described M2 marker is Mannose Receptor C-Type 1 (Mrc1), also known as CD206.

With the aim of assessing the activation state of RAW macrophages after anti-Sema4D treatment, we tried to perform a Western Blot analysis to detect CD206, but it proved technically challenging (data not shown). Therefore, we analyzed RNA expression of some canonical M1 and M2 markers in control, IgG1 treated and anti-Sema4D treated RAW macrophages (Figure 56). As M1 markers, we chose to assay *IL12b* and *Nos2* expression, whereas *Mrc1* and *Arg1* were elected to delimit M2 macrophages. We also checked expression of *Sema4D*, *PlexinB1*, *CD72* and *Adgre1* (F4/80).

As previously described for the *in vivo* samples of RIP1-Tag2 tumors (Figure 49), expression of Sema4D and F4/80 slightly increased at the transcriptional level after anti-Sema4D therapy. We did not expect expression of Plexin B1, but we were intrigued to find an increase in CD72 receptor expression (Figure 56). Regarding M1 and M2 markers, no expression of *Il12b* and *Arg1* genes was found.

Surprisingly, *Nos2* M1 marker was highly expressed in anti-Sema4D treated samples, whereas Arg1 M2 marker expression decreased with the treatment (Figure 56). Those were rather unexpected results since they contradicted what we had previously seen.

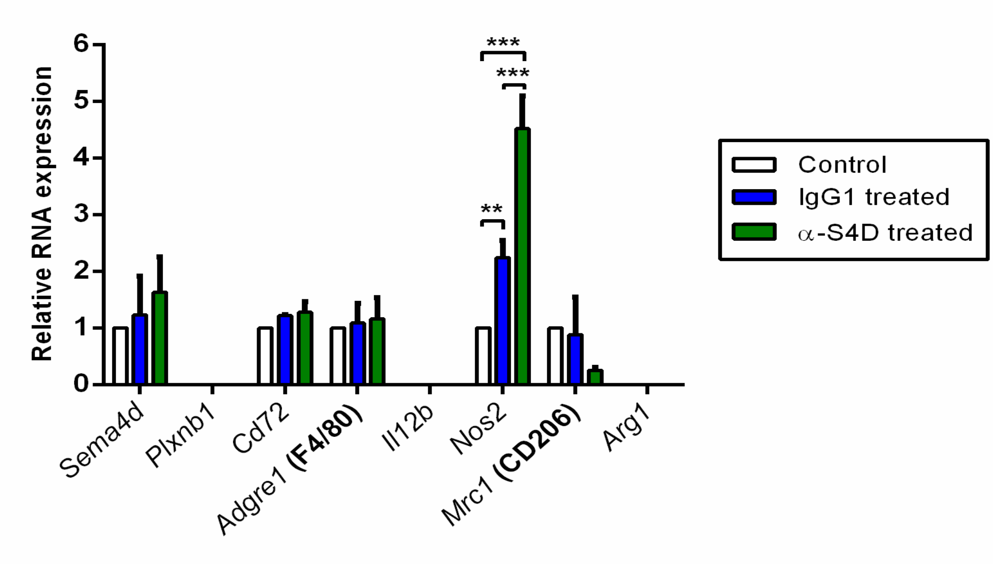

Figure 56 **Anti-Sema4D treatment abruptly increases Nos2 expression in macrophages, whereas slightly modifying Sema4D, CD72, F4/80 and Mrc1 expression at the transcriptional level.** qRT-PCR analysis of *Sema4d*, *Plxnb1*, *Cd72*, *Adgre1* (F4/80), *Il12b*, *Nos2*, *Mrc1* (CD206) and *Arg1* genes in control, IgG treated and anti-Sema4D (α-S4D) treated RAW macrophages at conditioned media harvesting time point. Relative expression to *β-actin* gene and normalized to control samples. At least 3 independent cell extracts were analyzed per group. **p<0.01, ***p < 0.001 by Mann-Whitney test Error bars indicate ± SEM.

There are certain drawbacks associated with using Western Blot or RNA expression analysis to characterize macrophage activation. Both techniques are highly specific but rely in a small number of genes to characterize a particular phenotype. Thus, we decided to use a bioinformatic approach to compare filtered data from the proteomic analysis with data from other previously published experiments containing differentially activated macrophages. Once again, for simplification, we focused only in the expression of the 391 proteins of the proteomic data, obtained as previously explained (Annex 2).

For comparison, we chose expression data from two studies named GSE5099 and GSE68817 (Figure 57A and B respectively). In GSE5099, freshly isolated monocytes were cultured in the presence of M-CSF (100 ng/ml) for 7 days, and then activated. The study includes Monocytes at day 0, macrophages at day 3 and 7, Interferon Gamma and LPS treated macrophages (M1 type) and IL4 treated macrophages (M2 type) (Martinez et al., 2006). In GSE68817, Kratochvill et al. analyzed gene expression profiles of macrophages isolated from tumor spheres, or the macrophages from the same cultures that did not enter the spheres (Kratochvill et al., 2015).

In collaboration with Luis Palomero (ProCURE, ICO-IDIBELL, L'Hospitalet), we first performed a supervised heatmap analysis of the expression of the 391 genes of the proteomic data in both selected datasets (Figure 57A-B, left panel). None of the analyses revealed any clear correlations with the different macrophage subtypes. We then decided to reanalyze the expression of the enriched genes in anti-Sema4D treated samples in an unsupervised heatmap analysis (Figure 57A-B, right panel).

Regarding the GSE5099 gene set, we observed that genes enriched in anti-Sema4D treated samples correlated both to differentiated macrophages, and M1 or M2 macrophages, indicating a potential mixture of variably activated macrophages in our samples. Similar results were obtained with GSE68817, where enriched genes were found in both types of macrophages. Those results shed light into our previous findings regarding IL4 activity together with IL12b expression in anti-Sema4D treated macrophages, validating a mixture of different subtypes of macrophages after the treatment.

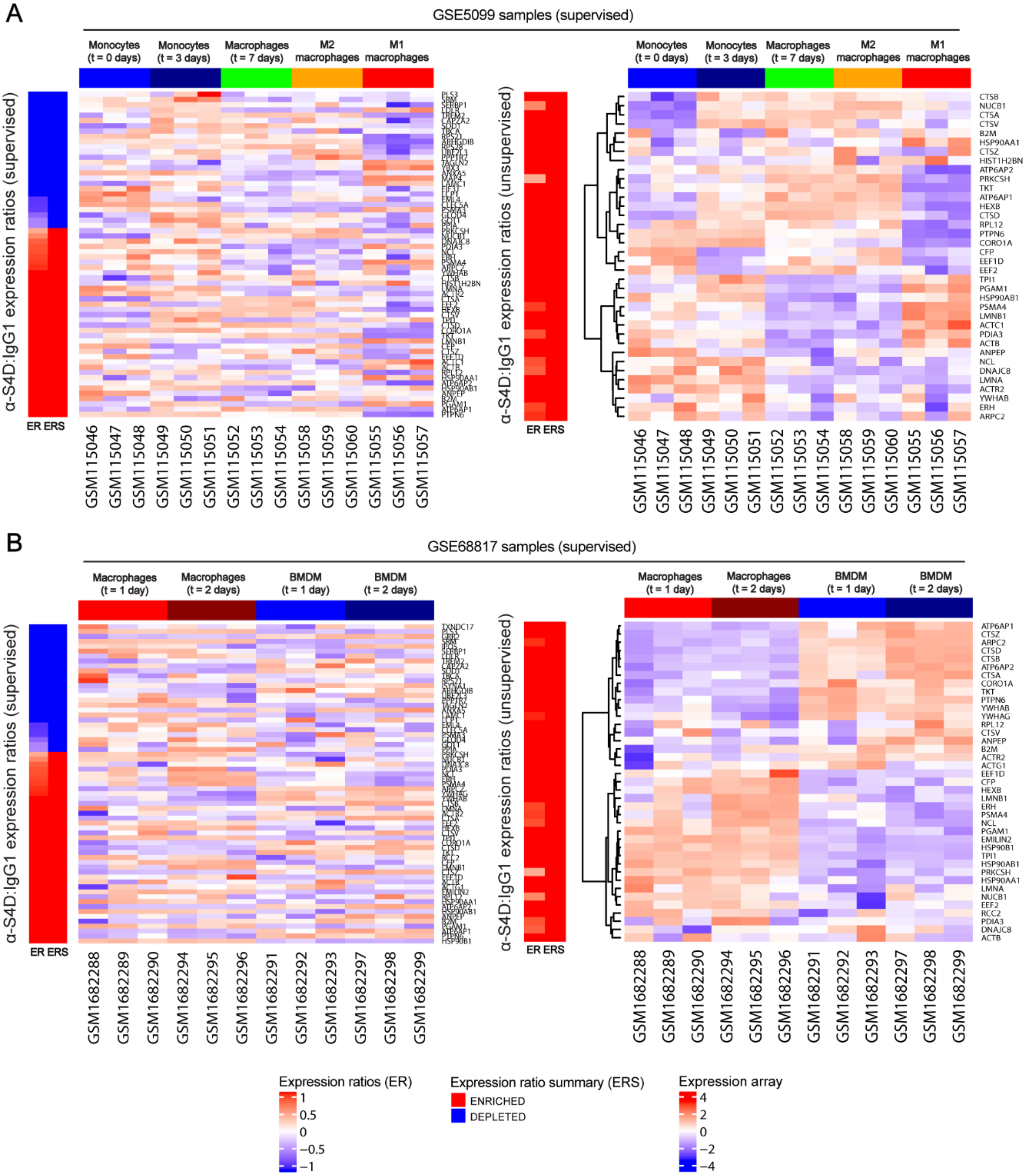

Figure 57 **Bioinformatic analysis of the anti-Sema4D treated macrophage conditioned media reveals a mixture of macrophage subtypes.** Heatmap representations comparing the expression of proteins in anti-Sema4D treated RAW conditioned media with gene expression datasets A) GSE5099 and B) GSE68817. IgG1 treated RAW conditioned media was used as control. Enriched and depleted proteins from anti-Sema4D treated proteomic data were used in the comparative analysis, creating

supervised heatmaps (Left panel). Only enriched proteins from anti-Sema4D treated proteomic data were used in the comparative analysis, creating unsupervised heatmaps (Right panel).

3.6. Increase in peritumoral Sema4D positive macrophages

One of the main consequences of anti-Sema4D treatment was the increase in local invasiveness of RIP1-Tag2 tumors after the treatment. This increase in invasion was comparable to the one produced when traditional antiangiogenic treatments, such as anti-VEGFR2, are used, but in the absence of hypoxia and c-met activation, as previously demonstrated. After demonstrating an increase of intratumoral Sema4D positive macrophages, we sought to decipher their role in tumor periphery, together with their potential contribution to the invasive phenotype of the tumor.

In order to check the behavior of TAMs in the tumor periphery, the number of macrophages in the perimeter of the base protrusions of invasive fronts was determined by immunofluorescence of Sema4D, F4/80 macrophage marker and the RIP1-Tag2 tumor cell marker insulin (Figure 58A). Contrary to our results regarding the intratumoral fraction, the number of macrophages in the invasive fronts remained unaltered after Sema4D blockade (Figure 58B). The number of peritumoral Sema4D negative macrophages decreased nearly a 50% (from 0.042 to 0.021 macrophages per tumor front μm), while the number of Sema4D positive macrophages strongly increased after the treatment (Figure 58C-D). In fact, the number of Sema4D positive macrophages in the tumor front showed more than a sixty-fold increase (from 0.0003 to 0.0181 macrophages per tumor front μm). Overall, the percentage of Sema4D positive cells in the tumor front increased from a 0,7% to a 41,8% (Figure 58E).

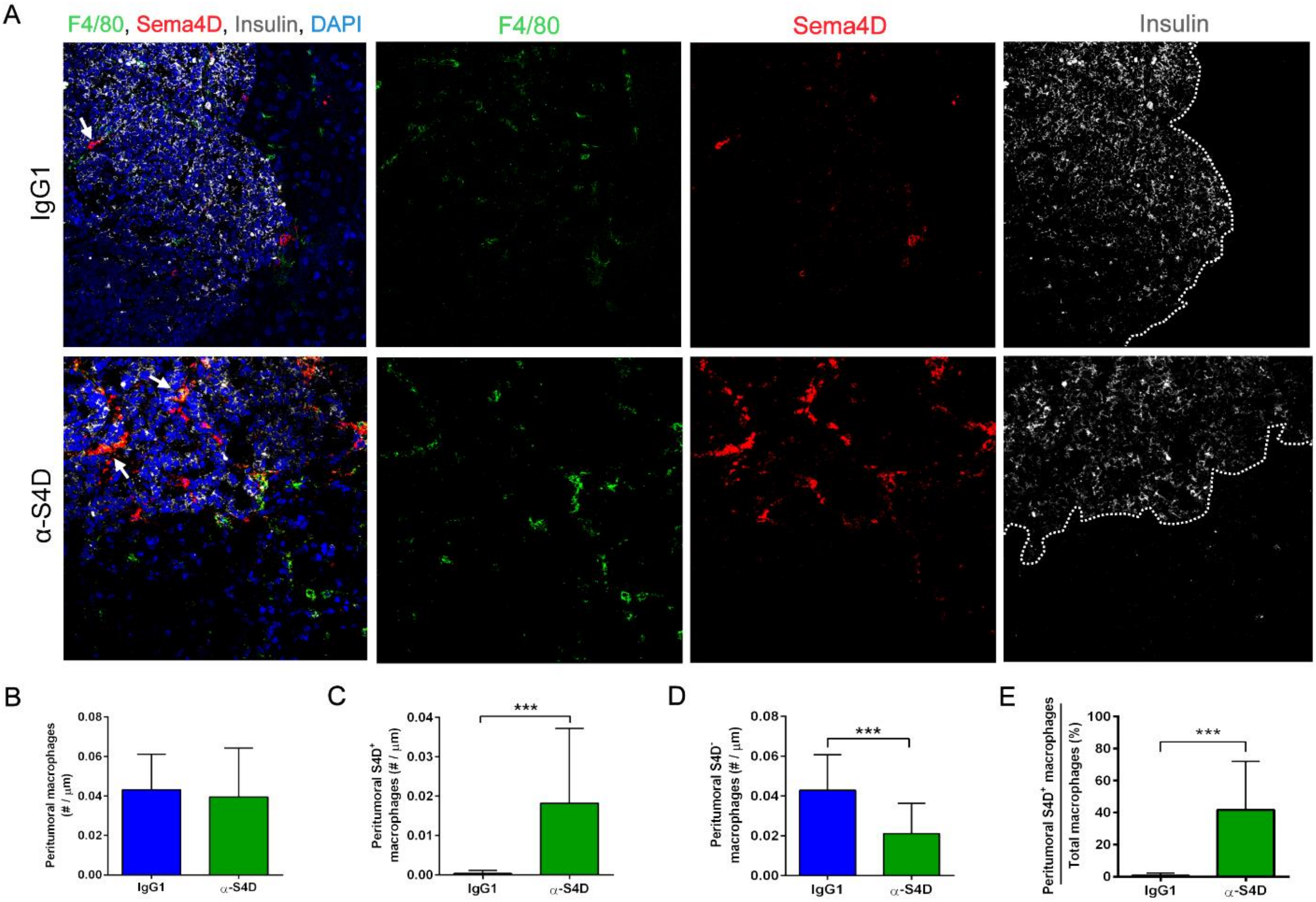

Figure 58 **Anti-Sema4D treatment increases the number of peritumoral Sema4D positive macrophages without altering the total number of macrophages. A)** Immunohistofluorescence analysis of peritumoral Sema4D positive (S4D$^+$, in red) and negative (S4D$^-$) F4/80$^+$ macrophages (in green) in IgG1 treated and anti-Sema4D (α-S4D) treated RIP1-Tag2 tumors. Insulin (in white) is used to stain for tumor cells. White arrows mark some S4D$^+$ macrophages. Representative fields from at least 18 tumors of three RIP1-Tag2 mice for each condition are shown. Images were taken at 40X magnification. Tumor front was determined at the interface between insulin positive and negative cells (white dotted line) and measured in µm. **B)** Quantification of the number (#) of total F4/80$^+$ macrophages per µm of tumor front perimeter per field for each condition. **C)** Quantification of the number (#) of peritumoral S4D$^+$ macrophages per µm of tumor front perimeter per field for each condition. **D)** Quantification of the number (#) of peritumoral S4D$^-$ macrophages per µm of tumor front perimeter per field for each condition. **E)** Percentage of intratumoral S4D$^+$ macrophages per total number of macrophages. At least 18 tumors were analyzed per group. IgG1 treated mice were used as a control. ***$p < 0.001$ by Mann-Whitney test. Error bars indicate ± SD.

3.6.1. βTC4 tumor cells mimic intratumoral tumor cells

After describing the increase in the number of Sema4D positive macrophages in the tumor front, we aimed at functionally validating its consequences, recapitulating what we had previously done with RAW cells. To this purpose, we chose an *in vitro* system based on βTC4 primary murine PanNET cell line derived from a RIP1-Tag2 tumor. Firstly, we proved that βTC4 cells mimicked the phenotype of the tumor cells of the RIP1-Tag2 tumor stroma *in vivo*. βTC4 cells were slightly positive for Sema4D and Plexin B1 and negative for CD72 by RNA expression analysis (Figure 59A). At the protein level, by immunocytofluorescence assay, βTC4 cells were negative for CD72 expression and showed slight PlexinB1 and Sema4D positivity (Figure 59B). PlexinB1 expression was, as for RAW cells, localized in specific parts of the cell membrane and only in some cells. Sema4D, in this case, appeared homogeneously distributed throughout all the cell membrane and cytoplasm and its expression was so dim that it was barely noticeable. If compared to tumor cells *in vivo*, βTC4 cells mostly imitate them, especially regarding Sema4D and CD72 expression. Strikingly, they slightly express PlexinB1 receptor, which does not match with our in vivo data.

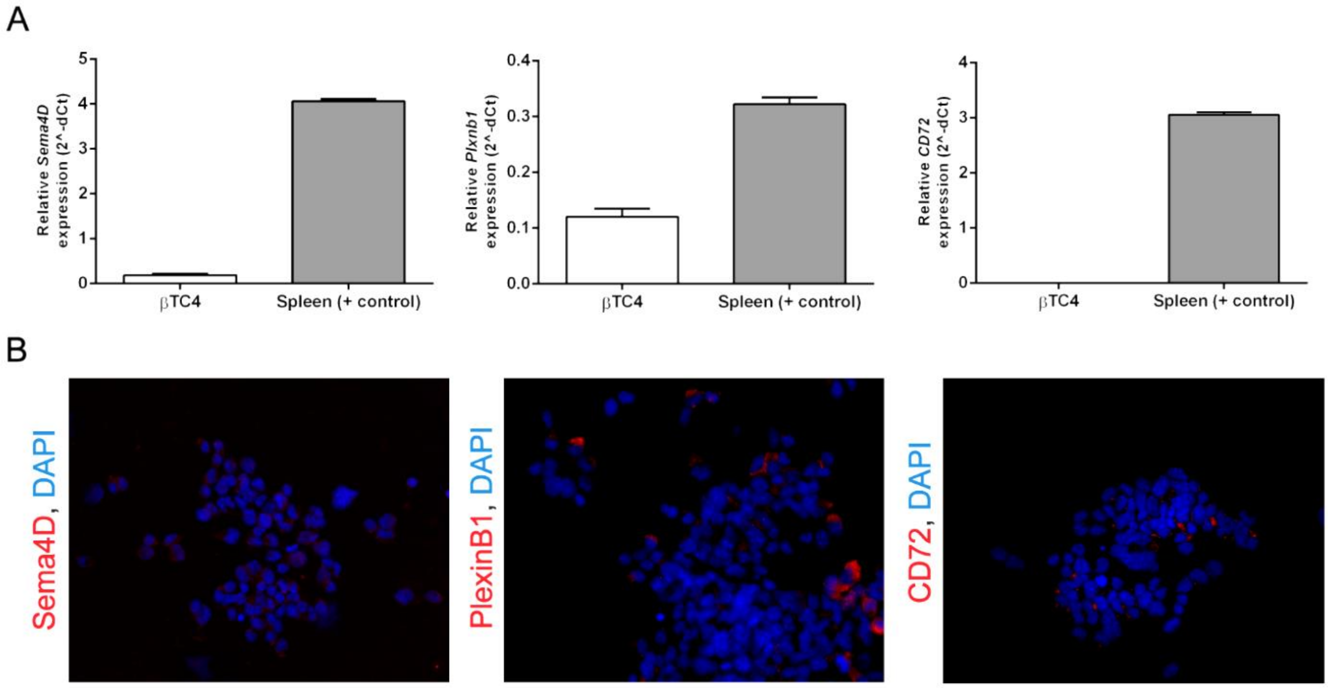

Figure 59 **βTC4 tumor cell line mostly reproduces the expression profile of RIP1-Tag2 tumor cells *in vivo*.** **A)** qRT-PCR analysis of *Sema4D*, *Plxnb1* and *CD72* genes in βTC4 cell line. Murine spleen is used as a positive control. Relative expression to *Hprt1* gene. At least 3 samples were analyzed per group. Error bars indicate ± SEM. **B)** Immunocytofluorescence analysis of Sema4D,

PlexinB1 and CD72 (in red) protein expression in βTC4 cell line. Representative fields from at least 3 slides of βTC4 cells. Images were taken at 40X magnification.

3.6.2. βTC4 tumor cells do not directly respond to anti-Sema4D

We have previously demonstrated that Sema4D-mediated malignization mechanism does not involve direct c-met activation in tumor cells from RIP1-Tag2 stroma (Figure 46). Besides, several studies describe an alternative activation of c-met via its coupling to PlexinB1 after Sema4D binding (Conrotto et al., 2005; Soong et al., 2012). Even though RIP1-Tag2 tumor cells do not express Plexin B1, their in vitro counterpart βTC4 cells do slightly express it. For this reason, in order to discard c-met activation as a consequence of the direct effect of Sema4D in those cells, we validated c-met expression in βTC4 cells (Figure 60). βTC4 cells showed low expression levels of c-met by RNA analysis (Figure 60A). We then assayed the presence of its precursor protein and its active form, phosphorylated c-met, by western blotting (Figure 60B). We observed no expression of the precursor and no activation of c-met signaling pathway, neither in the untreated nor in the anti-Sema4D treated conditions (Figure 60B). Indeed, no activation of c-met was even observed after the addition of HGF, the natural c-met ligand. Overall, these data suggest, as in the case of RIP1-Tag2 mice, that malignization effects are restricted to an indirect effect of Sema4D blockade over tumor cells, rather than to a direct action of the proangiogenic molecule inhibition upon tumor cell derived c-met.

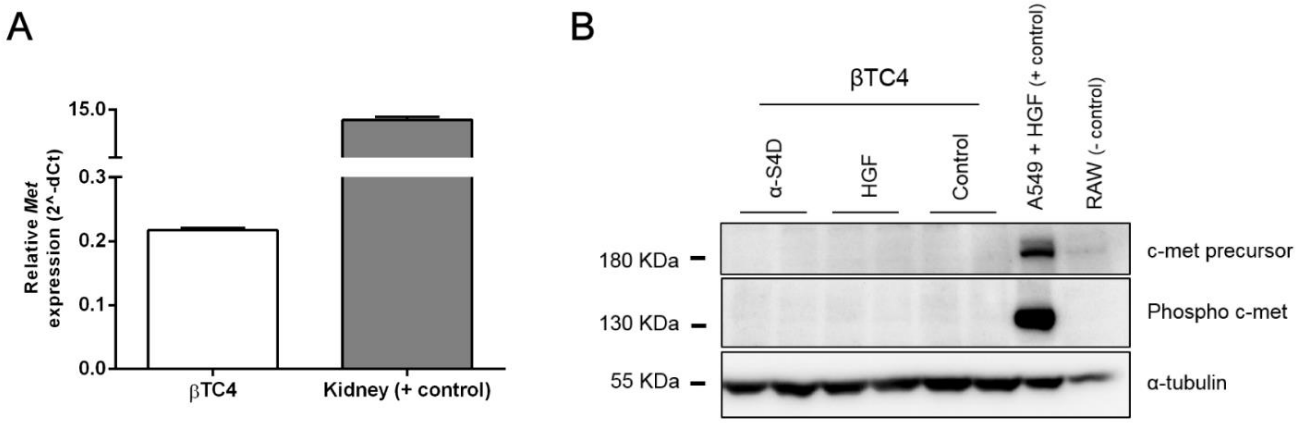

Figure 60 **Presence of c-Met RNA in βTC4 cells does not translate into pathway activation in response to anti-Sema4D. A)** qRT-PCR analysis of *Met* gene in βTC4 cell line. Murine kidney is used as a positive control. Relative expression to *Hprt1* gene. At least 3 samples were

analyzed per group. Error bars indicate ± SEM. **B)** Western blot analysis of the active form of c-Met protein (phospho c-met) in two independent samples of control, anti-Sema4D (α-S4D) and HGF treated βTC4 cells. α-tubulin protein is used as a housekeeping control. Lysate from A549 cells treated with HGF in equal conditions was used as a positive control for c-met phosphorylation. RAW cell line was used as a negative control.

3.7. βTC4 tumor cell migration does not increase

Once we both discarded a direct effect of Sema4D in βTC4 cells and proved their high resemblance to the *in vivo* RIP1-Tag2 setting, we assessed in an *in vitro* setting whether macrophages could be responsible for their invasive phenotype after anti-Sema4D treatment. We hypothesized that if anti-Sema4D produced a switch of the macrophage phenotype that could induce the invasive capacity of tumor cells, we would be able to see *in vitro* increase of their migratory speed in co-culture conditions. To this aim, we first performed a 2D wound-healing assay in a βTC4-RAW coculture in the presence of anti-Sema4D (Figure 61). Unfortunately, we saw no differences in the wound closure ability of βTC4 cells, regardless of the presence of RAW or anti-Sema4D treatment (Figure 61A). The migratory speed ($V_{migration}$) also remained invariable (Figure 61B).

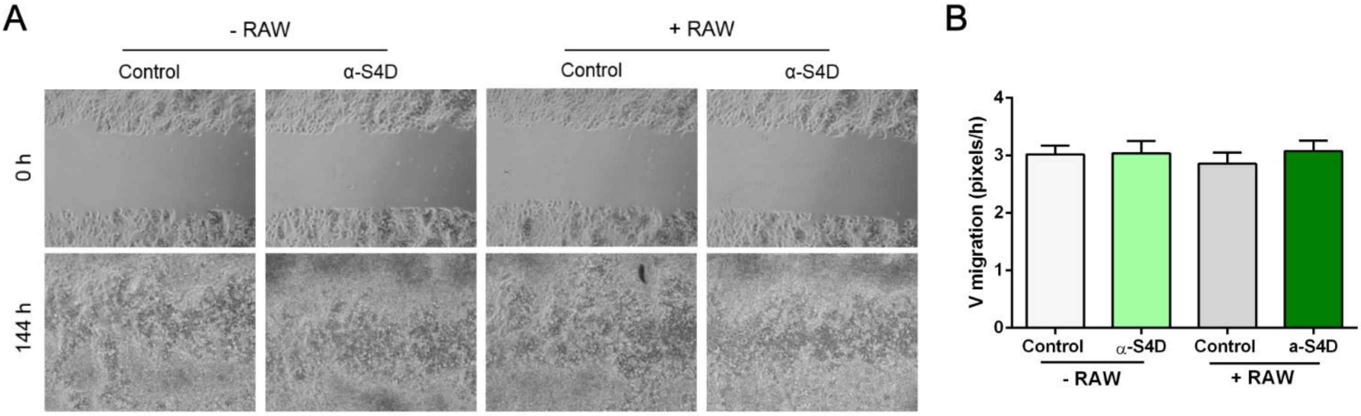

Figure 61 **Anti-Sema4D treatment does not increase migration of βTC4 tumor cells. A)** Wound healing analysis of control and anti-Sema4D (α-S4D) treated monolayers of βTC4 cell line in the presence or absence of RAW cells. Representative fields for two wells of βTC4 cells at the start (0 h) and end (144 h) of the experiment, when the wounds were closed. Images were taken at 40X magnification. **B)** Migratory speed (V migration) of each of the conditions of the wound healing assay calculated as pixels per hour. No significant differences are found by Mann-Whitney test. Error bars indicate ± SEM.

3.8. βTC4 spheroids are able to invade in response to macrophage conditioned media treated with anti-Sema4D

Since we did not obtain any results in the 2D migration assay, we theorized that βTC4 cells might need a scaffold that resembled more the *in vivo* architecture of the tumor in order to invade. Thus, we developed a 3D model with βTC4 spheroids, which spontaneously generated from overconfluent 2D cultures. For the invasion assay, we placed those spheroids in Matrigel® drops in the presence of control, IgG1 and Sema4D treated RAW macrophage conditioned media. We cultured an additional control with βTC4 full culture media containing FBS. After five days of culture, we observed that the spheroids under anti-Sema4D treated conditioned media resembled more to control spheroids, showing some invasive protrusions (Figure 62, pointed with white arrows). Unfortunately, counting the number of protrusions brought about a lot of technical difficulties and the results were not conclusive.

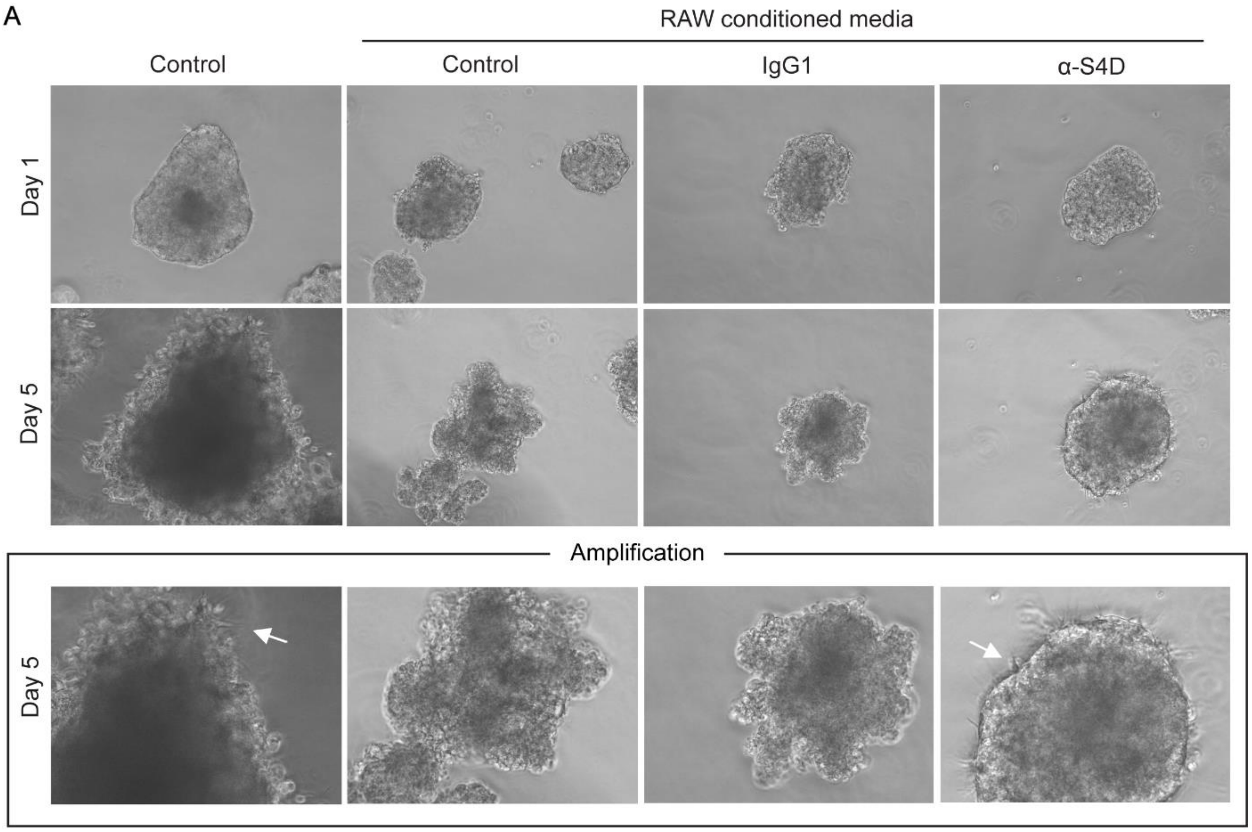

Figure 62 **Exposure to anti-Sema4D treated macrophage conditioned media in nutrient serum-deprived conditions partially increases 3D βTC4 tumor spheroid invasion.** 3D invasion assay of βTC4 spheroids embedded in Matrigel® in presence of untreated, IgG1 treated, and anti-Sema4D

(α-S4D) treated RAW conditioned media. Culture FBS rich media is used as control. Representative fields from at least 30 spheroids for each condition of two independent wells at the starting point (Day 0) and end of experiment (Day 5). Images were taken at 20X magnification. A 2X amplification is performed for better visualization of the invasive protrusions (pointed with white arrows).

3.9. βTC4 tumor cells increase their invasion in response to anti-Sema4D treated macrophage conditioned media

Neither the 2D migration nor the 3D invasion experimental models have allowed us to study the effect of anti-Sema4D treatment. Whereas the 2D model remained too simple to mimic the invasion process of a tumor cell surrounded by a rich extracellular matrix, the 3D model was too complex to be analyzed with the resources currently available in our laboratory. Therefore, we decided to explore an intermediate model, one that combined the simplicity of 2D culture with the presence of a surrounding matrix: a transwell invasion assay.

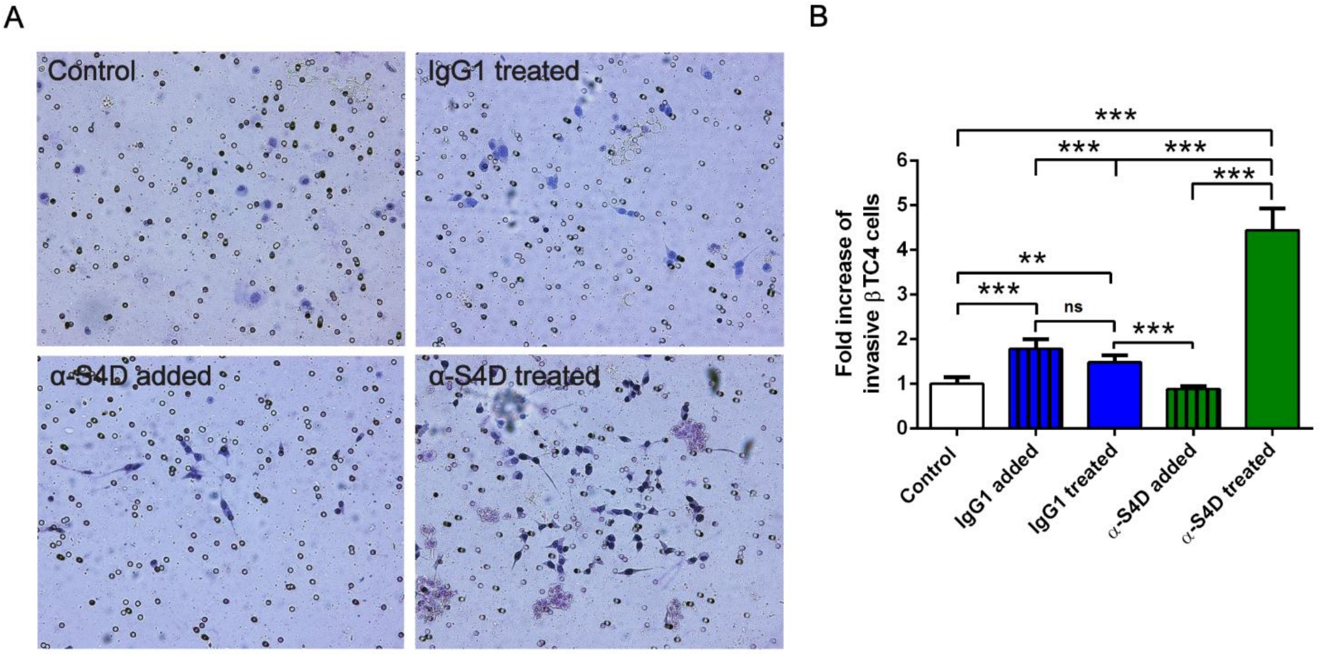

Figure 63 **Exposure to anti-Sema4D treated macrophage conditioned media increases *in vitro* βTC4 tumor cell invasive capacity. A)** Transwell invasion assay of βTC4 tumor cells in presence of untreated, IgG1 treated, IgG1 added (not shown), anti-Sema4D (α-S4D) added or anti-Sema4D treated RAW conditioned media. Untreated RAW cells are used as control. Representative fields from at least 20 fields for each condition of three independent experiments. Images were taken at 20X magnification. **B)** Fold increase of the number of invasive βTC4 cells per field. Quantification of the invading haematoxylin stained cells from at least 20 fields for each condition taken at 20X.

The untreated control βTC4 condition was used for normalization. **$p < 0.01$ and ***$p < 0.001$ by Mann-Whitney test. Error bars indicate ± SEM.

We performed a Matrigel® invasion assay using transwells. βTC4 cells were seeded on the top side and subjected to a potential chemoattractant effect of RAW conditioned media, placed in the bottom area (Figure 63). The presence of conditioned media of RAW cells treated with anti-Sema4D increased 4 fold the invasive properties of βTC4 cells (Figure 63B). Little difference was observed both in untreated and IgG treated control conditions. Interestingly, no effect on βTC4 cell invasion was observed in IgG1 and anti-Sema4D added conditions, meaning that the effect on invasion is indirectly mediated by macrophage cells. We further confirmed that this effect is target-specific, since inhibition of Sema4D using a different antibody (clone 3B4, Abnova) in the same in vitro setting led to similar effects on tumor cell invasion (data not shown). Overall, we conclude that Sema4D inhibition in macrophages produces a switch of their phenotype that potentiates tumor cell invasion.

3.10. Pro-invasive candidate validation by cytokine array

Macrophage-derived Anti-Sema4D treated conditioned media demonstrated invasive properties upon tumor cells, which may indicate that the invasive effect would be mediated by a paracrine mechanism rather than by direct cell-cell contact (Figure 63). As previously explained, macrophages increased their migration, proliferation and became activated when Sema4D was blocked (Figure 55). Moreover, we found that their activation was also related to cytokine activity (Figure 57). Altogether, our findings indicate that the macrophage-derived Sema4D-related chemokine profile may have pro-invasive effects on tumor cells. In this context, identification of the pro-invasive molecules mediating tumor cell invasion was our next step.

In pursuance of identifying the pro-invasive molecule secreted by macrophages responsible for tumor cell invasion after Sema4D blockade, a mouse cytokine microarray was performed with anti-Sema4D treated, IgG treated and anti-

Sema4D added conditioned media from RAW cells. From all 94 cytokines included in the analysis (Annex 4), only one of them showed high statistical significance ($p<0.05$) when comparing anti-Sema4D and IgG treated samples: Stromal Derived Factor 1 (SDF1), also known as CXCL12. Together with CXCL12, we selected the two upregulated and the three downregulated cytokines with highest statistical significance (Figure 64).

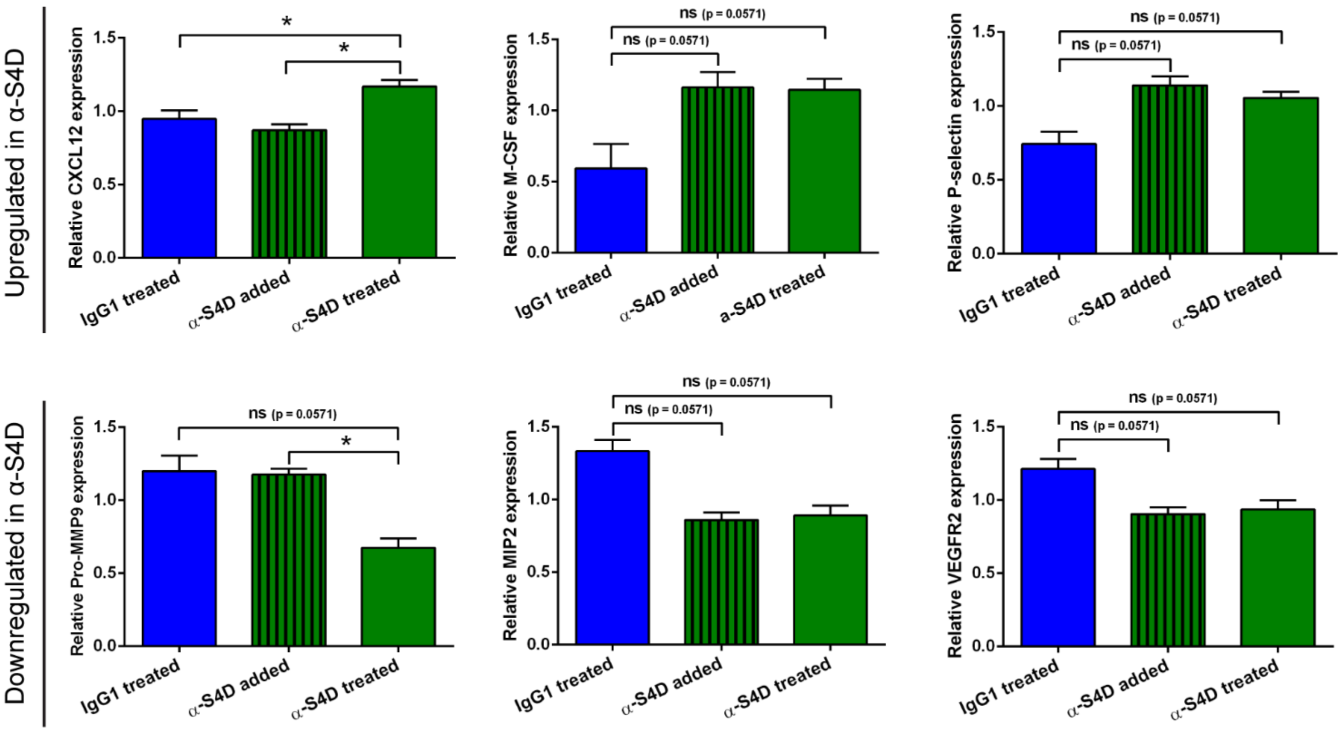

Figure 64 **Anti-Sema4D treatment alters macrophage derived secretome at the cytokine profile level.** Murine macrophage cytokine array analysis of IgG1 treated, anti-Sema4D (α-S4D) added and anti-Sema4D treated RAW conditioned media. Relative levels of the most significantly upregulated (CXCL12, M-CSF, P selectin) and downregulated (Pro-MMP9, MIP2, VEGFR2) proteins in anti-Sema4D treated samples. Relative expression to anti-Sema4D added condition. Four independent samples were analysed per group. $^*p < 0.05$ by Mann-Whitney test. Error bars indicate ± SEM.

Amongst the most upregulated cytokines in anti-Sema4D treated conditioned media, we found CXCL12, M-CSF and P-selectin. However, both M-CSF and P-selectin, even though they appear upregulated in anti-Sema4D treated conditions, showed an increased expression also in the anti-Sema4D added condition (Figure 64, **top**). This finding implies an unspecific effect of IgG1 addition, which is not related to the therapeutic action of anti-Sema4D on macrophages. The same applies for downregulated proteins after Sema4D blockade. Whereas MMP9 expression seems to be Sema4D treatment-specific, both MIP2 and VEGFR2 molecules are not (Figure 64, **bottom**). Overall, our data indicate that CXCL12 could be one of the pro-invasive molecules present in the macrophage conditioned media after anti-Sema4D treatment, while MMP9 could be acting as an inhibitor of invasion in our setting. In order to prove this hypothesis, we decided to validate the effect of both molecules in the RIP1-Tag2 model.

3.10.1. MMP9

The MMP protein family is composed of more than 20 metallopeptidases (Vandooren et al., 2013). The family includes gelatinases, collagenases, stromelysins, matrilysins and membrane type MMPs (MT-MMPs). MMP9, also known as gelatinase B for its catalytic activity, was first studied as a ECM remodeling enzyme involved in the degradation of mainly denatured collagens (gelatins) (Collier et al., 1988). Besides, MMP9 is able to convert cytokines and chemokines into active (pro-IL-1b, IL-8) or inactive (CTAP-III, PF-4) immune signals (Vandooren et al., 2013). Membrane-bound proteins or molecules at the extracellular compartment can also be processed by MMP9 (Cauwe et al., 2007). Similarly, cell-cell adhesion dependent permeability is regulated by MMP9, which is able to degrade occludins in tight junctions (Vandooren et al., 2013).

Surprisingly, there is a large assortment of intracellular proteins such as cytoskeletal components which can also be processed by MMP9 (Cauwe et al., 2009). Hence, MMP9 is considered a multi-domain enzyme with many functions, all converging in the modulation of motility. The gelatinase is produced by osteoblasts, fibroblasts, endothelial cells and a range of immune cells. Particularly, MMP9 expression has been found in macrophages *in vivo* and macrophage cell lines (such as RAW cell line), as thoroughly reviewed by Vandooren et al., 2013.

Overall, tumor-surrounding stromal cells are the major producers of tumor-related proteases in the tumor ecosystem (Overall and López-Otín, 2002; Stuelten et al., 2005). Commonly, MMPs are implicated in early stages of tumor progression, acting in ECM and basement-membrane degradation. In later stages, MMP expression has been related to metastasis promotion (Overall and López-Otín, 2002). Similar effects have been noted regarding the role of MMP9 inhibitor TIMP-1, which is described to elicit antimetastatic effects (Krüger et al., 1998). Surprisingly, paradoxical effects have been also described both for MMP9 and TIMP-1. While TIMP-1 was discovered as a factor that contributes to liver metastasis (Kopitz et al., 2007), knock-out or downregulation of MMP9 increased tumor progression and metastasis *in vivo* (Deryugina et al., 2005; Roy et al., 2007).

3.10.2. Sema4D treatment alters MMP9 expression pattern in RIP1-Tag2 tumor stroma

In contrast to profoundly established literature regarding MMP9, where its involvement in tumor progression is beyond discussion apart from counted exceptions, we observed a decrease in MMP9 expression in RAW conditioned media treated with anti-Sema4D. We decided to check MMP9 expression in RIP1-Tag2 tumors *in vivo*, performing an *in situ* zymography of gelatinase activity to detect MMP9 activity in both control and anti-Sema4D treated mice (Figure 65). In order to identify the origin of the observed MMP activity, we co-stained samples with F4/80 macrophage marker. In control tumors, all MMP activity was related to macrophage presence, suggesting that these cells are the main producers of MMPs in RIP1-Tag2 tumors. However, not all macrophages had MMP activity. Surprisingly, in anti-Sema4D treated tumors, MMP expression decreased and seemed to delocalize from macrophages.

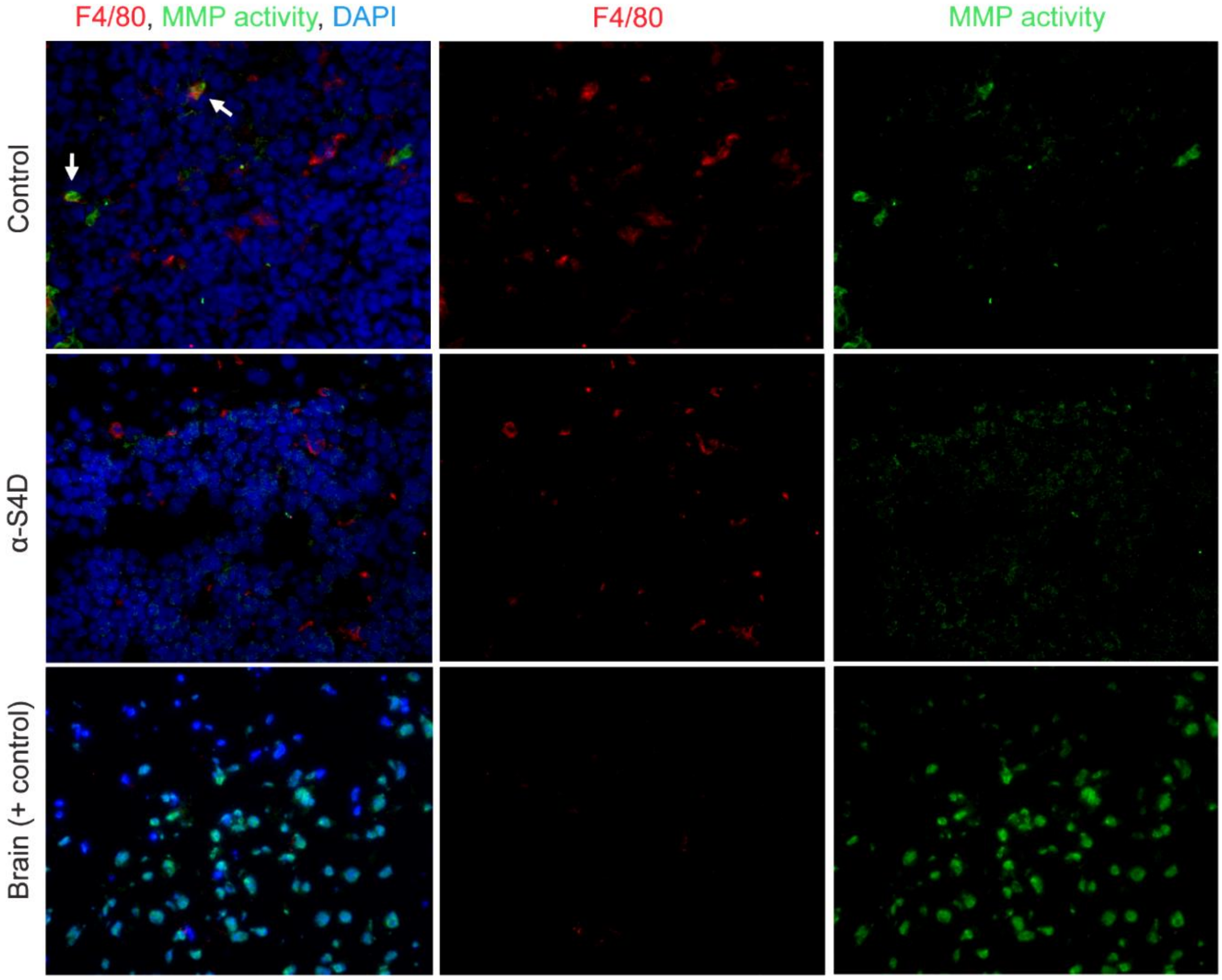

Figure 65 **Anti-Sema4D treatment decreases MMP activity. A)** Immunohistofluorescence analysis of MMP activity (in green) and F4/80+ macrophage (in red) localization in control and anti-Sema4D (α-S4D) treated RIP1-Tag2 tumors. Brain is used as a positive control for MMP activity. White arrows mark some macrophages with MMP activity. Representative fields from at least 10 tumors of three RIP1-Tag2 mice for each condition are shown. Images were taken at 40X magnification.

Results from both the cytokine array and the in situ zymography indicate that anti-Sema4D therapy alters MMP9 expression in macrophages. As explained in the Introduction section, anti-Sema4D treated tumors show a more invasive phenotype, which in RIP1-Tag2 tumors has been described to be collective rather than single-cell EMT like. Kumar and colleagues have described a model which predicts that collective cell invasion requires lesser ECM degradation when compared to individual cells (Kumar et al., 2016). This fact suggests that collective cell invasion could be more efficient than single cell invasion, since lesser expression of MMPs was needed. In fact, inhibition of MMP production causes a transition to collective cell invasion (Haeger et al., 2014). We checked the invasion pattern in control and anti-Sema4D treated tumors with haematoxylin-eosin stained samples, and validated that the treatment does not alter the collective-cell invasion phenotype (Figure 66).

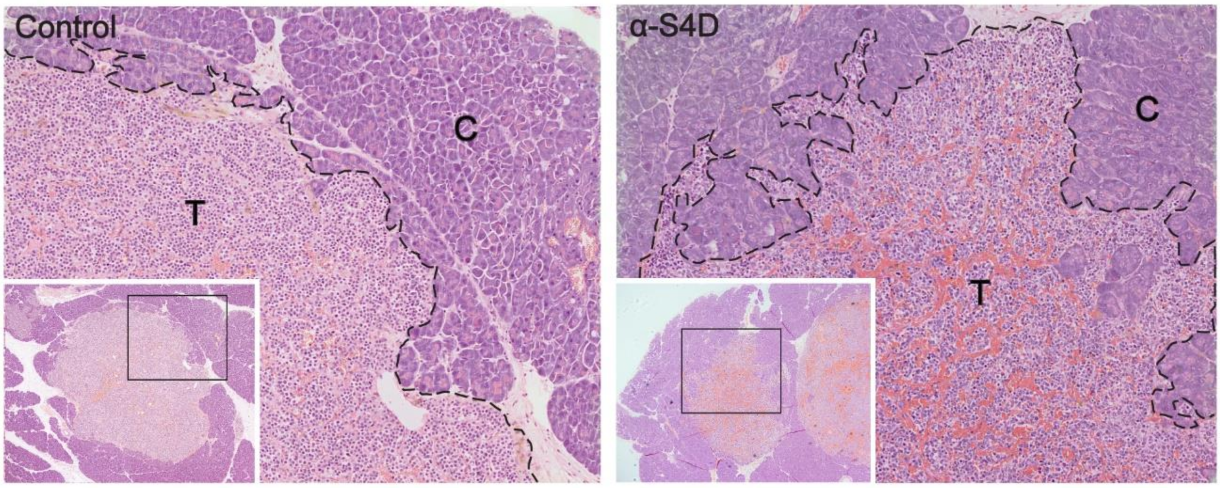

Figure 66 **Anti-Sema4D treated tumors maintain collective invasion phenotype.** Haematoxylin-Eosin staining of control and anti-Sema4D (α-S4D) treated RIP1-Tag2 tumors. Tumor fronts are marked with a dotted black line. T: tumor; C: Acinar tissue. Representative fields from at least 40 tumors of three TIP1-Tag2 mice for each condition are shown. Images were taken at 10X magnification. A 4X magnification of the whole tumor is shown on the bottom left.

Interestingly, TIMP1, the MMP9 inhibitor, is one of the cytokines that appears to be augmented in the cytokine array assay of RAW conditioned media (Annex 4). Nevertheless, while the fold-change between anti-Sema4D treated and IgG treated conditioned media corresponded to top differences (0.4033), its statistical significant was quite poor (p. value = 0.4). Overall, our results regarding MMP9 and TIMP1 expression in RIP1-Tag2 mice after anti-Sema4D treatment could fit inside the paradoxical effects of these molecules and related to collective cell invasion.

3.10.3. CXCL12

CXCL12 chemokine, also known as SDF1, is a low molecular weight protein that structurally belongs to the CXC family. The CXC family members differ from CC chemokines in that they have an aminoacid in between their conserved NH_2-

terminal cysteine residues (Zlotnik and Yoshie, 2012). Functionally, CXCL12 is a homeostatic chemokine, initially discovered as a key factor for lymphopoiesis and embryogenesis (Nagasawa et al., 1996). Eventually, it was found to be expressed constitutively by bone marrow stromal cells, for which it was named stromal derived factor 1 (SDF1) (Bleul et al., 1996). CXCL12 is involved in the retention of hematopoietic progenitor and stem cells in the stroma (Kim and Broxmeyer, 1998).

The biological function of CXCL12 is fulfilled by activating a seven-transmembrane domain G protein-coupled receptor (GPCRs), known as CXCR4 (Bachelerie et al., 2014). Contrary to most promiscuous receptors for inflammatory chemokines, CXCR4 only has CXCL12 as a ligand. However, other non-chemokine ligands can also bind and induce signal transduction via CXCR4, such as the macrophage Migration Inhibitory Factor (MIF) (Janssens et al., 2018). The importance of CXCR4 is further highlighted by the discovery of increasing numbers of cell types expressing it, including most leukocyte subsets, circulating hematopoietic progenitor and stem cells, lymphoid-derived cells and some endothelial, stromal and epithelial cells (Pawig et al., 2015). This allows them to migrate along CXCL12 gradients.

CXCL12 binding to CXCR4 induces G protein-coupled signal transduction, following with the activation of many diverse signaling cascades such as MAPK, phospholipase C and PI3K pathways (Janssens et al., 2018) (Figure 67). As a result, the activation of CXCR4 ends up contributing to tumor angiogenesis, tumor cell survival, proliferation, chemoresistance, cellular migration and activation of adhesion molecules (Teixidó et al., 2018). CXCL12/CXCR4 levels have been described to be increased in many types of cancer, such as breast, pancreas, ovary, cervical and leukemia (Meng et al., 2018; Teixidó et al., 2018).

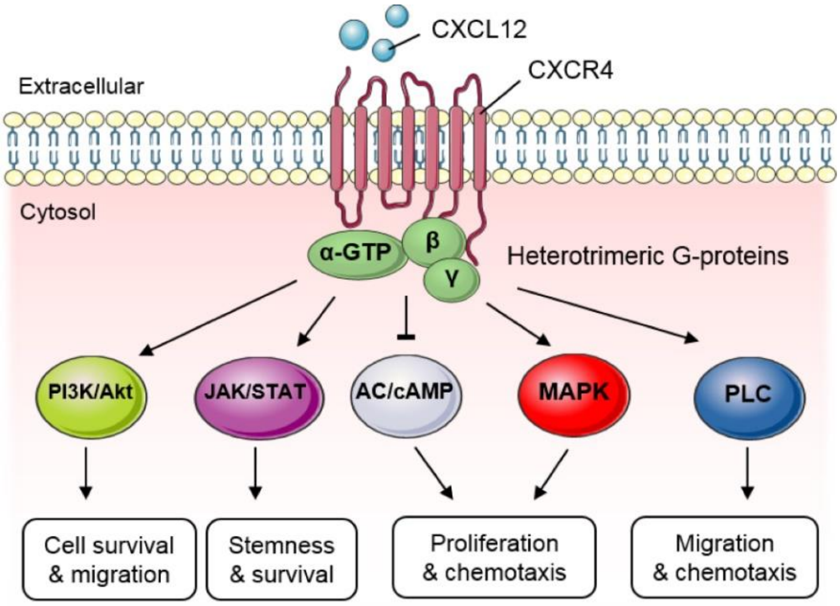

Figure 67 **Signaling pathways promoted by the CXCL12/CXCR4 axis.** Upon CXCL12 binding to the 7TM receptor CXCR4, GTP-Gα and the Gβγ-dimer activate several different downstream signaling pathways including PI3K-Akt, JAK-STAT, MAPK and PLC, while blocking AC and cAMP production. Together, activation of these pathways leads to cell migration, proliferation, survival and gene expression. Adapted from Teixidó et al., 2018.

For many years, it was believed that CXCR4 was the only receptor for CXCL12, until CXCR7/Ackr3 was firstly described by Balabanian and collegues as the orphan RDC-1 chemokine receptor and shortly after redefined in CXCR4 knock-out mice (Balabanian et al., 2005; Burns et al., 2006). Binding of CXCL12 to CXCR7 occurs with a 10-fold higher affinity than that for CXCR4 (Balabanian et al., 2005). Membrane-associated CXCR7 is expressed in many tumor cell lines, activated endothelial cells, fetal liver cells and T lymphocytes (Balabanian et al., 2005; Pawig et al., 2015) (Figure 68). Studies have shown that CXCR7 could reduce tumor cell apoptosis, promote proliferation and tumor angiogenesis (Burns et al., 2006; Wang et al., 2008). Moreover, a role for CXCR7 in metastasis and tumor invasion has been also described, where it regulated the levels of cell adhesion molecules (EN1, CDH11 and CD44) and MMPs (Wang et al., 2008). In addition to its signaling properties, CXCR7 primarily acts as a scavenger receptor that removes CXCL12 from the environment (Boldajipour et al., 2008). Together with its high affinity towards CXCL12, the sequestering is achieved by the continuous internalization and recycling of CXCR7.

Regarding the effects of CXCL12 over cell adhesion promotion, it is able to regulate adhesion of tumor cells with laminin, fibrinogen, stromal cells and endothelial cells by activating surface adhesion molecules such as integrins (Meng et al., 2018) (Figure 68). For instance, it has been shown that CXCL12 increases the adhesion rate of pancreatic cancer cells to laminin, one of the main components of the basement membrane, thus enhancing their ability to penetrate the extracellular matrix (Mori et al., 2004). Engl and colleagues described that CXCL12 increases integrin a5β3 expression in the tumor cell membrane, which enhanced adhesion of prostate tumor cells to human endothelia and ECM components (Engl et al., 2006).

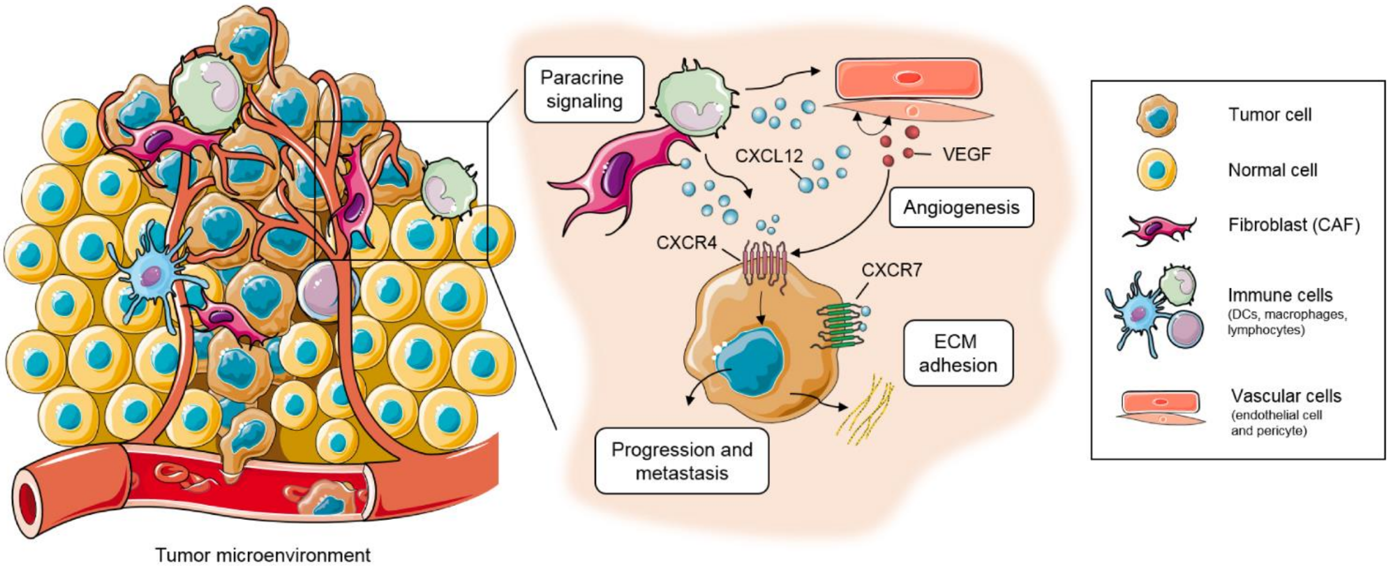

Figure 68 **CXCL12/CXCR4 signaling axis plays a critical role in tumor growth, progression and metastasis.** In the tumor microenvironment, cancer-associated fibroblasts (CAFs) and immune cells express CXCL12. Paracrine signaling in tumor cells via CXCR4 enhances proliferation and survival of tumor cells. CXCL12 also increases tumor cell adhesion to the ECM, contributing to their migration. Stromal derived CXCL12 is able to induce VEGF expression, which in an autocrine loop increases CXCL12 expression by vascular cells. VEGF is also able to promote tumor angiogenesis and CXCR4 expression in tumor cells.

CXCL12 can stimulate tumor angiogenesis in a direct or indirect fashion (Meng et al., 2018) (Figure 68). As an example, CXCL12 is able to induce endothelial cell-derived VEGF expression, while VEGF, in turn, can promote CXCL12 expression in vascular endothelial cells (Salvucci et al., 2002). Besides, VEGF can also induce expression of CXCR4 in tumor cells in a paracrine fashion, thereby promoting cancer cell migration. Regarding metastasis, CXCL12 increases expression and activity of different metalloproteinases such as MMP2, improving migration of nerve cells (Mao et al., 2016). In colorectal cancer, CXCR4 was highly expressed in tumor cells from patients with liver metastases, whereas high expression of CXCL12 was found in the most common sits for metastasis (e.g. lymph nodes, liver and lung) (Kim et al., 2006) (Figure 68). Additionally, down-regulation of CXCR4 expression or the use of neutralizing antibodies or specific peptides that block CXCL12/CXCR4 pathway activation significantly inhibited metastasis in prostate and breast cancer (Skobe et al., 2001; Sun et al., 2004).

In the tumor ecosystem, binding of immune cell- or fibroblast-derived CXCL12 to CXCR4 induces proliferation of various types of tumor cells by ERK and AKT activation in a paracrine loop (Meng et al., 2018) (Figure 68). While ERK regulates gene expression and cell cycle progression, AKT improves tumor cell survival through inactivation of BCL-2 antagonist, GSK3β, and the stabilization of β-catenin (Figure). The stabilized β-catenin moves to the nucleus to promote proliferation (Barbero et al., 2003). Sustained inhibition of cyclic AMP (cAMP) production has been also described, highlighting the role of CXCL12 in cell proliferation (Yang et al., 2007) (Figure).

To date, several molecular strategies have been developed to target CXCL12 and CXCR4 with the aim of interfering with tumor growth (reviewed in Meng et al., 2018). One of the most promising drugs is Plerixafor/Mozofil (AMD3100), a CXCR4 small molecule inhibitor that mobilizes hematopoietic stems cells while competitively blocks CXCL12 binding to CXCR4. AMD3100 inhibited the establishment of prostate tumors in the bone (Conley-LaComb et al., 2016), reduced growth of ovarian cancer cells and modestly improved the survival rates of mice with metastatic ovarian cancer (Ray et al., 2011). Furthermore, it also undermined the tumor-stroma interaction, inhibited leukemic cell adhesion and weakened tumor cell migration ability to the bone marrow. The most relevant clinical trials using AMD3100 as an effective anti-CXCL12/CXCR4 signaling drug are summarized in Table 21.

Table 21 **Effective clinical targeting of CXCL12/CXCR4 with AMD3100 specific small molecule.** Adapted from Meng et al., 2018.

Indication/Condition	Function	Trial number
Glioma, Anaplastic Astrocytoma, Anaplastic Oligodendroglioma, Mixed anaplastic Oligoastrocytoma	HSC mobilization in patients with NH1 and multiple myeloma	NCT01339039
Acute Myeloid Leukemia (AML)	Mobilization of Leukemic Cells	NCT01141543
Chronic lymphocytic leukemia	Mobilization of Leukemic Cells	NCT01373229
Hematologic Neoplasms	Mobilization and Transplantation of HLA-matched Sibling Donor Hematopoietic Stem Cells	NCT00914849
Chronic Lymphocytic Leukemia (CLL); Small Lymphocytic Lymphoma (SLL)	Make CLL/SLL cells more sensitive to being killed by rituximab	NCT00694590
Acute Myeloid Leukemia (AML)	Disrupting the interaction between AML blasts and the marrow microenvironment	NCT00512252
Myelokathexis (WHIM syndrome)	Mobilizing hematopoietic stem cells	NCT0967785
Multiple Myeloma, Lymphoma, Non-Hodgkin Lymphoma	Stem cell mobilization	NCT02098109
Lymphoma	Mobilization and Collection of Peripheral Hematopoietic Stem Cells	NCT02221492
Ewing sarcoma, Neuroblastoma, Brain Tumors	Mobilization of Hematopoietic Stem Cells into Peripheral Blood	NCT01288573
Multiple Myeloma	Mobilize Peripheral Blood Progenitor Cells	NCT00396383
Healthy volunteers	Peripheral Blood Hematopoietic Progenitor Cell Mobilization with G-CSF	NCT00082329
Chronick Lymphocytic Leukemia, Lymphoma, Multiple Myeloma	Interrupting communication between stromal cell and cancer	NCT01610999

3.10.4. βTC4 cells respond to CXCL12/CXCR4 signaling activation and inhibition

Based on the literature, we wanted to validate if the increase of CXCL12 could be responsible for tumor cell invasion in the RIP1-Tag2 model. First, we checked whether βTC4 cells alone were able to respond to CXCL12 by a Matrigel® transwell invasion assay. As expected, βTC4 cells responded to recombinant SDF1 stimulation in vitro by increasing their invasion (Figure 69). This phenomenon was countered when CXCR4 receptor was blocked by its antagonist AMD3100. The inhibitor alone did not produce a significant reduction in the invasion of βTC4 cells.

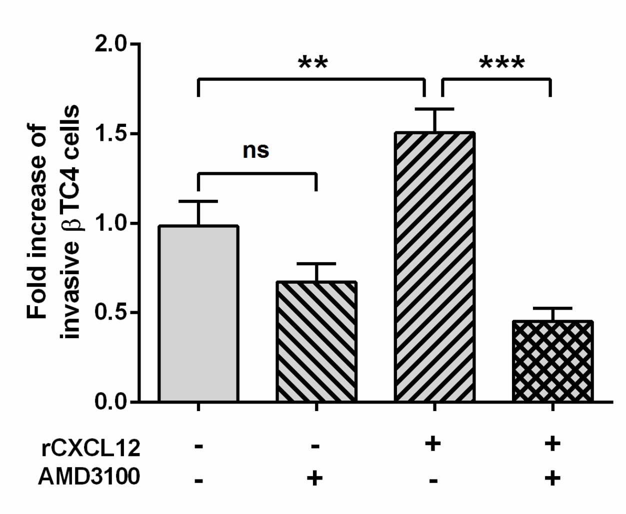

Figure 69 **βTC4 tumor cells respond to CXCL12 stimulation or inhibition by changing their invasive capacity.** Fold increase of the number of invasive βTC4 cells per field of a transwell invasion assay in presence of recombinant CXCL12 (rCXCL12), its CXCR4 receptor inhibitor (AMD3100) or both. Control untreated βTC4 condition was used for normalization. At least 20 fields at 20X magnification were analyzed for each condition of three independent experiments. **p < 0.01 and ***p < 0.001 by Mann-Whitney test. Error bars indicate ± SEM.

3.10.5. βTC4 cells increase their invasion in response to SDF1 CM

Once the ability of βTC4 cells to respond to CXCL12/CXCR4 pathway activation or inhibition was ascertained, we checked whether such effect was reproduced in the macrophage-tumor cell setting. In this line, we performed another Matrigel® transwell invasion assay, this time placing untreated, IgG1 and anti-Sema4D treated macrophage conditioned media as a chemoattractant (Figure 70). The increase in βTC4 cell invasion after Sema4D treatment was comparable to the increase produced when CXCL12 was added to IgG1 treated control condition. Indeed, the addition of recombinant CXCL12 to anti-Sema4D treated conditioned media did not further increase the invasive capacity of βTC4 cells. Contrarily, when AMD3100 inhibitor was added to anti-Sema4D treated conditioned media, the invasive capability of βTC4 cells dropped to basal levels, confirming that CXCL12 is one of the factors secreted by macrophages after Sema4D blockade responsible for tumor cell invasion.

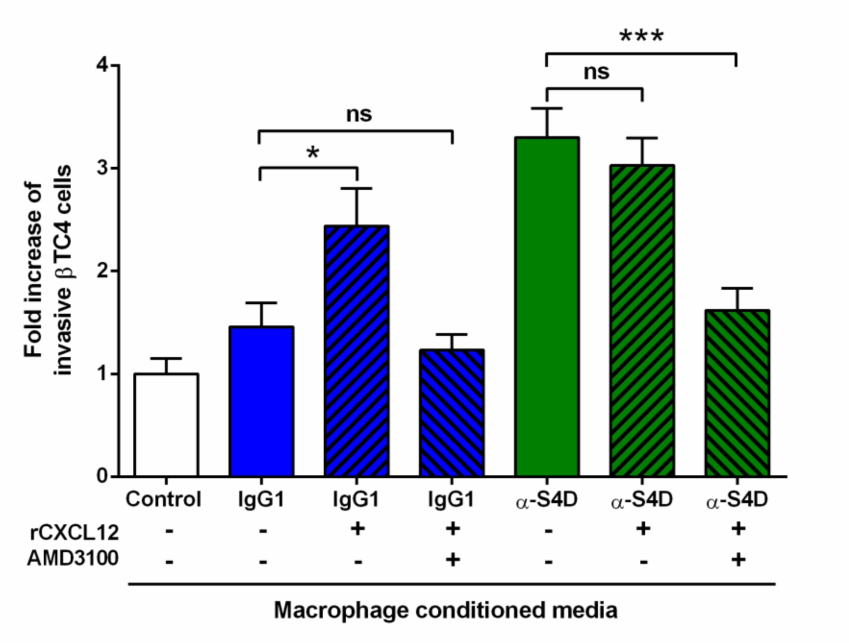

Figure 70 **βTC4 tumor cells treated with macrophage derived conditioned media respond to CXCL12 stimulation or inhibition by changing their invasive capacity.** Fold increase of the number of invasive βTC4 cells per field of a transwell invasion assay in presence of untreated, IgG1 treated or anti-Sema4D α-S4D treated RAW conditioned media, together with recombinant CXCL12 (rCXCL12), its CXCR4 receptor inhibitor (AMD3100) or both. Control untreated βTC4 condition was used for normalization. At least 20 fields at 20X magnification were analysed for each condition of three independent experiments *p < 0.05 and ***p < 0.001 by Mann-Whitney test. Error bars indicate ± SEM.

3.10.6. SDF1/CXCR4 signaling axis members are expressed in RIP1-Tag2 tumors

After proving in the *in vitro* setting that CXCL12 acted as a pro-invasive molecule, we sought to check whether in the RIP1-Tag2 model the CXCL12/CXCR4 signaling axis was active and affected by anti-Sema4D treatment. First, we found an upward trend of both *Cxcl12* and *Cxcr4* gene expression levels in anti-Sema4D treated tumors (Figure 71).

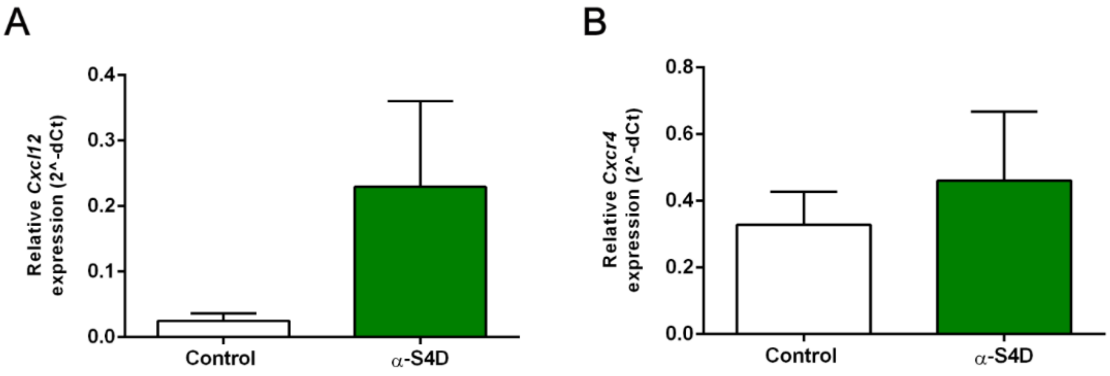

Figure 71 **Anti-Sema4D treatment increases CXCL12 and CXCR4 expression at the transcriptional level.** qRT-PCR analysis of **A)** *Cxcl12* and **B)** *Cxcr4* genes in control and anti-Sema4D (α-S4D) treated RIP1-Tag2 tumors. Relative expression to *Hprt1* gene. At least 5 tumors were analyzed per group. No significant difference is found by Mann-Whitney test. Error bars indicate ± SD.

In order to localize the expression of CXCL12 and CXCR4 in the tumor stroma of the RIP1-Tag2 mice, we performed an immunohistochemistry assay for each molecule in control and anti-Sema4D treated tumor samples (Figure 72). Whereas we found nearly no expression of CXCL12 in control samples, some scattered cells in the tumor stroma of anti-Sema4D treated samples showed strong CXCL12 expression in their membranes and cytoplasms (Figure 72A, left panel). The phenotype of these cells resembled that of immune cell infiltrates, compatible with tumor-associated macrophages. Moreover, a quantification of those CXCL12 expressing cells showed an increase of nearly the 60% in their number after anti-Sema4D therapy (Figure 72A, right panel).

With regard to CXCR4 receptor, it appeared to be homogeneously expressed by RIP1-Tag2 tumor cells, while being mainly absent in control samples and highly present in anti-Sema4D treated mice (Figure 72B, left panel). In fact, a quantification of the incidence of CXCR4 expressing tumors revealed a positive correlation between CXCR4 expression intensity and treatment (Figure 72B, right panel). A deeper analysis correlating CXCL12 levels and invasive capacity of the tumor front revealed a relationship between the invasive ability and ligand concentration in control tumors (Figure 72C). This relationship was slightly lost after anti-Sema4D treatment. Altogether, the *in vivo* results may suggest a tumor cell-independent origin of CXCL12 that could bind to its CXCR4 receptor in RIP1-Tag2 tumors.

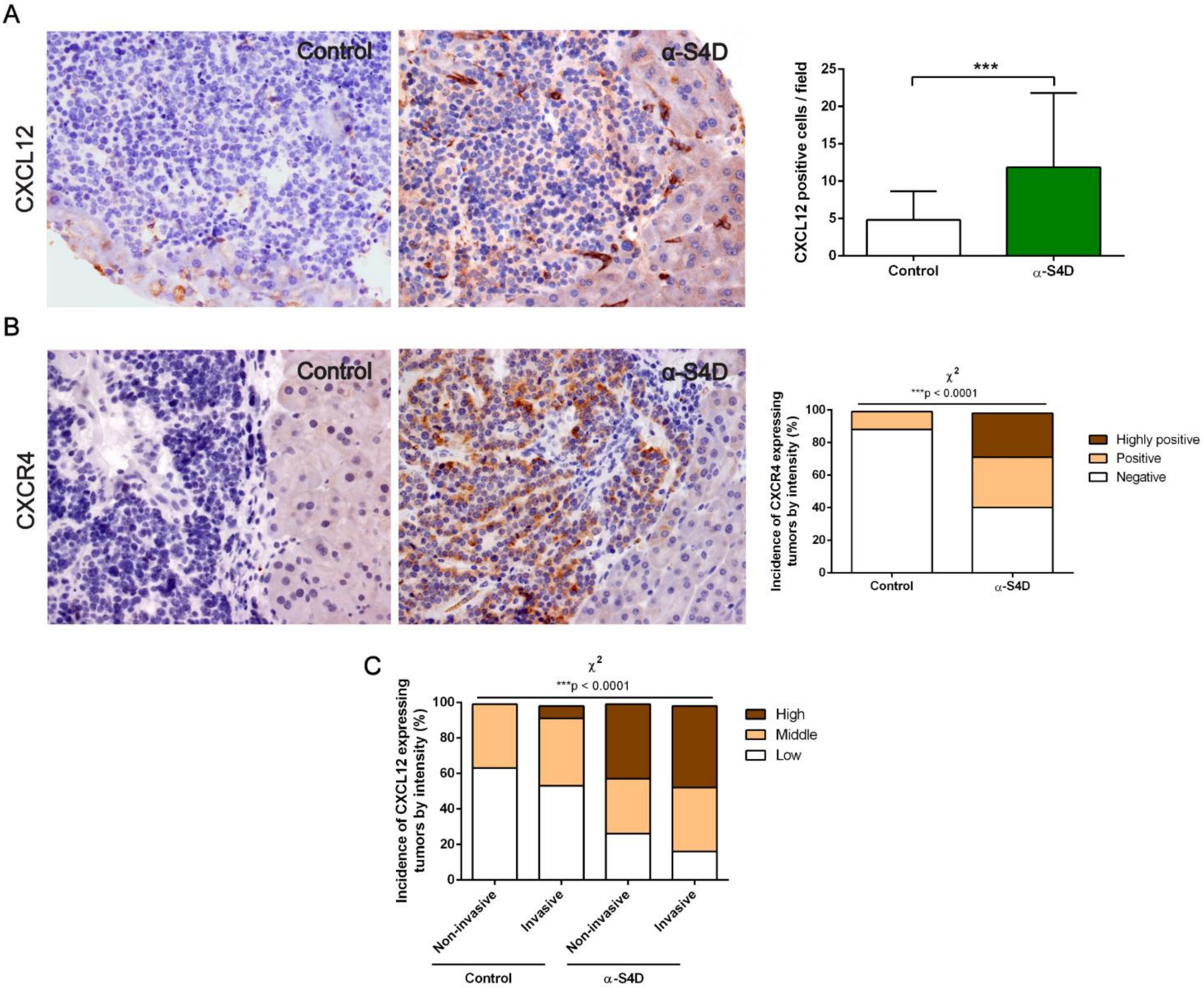

Figure 72 **Anti-Sema4D treatment increases the number of CXCL12 positive stromal cells and CXCR4 tumor expression. A) Left:** Immunohistochemistry analysis of tumor stromal SDF1 expression (in brown) in control and anti-Sema4D (α-S4D) treated RIP1-Tag2 tumors. Representative fields from at least 40 tumors from three RIP1-Tag2 mice for each condition are shown. Images were taken at 40X magnification. **Right:** Quantification of the number of round CXCL12 positive intratumoral cells per tumor field for each condition. CXCL12 positive cells in the surrounding pancreatic normal tissue were excluded from the analysis. Mann-Whitney test. Error bars indicate ± SD. **B) Left:** Immunohistochemistry analysis of CXCR4 expression (in brown) in control and anti-Sema4D (α-S4D) treated RIP1-Tag2 tumors. Representative fields from at least 17 tumors of three RIP1-Tag2 mice for each condition are shown. Images were taken at 40X magnification. **Right:** Quantification of the incidence of CXCR4 expressing tumors classified according to their expression intensity in highly positive, positive or negative. Chi-square test. **C)** Quantification of the incidence of CXCL12 expressing tumors regarding their intensity and invasive capacity per tumor determined at 20X. CXCL12 expression was determined according to the

CXCL12 positive cell count in panel **A left** as low (0-4.99 positive cells), middle (5-9.99 positive cells) or high (10-32 positive cells). Chi-square test. ***$p < 0.001$.

Overall, our results have demonstrated both *in vitro* and *in vivo* the functional implication of macrophages in establishing the malignization process as a consequence of anti-Sema4D therapy in RIP1-Tag2 PanNET mouse model.

4. Clinical relevance of Sema4D and SDF1/CXCR4

4.1. Expression of Sema4D, SDF1 and CXCR4 in patient samples

After demonstrating both *in vitro* and *in vivo* the role of Sema4D and CXCL12/CXCR4 signaling axis in tumor malignization of the RIP1Tag2 mouse model, we sought to decipher whether these same mechanisms could be also playing their part in the clinical setting. Given that there are no available anti-Sema4D treated patient samples, we performed a detailed analysis of an independent gene expression study of a set of mRNA transcriptomes of PanNET patients (GSE73338). As described previously, the patient dataset contains 97 samples of a PanNET study containing normal pancreas, normal pancreas islets, primary non-functional tumors, primary functional tumors, a gastrinoma and metastases (Missiaglia et al., 2009; Sadanandam et al., 2015).

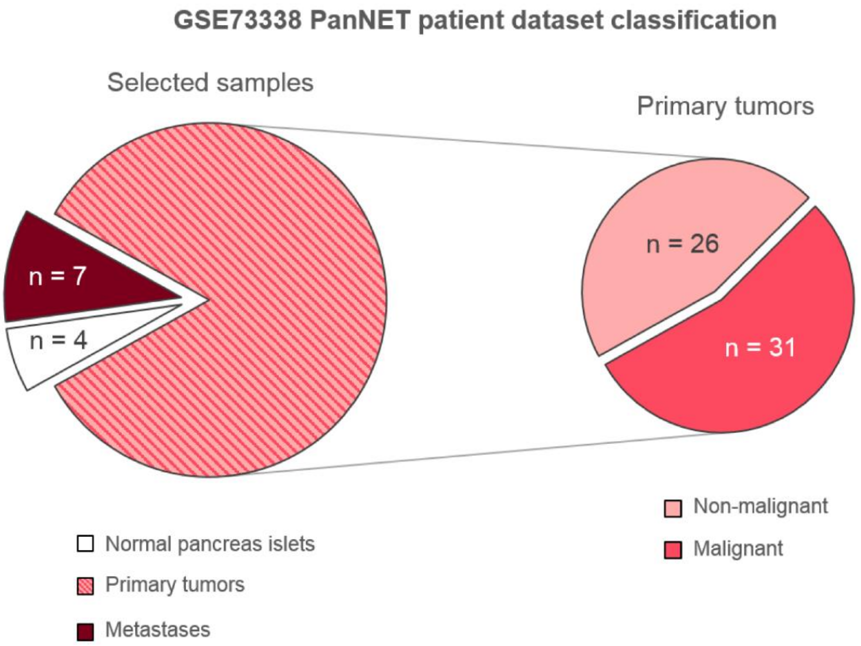

Figure 73 **PanNET patient dataset description.** Graphical description of the GSE73338 PanNET patient dataset as described in Missiaglia et al., 2010. Selected samples for analysis comprised for 57 primary tumors (further divided into 26 non-

malignant and 31 malignant samples), 4 normal pancreas islets and 7 metastases associated to 6 of the primary tumors.

Considering that we sought to extrapolate the data obtained in RIP1-Tag2 mice, we chose to analyze only data from primary non-functional tumors. Even though primary non-functional tumors do not secrete insulin as RIP1-Tag2 mice tumors do, they are classified according to the WHO as high-grade tumors. High grade tumors are characterized as more aggressive and proliferative tumors, which happen to be more similar to RIP1-Tag2 mice tumors. Thus, we performed all our clinical analysis with data from 57 non-functional primary tumors, from which 31 had synchronic metastasis and were termed as malignant (Figure 73). From 6 out of those 31 patients, we had 7 samples of metastases. The remaining 26 non-functional primary tumor patients did not have metastasis at the time of sample extraction and were classified as non-malignant. We took normal pancreas islet samples as control for healthy donors.

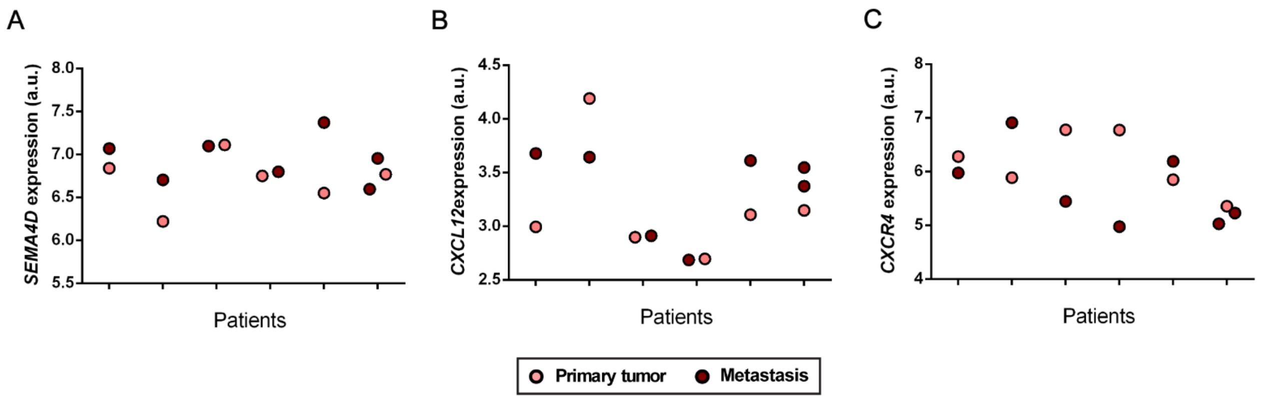

Figure 74 **Paired analysis of Sema4D, CXCL12 and CXCR4 expression in PanNET patients and their associated metastases.** Analysis of RNA expression of Sema4D **(A)**, CXCL12 **(B)** and CXCR4 **(C)** according to sample classification. No significant differences are found by Wilcoxon paired t test. Data was obtained from GSE73338 as described in Missiaglia et al., 2010.

Since we had data from 6 of the primary tumor patients with their 7 associated metastases, we first decided to check the expression of Sema4D, CXCL12 and CXCR4 in those patients. With that aim, we performed three independent paired analyses (Figure 74). Due to the limited cohort size (n=6), there were no observable differences among the expression of any of the proteins in this setting. We decided to perform this same analysis with all selected samples in an unpaired fashion (Figure 75).

Regarding Sema4D, we found its expression to be significantly increased in metastatic samples when compared to either primary non-malignant and malignant tumors or normal pancreatic controls (Figure 75A). Accordingly, in PanNET patients, Sema4D may be important not for the malignization process, but for the dissemination of the primary tumor for metastasizing. Besides, whereas SDF1 expression remained practically unaltered, we found a significant increase in CXCR4 receptor expression between normal and both primary tumor subtypes and metastases (Figure 75B-C). In fact, there is a gradual increase of CXCR4 that correlates with malignization, thus hinting a role for this protein as a tumor progression driver.

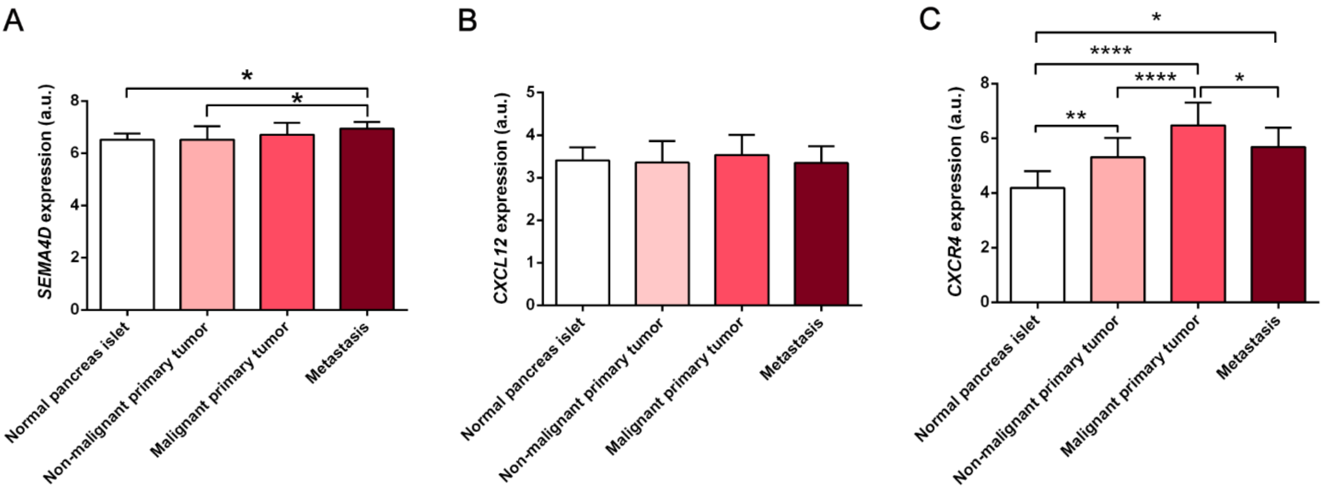

Figure 75 **Sema4D and CXCR4 are involved in malignization and metastasis processes in PanNET patients.** Analysis of RNA expression of Sema4D **(A)**, CXCL12 **(B)** and CXCR4 **(C)** according to sample classification. *p < 0.05, p<0.01 and ***p < 0.001 by Mann-Whitney test. Error bars indicate ± SD. Data was obtained from GSE73338 as described in Missiaglia et al., 2010.

A deep analysis of tumor progression related parameters such as tumor grade, malignancy and Ki67 percentage of each tumor, as detailed by Missiaglia et al. also supported our previous findings (Table 22) (Missiaglia et al., 2009). CXCR4 was strongly correlated to Ki67, which is a marker of proliferation and malignancy.

Interestingly, neither Sema4D nor CXCL12 correlated with any of the parameters. These could be suggestive of their stromal origin in PanNETs. In summary, our analysis from PanNET patients validates the results we have previously obtained *in vivo* and *in vitro*, using the RIP1-Tag2 mouse model of PanNET. In the absence of anti-Sema4D treated patients, our results demonstrate that both Sema4D and CXCR4 signaling axes could be involved in malignization and tumor progression in this type of tumors.

Table 22 **CXCR4 is involved in malignization and/or proliferation processes of PanNET patients.** Metrics analysis of grade, malignancy and Ki67 percentatge of Sema4D, CXCL12, PlexinB1, CD72 and CXCR4 by in selected PanNET patient samples. p. values of ANNOVA analysis are shown for each condition. Statistically significant metrics are depicted in red. Data was obtained from GSE73338 as described in Missiaglia et al., 2010.

	SEMA4D	*CXCL12*	*CXCR4*
Grade	0.2162	0.8440	0.4879
Malignancy	0.6920	0.5053	0.0082
Ki67 percentage	0.9663	0.2656	0.0000

4.2. Multiple Cell Population-counter analysis of Sema4D

In order to deepen into the origin of Sema4D in PanNET patients, a bioinformatic approach that included the estimation of stromal and immune cells from whole tumor data was carried out. For that, the Multiple Cell Population-counter (MCP) method was applied as previously described (Becht et al., 2016). This method relies on the differential expression of a group of genes allowing to discriminate between different stromal cell populations, including: CD8 T cells, endothelial cells, myeloid dendritic cells, neutrophils, cytotoxic lymphocytes, T cells, B lineage, NK cells, fibroblasts and monocytic lineage (e.g. macrophages) (Annex 5). By analyzing the expression of each group of genes in a complex sample such as a tumor, we can infer the contribution or quantity of that stromal cell population to the whole sample.

Therefore, we checked the expression pattern of each stromal cell population in each primary tumor and metastasis sample, together with their Sema4D expression. In collaboration with Luis Palomero (Procure, ICO-IDIBELL, L'Hospitalet), we created an unsupervised heatmap with this information (Figure 76). Strikingly, Sema4D expression mostly aligned to the monocytic lineage pattern in PanNET patients, which was in accordance with our results in RIP1-Tag2 mice. Next, Sema4D expression correlated to fibroblast presence. Weaker correlations were found between Sema4D and endothelial and CD8 T cells.

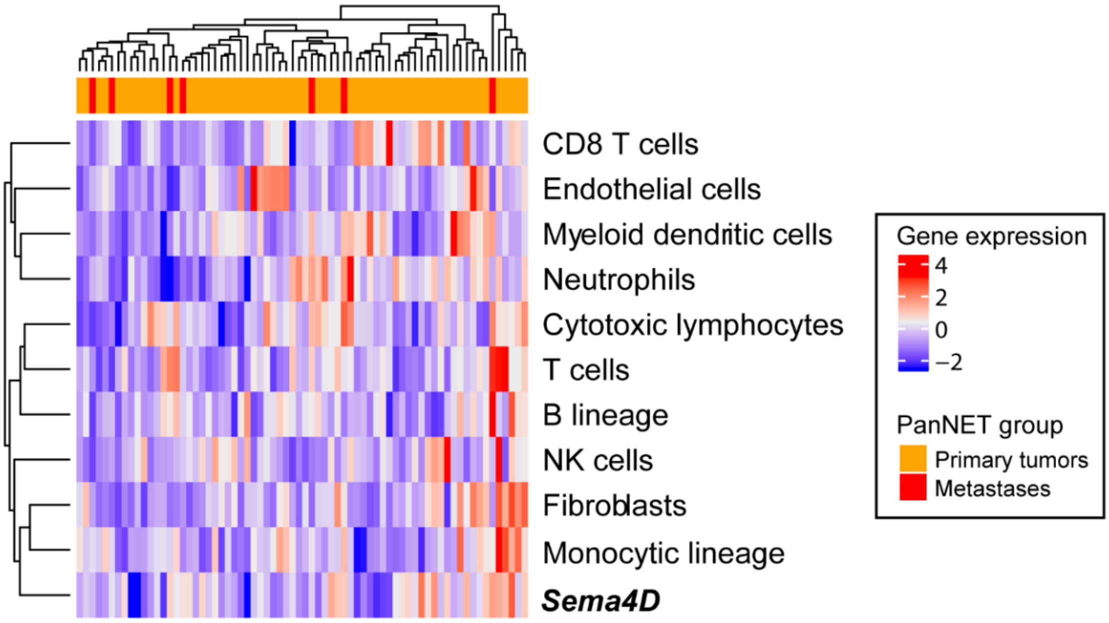

Figure 76 **High Sema4D expression is related to monocyte and fibroblast enriched tumors in PanNET patient.** Unsupervised heatmap of Sema4D expression compared to stromal and immune cell-specific gene set expression obtained by MCP method (Becht et al., 2016) in selected PanNET primary tumors and metastases. Data was obtained from GSE73338 as described in Missiaglia et al., 2010.

We repeated the MCP analysis with Sema4D and its receptors CD72 and PlexinB1, together with CXCL12 and its receptor CXCR4. In this case, we constructed a dot-plot to better visualize the correlation and the statistical significance between protein expression and the stromal cell composition (Figure 77). In this case, surprisingly, Sema4D expression strongly correlated with fibroblast markers. Since RIP1-Tag2 mice are depleted in intratumoral fibroblasts, the murine model fails to completely mimic the clinical setting. However, once again it reveals that Sema4D expression of primary and metastases samples is mostly associated to monocyte markers, validating our results in RIP1-Tag2 mice. Contrary to what it was expected, PlexinB1 was only found to be slightly expressed by some immune cells such as NK cells and CD8 T cells. We expected PlexinB1 to be expressed in endothelial cells. The low affinity receptor, CD72, as expected, was found highly expressed in immune cells. Similar results were obtained with CXCR4, which was expressed by most immune cells, fibroblasts and endothelial cells, as previously reported. Finally, CXCL12 was slightly expressed by monocytes and highly by fibroblasts, as reviewed in the literature.

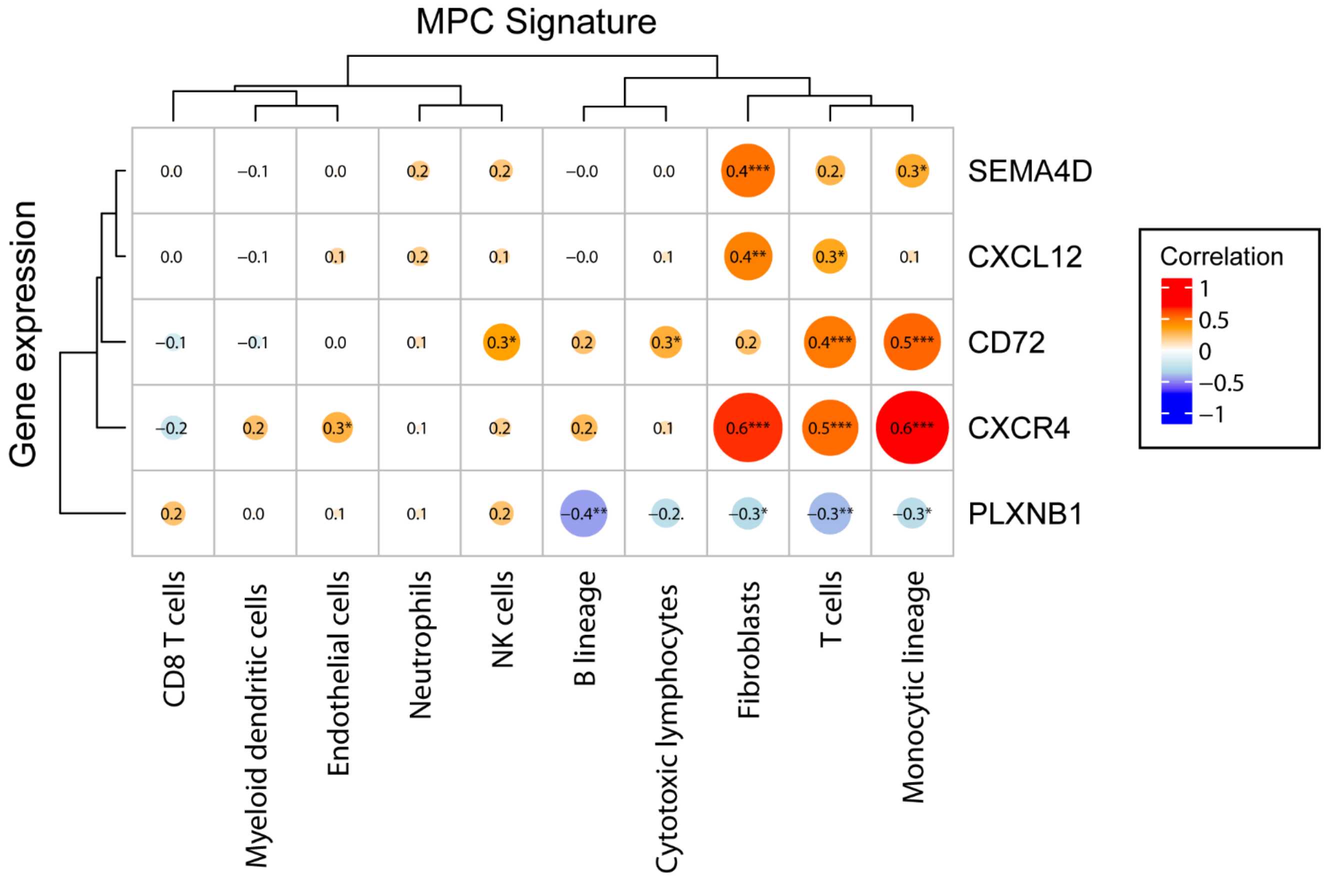

Figure 77 **CXCR4 and CD72 expression is strongly related to the stromal component of PanNET tumors, whereas PlexinB1, CXCL2 and Sema4D expression are not stroma-exclusive.** Dotplot representation of the correlation of CXCR4, CD72, Sema4D, CXCL12 and PlexinB1 expression compared to stromal and immune cell-specific gene set expression obtained by MCP method (Becht et al., 2016), together with PanNET tumor cell specific signature (Carr et al., 2012) in selected PanNET primary tumors and metastases. Pearson

correlation is depicted for each condition. *$p<0.05$, **$p<0.01$ and ***$p < 0.001$. Data was obtained from GSE73338 as described in Missiaglia et al., 2010.

Overall, we have found that TAMs, after anti-Sema4D treatment, increase their migration, become activated and, consequently, secrete chemokines. We successfully identified CXCL12 as one of the main chemoattractant molecules responsible for the increased invasive properties of βTC4 cells *in vitro* and demonstrated its presence *in vivo*, in the RIP1-Tag2 mouse model of PanNETs. Importantly, we have also validated the putative role of Sema4D and CXCR4 signaling axes in malignization and tumor progression events in PanNET patients.

Discussion

Science is the acceptance of what works
and the rejection of what does not.
That needs more courage than we may think.

Jacob Bronowski

1. Anti-Sema4D acts as a double-edged sword in RIP1-Tag2 tumor progression

Tumor development is a complex event that involves not only tumor cells, but also the surrounding stroma. In recent years, data collected from both experimental and clinical observations have reinforced the idea that neoplastic cells and the tumor microenvironment act in concert, contributing as a functional whole to the growth and progression of the tumor (Albini and Sporn, 2007; Quail and Joyce, 2013). Reckoning with the natural dependency of tumors on angiogenesis, its therapeutic targeting remains a valid microenvironment-directed strategy in the fight against cancer (Jain, 2014; Scarpa et al., 2017; Viallard and Larrivée, 2017). Nevertheless, antiangiogenics directed towards canonical proangiogenic molecules such as VEGF do not produce enduring beneficial effects due to the appearance of intratumor hypoxia (Casanovas et al., 2005; Pàez-Ribes et al., 2009). Focusing on NETs, characterized by their aggressiveness, high heterogeneity and vessel content, where conventional therapy has failed to produce long-term effectivity, new therapeutic approaches are needed (Carrasco et al., 2017).

One among such alternative strategies relies on Sema4D blockade, which in the RIP1-Tag2 preclinical mouse model of PanNETs demonstrated beneficial antitumor effects (Martín-Mitjana, 2014). Unfortunately, the decrease in tumor burden and increase in survival of anti-Sema4D treated mice followed an increase in local invasion and metastases, mimicking the effects produced by antiangiogenic therapies such as anti-VEGFR2. Surprisingly enough, the malignization mechanism of anti-Sema4D was not related to intratumor hypoxia, which arises the question of how Sema4D blockade would aberrantly affect tumor progression. Therefore, the aim of this thesis was to decipher the mechanisms through which anti-Sema4D treatment acted as a double-edged sword in PanNET treatment. In summary, we have described that Sema4D targeting produces a beneficial antiangiogenic effect first, mediated by a pericyte-endothelial cell crosstalk, while it later increases malignization by macrophage activation.

2. Antitumor and antiangiogenic effect of anti-Sema4D

When released by tumor or stromal cells, Sema4D behaves as an endothelial cell chemoattractant that can enhance blood vessel content with the aim of promoting tumor growth (Basile et al., 2006; Sierra et al., 2008; Zhou et al., 2012b). Interestingly, our immunofluorescence results show that Sema4D expression is mainly found in scattered cells that resemble immune cells, rather than in tumor cells. This finding suggests that RIP1-Tag2-derived Sema4D arises from the stromal portion of the tumor. In order to initiate the angiogenic cascade in blood vessels, Sema4D needs to bind to its PlexinB1 receptor (Conrotto et al., 2005; Swiercz et al., 2004). Since the most striking vascular difference produced by anti-Sema4D treatment implied a change in pericyte coverage (Martín-Mitjana, 2014), we first analyzed the expression of the high affinity receptor Plexin B1 in perivascular cells of the RIP1-Tag2 stroma. Intriguingly, none of the pericyte subtypes assayed (Desmin, NG2 or α-SMA positive) expressed either PlexinB1, or the low affinity receptor CD72. Instead, in the RIP1-Tag2 model, PlexinB1 was found to be expressed by a small fraction of endothelial cells, representing only a 30% of tumor vessels positive for the high affinity Sema4D receptor.

Contextualized, our results suggest that Sema4D protein would act directly on its PlexinB1 high affinity receptor over endothelial cells of the RIP1-Tag2 tumor vasculature. Anti-Sema4D, as expected, produces a structural change of these vessels, decreasing the number of endothelial cell nuclei. However, contrary to what it is described in the literature (Basile et al., 2006; Zhou et al., 2012b), we do not see a reduction in vessel density after Sema4D blockade. We hypothesize that, since less than half of our vessels are PlexinB1-positive, we only observe a modest antiangiogenic effect of anti-Sema4D in the absence of vessel trimming. This is also applicable to other angiogenic features such as tumor hemorrhage, which showed an intermediate reduction between control and anti-VEGFR2 treatment. Besides, the angiogenic activity of Sema4D is mostly related to the directional motility of endothelial cells, which means that anti-Sema4D therapy could mainly hamper the branching of new blood vessels, when new tubular structures are formed, but not proliferation (Conrotto et al., 2005). Indeed, effects of the therapy over later stages of tumor angiogenesis would also explain why we observe structural changes in endothelial cells without vessel number alteration. On the contrary, VEGF acts early during tumor angiogenesis progression, thus meaning that its inhibition directly affects vessel proliferation, growing and maintenance. Finally, the subtle antiangiogenic effect observed after Sema4D blockade may also be explained by the avidity of PanNETs, and more specially RIP1-Tag2 tumors, for VEGF. Since tumor angiogenesis is strongly driven by VEGF, anti-Sema4D treatment has little effect upon tumor vasculature in this tumor types.

Regarding the downstream effectors on endothelial cells, Basile et al. also showed that many of the proangiogenic effects of PlexinB1 signaling are mediated by the small GTPase RhoA, including activation of genes involved in cell migration and adhesion (Basile et al., 2007a). Since *in vitro* models of endothelial cells currently available in our laboratory consist of HUVEC or primary mouse lung endothelial cells that uniformly express PlexinB1, we are still not able to mimic the *in vivo* setting of RIP1-Tag2 tumor vasculature to test these and other angiogenic properties. Nevertheless, in the absence of an adequate *in vitro* model, it would be interesting in the future to perform a direct *in vivo* angiogenesis assay (DIVAA) using angioreactors, as described by Zhou et al., in anti-Sema4D treated mice (Zhou et al., 2012b).

Surprisingly, anti-Sema4D treatment duplicated the percentage of PlexinB1 positive vessels without altering PlexinB1 expression at the transcriptional level (Figure 78). This finding could be explained by a compensatory mechanism produced due to the blockade of its ligand Sema4D. Using a murine model of Huntington disease, Southwell et al. have also reported this compensation in the brain, describing that an increase of soluble Sema4D produced the downregulation of its receptor (Southwell et al., 2015). Even though no vascular trimming was observed after anti-Sema4D therapy (Martín-Mitjana, 2014), the increased number of PlexinB1-positive vessels indicates that a structural change of the vessels which may have a functional implication is taking place as a consequence of Sema4D blockade. Deciphering the direct implication over the functionality of the vasculature is one of the possibilities we are currently studying. It has been described that Sema4D mediates induction of ANGPTL4, a protein that exerts a VEGF-independent proangiogenic effect and promotes vascular permeability (Figure 78) (Zhou et al., 2014). Other studies have shown that ANGPTL4 produced by endothelial cells disrupts vascular endothelial cell-cell junctions by directly interacting with VE-cadherin, increases permeability of capillaries and facilitates trans-endothelial passage of tumor cells (Padua et al., 2008). Therefore, in the absence of Sema4D, endothelial cells would be less permeable concurrent with a reduction in ANGPTL4 (Figure 78). In view of these recent findings, it will be of interest to determine whether ANGPTL4 is reduced in our mouse model after anti-Sema4D therapy. If so, the consequences of the decreased permeability of the vessels after anti-Sema4D treatment should be studied, but we believe that the decrease in the hemorrhagic phenotype we observe after the treatment could be one. In fact, the excess of tumor vascular permeability induces a range of deteriorating effects on the tumor ecosystem, including vessel leakiness, which facilitates tumor cell extravasation and increased interstitial pressure leading to impaired therapeutic delivery (Azzi et al., 2013). Diminution of vessel permeability by anti-Sema4D treatment could partially explain the antitumor efficacy of the therapy.

Following Sema4D engagement, PlexinB1 positive endothelial cells would act over pericytes that do not harbor any of the receptors for Sema4D by a crosstalk mechanism (Figure 78). Crosstalk and interactions between endothelial cells and pericytes in the vessel walls have been broadly identified as central processes in the regulation of vascular formation, stabilization, remodeling, and function (von Tell et al., 2006). Recent studies have shown that Sema4D can promote angiogenesis by acting upon endothelial cells to recruit pericytes to newly formed vessels (Sierra et al., 2008; Zhou et al., 2014). This process stabilizes and protects vessels from antiangiogenic intervention. In RIP1-Tag2 mice, we also suggest a direct action of Sema4D upon endothelial cells and an indirect effect of this ligand over pericyte cells by a crosstalk mechanism between endothelium and mural cells. In detail, anti-Sema4D treatment produced a decrease of α-SMA-positive pericytes, following an increase in Desmin and NG2 positive perivascular cells (Figure 78). Whereas the former is a marker of maturation of pericytes, the latter two are markers of pericyte remodeling and recruitment (Bergers and Song, 2005). Similarly, Zhou et al. have described that Sema4D RNA silencing produces a disruption of vessel-pericyte interactions of a HNSCC tumor model, rendering tumor vessels with less PDGFRβ pericyte coverage (Zhou et al., 2012b). In order to gain further insight into pericyte biology after Sema4D treatment, PDGFRβ expression should also be assessed in RIP1-Tag2 control and anti-Sema4D treated mice.

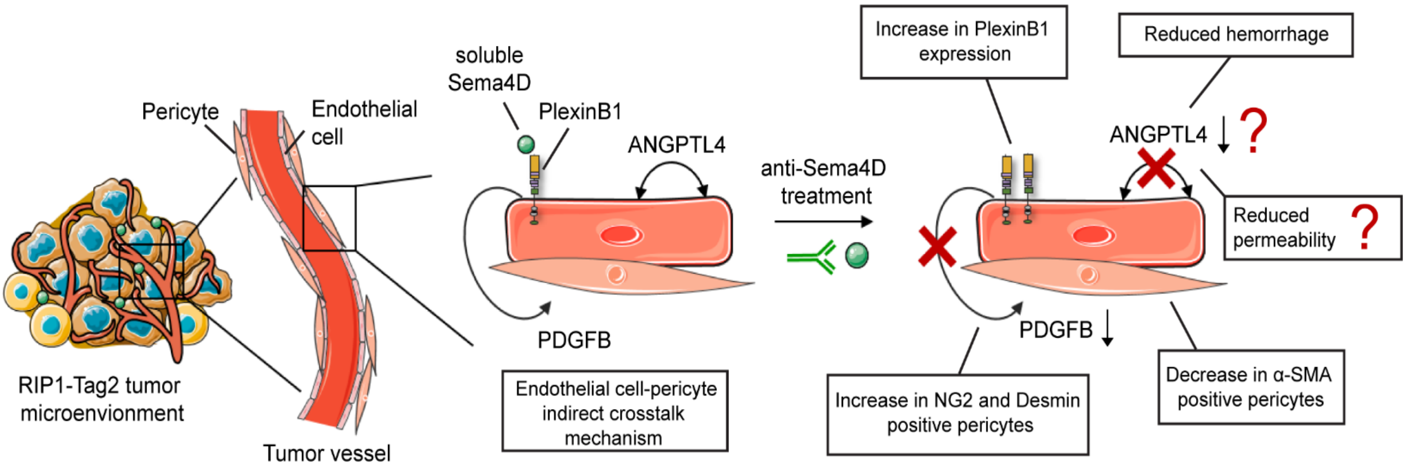

Figure 78 **The antiangiogenic effects of Anti-Sema4D in RIP1-Tag2 tumors are mediated by its direct action upon endothelial cells which, by an indirect crosstalk mechanism, induce changes in pericytes.** Sema4D/PlexinB1 signalling induces PDGFB secretion, altering pericyte biology, and ANGPTL4 autocrine release, inducing endothelial cell activation. Anti-Sema4D treatment induces increase of PlexinB1 expression by endothelial cells, reduces haemorrhage and α-SMA positive pericytes while increasing NG2 and desmin positive pericytes. It is still undescribed whether in the RIP1-Tag2 model Sema4D blockade would decrease ANGPTL4 expression and reduce vessel permeability.

When pericyte coverage of PlexinB1-positive vessels was analyzed considering the three different pericyte markers, we observed no change in vessel coverage, regardless of PlexinB1 positivity. However, a deeper analysis revealed that coverage by Desmin positive pericytes, the more abundant subtype, was deeply increased in PlexinB1 negative vessels. Even though PlexinB1 positive vessels also showed a slight tendency to be more covered by Desmin pericytes, the conclusion might be that the crosstalk between PlexinB1 positive endothelial cells and pericytes does not depend on whether those pericytes are covering them. In fact, the mechanism seems to occur in a paracrine fashion, acting in all pericytes regardless of their position. It is to be noted that even if only a small fraction of endothelial cells is able to respond to Sema4D stimuli, its signaling cascade affects all tumor vasculature. The consequences of the changes in the pericyte coverage of RIP1-Tag2 blood vessels were not studied in this Thesis due to the lack of an *in vitro* model that reproduced the RIP1-Tag2 pericyte phenotype. In fact, the primary brain pericyte cell lines obtained in our laboratory did express PlexinB1 receptor, making them impractical for use.

Regarding the molecular players of the endothelial cell-pericyte crosstalk, endothelial cell-derived production of PDGFB in a PlexinB1/RhoA dependent manner has been described (Figure 78). PDGFB is a key mediator in the activation and recruitment of pericytes to newly formed vessels (Furuhashi et al., 2004). PDGFB is normally expressed by sprouting capillary endothelial cells, only at sites where active angiogenesis is taking place, while its receptor, PDGFRβ, is found on pericytes. Hyperactivation of PDGFRβ signaling within the tumor ecosystem increases pericyte coverage, improving vessel stability and perfusion, which favors tumor growth (Ribeiro and Okamoto, 2015). Sema4D induces PDFGB production from endothelial cells, thus influencing pericyte proliferation and migration, as seen when media conditioned by Sema4D treated HUVEC was administered to pericyte cell cultures (Zhou et al., 2014). Blockade of Sema4D would therefore produce a diminution of PDGFB, thus reducing the number of mature pericytes and changing the pericyte coverage of vessels, as previously described in the literature (Figure

78) (Zhou et al., 2012b). As expected, in RIP1-Tag2 tumors, PDGFB levels were decreased both at protein and RNA levels after anti-Sema4D treatment, while pericyte coverage changed into a more immature phenotype and tumor growth was compromised. Overall, our findings confirm that there is a crosstalk between endothelial cells and pericytes that is mediated by PDGFBB signaling. The extent of its implication in establishing the antiangiogenic phenotype observed after Sema4D blockade could be analyzed by using a knockdown approach or pharmacological inhibition of PDGFRβ in anti-Sema4D treated mice.

Genetic or pharmacological blockade of specific targets could produce different biological effects. The blocking mechanism of the former grounds on the inhibition of transcription or translation, while pharmacological blockade relies on protein-protein interactions that could only inhibit certain functions of the target molecule. Contrarily to our observations, in other tumor models, Sema4D genetic blockade produced a decrease in tumor vasculature (Zhou et al., 2012). In another study by Sierra et al., where soluble Sema4D was produced by TAMs, microvessel density was similar both in Sema4D knockout and wild type breast cancer model mice (Sierra et al., 2008). However, a decrease was found in mean vessel area and mean vessel size in Sema4D KO mice, by determining only structures with a lumen at higher enlargement. Those parameters were not analyzed in our study and should be taken into consideration for further experiments. Up to date, no *in vivo* studies of anti-angiogenic efficacy have been published with Sema4D blocking antibodies. Overall, it seems that the effects of Sema4D blockade are both context and inhibition mechanism dependent.

On another note, the biological nature of semaphorin family members could be useful to explain the effects observed for anti-Sema4D treatment in RIP1-Tag2 mouse model. Despite the high homology between family members, different semaphorins sometimes have rather opposing effects, it being the case for Sema3A and Sema4D. Sema3A is an endogenous angiogenic inhibitor, unlike Sema4D, lost during tumor progression, when abnormal angiogenesis takes place (Gu and

Giraudo, 2013). In RIP1-Tag2 tumors, its re-expression inhibits tumor growth and increases survival through vessel normalization and reduced tumor hypoxia (Maione et al., 2009, 2012). Those results corroborate evidence describing that the poorly functional tumor vasculature appears as a consequence of an imbalance between pro and antiangiogenic factors, due to an overproduction of the former and a loss of the latter (Jain, 2005; Viallard and Larrivée, 2017). Restoration of the equilibrium, achieved by inhibition of proangiogenic molecules or by increasing the availability of its negative regulators, induces a more functional and normalized vasculature. Tumor vessel normalization represents a remarkably advantageous anticancer strategy, favoring chemotherapy delivery and impeding hypoxia-related resistance (Maione et al., 2012). Compiling our own results, it is plausible to think that, in the absence of hypoxia and vessel trimming combined with an increased survival and decreased tumor burden, RIP1-Tag2 mice treated with anti-Sema4D might undergo a vessel normalization process comparable to the one produced by the addition of Sema3A. Indeed, alteration of vessel pericyte coverage and decreased hemorrhagic phenotype further support this hypothesis. In previous results from our group, we have also observed an increase in Ang1 protein, involved in vessel tightening by affecting junctional molecules and promoting endothelial-pericyte interactions (Carlson et al., 2001; Thurston et al., 2000). Upregulation of this adhesive protein after Sema4D blockade probably tightens vessels and decreases hemorrhage, further supporting vessel normalization. There are no reports in the literature that directly relate Sema4D with vessel normalization processes.

3. Malignization effect of Sema4D via macrophage polarization

One of the current lines of thought in the field of antiangiogenics is that a partial inhibition of angiogenesis would not produce an increase of hypoxia within the tumor, thus avoiding the appearance of secondary unwanted malignant effects of such therapies. However, beneficial effects of anti-Sema4D antiangiogenic targeting ultimately led to an increase in local invasion and metastasis. Careful analysis of our *in vivo* data revealed that none of the vascular features of RIP1-Tag2 tumors could explain the malignization and protumoral mechanism, which is undoubtedly independent from the vascular fraction of the tumor ecosystem and from intratumor hypoxia. In search for the culprit, given that the main source of Sema4D in our RIP1-Tag2 system were macrophages infiltrating the tumor ecosystem, we postulated a macrophage-mediated effect on tumor cells.

Although it is known that Sema4D is expressed in macrophages (Suzuki et al., 2008), few studies have reported its effects. As previously explained, one of them analyzed the role of macrophage-shed Sema4D in tumor angiogenesis and progression (Sierra et al., 2008). No direct link between macrophage-derived Sema4D and its receptors in tumor cells has yet been described. PlexinB1 overexpression by different types of tumor cells, such as breast and ovary, have been related to poor outcome (Capparuccia and Tamagnone, 2009; Ch’ng and Kumanogoh, 2010; Valente et al., 2009). Surprisingly, one of the most disturbing findings was that RIP1-Tag2 tumor cells do not harbor any Sema4D receptors, thus discarding a direct action of macrophage-derived Sema4D upon them. We also checked for c-met activation both in RIP1-Tag2 tumor and their derived βTC4 tumor cells, one of the main drivers for RIP1-Tag2 malignization (Sennino et al., 2012; You et al., 2011), but it was unaffected by the anti-Sema4D treatment. All our findings led us to hypothesize that anti-Sema4D affected tumor cell behavior in an indirect fashion through macrophage modulation.

Anti-Sema4D therapy increased the number of intratumor TAMs, feature that has been extensively related to poor survival in thyroid, lung and hepatocellular cancers (Aras and Zaidi, 2017; Qian and Pollard, 2010). This finding could explain the malignant outcome we observe *in vivo* after anti-Sema4D treatment. The abundance of TAMs in tumors often correlates with the acquisition of specific cancer hallmarks such as immunosuppression, neovascularization, invasiveness, metastasis and poor response to therapy (Hanahan and Weinberg, 2011; Ostuni et al., 2015).

Recently, Evans et al. have similarly reported an increased immune infiltrate as a consequence of anti-Sema4D treatment (Evans et al., 2015). By using a colon cancer murine mouse model, they demonstrate that Sema4D expression at the invasive tumor edge creates a barrier to immune infiltration and biases the balance of regulatory and effector cells and signals. In their setting, antibody-mediated Sema4D blockade “opens the gates” to the tumor, increasing the number of infiltrating CD86-positive monocyte cells and T lymphocytes. Contrarily, previous results from our group showed no increase in cells from the acquired immune system in the RIP1-Tag2 mice model. Transgenic mice better mimic the stepwise pathogenesis of human cancers that transplanted tumors, as the ones used in Evans et al., providing a more reliable model to study the interplay between tumor and stromal cells (Babu et al., 2013). Unfortunately, transgene expression in RIP1-Tag2 mice begins early at about E8.5 in progenitor cells of the endocrine pancreas, before the complete formation of the immune system, thus rendering immune cells unable to recognize tumor cells as aberrant insults that need to be eliminated. Since islet tumors are regarded as innocuous by the immune system, no lymphocyte infiltration is observed in them. This handicap could be averted by analyzing RIP1-Tag5 mice instead, which mimic RIP1-Tag2 tumor progression steps but differ in the temporal onset of oncogene expression, which starts later in the pancreatic islet. Therefore, RIP1-Tag5 mice are not tolerant toward the Tag tumor antigen, thus hampering the before-mentioned evasion of immune surveillance, and serve as a better model to study tumor infiltrating immune cell biology (Ganss et al., 2002; Hager et al., 2004).

Apart from Sema4D, we also found that a fraction of macrophages, but not other immune cells, such as T or B lymphocytes, expressed PlexinB1, as previously described in the literature (Basile et al., 2004). Reports suggest that PlexinB1 expressed by stromal cells plays an important regulatory role in cancer, acting as an oncogene to promote tumor cell survival, proliferation, invasion and metastasis in B-cell chronic lymphocytic leukemia (CCL) (Deaglio et al., 2005; Granziero et al., 2003). In CLL, interaction between Sema4D and PlexinB1 expressed by bone marrow stromal cells, follicular dendritic cells and activated T lymphocytes increases tumoral proliferative activity and tumor cell survival. Inhibition of Sema4D/PlexinB1 axis in stromal cells is, therefore, assumed to be a valid therapeutic strategy to treat cancer. Strikingly, Sema4D signaling blockade in the RIP1-Tag2 stroma provokes the opposite effect, meaning that the effects we observe are not PlexinB1-dependent.

On the other hand, CD72, the immune receptor of Sema4D, was also expressed in a fraction of TAMs from the tumor microenvironment (Figure 79). CD72 signaling in the immune system is linked with inhibition of cell migration and homeostasis regulation (Chabbert-de Ponnat et al., 2005; Delaire et al., 2001; Kumanogoh et al., 2002b). Therefore, anti-Sema4D in the RIP1-Tag2 tumor stroma could be lifting up the migratory restrain induced by Sema4D/CD72 engagement. Without Sema4D, ligand orphan CD72 positive cells would have their migration abilities unaffected, thus increasing tumor infiltration, as observed in RIP1-Tag2 tumors (Figure 79). By using the RAW murine macrophage cell line, we functionally validated the role of anti-Sema4D in tumor infiltration by proving that macrophage migration is enhanced *in vitro* after Sema4D blockade. We also noted a striking increase in Sema4D positive TAMs, suggesting a phenotype switch of these cells after treatment (Figure 79). This shift could be caused by an autoregulatory effort of macrophages to hamper the migratory signaling by reactivating CD72.

Unfortunately, we could not confirm the Sema4D/CD72 crosstalk since in the *in vitro* model all cells expressed CD72, thereby not mimicking the *in vivo* phenotype. The election of RAW cells as an *in vitro* model aroused many reservations, since we initially thought that the *in vivo* isolation of RIP1-Tag2 TAMs or bone marrow-derived cells latter differentiated into macrophages would have been better options. We finally chose the RAW cell line due to its simplicity and stability, which have been recently revisited (Taciak et al., 2018).

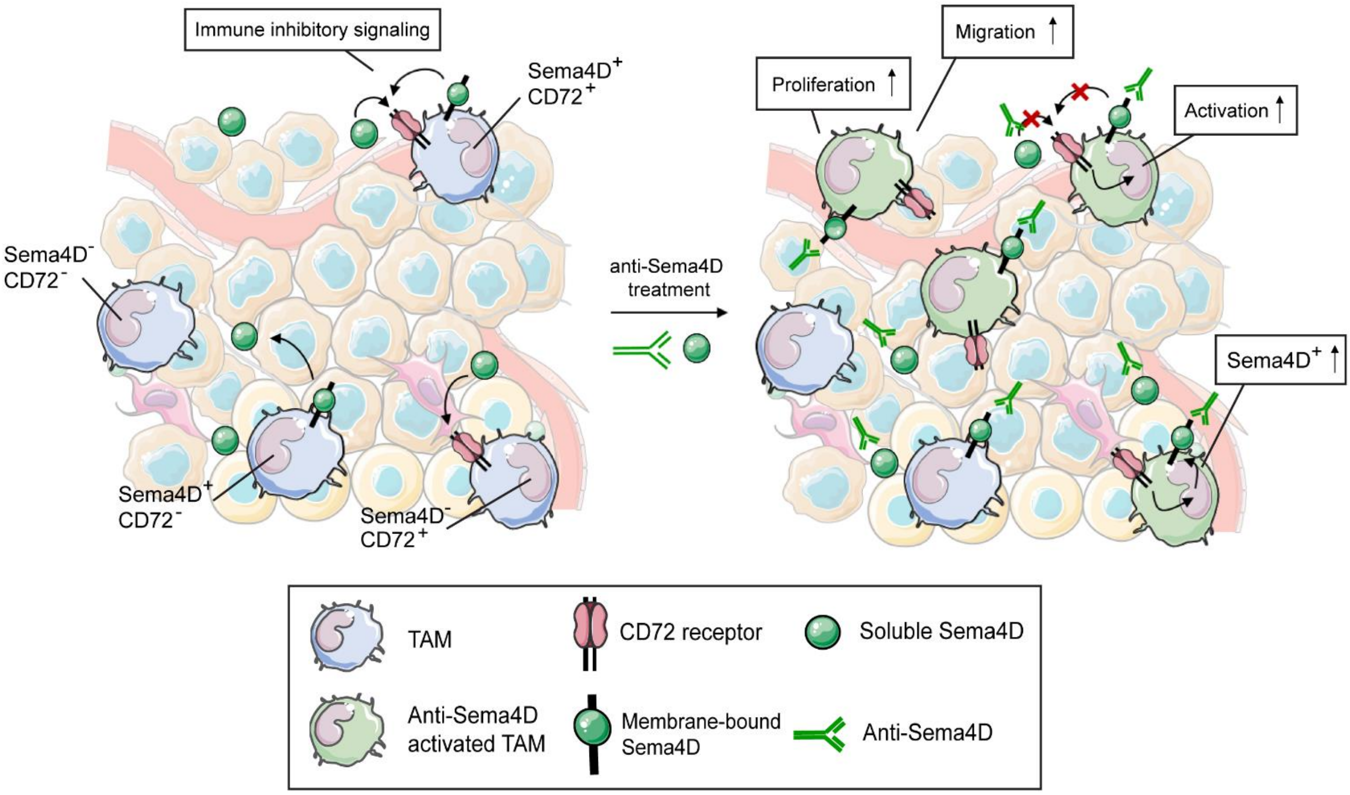

Figure 79 **Anti-Sema4D treatment blocks Sema4D/CD72 inhibitory signaling of tumor-associated macrophages (TAMs).** Sema4D/CD72 signaling blockade by anti-Sema4D treatment produces an increase of Sema4D positive TAMs, macrophage migration, proliferation and activation.

With respect to the molecular changes governing macrophage switch after anti-Sema4D therapy, the proteomic and GSEA analysis of their conditioned media revealed changes in macrophage activation, migration and proliferation (Figure 79). In fact, we found that even some top enriched proteins shared some of these functions, meaning that macrophage activation is profoundly interconnected. These results can be linked to the previously described *in vivo* increase in tumor immune infiltrate, further validating that Sema4D blockade produces an activation of macrophages, specially boosting their migratory properties (Delaire et al., 2001). Noteworthy, we were startled to find that many of the proteins in the proteomic analysis were not secreted. The simplest explanation would be that, during conditioned media harvesting, some cell membranes were disrupted and intracellular proteins were dumped. Besides, cell death as a consequence of cell overconfluence should not be ruled out, even though some of the secreted proteins showed survival-related activity.

Secreted protein functions of macrophage conditioned media were also, as expected, related to cytokine and receptor binding activity, further confirming macrophage activation upon Sema4D binding. Interestingly, an upregulation of IL4 response was also noted. IL4 has been thoroughly described in the literature as a classical stimulus for alternatively activated M2 macrophages or TAMs with pro-tumorigenic activity (Aras and Zaidi, 2017; Jablonski et al., 2015; Poh and Ernst, 2018). M2 macrophage activation after anti-Sema4D therapy would explain the malignization phenotype observed, since TAMs are involved in angiogenesis, migration, invasion, immunosuppression and metastasis (Aras and Zaidi, 2017). Seeking to demonstrate this hypothesis, RNA analysis revealed that, after Sema4D blockade, the same cells were also highly positive for Nos2, an enzyme from the nitric oxide pathway related to M1 pro-inflammatory and anti-tumorigenic activity. Moreover, CD206 or Mrc1, another classical M2 marker, was unexpectedly decreased after anti-Sema4D treatment, contradicting our previous findings regarding IL4. What seemed to be a mixture of different macrophage phenotypes was confirmed by the bioinformatic approach. The conventional binary M1/M2 model of macrophage polarization is becoming antiquated, since a newer model of polarization spectrum is arising, focusing on the involvement of an array of differentiated macrophages in tumor progression (Aras and Zaidi, 2017; Xue et al., 2014). Many authors have described tumor-infiltrating macrophages that promote tumor progression without using the traditional M1/M2 classification. Such is the case for Tie2 positive macrophages, which have an important role in tumor angiogenesis (Chen et al., 2016; De Palma et al., 2005). We therefore postulate Sema4D positive macrophages as a new subtype of TAMs with mixed biological functions that engage tumor malignization after anti-Sema4D blockade in RIP1-Tag2 PanNET mouse model.

Regarding macrophage-tumor cell interaction, we have observed an increase in Sema4D-positive macrophages at the tumor fronts. Certainly, this increase may have an implication in tumor cell invasion, as demonstrated by the addition of anti-Sema4D treated macrophage conditioned media to the in vitro βTC4 PanNET cells. It is important to highlight that anti-Sema4D mediated effects are therapy-specific and macrophage-mediated, as we demonstrate by using the isotype and added conditions. The potential of tumor cells to invade and metastasize depends on the tumor microenvironment, where TAMs constitute a major component (Aras and Zaidi, 2017). TAMs primarily promote tumor cell invasion via secretion of cytokines, chemokines and ECM remodeling enzymes. As an example, a novel real-time multiphoton imaging system demonstrated that invasion of breast cancer cells occurred in association with TAMs (Wyckoff et al., 2007). Moreover, in pancreatic tumors, TAM targeting by colony-stimulating factor-1 receptor (CSF1R) or CCR2 decreased the number of tumor-initiating cells and inhibited metastasis (Mitchem et al., 2013). Anti-Sema4D treated macrophages become activated, increase chemokine signaling, and secrete a conundrum of molecules that act as chemoattractants of tumor cells in a paracrine fashion, thereby potentiating their invading capability. We speculate that the activation of macrophages as a consequence of Sema4D/CD72 signaling abrogation is the main mechanism underlying chemokine secretion. The contribution of CD72, together with the precise molecules involved in downstream macrophage signaling are beyond the scope of this Thesis and should be investigated in the future.

In search for the pro-invasive candidate, we found that the two main cytokines whose expression was altered after anti-Sema4D therapy were CXCL12 (or SDF1) (Figure 80) and Pro-MMP9 (the precursor of MMP9). We were skeptical to find that MMP9 production was downregulated after anti-Sema4D therapy, since MMP secretion is one of the effects best described as drivers of TAM-induced tumor cell migration and invasion (Aras and Zaidi, 2017; Overall and López-Otín, 2002). We found that, in control tumors, MMP expression was mainly related to macrophage localization, as expected, whereas the association was lost in anti-Sema4D treated macrophages. There is no piece of literature that associates loss of Sema4D expression with MMP downregulation. Nevertheless, a relationship between a decrease in MMP activity and collective invasion properties of the tumor has recently been described (Haeger et al., 2014; Kumar et al., 2016). In fact, RIP1-Tag2 tumor invasion model does not follow a classical EMT, but it rather relies on collective invasion and tight cell-cell contacts. Therefore, an increased invasion could be partially related to anti-Sema4D mediated downregulation of MMP9, which boosts the collective cell invasion mechanism.

Immune cytokines such as CXCL12 are master regulators of pro-tumorigenic immune infiltrating cells, orchestrating their mobilization from the bone marrow and blood to the tumor and polarizing their phenotype inside the tumor ecosystem (Duda et al., 2011; Janssens et al., 2018). Undeniably, we have demonstrated that stromal CXCL12 is able to potentiate PanNET tumor cell invasion through activation of the CXCR4 signaling pathway (Figure 80). Recently, CXCL12/CXCR4 signaling axis was validated as a prognostic factor in different types of NETs (Circelli et al., 2016). Moreover, we have also demonstrated that the invasive ability is mostly dependent on CXCL12 release by anti-Sema4D treated macrophages by using a specific CXCR4 inhibitor already used in the clinic (Table 21). In this context, it would be informative to perform an *in vivo* experiment where animals were treated with anti-Sema4D and AMD3100 simultaneously. Both CXCL12 and CXCR4 were upregulated at protein and RNA levels after Sema4D blockade, a mechanism not described in the literature. In fact, the correlation between the invasive capacity of the tumor and CXCL12 concentration in control tumors, which is lost after anti-Sema4D treatment, suggests that the CXCL12/CXCR4 signaling cascade is activated early during tumor progression. Anti-Sema4D treatment, in turn, increases CXCL12 expression from macrophages, regardless of the invasive ability of the tumor.

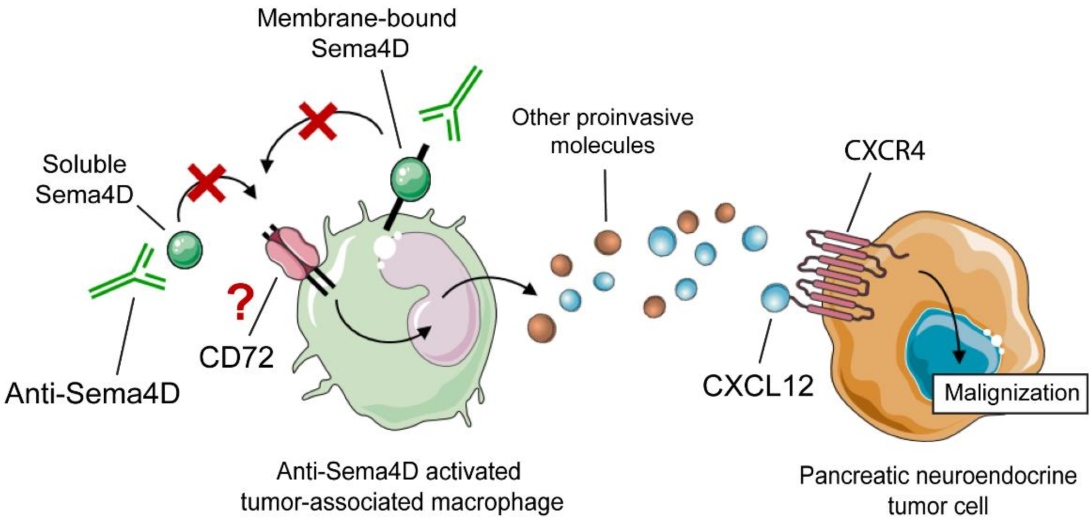

Figure 80 **Anti-Sema4D mediated malignization is driven by macrophage-mediated release of proinvasive molecules, such as CXCL12.** Anti-Sema4D mediated soluble and membrane bound Sema4D blockade impairs its signaling, probably via CD72, activating Sema4D positive macrophages. Anti-Sema4D activated TAMs release a conundrum of proinvasive molecules, such as CXCL12. CXCL12 is able to bind to CXCR4 receptor expressed in tumor cells. Its engaging initiates a malignization program characterized by increased invasiveness.

On another note, CXCL12/CXCR4 interaction, apart from allowing the spontaneous migration of malignant cells, also protects tumor cells from apoptosis in a chronic B-lymphocytic leukemia model (Burger et al., 2000). Performing a TUNNEL or Ki-67 assay in our samples will be a nice approach to better characterize the effects of anti-Sema4D derived CXCL12. Besides, recent reports show that CXCL12 is constitutively expressed in metastasis sites, including the lung, bone marrow and liver, to where it drives cancer cells (Ray et al., 2015; Taichman et al., 2002). These findings point a role for CXCL12 in the "seed and soil" paradigm. Also known as the organ tropism hypothesis, this paradigm is based on the fact that, before metastatic colonization, primary tumors secrete factors that prepare a pre-metastatic niche at a distant site to become receptive (Aras and Zaidi, 2017). It is characterized by the accumulation of bone marrow-derived cell types, such as macrophages, oncoproteins and cytokines, like CXCL12. A future experiment is to check both macrophage infiltrates and CXCL12 expression in anti-

Sema4D treated livers and lymphatic nodules in order to verify whether there is a CXCL12 dependent gradient that promotes hypoxia-independent distant metastases in RIP1-Tag2 mice.

Overall, we hereby describe a new subtype of macrophages, which are Sema4D-positive, that are able to increase the invasive and metastatic abilities of PanNET RIP1-Tag2 tumor cells in a CXCL12/CXCR4 and MMP9 dependent manner when they become inhibited. This is a novel, up to date undescribed, hypoxia-independent mechanism that relies on Sema4D blockade and the derived macrophage switch rather than on its anti-angiogenic capacity.

4. From bench to bedside: Clinical relevance of anti-Sema4D therapy

The malignization mechanism herein described adds a new layer of complexity to the already difficult crosstalk mechanisms governing interactions between tumor cells and their surrounding microenvironment. Yet it is necessary to ascertain if the chain of events triggered after anti-Sema4D therapy could be translated from the preclinical RIP1-Tag2 model to human PanNET patients. We therefore used a clinical set of PanNET patients, from which data regarding non-functional primary tumors were analyzed, due to their high molecular and phenotypical resemblance to RIP1-Tag2 invasive tumors, as previously explained (Sadanandam et al., 2015).

Our analysis demonstrated that both Sema4D and CXCR4 expression increase with tumor progression, being higher in metastasis samples. Importantly, Sema4D expression seems to be exclusive to metastasis, since there is no gradual increase of its expression through malignization stages. Moreover, Sema4D does not correlate with grade, malignancy or proliferation. Altogether, these results remark a role for Sema4D in the late steps of tumor progression process, specifically in metastasis of PanNETs. Sema4D overexpression has already been described in other types of tumors such as breast, pancreatic, colon, ovarian, urogenital, and head and neck (Basile et al., 2006), but never in PanNETs. Taken together, we conclude that Sema4D does not serve as a diagnostic marker of tumor malignization in this type of tumors, but its targeting could theoretically limit metastasis. Meanwhile, CXCR4 expression correlates with the whole malignization process, behaving as a classical tumor progression driver gene in PanNETs. Traditionally, genes involved in malignization are classified into three main groups: metastasis initiation, metastasis progression and metastasis virulence genes (Nguyen et al., 2009). Sema4D seems to behave, at least in PanNET patients, as a metastasis virulence gene, being relevant for metastatic infiltration, survival and colonization during the “seed and soil” process. Contrarily, CXCR4 seems to be a metastasis initiating gene, involved in the early steps of the process and therefore providing an advantage for primary tumor survival and growth. CXCR4 did, indeed, correlate with grading, Ki67 index and tumor stage of PanNETs, as previously described for other NETs (Circelli et al., 2016; Kaemmerer et al., 2015).

Regarding CXCL12, its levels remained unchanged, while its basal expression was significantly lower than Sema4D and CXCR4 expression. As in the case of Sema4D, no direct relation between CXCL12 and tumor grade, malignancy or proliferation was found. Absence of CXCL12 upregulation with tumor progression could indicate that anti-Sema4D mediated malignization effect is totally independent from the natural malignization process in PanNETs. Besides, we hypothesize that the rather unchanging profiles for both Sema4D and CXCL12, in comparison to CXCR4, indicate that they are originally stromal molecules. Therefore, their expression is independent from tumor cells, which compose the majority of the tumor, and could dilute small stromal variations that are camouflaged in the RNA profiling of whole tumor biopsies. For instance, Cives et al. have demonstrated the implication of CXCL12/CXCR4 axis in the bone colonization in other PanNET in vitro models. Interestingly, they defined tumor cells as CXCR4^{high}/CXCL12^{low} that responded to exogenous CXCL12 by increasing their invasion (Cives et al., 2017). In their models, they blame this effect on EMT engagement after CXCL12/CXCR4 activation. We believe that EMT or collective invasion, as in our case, could be indistinctively activated after CXCL12 stimulus, although it should be checked in PanNET human patient samples.

The main drawbacks in our clinical study, which partially limits the comparison to our preclinical results, are that: 1) Expression of candidate genes is not decomposed by tumor microenvironment forming cell type; 2) There are no data from anti-Sema4D treated PanNET patients. Firstly, the hurdle of having data from mixed cell populations of the tumor microenvironment that did not allow to test the conclusions from the RIP1-Tag2-derived findings was successfully overcome by using the computational MCP-counter analysis (Becht et al., 2016). The MCP-counter enables robust quantification of the abundance of multiple immune and non-immune stromal populations in the transcriptome of heterogeneous tissue. We demonstrated that Sema4D expression is highly associated to monocytes and fibroblasts in PanNET patients. In RIP1-Tag2, we did not evaluate the expression of Sema4D by fibroblasts since murine stroma is poorly enriched with this cell type. Interestingly, other immune cells such as T and B cells were less associated to Sema4D expression, indicating that the main source of endogenous Sema4D in PanNET tumor are macrophages. CXCR4 was expressed by immune cells and by endothelial cells, as explained in the literature (Duda et al., 2011; Teixidó et al., 2018). Since MCP-counter method is only designed to detect stromal and immune cells, we were not able to analyze the expression of those selected molecules in PanNET tumor cells. In the future, it would be interesting to develop a PanNET specific molecular signature, which would allow the validation of the expression of target proteins on the whole tumor ecosystem. Regarding CD72, as expected, it was strongly related to immune cells and fibroblasts, whereas PlexinB1 was only slightly expressed by endothelial cells and some other immune cells, but not in macrophages, supporting our preclinical findings.

Many controversies arise from the effects of Sema4D blockade due to its pleiotropic and context-dependent effects (Lontos et al., 2018). For instance, in a gene transcription array, Sema4D mRNA was highest during early stage breast cancer compared to normal tissue and downregulated in advanced disease (Gabrovska et al., 2011). Contrarily, knockdown of Sema4D by shRNA inhibited breast cancer proliferation and tumor growth in xenografts (Jiang et al., 2016). However, Malik et al. showed an opposite result of decreased Sema4D in primary breast tumors of patients who subsequently developed local recurrence, compared to patients who remained disease-free (Malik et al., 2015). Overall, these studies used whole tumor tissues and may be confounded by different types of cells comprising the tissue that express Sema4D. In addition, most data on Sema4D and clinical outcomes are based on small sample sizes with subjects that receive different types of treatments and are not controlled for other prognostic markers.

Therefore, it is necessary to assume the promiscuous nature of Sema4D and the heterogeneity of tumors before extracting global conclusions of its effects.

Sema4D regulation is crucial in immune escape of cancer cells. For instance, Sema4D affects both the activities of immune cells and their recruitment to the tumor microenvironment. In a head and neck cancer model, tumor-derived Sema4D promoted the expansion of myeloid-derived suppressor cells, in turn inhibiting T-cell activity (Younis et al., 2016). While other researchers and our group, during this Thesis, have noted that Sema4D inhibited both spontaneous and chemokine-induced migration of human monocytes (Delaire et al., 2001), Evans et al. found strong expression of Sema4D at the invasive margins of tumors growing actively using our same antibody from Vaccinex (Evans et al., 2015). They describe, in a colon cancer mouse model, that Sema4D changed infiltration and distribution of leukocytes within the tumor stroma towards an immune permissive microenvironment. Neutralization of Sema4D by anti-Sema4D blocking antibody disrupted this gradient of expression and enhanced recruitment of activated monocytes and lymphocytes into the tumor, shifting the balance of cytokines to a pro-inflammatory and antitumorigenic profile. These functions are at odds with the known roles of Sema4D in T and B cell activation (Kumanogoh et al., 2005), and also contradict our findings regarding macrophage switch toward a pro-tumorigenic phenotype.

All in all, we propose that the final function of Sema4D in the tumor depends on different aspects such as its concentration, location of the target and its receptors and the surrounding tumor microenvironment. For instance, for inhibition of myeloid cell migration and immunosuppressive effects (Chabbert-de Ponnat et al., 2005; Delaire et al., 2001), Sema4D concentration was effective at a range from <10 ng/ml and 80 ng/ml. The proangiogenic effects of Sema4D were detected in the range of 400 ng/ml (Yang et al., 2011). By contrast, increased activation of the immune system and induction of proinflammatory cytokines was observed in the micromolar range of soluble Sema4D, from 4-20 µg/ml (Kumanogoh et al., 2002b).

In the RIP1-Tag2 system, when Sema4D is inhibited, we observe partial anti-angiogenic and migration stimulation functions, suggesting that the amount of Sema4D is in the nanomolar range. We postulate that Sema4D from stromal origin will always be at a lower concentration range than that derived from tumor cells, which compose the majority of the tumor stroma. This would mean that effects on migration and activity of immune cells would be better observed than antiangiogenic effects in those systems, as we and others describe (Sierra et al., 2008).

Additionally, Sema4D is able to exert diverse effects depending on the surrounding stroma. Two main models of peritumoral stroma phenotype are described in the literature (Gajewski et al., 2013; Spranger and Gajewski, 2016). One is a T cell inflamed subtype, in which the tumor associated T cells are functionally inhibited through anergy and T cell checkpoints. This subtype will likely respond to checkpoint inhibitors and seems to be the one described in colon tumor murine models analyzed by Evans and collaborators (Evans et al., 2015). According to their results, anti-Sema4D therapy disrupts tumor immunosuppression and potentiates effector T cell infiltration. In fact, the combination of anti-Sema4D with immune checkpoint inhibitors, such as anti-CTLA4 or anti-PD1, reduces tumor volumes and increases survival. We were unable to detect Sema4D T lymphocytes in our RIP1-Tag2 stroma, due to tolerance of the immune system toward the tumor forming transgene.

As explained in previous sections of this Thesis, VX15/2503, the humanized anti-Sema4D antibody, showed promising results in the first-in-human phase I clinical trial, with a 45% of patients exhibiting the absence of disease progression for at least 8 weeks (Patnaik et al., 2016). Apart from antitumor activity, they evaluated lymphocyte levels, which remained generally unchanged from baseline during the treatment. Intriguingly, they found a positive correlation between the normalized baseline number of B and T cells and PFS duration (Spearman rank coefficient = 0.6133; $P \leq 0.001$). Neither the latter adaptive response to treatment nor antiangiogenic effects have been evaluated in those patients, but this result could vary in different tumor types (Singh et al., 2012) and in humans. Nevertheless, we postulate that RIP1-Tag2 mice could behave as patients with low immune potential, were the therapy fails to produce enduring effects. Overall, this result suggests that preexisting immune potential predisposes to a better outcome of the therapy, which could mean that anti-Sema4D therapy could not be effective in immunodeprived patients.

The other stroma subtype describes non-T cell infiltrated tumors with two main characteristics: a denser stroma and myeloid and macrophage inflammatory cells. In our case, when anti-Sema4D therapy is given to RIP1-Tag2 mice, we could be potentiating the latter phenotype, creating an immune permissive environment with pro-tumoral effects. Derakhshandeh et al. have recently described that, in head and neck cancer tissue, according to Sema4D expression, two distinct subtypes can be observed: Sema4D^{high} HNSCC tumor cells with dense non-inflamed stroma versus the Sema4D^{low} tumor cells with Sema4D^{high} tumor-associated inflammatory cells (TAIs) (Derakhshandeh et al., 2018). In summary, they showed that Sema4D^{low} TAIs and Sema4D^{high} tumor were associated to initial stages of tumor progression, whereas the last stages seemed to be more associated to the Sema4D^{high} tumor-associated inflammatory cell phenotype. The significance of this divergence regarding Sema4D origin has not been assessed yet.

Altogether, both literature and our own results support the idea that Sema4D targeting for tumor treatment is not as easy as it initially seemed, since many levels of regulation exist. The current notion in the field, however, is that its role in angiogenesis is being displaced in favor of its potential targeting for immunotherapy. In this context, understanding the mechanisms underlying Sema4D immunomodulation on lymphocytes and TAMs becomes imperative to improve current treatments. Since the depletion of immunosuppressive macrophages in the tumor ecosystem enhances antitumor response, TAM targeting is rapidly emerging as a promising therapeutic strategy for cancer patients (Ostuni et al., 2015; Poh and Ernst, 2018). In our setting, the most obvious conclusion would be to inhibit

Semaphorin4D together with CXCL12, therefore promoting the antiangiogenic effect of the therapy and avoiding the malignant effect upon tumor cells. However, inhibition of CXCL12 would still happen in the context of macrophage activation. To think that anti-Sema4D mediated malignization relies only on CXCL12 expression by macrophages is a rather naïve idea. In this line, we hypothesize that the activation of the macrophages changes the cytokine profile and extracellular environment in RIP1-Tag2 tumors. Since detection, determination, validation and blocking of all the proinvasive candidates is unfeasible, we propose TAM recruitment abolishment in combination with anti-Sema4D therapy (reviewed in Poh and Ernst, 2018). Currently, the most advanced approaches for TAM depletion are based on CSF1R targeting, which have already shown antiangiogenic and antimetastatic effects in melanoma and mammary xenografts. Finally, the strategy of trying to disrupt immunosuppression by combining anti-Sema4D with immune checkpoint inhibitors such as anti-PD1 and anti-CTLA4 antibodies has already demonstrated beneficial outcomes in patients (Evans et al., 2015). All these therapeutic options highlight the importance of tumor biopsies to determine the composition of the immune tumor microenvironment before starting any treatment regime. In this context, the development of computational tools such as the MCP-counter method proves its relevance in the clinical setting.

In conclusion, in this Doctoral Thesis we describe the opposing effects of anti-Sema4D treatment. While the antiangiogenic effect of vessel-pericyte targeting produces an antitumoral effect, the activation of tumor-infiltrating macrophages generates an unexpected hypoxia-independent proinvasive phenotype. As a consequence of the therapy, Sema4D positive macrophages are recruited to RIP1-Tag2 tumors, where secretion of proinvasive cytokines such as CXCL12 promotes tumor cell invasion. Altogether, our study reveals a new insight into the relevance of the tumor ecosystem for malignant progression in PanNETs. We have further demonstrated that these results could be applied into the clinical setting, since Sema4D and CXCR4 appear to be potential markers for tumor metastasis and malignization in PanNET patients. Due to the initial benefits of anti-Sema4D treatment, and the latter tumor malignization produced by macrophages, a combination of anti-Sema4D therapy and currently developing immunotherapies would constitute a valid approach to hamper tumor progression. If resistance arousing from tumor-stromal cell crosstalk is to be avoided, combined therapies taking into account better patient stratification, non-traditional antiangiogenics and novel immunotherapies are, undoubtedly, the way to follow.

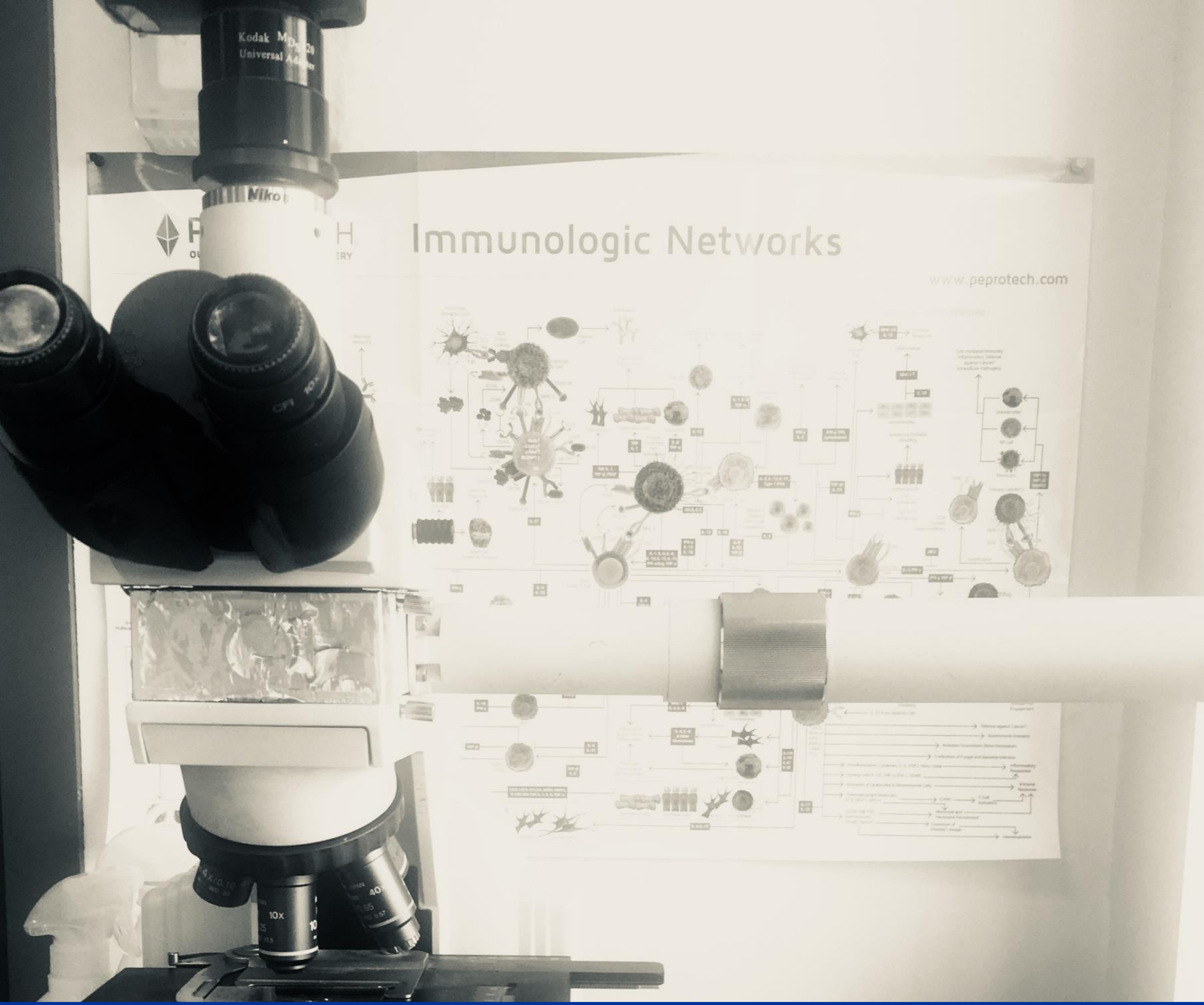

Conclusions

The good thing about Science is that it is true
whether or not you believe in it.

Neil deGrasse Tyson

1. PlexinB1, the high affinity Sema4D receptor, is expressed by a subset of endothelial cells and macrophages, while absent in pericytes of the vascular system of RIP1-Tag2 mice tumors. CD72, the low affinity Sema4D receptor, is expressed by a subset of macrophages of RIP1-Tag2 mice tumors.

2. Anti-Sema4D treatment increases PlexinB1 expressing vessel number two-fold. Alteration in the pericyte coverage after anti-Sema4D is not exclusively related to PlexinB1 expressing vessels.

3. Anti-Sema4D directly acts upon vessels through its PlexinB1 receptor in order to provoke structural alterations in the vasculature. In turn, an indirect crosstalk mechanism, probably governed by PDGFB, induces pericyte alterations.

4. Anti-Sema4D therapy activates macrophages by increasing their migratory abilities and the number of tumor-infiltrating macrophages in the RIP1-Tag2 tumor stroma.

5. Anti-Sema4D treated macrophages do not behave as classical M1 or M2 macrophages, but they show a mixed phenotype.

6. Anti-Sema4D does not directly affect tumor cells, but it rather indirectly activates malignization processes through tumor-associated macrophage targeting in a paracrine fashion.

7. CXCL12 is one of the proinvasive cytokines secreted by anti-Sema4D activated macrophages that, upon recognition by CXCR4 receptor in tumor cells, potentiates tumor cell invasion.

8. Sema4D expression in PanNET patients is strongly associated to the monocytic lineage.

9. In PanNET patients, Sema4D is associated to metastasis, whereas CXCR4 expression is linked to tumor progression.

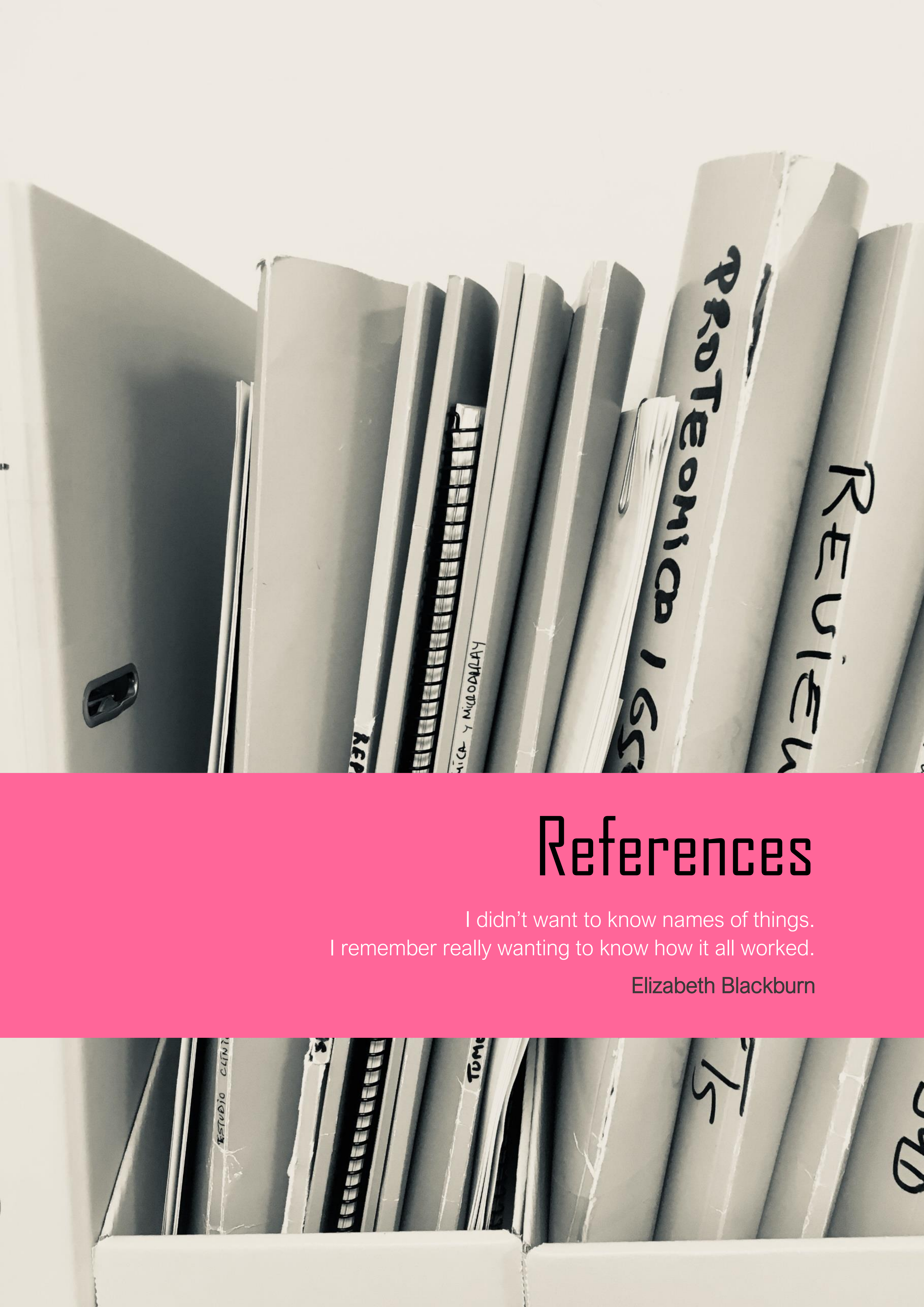

References

> I didn’t want to know names of things.
> I remember really wanting to know how it all worked.
>
> Elizabeth Blackburn

References

A

Aharinejad, S., Paulus, P., Sioud, M., Hofmann, M., Zins, K., Schäfer, R., et al. (2004). Colony-Stimulating Factor-1 Blockade by Antisense Oligonucleotides and Small Interfering RNAs Suppresses Growth of Human Mammary Tumor Xenografts in Mice. *Cancer Res.* 64, 5378–5384. doi:10.1158/0008-5472.CAN-04-0961.

Albini, A., and Sporn, M. B. (2007). The tumour microenvironment as a target for chemoprevention. *Nat. Rev. Cancer* 7, 139–147. doi:10.1038/nrc2067.

Alto, L. T., and Terman, J. R. (2017). Semaphorins and their Signaling Mechanisms. *Methods Mol. Biol.* 1493, 1–25. doi:10.1007/978-1-4939-6448-2_1.

Aras, S., and Zaidi, M. R. (2017). TAMeless traitors: macrophages in cancer progression and metastasis. *Br. J. Cancer* 117, 1583–1591. doi:10.1038/bjc.2017.356.

Artigiani, S., Barberis, D., Fazzari, P., Longati, P., Angelini, P., van de Loo, J.-W., et al. (2003). Functional Regulation of Semaphorin Receptors by Proprotein Convertases. *J. Biol. Chem.* 278, 10094–10101. doi:10.1074/jbc.M210156200.

Austyn, J. M., and Gordon, S. (1981). F4/80, a monoclonal antibody directed specifically against the mouse macrophage. *Eur. J. Immunol.* 11, 805–815. doi:10.1002/eji.1830111013.

Azzi, S., Hebda, J. K., and Gavard, J. (2013). Vascular Permeability and Drug Delivery in Cancers. *Front. Oncol.* 3, 211. doi:10.3389/fonc.2013.00211.

B

Babu, V., Paul, N., and Yu, R. (2013). Animal Models and Cell Lines of Pancreatic Neuroendocrine Tumors. *Pancreas* 42, 912–923. doi:10.1097/MPA.0b013e31827ae993.

Bachelerie, F., Graham, G. J., Locati, M., Mantovani, A., Murphy, P. M., Nibbs, R., et al. (2014). New nomenclature for atypical chemokine receptors. *Nat. Immunol.* 15, 207–208. doi:10.1038/ni.2812.

Balabanian, K., Lagane, B., Infantino, S., Chow, K. Y. C., Harriague, J., Moepps, B., et al. (2005). The Chemokine SDF-1/CXCL12 Binds to and Signals through the Orphan Receptor RDC1 in T Lymphocytes. *J. Biol. Chem.* 280, 35760–35766. doi:10.1074/jbc.M508234200.

Banu, N., Teichman, J., Dunlap-Brown, M., Villegas, G., and Tufro, A. (2006). Semaphorin 3C regulates endothelial cell function by increasing integrin activity. *FASEB J.* 20, 2150–2152. doi:10.1096/fj.05-5698fje.

Barbero, S., Bonavia, R., Bajetto, A., Porcile, C., Pirani, P., Ravetti, J. L., et al. (2003). Stromal cell-derived factor 1alpha stimulates human glioblastoma cell growth through the activation of both extracellular signal-regulated kinases 1/2 and Akt. *Cancer Res.* 63, 1969–74. Available at: http://www.ncbi.nlm.nih.gov/pubmed/12702590 [Accessed July

16, 2018].

Basile, J. R., Barac, A., Zhu, T., Guan, K.-L., and Gutkind, J. S. (2004). Class IV semaphorins promote angiogenesis by stimulating Rho-initiated pathways through plexin-B. *Cancer Res.* 64, 5212–24. doi:10.1158/0008-5472.CAN-04-0126.

Basile, J. R., Castilho, R. M., Williams, V. P., and Gutkind, J. S. (2006). Semaphorin 4D provides a link between axon guidance processes and tumor-induced angiogenesis. *Proc. Natl. Acad. Sci. U. S. A.* 103, 9017–22. doi:10.1073/pnas.0508825103.

Basile, J. R., Gavard, J., and Gutkind, J. S. (2007a). Plexin-B1 utilizes RhoA and Rho kinase to promote the integrin-dependent activation of Akt and ERK and endothelial cell motility. *J Biol Chem* 282, 34888–34895. doi:M705467200 [pii]10.1074/jbc.M705467200.

Basile, J. R., Holmbeck, K., Bugge, T. H., and Gutkind, J. S. (2007b). MT1-MMP controls tumor-induced angiogenesis through the release of semaphorin 4D. *J. Biol. Chem.* 282, 6899–905. doi:10.1074/jbc.M609570200.

Bateman, A., Martin, M. J., O'Donovan, C., Magrane, M., Alpi, E., Antunes, R., et al. (2017). UniProt: the universal protein knowledgebase. *Nucleic Acids Res.* 45, D158–D169. doi:10.1093/nar/gkw1099.

Bates, D., Taylor, G. I., Minichiello, J., Farlie, P., Cichowitz, A., Watson, N., et al. (2003). Neurovascular congruence results from a shared patterning mechanism that utilizes Semaphorin3A and Neuropilin-1. *Dev Biol* 255, 77–98. doi:S0012160602000453 [pii].

Becht, E., Giraldo, N. A., Lacroix, L., Buttard, B., Elarouci, N., Petitprez, F., et al. (2016). Estimating the population abundance of tissue-infiltrating immune and stromal cell populations using gene expression. *Genome Biol.* 17, 218. doi:10.1186/s13059-016-1070-5.

Bergers, G., and Benjamin, L. E. (2003). Tumorigenesis and the angiogenic switch. *Nat. Rev. Cancer* 3, 401–410. doi:10.1038/nrc1093.

Bergers, G., and Hanahan, D. (2008). Modes of resistance to anti-angiogenic therapy. *Nat. Rev. Cancer* 8, 592–603. doi:10.1038/nrc2442.

Bergers, G., Javaherian, K., Lo, K. M., Folkman, J., and Hanahan, D. (1999). Effects of angiogenesis inhibitors on multistage carcinogenesis in mice. *Science* 284, 808–12. Available at: http://www.ncbi.nlm.nih.gov/pubmed/10221914 [Accessed March 5, 2018].

Bergers, G., and Song, S. (2005). The role of pericytes in blood-vessel formation and maintenance. *Neuro. Oncol.* 7, 452–64. doi:10.1215/S1152851705000232.

Bielenberg, D. R., Pettaway, C. A., Takashima, S., and Klagsbrun, M. (2006). Neuropilins in neoplasms: expression, regulation, and function. *Exp Cell Res* 312, 584–593. doi:S0014-4827(05)00555-0 [pii]10.1016/j.yexcr.2005.11.024.

Binmadi, N. O., Yang, Y.-H., Zhou, H., Proia, P., Lin, Y.-L., Batista De Paula, A. M., et al. (2012). Plexin-B1 and Semaphorin 4D Cooperate to Promote Perineural Invasion in a RhoA/ROK-Dependent Manner. *Am. J. Pathol.* 180, 1232–1242. doi:10.1016/j.ajpath.2011.12.009.

Bissell, M. J., and Radisky, D. (2001). Putting tumours in context. *Nat. Rev. Cancer* 1, 46–54. doi:10.1038/35094059.

Biswas, S. K., Allavena, P., and Mantovani, A. (2013). Tumor-associated macrophages: functional diversity, clinical significance, and open questions. *Semin. Immunopathol.* 35, 585–600. doi:10.1007/s00281-013-0367-7.

Bleul, C. C., Fuhlbrigge, R. C., Casasnovas, J. M., Aiuti, A., and Springer, T. A. (1996). A highly efficacious lymphocyte chemoattractant, stromal cell-derived factor 1 (SDF-1). *J. Exp.*

Med. 184, 1101–9. Available at: http://www.ncbi.nlm.nih.gov/pubmed/9064327 [Accessed July 16, 2018].

Blouw, B., Song, H., Tihan, T., Bosze, J., Ferrara, N., Gerber, H. P., et al. (2003). The hypoxic response of tumors is dependent on their microenvironment. *Cancer Cell* 4, 133–46. Available at: http://www.ncbi.nlm.nih.gov/pubmed/12957288 [Accessed May 3, 2018].

Boldajipour, B., Mahabaleshwar, H., Kardash, E., Reichman-Fried, M., Blaser, H., Minina, S., et al. (2008). Control of Chemokine-Guided Cell Migration by Ligand Sequestration. *Cell* 132, 463–473. doi:10.1016/j.cell.2007.12.034.

Bottaro, D. P., and Liotta, L. A. (2003). Out of air is not out of action. *Nature* 423, 593–595. doi:10.1038/423593a.

Bougeret, C., Mansur, I. G., Dastot, H., Schmid, M., Mahouy, G., Bensussan, A., et al. (1992). Increased surface expression of a newly identified 150-kDa dimer early after human T lymphocyte activation. *J. Immunol.* 148, 318–23. Available at: http://www.ncbi.nlm.nih.gov/pubmed/1530858 [Accessed June 5, 2018].

Burger, J. A., Tsukada, N., Burger, M., Zvaifler, N. J., Dell'Aquila, M., and Kipps, T. J. (2000). Blood-derived nurse-like cells protect chronic lymphocytic leukemia B cells from spontaneous apoptosis through stromal cell-derived factor-1. *Blood* 96, 2655–63. Available at: http://www.ncbi.nlm.nih.gov/pubmed/11023495 [Accessed August 24, 2018].

Burns, J. M., Summers, B. C., Wang, Y., Melikian, A., Berahovich, R., Miao, Z., et al. (2006). A novel chemokine receptor for SDF-1 and I-TAC involved in cell survival, cell adhesion, and tumor development. *J. Exp. Med.* 203, 2201–2213. doi:10.1084/jem.20052144.

C

Capdevila, J., Meeker, A., García-Carbonero, R., Pietras, K., Astudillo, A., Casanovas, O., et al. (2014). Molecular biology of neuroendocrine tumors: from pathways to biomarkers and targets. *Cancer Metastasis Rev.* 33, 345–351. doi:10.1007/s10555-013-9468-y.

Capozzi, M., Von Arx, C., De Divitiis, C., Ottaiano, A., Tatangelo, F., Romano, G. M., Et Al. (2016). Antiangiogenic Therapy in Pancreatic Neuroendocrine Tumors. *Anticancer Res.* 36, 5025–5030. doi:10.21873/anticanres.11071.

Capparuccia, L., and Tamagnone, L. (2009). Semaphorin signaling in cancer cells and in cells of the tumor microenvironment - two sides of a coin. *J. Cell Sci.* 122, 1723–1736. doi:10.1242/jcs.030197.

Carlson, T. R., Feng, Y., Maisonpierre, P. C., Mrksich, M., and Morla, A. O. (2001). Direct Cell Adhesion to the Angiopoietins Mediated by Integrins. *J. Biol. Chem.* 276, 26516–26525. doi:10.1074/jbc.M100282200.

Carmeliet, P. (2005). VEGF as a Key Mediator of Angiogenesis in Cancer. *Oncology* 69, 4–10. doi:10.1159/000088478.

Caronni, N., Savino, B., and Bonecchi, R. (2015). Myeloid cells in cancer-related inflammation. *Immunobiology* 220, 249–53. doi:10.1016/j.imbio.2014.10.001.

Carr, J. C., Boese, E. A., Spanheimer, P. M., Dahdaleh, F. S., Martin, M., Calva, D., et al. (2012). Differentiation of small bowel and pancreatic neuroendocrine tumors by gene-expression profiling. *Surgery* 152, 998–1007. doi:10.1016/j.surg.2012.08.040.

Carrasco, P., Zuazo-Gaztelu, I., and Casanovas, O. (2017). Sprouting strategies and dead ends in anti-angiogenic targeting of nets. *J. Mol. Endocrinol.* 59. doi:10.1530/JME-17-0029.

Casanovas, O., Hicklin, D. J., Bergers, G., and Hanahan, D. (2005). Drug resistance by evasion of antiangiogenic targeting of VEGF signaling in late-stage pancreatic islet tumors. *Cancer Cell* 8, 299–309. doi:10.1016/j.ccr.2005.09.005.

Casazza, A., Fu, X., Johansson, I., Capparuccia, L., Andersson, F., Giustacchini, A., et al. (2011). Systemic and targeted delivery of semaphorin 3A inhibits tumor angiogenesis and progression in mouse tumor models. *Arter. Thromb Vasc Biol* 31, 741–749. doi:ATVBAHA.110.211920 [pii]10.1161/ATVBAHA.110.211920.

Cauwe, B., Martens, E., Proost, P., and Opdenakker, G. (2009). Multidimensional degradomics identifies systemic autoantigens and intracellular matrix proteins as novel gelatinase B/MMP-9 substrates. *Integr. Biol.* 1, 404. doi:10.1039/b904701h.

Cauwe, B., Van den Steen, P. E., and Opdenakker, G. (2007). The Biochemical, Biological, and Pathological Kaleidoscope of Cell Surface Substrates Processed by Matrix Metalloproteinases. *Crit. Rev. Biochem. Mol. Biol.* 42, 113–185. doi:10.1080/10409230701340019.

Ch'ng, E. S., and Kumanogoh, A. (2010). Roles of Sema4D and Plexin-B1 in tumor progression. *Mol. Cancer* 9, 251. doi:10.1186/1476-4598-9-251.

Ch'ng, E., Tomita, Y., Zhang, B., He, J., Hoshida, Y., Qiu, Y., et al. (2007). Prognostic significance of CD100 expression in soft tissue sarcoma. *Cancer* 110, 164–172. doi:10.1002/cncr.22764.

Chabbert-de Ponnat, I., Marie-Cardine, A., Pasterkamp, R. J., Schiavon, V., Tamagnone, L., Thomasset, N., et al. (2005). Soluble CD100 functions on human monocytes and immature dendritic cells require plexin C1 and plexin B1, respectively. *Int. Immunol.* 17, 439–447. doi:10.1093/intimm/dxh224.

Chen, L., Li, J., Wang, F., Dai, C., Wu, F., Liu, X., et al. (2016). Tie2 Expression on Macrophages Is Required for Blood Vessel Reconstruction and Tumor Relapse after Chemotherapy. *Cancer Res.* 76, 6828–6838. doi:10.1158/0008-5472.CAN-16-1114.

Chen, Y., Zhang, L., Lv, R., and Zhang, W.-Q. (2013). Overexpression of Semaphorin4D indicates poor prognosis and prompts monocyte differentiation toward M2 macrophages in epithelial ovarian cancer. *Asian Pac. J. Cancer Prev.* 14, 5883–90. Available at: http://www.ncbi.nlm.nih.gov/pubmed/24289594 [Accessed July 27, 2018].

Christofori, G., Naik, P., and Hanahan, D. (1994). A second signal supplied by insulin-like growth factor II in oncogene-induced tumorigenesis. *Nature* 369, 414–418. doi:10.1038/369414a0.

Circelli, L., Sciammarella, C., Guadagno, E., Tafuto, S., de Caro, M. del B., Botti, G., et al. (2016). CXCR4/CXCL12/CXCR7 axis is functional in neuroendocrine tumors and signals on mTOR. *Oncotarget* 7, 18865–75. doi:10.18632/oncotarget.7738.

Cives, M., Quaresmini, D., Rizzo, F. M., Felici, C., D'Oronzo, S., Simone, V., et al. (2017). Osteotropism of neuroendocrine tumors: role of the CXCL12/ CXCR4 pathway in promoting EMT in vitro. *Oncotarget* 8, 22534–22549. doi:10.18632/oncotarget.15122.

Collier, I. E., Wilhelm, S. M., Eisen, A. Z., Marmer, B. L., Grant, G. A., Seltzer, J. L., et al. (1988). H-ras oncogene-transformed human bronchial epithelial cells (TBE-1) secrete a single metalloprotease capable of degrading basement membrane collagen. *J. Biol. Chem.* 263, 6579–87. Available at: http://www.ncbi.nlm.nih.gov/pubmed/2834383 [Accessed July 16, 2018].

Conley-LaComb, M. K., Semaan, L., Singareddy, R., Li, Y., Heath, E. I., Kim, S., et al. (2016). Pharmacological targeting of CXCL12/CXCR4 signaling in prostate cancer bone metastasis. *Mol. Cancer* 15, 68. doi:10.1186/s12943-016-0552-0.

Conrotto, P., Corso, S., Gamberini, S., Comoglio, P. M., and Giordano, S. (2004). Interplay between scatter factor receptors and B plexins controls invasive growth. *Oncogene* 23, 5131–5137. doi:10.1038/sj.onc.1207650.

Conrotto, P., Valdembri, D., Corso, S., Serini, G., Tamagnone, L., Comoglio, P. M., et al. (2005). Sema4D induces angiogenesis through Met recruitment by Plexin B1. *Blood* 105, 4321–9. doi:10.1182/blood-2004-07-2885.

Crusz, S. M., and Balkwill, F. R. (2015). Inflammation and cancer: advances and new agents. *Nat. Rev. Clin. Oncol.* 12, 584–596. doi:10.1038/nrclinonc.2015.105.

D

De Dosso, S., Grande, E., Barriuso, J., Castellano, D., Tabernero, J., and Capdevila, J. (2013). The targeted therapy revolution in neuroendocrine tumors: in search of biomarkers for patient selection and response evaluation. *Cancer Metastasis Rev.* 32, 465–477. doi:10.1007/s10555-013-9421-0.

De Palma, M., Venneri, M. A., Galli, R., Sergi, L. S., Politi, L. S., Sampaolesi, M., et al. (2005). Tie2 identifies a hematopoietic lineage of proangiogenic monocytes required for tumor vessel formation and a mesenchymal population of pericyte progenitors. *Cancer Cell* 8, 211–226. doi:10.1016/j.ccr.2005.08.002.

Deaglio, S., Vaisitti, T., Bergui, L., Bonello, L., Horenstein, A. L., Tamagnone, L., et al. (2005). CD38 and CD100 lead a network of surface receptors relaying positive signals for B-CLL growth and survival. *Blood* 105, 3042–3050. doi:10.1182/blood-2004-10-3873.

Delaire, S., Billard, C., Tordjman, R., Chédotal, A., Elhabazi, A., Bensussan, A., et al. (2001). Biological activity of soluble CD100. II. Soluble CD100, similarly to H-SemaIII, inhibits immune cell migration. *J. Immunol.* 166, 4348–54. Available at: http://www.ncbi.nlm.nih.gov/pubmed/11254688 [Accessed December 19, 2017].

Delaire, S., Elhabazi, A., Bensussan, A., and Boumsell, L. (1998). CD100 is a leukocyte semaphorin. *Cell. Mol. Life Sci.* 54, 1265–76. doi:10.1007/s000180050252.

Dennis, G., Sherman, B. T., Hosack, D. A., Yang, J., Gao, W., Lane, H., et al. (2003). DAVID: Database for Annotation, Visualization, and Integrated Discovery. *Genome Biol.* 4, R60. doi:10.1186/gb-2003-4-9-r60.

Derakhshandeh, R., Sanadhya, S., Lee Han, K., Chen, H., Goloubeva, O., Webb, T. J., et al. (2018). Semaphorin 4D in human head and neck cancer tissue and peripheral blood: A dense fibrotic peri-tumoral stromal phenotype. *Oncotarget* 9, 11126–11144. doi:10.18632/oncotarget.24277.

Deryugina, E. I., Zijlstra, A., Partridge, J. J., Kupriyanova, T. A., Madsen, M. A., Papagiannakopoulos, T., et al. (2005). Unexpected Effect of Matrix Metalloproteinase Down-Regulation on Vascular Intravasation and Metastasis of Human Fibrosarcoma Cells Selected *In vivo* for High Rates of Dissemination. *Cancer Res.* 65, 10959–10969. doi:10.1158/0008-5472.CAN-05-2228.

Duda, D. G., Kozin, S. V, Kirkpatrick, N. D., Xu, L., Fukumura, D., and Jain, R. K. (2011). CXCL12 (SDF1alpha)-CXCR4/CXCR7 pathway inhibition: an emerging sensitizer for anticancer therapies? *Clin. Cancer Res.* 17, 2074–80. doi:10.1158/1078-0432.CCR-10-

2636.

E

Efrat, S., Linde, S., Kofod, H., Spector, D., Delannoy, M., Grant, S., et al. (1988). Beta-cell lines derived from transgenic mice expressing a hybrid insulin gene-oncogene. *Proc. Natl. Acad. Sci. U. S. A.* 85, 9037–41. Available at: http://www.ncbi.nlm.nih.gov/pubmed/2848253 [Accessed June 14, 2018].

Ehehalt, F., Saeger, H. D., Schmidt, C. M., and Grutzmann, R. (2009). Neuroendocrine Tumors of the Pancreas. *Oncologist* 14, 456–467. doi:10.1634/theoncologist.2008-0259.

Elhabazi, A., Delaire, S., Bensussan, A., Boumsell, L., and Bismuth, G. (2001). Biological activity of soluble CD100. I. The extracellular region of CD100 is released from the surface of T lymphocytes by regulated proteolysis. *J. Immunol.* 166, 4341–7. Available at: http://www.ncbi.nlm.nih.gov/pubmed/11254687 [Accessed December 25, 2017].

Engl, T., Relja, B., Marian, D., Blumenberg, C., Müller, I., Beecken, W.-D., et al. (2006). CXCR4 Chemokine Receptor Mediates Prostate Tumor Cell Adhesion through α5 and β3 Integrins. *Neoplasia* 8, 290–301. doi:10.1593/neo.05694.

Evans, E. E., Jonason, A. S., Bussler, H., Torno, S., Veeraraghavan, J., Reilly, C., et al. (2015). Antibody Blockade of Semaphorin 4D Promotes Immune Infiltration into Tumor and Enhances Response to Other Immunomodulatory Therapies. *Cancer Immunol. Res.* 3, 689–701. doi:10.1158/2326-6066.CIR-14-0171.

F

Faivre, S., Demetri, G., Sargent, W., and Raymond, E. (2007). Molecular basis for sunitinib efficacy and future clinical development. *Nat. Rev. Drug Discov.* 6, 734–745. doi:10.1038/nrd2380.

Fazzari, P., Penachioni, J., Gianola, S., Rossi, F., Eickholt, B. J., Maina, F., et al. (2007). Plexin-B1 plays a redundant role during mouse development and in tumour angiogenesis. *BMC Dev. Biol.* 7, 55. doi:10.1186/1471-213X-7-55.

Feiner, L., Koppel, A. M., Kobayashi, H., and Raper, J. A. (1997). Secreted Chick Semaphorins Bind Recombinant Neuropilin with Similar Affinities but Bind Different Subsets of Neurons In Situ. *Neuron* 19, 539–545. doi:10.1016/S0896-6273(00)80370-0.

Ferrara, N., Gerber, H.-P., and LeCouter, J. (2003). The biology of VEGF and its receptors. *Nat. Med.* 9, 669–76. doi:10.1038/nm0603-669.

Fisher, T. L., Reilly, C. A., Winter, L. A., Pandina, T., Jonason, A., Scrivens, M., et al. (2016). Generation and preclinical characterization of an antibody specific for SEMA4D. *MAbs* 8, 150–62. doi:10.1080/19420862.2015.1102813.

Fjällskog, M.-L. H., Lejonklou, M. H., Oberg, K. E., Eriksson, B. K., Janson, E. T., Fjallskog, M. L., et al. (2003). Expression of molecular targets for tyrosine kinase receptor antagonists in malignant endocrine pancreatic tumors. *Clin Cancer Res* 9, 1469–1473. Available at: http://www.ncbi.nlm.nih.gov/pubmed/12684421 [Accessed July 27, 2018].

Fjällskog, M.-L., Hessman, O., Eriksson, B., and Tiensuu Janson, E. (2007). Upregulated expression of PDGF receptor beta in endocrine pancreatic tumors and metastases compared to normal endocrine pancreas. *Acta Oncol. (Madr).* 46, 741–746. doi:10.1080/02841860601048388.

Folkman, J., Watson, K., Ingber, D., and Hanahan, D. (1989). Induction of angiogenesis during the transition from hyperplasia to neoplasia. *Nature* 339, 58–61. doi:10.1038/339058a0.

Fraisl, P., Mazzone, M., Schmidt, T., and Carmeliet, P. (2009). Regulation of Angiogenesis by Oxygen and Metabolism. *Dev. Cell* 16, 167–179. doi:10.1016/j.devcel.2009.01.003.

Franco, M., and Tamagnone, L. (2008). Tyrosine phosphorylation in semaphorin signalling: shifting into overdrive. *EMBO Rep.* 9, 865–71. doi:10.1038/embor.2008.139.

Franklin, R. A., and Li, M. O. (2016). Ontogeny of Tumor-Associated Macrophages and Its Implication in Cancer Regulation. *Trends in Cancer* 2, 20–34. doi:10.1016/j.trecan.2015.11.004.

Franklin, R. A., Liao, W., Sarkar, A., Kim, M. V., Bivona, M. R., Liu, K., et al. (2014). The cellular and molecular origin of tumor-associated macrophages. *Science (80-.).* 344, 921–925. doi:10.1126/science.1252510.

Furuhashi, M., Sjöblom, T., Abramsson, A., Ellingsen, J., Micke, P., Li, H., et al. (2004). Platelet-derived growth factor production by B16 melanoma cells leads to increased pericyte abundance in tumors and an associated increase in tumor growth rate. *Cancer Res.* 64, 2725–33. Available at: http://www.ncbi.nlm.nih.gov/pubmed/15087386 [Accessed May 3, 2018].

Furuyama, T., Inagaki, S., Kosugi, A., Noda, S., Saitoh, S., Ogata, M., et al. (1996). Identification of a novel transmembrane semaphorin expressed on lymphocytes. *J. Biol. Chem.* 271, 33376–81. Available at: http://www.ncbi.nlm.nih.gov/pubmed/8969198 [Accessed July 27, 2018].

G

Gabrovska, P. N., Smith, R. A., Tiang, T., Weinstein, S. R., Haupt, L. M., and Griffiths, L. R. (2011). Semaphorin–plexin signalling genes associated with human breast tumourigenesis. *Gene* 489, 63–69. doi:10.1016/j.gene.2011.08.024.

Gajewski, T. F., Schreiber, H., and Fu, Y.-X. (2013). Innate and adaptive immune cells in the tumor microenvironment. *Nat. Immunol.* 14, 1014–1022. doi:10.1038/ni.2703.

Galani, E., Sgouros, J., Petropoulou, C., Janinis, J., Aravantinos, G., Dionysiou-Asteriou, D., et al. (2002). Correlation of MDR-1, nm23-H1 and H Sema E gene expression with histopathological findings and clinical outcome in ovarian and breast cancer patients. *Anticancer Res* 22, 2275–2280. Available at: http://www.ncbi.nlm.nih.gov/entrez/query.fcgi?cmd=Retrieve&db=PubMed&dopt=Citation&list_uids=12174914.

Ganss, R., Ryschich, E., Klar, E., Arnold, B., and Hämmerling, G. J. (2002). Combination of T-cell therapy and trigger of inflammation induces remodeling of the vasculature and tumor eradication. *Cancer Res.* 62, 1462–70. Available at: http://www.ncbi.nlm.nih.gov/pubmed/11888921 [Accessed August 23, 2018].

Geevarghese, A., and Herman, I. M. (2014). Pericyte-endothelial crosstalk: implications and opportunities for advanced cellular therapies. *Transl. Res.* 163, 296–306. doi:10.1016/j.trsl.2014.01.011.

Gerhardt, H., and Betsholtz, C. (2003). Endothelial-pericyte interactions in angiogenesis. *Cell Tissue Res.* 314, 15–23. doi:10.1007/s00441-003-0745-x.

Goodman, C. ., Kolodkin, A. ., Luo, Y., Püschel, A. ., and Raper, J. . (1999). Unified nomenclature for the semaphorins/collapsins. Semaphorin Nomenclature Committee.

Cell 97, 551–2. doi:10.1016/S0092-8674(00)80766-7.

Gordon, J. (1994). B-cell signalling via the C-type lectins CD23 and CD72. *Immunol. Today* 15, 411–7. doi:10.1016/0167-5699(94)90270-4.

Granziero, L., Circosta, P., Scielzo, C., Frisaldi, E., Stella, S., Geuna, M., et al. (2003). CD100/Plexin-B1 interactions sustain proliferation and survival of normal and leukemic CD5+ B lymphocytes. *Blood* 101, 1962–9. doi:10.1182/blood-2002-05-1339.

Gu, C., and Giraudo, E. (2013). The role of semaphorins and their receptors in vascular development and cancer. *Exp Cell Res* 319, 1306–1316. doi:S0014-4827(13)00046-3 [pii]10.1016/j.yexcr.2013.02.003.

Guttmann-Raviv, N., Shraga-Heled, N., Varshavsky, A., Guimaraes-Sternberg, C., Kessler, O., and Neufeld, G. (2007). Semaphorin-3A and semaphorin-3F work together to repel endothelial cells and to inhibit their survival by induction of apoptosis. *J Biol Chem* 282, 26294–26305. doi:M609711200 [pii]10.1074/jbc.M609711200.

H

Haeger, A., Krause, M., Wolf, K., and Friedl, P. (2014). Cell jamming: Collective invasion of mesenchymal tumor cells imposed by tissue confinement. *Biochim. Biophys. Acta - Gen. Subj.* 1840, 2386–2395. doi:10.1016/j.bbagen.2014.03.020.

Hager, J. H., Hodgson, J. G., Fridlyand, J., Hariono, S., Gray, J. W., and Hanahan, D. (2004). Oncogene expression and genetic background influence the frequency of DNA copy number abnormalities in mouse pancreatic islet cell carcinomas. *Cancer Res.* 64, 2406–10. Available at: http://www.ncbi.nlm.nih.gov/pubmed/15059892 [Accessed August 23, 2018].

Hanahan, D. (1985). Heritable formation of pancreatic beta-cell tumours in transgenic mice expressing recombinant insulin/simian virus 40 oncogenes. *Nature* 315, 115–22. Available at: http://www.ncbi.nlm.nih.gov/pubmed/2986015 [Accessed December 25, 2017].

Hanahan, D. (1988). Dissecting Multistep Tumorigenesis in Transgenic Mice. *Annu. Rev. Genet.* 22, 479–519. doi:10.1146/annurev.ge.22.120188.002403.

Hanahan, D., and Folkman, J. (1996). Patterns and emerging mechanisms of the angiogenic switch during tumorigenesis. *Cell* 86, 353–64. Available at: http://www.ncbi.nlm.nih.gov/pubmed/8756718 [Accessed May 3, 2018].

Hanahan, D., and Weinberg, R. A. (2000). The hallmarks of cancer. *Cell* 100, 57–70. Available at: http://www.ncbi.nlm.nih.gov/pubmed/10647931 [Accessed July 27, 2018].

Hanahan, D., and Weinberg, R. A. (2011). Hallmarks of Cancer: The Next Generation. *Cell* 144, 646–674. doi:10.1016/j.cell.2011.02.013.

Hansel, D. E., Rahman, A., Hermans, J., de Krijger, R. R., Ashfaq, R., Yeo, C. J., et al. (2003). Liver Metastases Arising from Well-Differentiated Pancreatic Endocrine Neoplasms Demonstrate Increased VEGF-C Expression. *Mod. Pathol.* 16, 652–659. doi:10.1097/01.MP.0000077416.68489.50.

Herman, J. G., and Meadows, G. G. (2007). Increased class 3 semaphorin expression modulates the invasive and adhesive properties of prostate cancer cells. *Int J Oncol* 30, 1231–1238. Available at: http://www.ncbi.nlm.nih.gov/entrez/query.fcgi?cmd=Retrieve&db=PubMed&dopt=Citation&list_uids=17390026.

Herold, C., Elhabazi, A., Bismuth, G., Bensussan, A., and Boumsell, L. (1996). CD100 is associated with CD45 at the surface of human T lymphocytes. Role in T cell homotypic adhesion. *J. Immunol.* 157, 5262–8. Available at: http://www.ncbi.nlm.nih.gov/pubmed/8955171 [Accessed July 27, 2018].

Hodgson, G., Hager, J. H., Volik, S., Hariono, S., Wernick, M., Moore, D., et al. (2001). Genome scanning with array CGH delineates regional alterations in mouse islet carcinomas. *Nat. Genet.* 29, 459–464. doi:10.1038/ng771.

Hota, P. K., and Buck, M. (2012). Plexin structures are coming: opportunities for multilevel investigations of semaphorin guidance receptors, their cell signaling mechanisms, and functions. *Cell. Mol. Life Sci.* 69, 3765–3805. doi:10.1007/s00018-012-1019-0.

I

Inoue, M., Hager, J. H., Ferrara, N., Gerber, H.-P., and Hanahan, D. (2002). VEGF-A has a critical, nonredundant role in angiogenic switching and pancreatic beta cell carcinogenesis. *Cancer Cell* 1, 193–202. Available at: http://www.ncbi.nlm.nih.gov/pubmed/12086877 [Accessed December 25, 2017].

J

Jablonski, K. A., Amici, S. A., Webb, L. M., Ruiz-Rosado, J. de D., Popovich, P. G., Partida-Sanchez, S., et al. (2015). Novel Markers to Delineate Murine M1 and M2 Macrophages. *PLoS One* 10, e0145342. doi:10.1371/journal.pone.0145342.

Jain, R. K. (2005). Normalization of Tumor Vasculature: An Emerging Concept in Antiangiogenic Therapy. *Science (80-.).* 307, 58–62. doi:10.1126/science.1104819.

Jain, R. K. (2014). Antiangiogenesis strategies revisited: from starving tumors to alleviating hypoxia. *Cancer Cell* 26, 605–22. doi:10.1016/j.ccell.2014.10.006.

Janssens, R., Struyf, S., and Proost, P. (2018). The unique structural and functional features of CXCL12. *Cell. Mol. Immunol.* 15, 299–311. doi:10.1038/cmi.2017.107.

Jiang, H., Chen, C., Sun, Q., Wu, J., Qiu, L., Gao, C., et al. (2016). The role of semaphorin 4D in tumor development and angiogenesis in human breast cancer. *Onco. Targets. Ther.* 9, 5737–5750. doi:10.2147/OTT.S114708.

Joyce, J. A., Baruch, A., Chehade, K., Meyer-Morse, N., Giraudo, E., Tsai, F.-Y., et al. (2004). Cathepsin cysteine proteases are effectors of invasive growth and angiogenesis during multistage tumorigenesis. *Cancer Cell* 5, 443–53. Available at: http://www.ncbi.nlm.nih.gov/pubmed/15144952 [Accessed July 26, 2018].

K

Kaemmerer, D., Träger, T., Hoffmeister, M., Sipos, B., Hommann, M., Sänger, J., et al. (2015). Inverse expression of somatostatin and CXCR4 chemokine receptors in gastroenteropancreatic neuroendocrine neoplasms of different malignancy. *Oncotarget* 6, 27566–79. doi:10.18632/oncotarget.4491.

Kanehisa, M., Goto, S., Sato, Y., Furumichi, M., and Tanabe, M. (2012). KEGG for integration and interpretation of large-scale molecular data sets. *Nucleic Acids Res.* 40, D109–D114. doi:10.1093/nar/gkr988.

Kato, S., Kubota, K., Shimamura, T., Shinohara, Y., Kobayashi, N., Watanabe, S., et al. (2011). Semaphorin 4D, a lymphocyte semaphorin, enhances tumor cell motility through binding its receptor, plexinB1, in pancreatic cancer. *Cancer Sci.* 102, 2029–2037. doi:10.1111/j.1349-7006.2011.02053.x.

Katt, M. E., Placone, A. L., Wong, A. D., Xu, Z. S., and Searson, P. C. (2016). In Vitro Tumor Models: Advantages, Disadvantages, Variables, and Selecting the Right Platform. *Front. Bioeng. Biotechnol.* 4, 12. doi:10.3389/fbioe.2016.00012.

Kelly-Goss, M. R., Sweat, R. S., Stapor, P. C., Peirce, S. M., and Murfee, W. L. (2014). Targeting Pericytes for Angiogenic Therapies. *Microcirculation* 21, 345–357. doi:10.1111/micc.12107.

Kessler, O., Shraga-Heled, N., Lange, T., Gutmann-Raviv, N., Sabo, E., Baruch, L., et al. (2004). Semaphorin-3F is an inhibitor of tumor angiogenesis. *Cancer Res* 64, 1008–1015. Available at: http://www.ncbi.nlm.nih.gov/entrez/query.fcgi?cmd=Retrieve&db=PubMed&dopt=Citation&list_uids=14871832.

Kim, C. H., and Broxmeyer, H. E. (1998). In vitro behavior of hematopoietic progenitor cells under the influence of chemoattractants: stromal cell-derived factor-1, steel factor, and the bone marrow environment. *Blood* 91, 100–10. Available at: http://www.ncbi.nlm.nih.gov/pubmed/9414273 [Accessed July 16, 2018].

Kim, J., and Bae, J.-S. (2016). Tumor-Associated Macrophages and Neutrophils in Tumor Microenvironment. *Mediators Inflamm.* 2016, 1–11. doi:10.1155/2016/6058147.

Kim, J., Mori, T., Chen, S. L., Amersi, F. F., Martinez, S. R., Kuo, C., et al. (2006). Chemokine Receptor CXCR4 Expression in Patients With Melanoma and Colorectal Cancer Liver Metastases and the Association With Disease Outcome. *Ann. Surg.* 244, 113–120. doi:10.1097/01.sla.0000217690.65909.9c.

Klagsbrun, M., Takashima, S., and Mamluk, R. (2002). The role of neuropilin in vascular and tumor biology. *Adv. Exp. Med. Biol.* 515, 33–48. Available at: http://www.ncbi.nlm.nih.gov/pubmed/12613541 [Accessed July 27, 2018].

Kolodkin, A. L., Matthes, D. J., and Goodman, C. S. (1993). The semaphorin genes encode a family of transmembrane and secreted growth cone guidance molecules. *Cell* 75, 1389–99. Available at: http://www.ncbi.nlm.nih.gov/pubmed/8269517 [Accessed December 25, 2017].

Kopitz, C., Gerg, M., Reddy Bandapalli, O., Ister, D., Pennington, C. J., Hauser, S., et al. (2007). Tissue Inhibitor of Metalloproteinases-1 Promotes Liver Metastasis by Induction of Hepatocyte Growth Factor Signaling. *Cancer Res* 67, 8615–8638. doi:10.1158/0008-5472.CAN-07-0232.

Kratochvill, F., Neale, G., Haverkamp, J. M., Van de Velde, L.-A., Smith, A. M., Kawauchi, D., et al. (2015). TNF Counterbalances the Emergence of M2 Tumor Macrophages. *Cell Rep.* 12, 1902–1914. doi:10.1016/j.celrep.2015.08.033.

Krause, D. S., and Van Etten, R. A. (2005). Tyrosine Kinases as Targets for Cancer Therapy. *N. Engl. J. Med.* 353, 172–187. doi:10.1056/NEJMra044389.

Krüger, A., Sanchez-Sweatman, O. H., Martin, D. C., Fata, J. E., Ho, A. T., Orr, F. W., et al. (1998). Host TIMP-1 overexpression confers resistance to experimental brain metastasis of a fibrosarcoma cell line. *Oncogene* 16, 2419–2423. doi:10.1038/sj.onc.1201774.

Kumanogoh, A., Marukawa, S., Suzuki, K., Takegahara, N., Watanabe, C., Ch’ng, E., et al. (2002a). Class IV semaphorin Sema4A enhances T-cell activation and interacts with Tim-

2. *Nature* 419, 629–633. doi:10.1038/nature01037.

Kumanogoh, A., Shikina, T., Watanabe, C., Takegahara, N., Suzuki, K., Yamamoto, M., et al. (2005). Requirement for CD100–CD72 interactions in fine-tuning of B-cell antigen receptor signaling and homeostatic maintenance of the B-cell compartment. *Int. Immunol.* 17, 1277–1282. doi:10.1093/intimm/dxh307.

Kumanogoh, A., Suzuki, K., Ch'ng, E., Watanabe, C., Marukawa, S., Takegahara, N., et al. (2002b). Requirement for the lymphocyte semaphorin, CD100, in the induction of antigen-specific T cells and the maturation of dendritic cells. *J. Immunol.* 169, 1175–81. Available at: http://www.ncbi.nlm.nih.gov/pubmed/12133937 [Accessed March 5, 2018].

Kumanogoh, A., Watanabe, C., Lee, I., Wang, X., Shi, W., Araki, H., et al. (2000). Identification of CD72 as a lymphocyte receptor for the class IV semaphorin CD100: a novel mechanism for regulating B cell signaling. *Immunity* 13, 621–31. Available at: http://www.ncbi.nlm.nih.gov/pubmed/11114375 [Accessed December 25, 2017].

Kumar, S., Kapoor, A., Desai, S., Inamdar, M. M., and Sen, S. (2016). Proteolytic and non-proteolytic regulation of collective cell invasion: tuning by ECM density and organization. *Sci. Rep.* 6, 19905. doi:10.1038/srep19905.

L

Laoui, D., Van Overmeire, E., De Baetselier, P., Van Ginderachter, J. A., and Raes, G. (2014). Functional Relationship between Tumor-Associated Macrophages and Macrophage Colony-Stimulating Factor as Contributors to Cancer Progression. *Front. Immunol.* 5, 489. doi:10.3389/fimmu.2014.00489.

Lawrence, B., Gustafsson, B. I., Chan, A., Svejda, B., Kidd, M., and Modlin, I. M. (2011). The Epidemiology of Gastroenteropancreatic Neuroendocrine Tumors. *Endocrinol. Metab. Clin. North Am.* 40, 1–18. doi:10.1016/j.ecl.2010.12.005.

Lewis, A., Li, D., Williams, J., and Singh, G. (2017). Pancreatic Neuroendocrine Tumors: State-of-the-Art Diagnosis and Management. *Oncology (Williston Park).* 31, e1–e12. Available at: http://www.ncbi.nlm.nih.gov/pubmed/29083468 [Accessed July 26, 2018].

Liotta, L. A., and Kohn, E. C. (2001). The microenvironment of the tumour-host interface. *Nature* 411, 375–379. doi:10.1038/35077241.

Liu, H., Yang, Y., Xiao, J., Yang, S., Liu, Y., Kang, W., et al. (2014). Semaphorin 4D expression is associated with a poor clinical outcome in cervical cancer patients. *Microvasc. Res.* 93, 1–8. doi:10.1016/j.mvr.2014.02.007.

Liu, L., and Shi, G.-P. (2012). CD31: beyond a marker for endothelial cells. *Cardiovasc. Res.* 94, 3–5. doi:10.1093/cvr/cvs108.

Lloyd, R. V., Osamura, R. Y., Klöppel, G., Rosai, J., World Health Organization., and International Agency for Research on Cancer. (2017). *WHO classification of tumours of endocrine organs*. 4th ed. WHO Available at: http://publications.iarc.fr/Book-And-Report-Series/Who-Iarc-Classification-Of-Tumours/Who-Classification-Of-Tumours-Of-Endocrine-Organs-2017 [Accessed July 26, 2018].

Lontos, K., Adamik, J., Tsagianni, A., Galson, D. L., Chirgwin, J. M., and Suvannasankha, A. (2018). The Role of Semaphorin 4D in Bone Remodeling and Cancer Metastasis. *Front. Endocrinol. (Lausanne).* 9, 322. doi:10.3389/fendo.2018.00322.

Lopez, T., and Hanahan, D. (2002). Elevated levels of IGF-1 receptor convey invasive and metastatic capability in a mouse model of pancreatic islet tumorigenesis. Available at:

https://www.cell.com/cancer-cell/pdf/S1535-6108(02)00055-7.pdf [Accessed December 25, 2017].

Love, C. A., Harlos, K., Mavaddat, N., Davis, S. J., Stuart, D. I., Jones, E. Y., et al. (2003). The ligand-binding face of the semaphorins revealed by the high-resolution crystal structure of SEMA4D. *Nat. Struct. Mol. Biol.* 10, 843–848. doi:10.1038/nsb977.

Luque, M. C. A., Gutierrez, P. S., Debbas, V., Martins, W. K., Puech-Leao, P., Porto, G., et al. (2013). Phage display identification of CD100 in human atherosclerotic plaque macrophages and foam cells. *PLoS One* 8, e75772. doi:10.1371/journal.pone.0075772.

M

Maione, F., Capano, S., Regano, D., Zentilin, L., Giacca, M., Casanovas, O., et al. (2012). Semaphorin 3A overcomes cancer hypoxia and metastatic dissemination induced by antiangiogenic treatment in mice. *J Clin Invest* 122, 1832–1848. doi:58976 [pii]10.1172/JCI58976.

Maione, F., Molla, F., Meda, C., Latini, R., Zentilin, L., Giacca, M., et al. (2009). Semaphorin 3A is an endogenous angiogenesis inhibitor that blocks tumor growth and normalizes tumor vasculature in transgenic mouse models. *J Clin Invest* 119, 3356–3372. doi:36308 [pii]10.1172/JCI36308.

Malik, M. F. A., Ye, L., and Jiang, W. G. (2014). The Plexin-B family and its role in cancer progression. *Histol. Histopathol.* 29, 151–65. doi:10.14670/HH-29.151.

MALIK, M. F. A., YE, L., and JIANG, W. G. (2015). Reduced expression of semaphorin 4D and plexin-B in breast cancer is associated with poorer prognosis and the potential linkage with oestrogen receptor. *Oncol. Rep.* 34, 1049–1057. doi:10.3892/or.2015.4015.

Mantovani, A., Bottazzi, B., Colotta, F., Sozzani, S., and Ruco, L. (1992). The origin and function of tumor-associated macrophages. *Immunol. Today* 13, 265–270. doi:10.1016/0167-5699(92)90008-U.

Mao, W., Yi, X., Qin, J., Tian, M., and Jin, G. (2016). CXCL12/CXCR4 Axis Improves Migration of Neuroblasts Along Corpus Callosum by Stimulating MMP-2 Secretion After Traumatic Brain Injury in Rats. *Neurochem. Res.* 41, 1315–1322. doi:10.1007/s11064-016-1831-2.

Martín-Mitjana, L. (2014). Study of tumor malignization as a result of semaphorin 4D blockade in a pancreatic neuroendocrine tumor mouse model.

Martinez, F. O., Gordon, S., Locati, M., and Mantovani, A. (2006). Transcriptional profiling of the human monocyte-to-macrophage differentiation and polarization: new molecules and patterns of gene expression. *J. Immunol.* 177, 7303–11. Available at: http://www.ncbi.nlm.nih.gov/pubmed/17082649 [Accessed July 22, 2018].

Massironi, S., Sciola, V., Peracchi, M., Ciafardini, C., Spampatti, M. P., and Conte, D. (2008). Neuroendocrine tumors of the gastro-entero-pancreatic system. *World J. Gastroenterol.* 14, 5377–84. doi:10.3748/wjg.14.5377.

Meehan, T. F., Witherden, D. A., Kim, C.-H., Sendaydiego, K., Ye, I., Garijo, O., et al. (2014). Protection against colitis by CD100-dependent modulation of intraepithelial γδ T lymphocyte function. *Mucosal Immunol.* 7, 134–142. doi:10.1038/mi.2013.32.

Mendel, D. B., Laird, A. D., Xin, X., Louie, S. G., Christensen, J. G., Li, G., et al. (2003). In vivo antitumor activity of SU11248, a novel tyrosine kinase inhibitor targeting vascular endothelial growth factor and platelet-derived growth factor receptors: determination of a pharmacokinetic/pharmacodynamic relationship. *Clin. Cancer Res.* 9, 327–37. Available at: http://www.ncbi.nlm.nih.gov/pubmed/12538485 [Accessed July 27, 2018].

Meng, W., Xue, S., and Chen, Y. (2018). The role of CXCL12 in tumor microenvironment. *Gene* 641, 105–110. doi:10.1016/j.gene.2017.10.015.

Miller, B., Sheppard, A. M., Bicknese, A. R., and Pearlman, A. L. (1995). Chondroitin sulfate proteoglycans in the developing cerebral cortex: The distribution of neurocan distinguishes forming afferent and efferent axonal pathways. *J. Comp. Neurol.* 355, 615–628. doi:10.1002/cne.903550410.

Missiaglia, E., Dalai, I., Barbi, S., Beghelli, S., Falconi, M., della Peruta, M., et al. (2009). Pancreatic endocrine tumors: expression profiling evidences a role for AKT-mTOR pathway. *J Clin Oncol* 28, 245–255. doi:JCO.2008.21.5988 [pii] 10.1200/JCO.2008.21.5988.

Mitchem, J. B., Brennan, D. J., Knolhoff, B. L., Belt, B. A., Zhu, Y., Sanford, D. E., et al. (2013). Targeting Tumor-Infiltrating Macrophages Decreases Tumor-Initiating Cells, Relieves Immunosuppression, and Improves Chemotherapeutic Responses. *Cancer Res.* 73, 1128–1141. doi:10.1158/0008-5472.CAN-12-2731.

Miyato, H., Tsuno, N. H., and Kitayama, J. (2012). Semaphorin 3C is involved in the progression of gastric cancer. *Cancer Sci.* 103, 1961–1966. doi:10.1111/cas.12003.

Mo, H.-N., and Liu, P. (2017). Targeting MET in cancer therapy. *Chronic Dis. Transl. Med.* 3, 148–153. doi:10.1016/j.cdtm.2017.06.002.

Mori, T., Doi, R., Koizumi, M., Toyoda, E., Ito, D., Kami, K., et al. (2004). CXCR4 antagonist inhibits stromal cell-derived factor 1-induced migration and invasion of human pancreatic cancer. *Mol. Cancer Ther.* 3, 29–37. Available at: http://www.ncbi.nlm.nih.gov/pubmed/14749473 [Accessed July 16, 2018].

Morikawa, S., Baluk, P., Kaidoh, T., Haskell, A., Jain, R. K., and McDonald, D. M. (2002). Abnormalities in pericytes on blood vessels and endothelial sprouts in tumors. *Am. J. Pathol.* 160, 985–1000. doi:10.1016/S0002-9440(10)64920-6.

Mosser, D. M., and Edwards, J. P. (2008). Exploring the full spectrum of macrophage activation. *Nat. Rev. Immunol.* 8, 958–69. doi:10.1038/nri2448.

Mu, L., Wang, J., Chen, Y., Li, L., Guo, X., Zheng, S., et al. (2014). Hypoxia-inducible factor-1α and semaphorin4D genes involved with tumor-associated macrophage-induced metastatic behavior and clinical significance in colon cancer. *Chin. Med. J. (Engl).* 127, 3568–75. Available at: http://www.ncbi.nlm.nih.gov/pubmed/25316231 [Accessed July 27, 2018].

N

Nagasawa, T., Hirota, S., Tachibana, K., Takakura, N., Nishikawa, S., Kitamura, Y., et al. (1996). Defects of B-cell lymphopoiesis and bone-marrow myelopoiesis in mice lacking the CXC chemokine PBSF/SDF-1. *Nature* 382, 635–638. doi:10.1038/382635a0.

Negishi, M., Oinuma, I., and Katoh, H. (2005a). Plexins: axon guidance and signal transduction. *Cell. Mol. Life Sci.* 62, 1363–1371. doi:10.1007/s00018-005-5018-2.

Negishi, M., Oinuma, I., and Katoh, H. (2005b). R-Ras As a Key Player for Signaling Pathway of Plexins. *Mol. Neurobiol.* 32, 217–222. doi:10.1385/MN:32:3:217.

Neufeld, G., Mumblat, Y., Smolkin, T., Toledano, S., Nir-Zvi, I., Ziv, K., et al. (2016). The role of the semaphorins in cancer. *Cell Adh. Migr.* 10, 652–674.

doi:10.1080/19336918.2016.1197478.

Nguyen, D. X., Bos, P. D., and Massagué, J. (2009). Metastasis: from dissemination to organ-specific colonization. *Nat. Rev. Cancer* 9, 274–284. doi:10.1038/nrc2622.

O

Oberndofer, S. (1907). Karzinoide tumoren des dünndarms. *Frankf Z Pathol* 1, 426–43.

Oinuma, I., Katoh, H., and Negishi, M. (2006). Semaphorin 4D/Plexin-B1–mediated R-Ras GAP activity inhibits cell migration by regulating β_1 integrin activity. *J. Cell Biol.* 173, 601–613. doi:10.1083/jcb.200508204.

Ostuni, R., Kratochvill, F., Murray, P. J., and Natoli, G. (2015). Macrophages and cancer: from mechanisms to therapeutic implications. doi:10.1016/j.it.2015.02.004.

Overall, C. M., and López-Otín, C. (2002). Strategies for MMP inhibition in cancer: innovations for the post-trial era. *Nat. Rev. Cancer* 2, 657–672. doi:10.1038/nrc884.

P

Padua, D., Zhang, X. H.-F., Wang, Q., Nadal, C., Gerald, W. L., Gomis, R. R., et al. (2008). TGFβ Primes Breast Tumors for Lung Metastasis Seeding through Angiopoietin-like 4. *Cell* 133, 66–77. doi:10.1016/j.cell.2008.01.046.

Pàez-Ribes, M. (2010). La resistencia adaptativa a terapias antiangiogénicas en un modelo murino de cáncer.

Pàez-Ribes, M., Allen, E., Hudock, J., Takeda, T., Okuyama, H., Viñals, F., et al. (2009). Antiangiogenic therapy elicits malignant progression of tumors to increased local invasion and distant metastasis. *Cancer Cell* 15, 220–31. doi:10.1016/j.ccr.2009.01.027.

Pan, G., Lv, H., Ren, H., Wang, Y., Liu, Y., Jiang, H., et al. (2010). Elevated expression of semaphorin 5A in human gastric cancer and its implication in carcinogenesis. *Life Sci* 86, 139–144. doi:S0024-3205(09)00491-3 [pii]10.1016/j.lfs.2009.12.004.

Parnes, J. R., and Pan, C. (2000). CD72, a negative regulator of B-cell responsiveness. *Immunol. Rev.* 176, 75–85. Available at: http://www.ncbi.nlm.nih.gov/pubmed/11043769 [Accessed July 27, 2018].

Patnaik, A., Weiss, G. J., Leonard, J. E., Rasco, D. W., Sachdev, J. C., Fisher, T. L., et al. (2016). Safety, Pharmacokinetics, and Pharmacodynamics of a Humanized Anti-Semaphorin 4D Antibody, in a First-In-Human Study of Patients with Advanced Solid Tumors. *Clin. Cancer Res.* 22, 827–836. doi:10.1158/1078-0432.CCR-15-0431.

Pawig, L., Klasen, C., Weber, C., Bernhagen, J., and Noels, H. (2015). Diversity and Inter-Connections in the CXCR4 Chemokine Receptor/Ligand Family: Molecular Perspectives. *Front. Immunol.* 6, 429. doi:10.3389/fimmu.2015.00429.

Pennacchietti, S., Michieli, P., Galluzzo, M., Mazzone, M., Giordano, S., and Comoglio, P. M. (2003). Hypoxia promotes invasive growth by transcriptional activation of the met protooncogene. *Cancer Cell* 3, 347–61. Available at: http://www.ncbi.nlm.nih.gov/pubmed/12726861 [Accessed December 25, 2017].

Perkins, D. N., Pappin, D. J. C., Creasy, D. M., and Cottrell, J. S. (1999). Probability-based protein identification by searching sequence databases using mass spectrometry data. *Electrophoresis* 20, 3551–3567. doi:10.1002/(SICI)1522-

2683(19991201)20:18<3551::AID-ELPS3551>3.0.CO;2-2.

Perl, A.-K., Wilgenbus, P., Dahl, U., Semb, H., and Christofori, G. (1998). A causal role for E-cadherin in the transition from adenoma to carcinoma. *Nature* 392, 190–193. doi:10.1038/32433.

Pietras, K., and Hanahan, D. (2005). A Multitargeted, Metronomic, and Maximum-Tolerated Dose “Chemo-Switch” Regimen is Antiangiogenic, Producing Objective Responses and Survival Benefit in a Mouse Model of Cancer. *J. Clin. Oncol.* 23, 939–952. doi:10.1200/JCO.2005.07.093.

Pircher, A., Wellbrock, J., Fiedler, W., Heidegger, I., Gunsilius, E., and Hilbe, W. (2014). New Antiangiogenic Strategies beyond Inhibition of Vascular Endothelial Growth Factor with Special Focus on Axon Guidance Molecules. *Oncology* 86, 46–52. doi:10.1159/000356871.

Poh, A. R., and Ernst, M. (2018). Targeting Macrophages in Cancer: From Bench to Bedside. *Front. Oncol.* 8, 49. doi:10.3389/fonc.2018.00049.

Porta, C., Riboldi, E., Ippolito, A., and Sica, A. (2015). Molecular and epigenetic basis of macrophage polarized activation. *Semin. Immunol.* 27, 237–248. doi:10.1016/j.smim.2015.10.003.

Püschel, A. W. (2007). “GTPases in Semaphorin Signaling,” in *Semaphorins: Receptor and Intracellular Signaling Mechanisms* (New York, NY: Springer New York), 12–23. doi:10.1007/978-0-387-70956-7_2.

Q

Qian, B.-Z., and Pollard, J. W. (2010). Macrophage Diversity Enhances Tumor Progression and Metastasis. *Cell* 141, 39–51. doi:10.1016/J.CELL.2010.03.014.

Quail, D. F., and Joyce, J. A. (2013). Microenvironmental regulation of tumor progression and metastasis. *Nat. Med.* 19, 1423–1437. doi:10.1038/nm.3394.

R

Radisky, D., Hagios, C., and Bissell, M. J. (2001). Tumors are unique organs defined by abnormal signaling and context. *Semin. Cancer Biol.* 11, 87–95. doi:10.1006/scbi.2000.0360.

Rappsilber, J., Mann, M., and Ishihama, Y. (2007). Protocol for micro-purification, enrichment, pre-fractionation and storage of peptides for proteomics using StageTips. *Nat. Protoc.* 2, 1896–1906. doi:10.1038/nprot.2007.261.

Ray, P., Lewin, S. A., Mihalko, L. A., Schmidt, B. T., Luker, K. E., and Luker, G. D. (2011). Noninvasive imaging reveals inhibition of ovarian cancer by targeting CXCL12-CXCR4. *Neoplasia* 13, 1152–61. Available at: http://www.ncbi.nlm.nih.gov/pubmed/22241961 [Accessed July 16, 2018].

Ray, P., Stacer, A. C., Fenner, J., Cavnar, S. P., Meguiar, K., Brown, M., et al. (2015). CXCL12-γ in primary tumors drives breast cancer metastasis. *Oncogene* 34, 2043–2051. doi:10.1038/onc.2014.157.

Raymond, E., Dahan, L., Raoul, J.-L., Bang, Y.-J., Borbath, I., Lombard-Bohas, C., et al. (2011). Sunitinib Malate for the Treatment of Pancreatic Neuroendocrine Tumors. *N. Engl. J. Med.* 364, 501–513. doi:10.1056/NEJMoa1003825.

Rehman, M., and Tamagnone, L. (2013). Semaphorins in cancer: Biological mechanisms and therapeutic approaches. *Semin. Cell Dev. Biol.* 24, 179–189. doi:10.1016/j.semcdb.2012.10.005.

Ribeiro, A. L., and Okamoto, O. K. (2015). Combined effects of pericytes in the tumor microenvironment. *Stem Cells Int.* 2015, 868475. doi:10.1155/2015/868475.

Robinson, W. H., Landolfi, M. M., and Parnes, J. R. (1997). Allele-specific expression of the mouse B-cell surface protein CD72 on T cells. *Immunogenetics* 45, 195–200. Available at: http://www.ncbi.nlm.nih.gov/pubmed/8995186 [Accessed March 5, 2018].

Roodink, I., Kats, G., van Kempen, L., Grunberg, M., Maass, C., Verrijp, K., et al. (2008). Semaphorin 3E expression correlates inversely with Plexin D1 during tumor progression. *Am J Pathol* 173, 1873–1881. doi:S0002-9440(10)61570-2 [pii]10.2353/ajpath.2008.080136.

Roy, J.-S., Van Themsche, C., Demers, M., Opdenakker, G., Arnold, B., and St-Pierre, Y. (2007). Triggering of T-cell leukemia and dissemination of T-cell lymphoma in MMP-9-deficient mice. *Leukemia* 21, 2506–2511. doi:10.1038/sj.leu.2404936.

S

Sadanandam, A., Rosenbaugh, E. G., Singh, S., Varney, M., and Singh, R. K. (2010a). Semaphorin 5A promotes angiogenesis by increasing endothelial cell proliferation, migration, and decreasing apoptosis. *Microvasc. Res.* 79, 1–9. doi:10.1016/j.mvr.2009.10.005.

Sadanandam, A., Sidhu, S. S., Wullschleger, S., Singh, S., Varney, M. L., Yang, C. S., et al. (2012). Secreted semaphorin 5A suppressed pancreatic tumour burden but increased metastasis and endothelial cell proliferation. *Br J Cancer* 107, 501–507. doi:bjc2012298 [pii]10.1038/bjc.2012.298.

Sadanandam, A., Varney, M. L., Kinarsky, L., Ali, H., Mosley, R. L., and Singh, R. K. (2007). Identification of functional cell adhesion molecules with a potential role in metastasis by a combination of in vivo phage display and in silico analysis. *OMICS* 11, 41–57. doi:10.1089/omi.2006.0004.

Sadanandam, A., Varney, M. L., Singh, S., Ashour, A. E., Moniaux, N., Deb, S., et al. (2010b). High gene expression of semaphorin 5A in pancreatic cancer is associated with tumor growth, invasion and metastasis. *Int J Cancer* 127, 1373–1383. doi:10.1002/ijc.25166.

Sadanandam, A., Wullschleger, S., Lyssiotis, C. A., Grotzinger, C., Barbi, S., Bersani, S., et al. (2015). A Cross-Species Analysis in Pancreatic Neuroendocrine Tumors Reveals Molecular Subtypes with Distinctive Clinical, Metastatic, Developmental, and Metabolic Characteristics. *Cancer Discov.* 5, 1296–1313. doi:10.1158/2159-8290.CD-15-0068.

Salvucci, O., Yao, L., Villalba, S., Sajewicz, A., Pittaluga, S., and Tosato, G. (2002). Regulation of endothelial cell branching morphogenesis by endogenous chemokine stromal-derived factor-1. *Blood* 99, 2703–11. Available at: http://www.ncbi.nlm.nih.gov/pubmed/11929756 [Accessed July 16, 2018].

Scarpa, A., Chang, D. K., Nones, K., Corbo, V., Patch, A.-M., Bailey, P., et al. (2017). Whole-genome landscape of pancreatic neuroendocrine tumours. *Nature* 543, 65–71. doi:10.1038/nature21063.

Schindl, M., Schoppmann, S. F., Samonigg, H., Hausmaninger, H., Kwasny, W., Gnant, M., et al. (2002). Overexpression of hypoxia-inducible factor 1alpha is associated with an unfavorable prognosis in lymph node-positive breast cancer. *Clin. Cancer Res.* 8, 1831–7. Available at: http://www.ncbi.nlm.nih.gov/pubmed/12060624 [Accessed December 25, 2017].

Schwarz, Q., Gu, C., Fujisawa, H., Sabelko, K., Gertsenstein, M., Nagy, A., et al. (2004). Vascular endothelial growth factor controls neuronal migration and cooperates with Sema3A to pattern distinct compartments of the facial nerve. *Genes Dev.* 18, 2822–2834. doi:10.1101/gad.322904.

Semenza, G. L. (2002). HIF-1 and tumor progression: pathophysiology and therapeutics. *Trends Mol. Med.* 8, S62-7. Available at: http://www.ncbi.nlm.nih.gov/pubmed/11927290 [Accessed December 25, 2017].

Sennino, B., Ishiguro-Oonuma, T., Wei, Y., Naylor, R. M., Williamson, C. W., Bhagwandin, V., et al. (2012). Suppression of tumor invasion and metastasis by concurrent inhibition of c-Met and VEGF signaling in pancreatic neuroendocrine tumors. *Cancer Discov.* 2, 270–87. doi:10.1158/2159-8290.CD-11-0240.

Serini, G., Valdembri, D., Zanivan, S., Morterra, G., Burkhardt, C., Caccavari, F., et al. (2003). Class 3 semaphorins control vascular morphogenesis by inhibiting integrin function. *Nature* 424, 391–397. doi:10.1038/nature01784nature01784 [pii].

Sherwood, L. M., Parris, E. E., and Folkman, J. (1971). Tumor Angiogenesis: Therapeutic Implications. *N. Engl. J. Med.* 285, 1182–1186. doi:10.1056/NEJM197111182852108.

Sica, A., Erreni, M., Allavena, P., and Porta, C. (2015). Macrophage polarization in pathology. *Cell. Mol. Life Sci.* 72, 4111–4126. doi:10.1007/s00018-015-1995-y.

Sierra, J. R., Corso, S., Caione, L., Cepero, V., Conrotto, P., Cignetti, A., et al. (2008). Tumor angiogenesis and progression are enhanced by Sema4D produced by tumor-associated macrophages. *J. Exp. Med.* 205, 1673–1685. doi:10.1084/jem.20072602.

Singh, M., Couto, S. S., Forrest, W. F., Lima, A., Cheng, J. H., Molina, R., et al. (2012). Anti-VEGF antibody therapy does not promote metastasis in genetically engineered mouse tumour models. *J. Pathol.* 227, 417–430. doi:10.1002/path.4053.

Skobe, M., Hawighorst, T., Jackson, D. G., Prevo, R., Janes, L., Velasco, P., et al. (2001). Induction of tumor lymphangiogenesis by VEGF-C promotes breast cancer metastasis. *Nat. Med.* 7, 192–198. doi:10.1038/84643.

Smith, E. S., Jonason, A., Reilly, C., Veeraraghavan, J., Fisher, T., Doherty, M., et al. (2015). SEMA4D compromises blood–brain barrier, activates microglia, and inhibits remyelination in neurodegenerative disease. *Neurobiol. Dis.* 73, 254–268. doi:10.1016/j.nbd.2014.10.008.

Soker, S., Takashima, S., Miao, H. Q., Neufeld, G., and Klagsbrun, M. (1998). Neuropilin-1 is expressed by endothelial and tumor cells as an isoform-specific receptor for vascular endothelial growth factor. *Cell* 92, 735–45. Available at: http://www.ncbi.nlm.nih.gov/pubmed/9529250 [Accessed July 27, 2018].

Soong, J., Chen, Y., Shustef, E. M., and Scott, G. A. (2012). Sema4D, the ligand for Plexin B1, suppresses c-Met activation and migration and promotes melanocyte survival and growth. *J. Invest. Dermatol.* 132, 1230–8. doi:10.1038/jid.2011.414.

Southwell, A. L., Franciosi, S., Villanueva, E. B., Xie, Y., Winter, L. A., Veeraraghavan, J., et al. (2015). Anti-semaphorin 4D immunotherapy ameliorates neuropathology and some cognitive impairment in the YAC128 mouse model of Huntington disease. *Neurobiol. Dis.* 76, 46–56. doi:10.1016/j.nbd.2015.01.002.

Spranger, S., and Gajewski, T. F. (2016). Tumor-intrinsic oncogene pathways mediating immune avoidance. *Oncoimmunology* 5, e1086862. doi:10.1080/2162402X.2015.1086862.

Stevens, L., McClelland, L., Fricke, A., Williamson, M., Kuo, Ih., and Scott, G. (2010). Plexin B1 Suppresses c-Met in Melanoma: A Role for Plexin B1 as a Tumor-Suppressor Protein through Regulation of c-Met. *J. Invest. Dermatol.* 130, 1636–1645. doi:10.1038/jid.2010.13.

Stuelten, C. H., DaCosta Byfield, S., Arany, P. R., Karpova, T. S., Stetler-Stevenson, W. G., and Roberts, A. B. (2005). Breast cancer cells induce stromal fibroblasts to express MMP-9 via secretion of TNF-alpha and TGF-beta. *J. Cell Sci.* 118, 2143–53. doi:10.1242/jcs.02334.

Subramanian, A., Tamayo, P., Mootha, V. K., Mukherjee, S., Ebert, B. L., Gillette, M. A., et al. (2005). Gene set enrichment analysis: A knowledge-based approach for interpreting genome-wide expression profiles. *Proc. Natl. Acad. Sci.* 102, 15545–15550. doi:10.1073/pnas.0506580102.

Sun, Y.-X., Schneider, A., Jung, Y., Wang, J., Dai, J., Wang, J., et al. (2004). Skeletal Localization and Neutralization of the SDF-1(CXCL12)/CXCR4 Axis Blocks Prostate Cancer Metastasis and Growth in Osseous Sites In Vivo. *J. Bone Miner. Res.* 20, 318–329. doi:10.1359/JBMR.041109.

Suzuki, K., Kumanogoh, A., and Kikutani, H. (2008). Semaphorins and their receptors in immune cell interactions. *Nat. Immunol.* 9, 17–23. doi:10.1038/ni1553.

Swiercz, J. M., Kuner, R., and Offermanns, S. (2004). Plexin-B1/RhoGEF-mediated RhoA activation involves the receptor tyrosine kinase ErbB-2. *J. Cell Biol.* 165, 869–80. doi:10.1083/jcb.200312094.

Swiercz, J. M., Worzfeld, T., and Offermanns, S. (2008). ErbB-2 and met reciprocally regulate cellular signaling via plexin-B1. *J. Biol. Chem.* 283, 1893–901. doi:10.1074/jbc.M706822200.

Szebeni, G. J., Vizler, C., Kitajka, K., and Puskas, L. G. (2017). Inflammation and Cancer: Extra- and Intracellular Determinants of Tumor-Associated Macrophages as Tumor Promoters. *Mediators Inflamm.* 2017, 9294018. doi:10.1155/2017/9294018.

Szklarczyk, D., Franceschini, A., Wyder, S., Forslund, K., Heller, D., Huerta-Cepas, J., et al. (2015). STRING v10: protein-protein interaction networks, integrated over the tree of life. *Nucleic Acids Res.* 43, D447-52. doi:10.1093/nar/gku1003.

T

Taciak, B., Białasek, M., Braniewska, A., Sas, Z., Sawicka, P., Kiraga, Ł., et al. (2018). Evaluation of phenotypic and functional stability of RAW 264.7 cell line through serial passages. *PLoS One* 13, e0198943. doi:10.1371/journal.pone.0198943.

Taichman, R. S., Cooper, C., Keller, E. T., Pienta, K. J., Taichman, N. S., and McCauley, L. K. (2002). Use of the stromal cell-derived factor-1/CXCR4 pathway in prostate cancer metastasis to bone. *Cancer Res.* 62, 1832–7. Available at: http://www.ncbi.nlm.nih.gov/pubmed/11912162 [Accessed August 24, 2018].

Teixidó, J., Martínez-Moreno, M., Díaz-Martínez, M., and Sevilla-Movilla, S. (2018). The good and bad faces of the CXCR4 chemokine receptor. *Int. J. Biochem. Cell Biol.* 95, 121–131. doi:10.1016/j.biocel.2017.12.018.

Thurston, G., Rudge, J. S., Ioffe, E., Zhou, H., Ross, L., Croll, S. D., et al. (2000). Angiopoietin-

1 protects the adult vasculature against plasma leakage. *Nat. Med.* 6, 460–463. doi:10.1038/74725.

Toguchi, M., Gonzalez, D., Furukawa, S., and Inagaki, S. (2009). Involvement of Sema4D in the control of microglia activation. *Neurochem. Int.* 55, 573–580. doi:10.1016/j.neuint.2009.05.013.

Tong, Y., Hota, P. K., Penachioni, J. Y., Hamaneh, M. B., Kim, S., Alviani, R. S., et al. (2009). Structure and Function of the Intracellular Region of the Plexin-B1 Transmembrane Receptor. *J. Biol. Chem.* 284, 35962–35972. doi:10.1074/jbc.M109.056275.

V

Valente, G., Nicotra, G., Arrondini, M., Castino, R., Capparuccia, L., Prat, M., et al. (2009). Co-expression of plexin-B1 and Met in human breast and ovary tumours enhances the risk of progression. *Cell. Oncol.* 31, 423–36. doi:10.3233/CLO-2009-0504.

Vandooren, J., Van den Steen, P. E., and Opdenakker, G. (2013). Biochemistry and molecular biology of gelatinase B or matrix metalloproteinase-9 (MMP-9): The next decade. *Crit. Rev. Biochem. Mol. Biol.* 48, 222–272. doi:10.3109/10409238.2013.770819.

Varshavsky, A., Kessler, O., Abramovitch, S., Kigel, B., Zaffryar, S., Akiri, G., et al. (2008). Semaphorin-3B is an angiogenesis inhibitor that is inactivated by furin-like pro-protein convertases. *Cancer Res* 68, 6922–6931. doi:68/17/6922 [pii]10.1158/0008-5472.CAN-07-5408.

Vaupel, P. (2004). The Role of Hypoxia-Induced Factors in Tumor Progression. *Oncologist* 9, 10–17. doi:10.1634/theoncologist.9-90005-10.

Viallard, C., and Larrivée, B. (2017). Tumor angiogenesis and vascular normalization: alternative therapeutic targets. *Angiogenesis* 20, 409–426. doi:10.1007/s10456-017-9562-9.

Vogelstein, B., and Kinzler, K. W. (1993). The multistep nature of cancer. *Trends Genet.* 9, 138–41. Available at: http://www.ncbi.nlm.nih.gov/pubmed/8516849 [Accessed July 26, 2018].

von Tell, D., Armulik, A., and Betsholtz, C. (2006). Pericytes and vascular stability. *Exp. Cell Res.* 312, 623–9. doi:10.1016/j.yexcr.2005.10.019.

W

Wang, J. S., Jing, C. Q., Shan, K. S., Chen, Y. Z., Guo, X. B., Cao, Z. X., et al. (2015). Semaphorin 4D and hypoxia-inducible factor-1alpha overexpression is related to prognosis in colorectal carcinoma. *World J Gastroenterol* 21, 2191–2198. doi:10.3748/wjg.v21.i7.2191.

Wang, J., Shiozawa, Y., Wang, J., Wang, Y., Jung, Y., Pienta, K. J., et al. (2008). The Role of CXCR7/RDC1 as a Chemokine Receptor for CXCL12/SDF-1 in Prostate Cancer. *J. Biol. Chem.* 283, 4283–4294. doi:10.1074/jbc.M707465200.

Weiskopf, K., and Weissman, I. L. (2015). Macrophages are critical effectors of antibody therapies for cancer. *MAbs* 7, 303–10. doi:10.1080/19420862.2015.1011450.

Witherden, D. A., Watanabe, M., Garijo, O., Rieder, S. E., Sarkisyan, G., Cronin, S. J. F., et al. (2012). The CD100 receptor interacts with its plexin B2 ligand to regulate epidermal γδ T cell function. *Immunity* 37, 314–25. doi:10.1016/j.immuni.2012.05.026.

Worzfeld, T., and Offermanns, S. (2014). Semaphorins and plexins as therapeutic targets. *Nat. Rev. Drug Discov.* 13, 603–621. doi:10.1038/nrd4337.

Wu, M., Li, J., Gao, Q., and Ye, F. (2016). The role of Sema4D/CD100 as a therapeutic target for tumor microenvironments and for autoimmune, neuroimmune and bone diseases. *Expert Opin. Ther. Targets* 20, 885–901. doi:10.1517/14728222.2016.1139083.

Wyckoff, J. B., Wang, Y., Lin, E. Y., Li, J. -f., Goswami, S., Stanley, E. R., et al. (2007). Direct Visualization of Macrophage-Assisted Tumor Cell Intravasation in Mammary Tumors. *Cancer Res.* 67, 2649–2656. doi:10.1158/0008-5472.CAN-06-1823.

X

Xue, J., Schmidt, S. V., Sander, J., Draffehn, A., Krebs, W., Quester, I., et al. (2014). Transcriptome-Based Network Analysis Reveals a Spectrum Model of Human Macrophage Activation. *Immunity* 40, 274–288. doi:10.1016/j.immuni.2014.01.006.

Y

Yang, L., Jackson, E., Woerner, B. M., Perry, A., Piwnica-Worms, D., and Rubin, J. B. (2007). Blocking CXCR4-Mediated Cyclic AMP Suppression Inhibits Brain Tumor Growth In vivo. *Cancer Res.* 67, 651–658. doi:10.1158/0008-5472.CAN-06-2762.

Yang, Y.-H., Zhou, H., Binmadi, N. O., Proia, P., and Basile, J. R. (2011). Plexin-B1 Activates NF-κB and IL-8 to Promote a Pro-Angiogenic Response in Endothelial Cells. *PLoS One* 6, e25826. doi:10.1371/journal.pone.0025826.

Yao, J. C., Hassan, M., Phan, A., Dagohoy, C., Leary, C., Mares, J. E., et al. (2008). One hundred years after "carcinoid": epidemiology of and prognostic factors for neuroendocrine tumors in 35,825 cases in the United States. *J. Clin. Oncol.* 26, 3063–72. doi:10.1200/JCO.2007.15.4377.

Yao, V. J., Sennino, B., Davis, R. B., Christensen, J., Hu-Lowe, D., Roberts, G., et al. (2006). Combined anti-VEGFR and anti-PDGFR actions of sunitinib on blood vessels in preclinical tumor models. *Eur. J. Cancer Suppl.* 4, 27–28. doi:10.1016/S1359-6349(06)70084-2.

Yap, T. A., Sandhu, S. K., Alam, S. M., and de Bono, J. S. (2011). HGF/c-MET targeted therapeutics: novel strategies for cancer medicine. *Curr. Drug Targets* 12, 2045–58. Available at: http://www.ncbi.nlm.nih.gov/pubmed/21777195 [Accessed July 27, 2018].

You, W.-K., Sennino, B., Williamson, C. W., Falcón, B., Hashizume, H., Yao, L.-C., et al. (2011). VEGF and c-Met blockade amplify angiogenesis inhibition in pancreatic islet cancer. *Cancer Res.* 71, 4758–68. doi:10.1158/0008-5472.CAN-10-2527.

Younis, R. H., Han, K. L., and Webb, T. J. (2016). Human Head and Neck Squamous Cell Carcinoma–Associated Semaphorin 4D Induces Expansion of Myeloid-Derived Suppressor Cells. *J. Immunol.* 196, 1419–1429. doi:10.4049/jimmunol.1501293.

Z

Zanoni, M., Piccinini, F., Arienti, C., Zamagni, A., Santi, S., Polico, R., et al. (2015). 3D tumor spheroid models for in vitro therapeutic screening: a systematic approach to enhance the biological relevance of data obtained. *Nat. Publ. Gr.* doi:10.1038/srep19103.

Zhong, H., De Marzo, A. M., Laughner, E., Lim, M., Hilton, D. A., Zagzag, D., et al. (1999).

Overexpression of hypoxia-inducible factor 1alpha in common human cancers and their metastases. *Cancer Res.* 59, 5830–5. Available at: http://www.ncbi.nlm.nih.gov/pubmed/10582706 [Accessed June 5, 2018].

Zhou, C., Zhang, J., Zheng, Y., and Zhu, Z. (2012a). Pancreatic neuroendocrine tumors: a comprehensive review. *Int J Cancer* 131, 1013–1022. doi:10.1002/ijc.27543.

Zhou, H., Binmadi, N. O., Yang, Y.-H., Proia, P., and Basile, J. R. (2012b). Semaphorin 4D cooperates with VEGF to promote angiogenesis and tumor progression. *Angiogenesis* 15, 391–407. doi:10.1007/s10456-012-9268-y.

Zhou, H., Yang, Y.-H., and Basile, J. R. (2014). The Semaphorin 4D-Plexin-B1-RhoA signaling axis recruits pericytes and regulates vascular permeability through endothelial production of PDGF-B and ANGPTL4. *Angiogenesis* 17, 261–74. doi:10.1007/s10456-013-9395-0.

Zhou, H., Yang, Y.-H., Binmadi, N. O., Proia, P., and Basile, J. R. (2012c). The hypoxia-inducible factor-responsive proteins semaphorin 4D and vascular endothelial growth factor promote tumor growth and angiogenesis in oral squamous cell carcinoma. *Exp. Cell Res.* 318, 1685–1698. doi:10.1016/j.yexcr.2012.04.019.

Zlotnik, A., and Yoshie, O. (2012). The chemokine superfamily revisited. *Immunity* 36, 705–16. doi:10.1016/j.immuni.2012.05.008.

Zuazo-Gaztelu, I., and Casanovas, O. (2018). Unraveling the Role of Angiogenesis in Cancer Ecosystems. *Front. Oncol.* 8, 248. doi:10.3389/fonc.2018.00248.

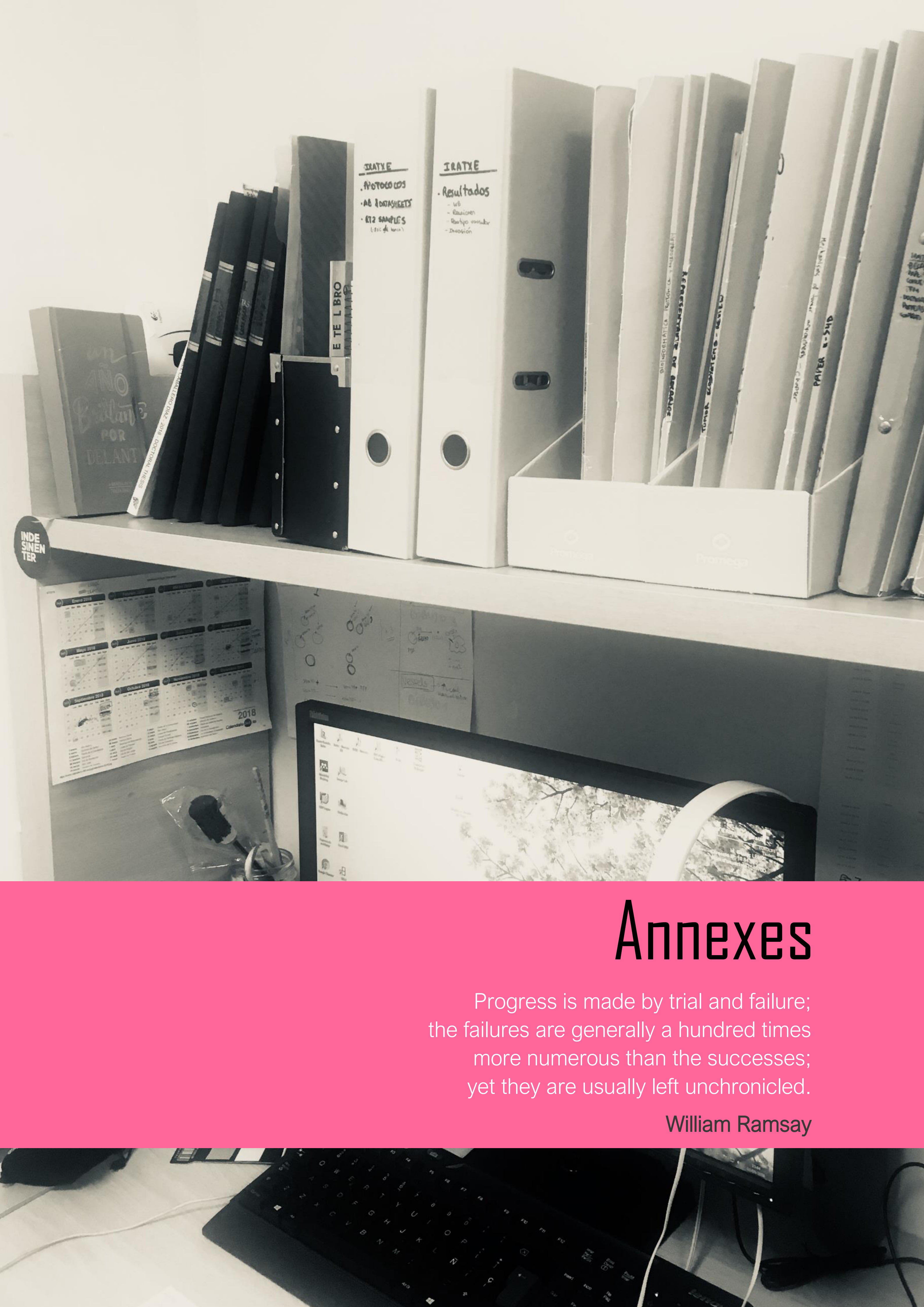

Annexes

Progress is made by trial and failure;
the failures are generally a hundred times
more numerous than the successes;
yet they are usually left unchronicled.

William Ramsay

Annexes

Annex 1 **Ranked list of proteins present in Sema4D treated macrophage conditioned media obtained in the GSEA analysis of the proteomic data.** Proteins are listed according to their rank metric score, which is the score used to position the gene in the ranked list of genes of the GSEA. Values are obtained from comparing Sema4D treated RAW conditioned media versus REST, which includes untreated, IgG treated and anti-Sema4D added RAW conditioned media. GSEA analysis was performed under standard conditions (explained in Materials & Methods) in November 2015.

Protein symbol	***Protein name***	***Rank metric score***
4F2	4F2 cell-surface antigen heavy chain	2.5000
PLOD3	Procollagen-lysine,2-oxoglutarate 5-dioxygenase 3	1.4815
ELOB	Transcription elongation factor B polypeptide 2	1.4350
ARPC5	Actin-related protein 2/3 complex subunit 5	1.2603
OSTF1	teoclast-stimulating factor 1	1.2500
RL5	60S ribomal protein L5	1.2135
SYK	Lysine--tRNA ligase	1.2135
RL10A	60S ribomal protein L10a	1.2135
TXNL1	Thioredoxin-like protein 1	1.1716
LIS1	Platelet-activating factor acetylhydrolase IB subunit alpha	1.1067
A4	Amyloid beta A4 protein	1.0911
H2B1M	Histone H2B type 1-M	1.0514
UB2V2	Ubiquitin-conjugating enzyme E2 variant 2	1.0381
PDCD5	Programmed cell death protein 5	1.0373
UCHL3	Ubiquitin carboxyl-terminal hydrolase isozyme L3	1.0061
PLEC	Plectin	1.0061
ITPA	Inine triphphate pyrophphatase	0.9524
IF5A1	Eukaryotic translation initiation factor 5A-1	0.9314
ARP2	Actin-related protein 2	0.8618
HNRPL	Heterogeneous nuclear ribonucleoprotein L	0.8576
DNJA3	DnaJ homolog subfamily A member 3, mitochondrial	0.8576
SERA	D-3-phphoglycerate dehydrogenase	0.8522
DDX5	Probable ATP-dependent RNA helicase DDX5	0.8522
OLA1	Obg-like ATPase 1	0.8522
TKT	Transketolase	0.8494
RLA1	60S acidic ribomal protein P1	0.8376
RL7A	60S ribomal protein L7a	0.8333
KCRB	Creatine kinase B-type	0.8232
H32	Histone H3.2	0.7948
H3C	Histone H3.3C	0.7948
RCC2	Protein RCC2	0.7930

HN1L	Hematological and neurological expressed 1-like protein	0.7899
EF2	Elongation factor 2	0.7644
NACA	Nascent polypeptide-associated complex subunit alpha	0.7641
PPIL1	Peptidyl-prolyl cis-trans isomerase-like 1	0.7641
PROP	Properdin	0.7577
PSA7	Proteasome subunit alpha type-7	0.7537
FAS	Fatty acid synthase	0.7522
ESTD	S-formylglutathione hydrolase	0.7520
1433B	14-3-3 protein beta/alpha	0.7503
CLIC4	Chloride intracellular channel protein 4	0.7492
XPP1	Xaa-Pro aminopeptidase 1	0.7349
PTPA	Serine/threonine-protein phphatase 2A activator	0.7349
EPIPL	Epiplakin	0.7342
1433G	14-3-3 protein gamma	0.7290
HNRPC	Heterogeneous nuclear ribonucleoproteins C1/C2	0.7268
TPP1	Tripeptidyl-peptidase 1	0.7253
RAN	GTP-binding nuclear protein Ran	0.7253
ALDR	Alde reductase	0.7175
LMNA	Prelamin-A/C	0.7120
PSA4	Proteasome subunit alpha type-4	0.7118
SEM4A	Semaphorin-4A	0.6667
PPAC	Low molecular weight phphotyrine protein phphatase	0.6606
ENPL	Endoplasmin	0.6474
HS90B	Heat shock protein HSP 90-beta	0.6413
SERC	Phpherine aminotransferase	0.6273
TCPQ	T-complex protein 1 subunit theta	0.6188
TCPA	T-complex protein 1 subunit alpha	0.6188
ROA1	Heterogeneous nuclear ribonucleoprotein A1	0.6188
SYG	Glycine--tRNA ligase	0.6188
HNRPU	Heterogeneous nuclear ribonucleoprotein U	0.6188
SK2L2	Superkiller viralicidic activity 2-like 2	0.6113
EIF3A	Eukaryotic translation initiation factor 3 subunit A	0.6113
DNJC8	DnaJ homolog subfamily C member 8	0.6113
SYRC	Arginine--tRNA ligase, cytoplasmic	0.6113
PROSC	Proline synthase co-transcribed bacterial homolog protein	0.6113
LG3BP	Galectin-3-binding protein	0.6113
PRDX5	Peroxiredoxin-5, mitochondrial	0.6113
DUS3	Dual specificity protein phphatase 3	0.6100
PUR9	Bifunctional purine biynthesis protein PURH	0.6100
RL23A	60S ribomal protein L23a	0.6100
RL29	60S ribomal protein L29	0.6100
CPIN1	Anamorsin	0.6100
PEPL1	Probable aminopeptidase NPEPL1	0.6100
KAP0	cAMP-dependent protein kinase type I-alpha regulatory subunit	0.6100

MYH9	Myin-9	0.6022
PSMD6	26S proteasome non-ATPase regulatory subunit 6	0.5996
TPIS	Triephphate isomerase	0.5905
AK1A1	Alcohol dehydrogenase [NADP(+)]	0.5833
COR1A	Coronin-1A	0.5821
RINI	Ribonuclease inhibitor	0.5817
CC112	Coiled-coil domain-containing protein 112	0.5745
TCPZ	T-complex protein 1 subunit zeta	0.5723
LMNB1	Lamin-B1	0.5723
CNDP2	Cytolic non-specific dipeptidase	0.5723
HA1L	H-2 class I histocompatibility antigen, L-D alpha chain	0.5703
AN32E	Acidic leucine-rich nuclear phphoprotein 32 family member E	0.5669
CUL3	Cullin-3	0.5664
EFR3B	Protein EFR3 homolog B	0.5560
CREG1	Protein CREG1	0.5470
XPO1	Exportin-1	0.5456
PSME2	Proteasome activator complex subunit 2	0.5456
ARPC2	Actin-related protein 2/3 complex subunit 2	0.5426
NP1L1	Nucleome assembly protein 1-like 1	0.5422
ATNG	Sodium/potassium-transporting ATPase subunit gamma	0.5421
CFAH	Complement factor H	0.5398
SUH	Recombining binding protein suppressor of hairless	0.5398
FEN1	Flap endonuclease 1	0.5398
MTPN	Myotrophin	0.5387
G6PI	Gluce-6-phphate isomerase	0.5323
PGK1	Phphoglycerate kinase 1	0.5238
THIO	Thioredoxin	0.5201
RT15	28S ribomal protein S15, mitochondrial	0.5176
RASF7	Ras association domain-containing protein 7	0.5176
GP113	Probable G-protein coupled receptor 113	0.5176
IBTK	Inhibitor of Bruton tyrine kinase	0.5176
HS90A	Heat shock protein HSP 90-alpha	0.5038
VIME	Vimentin	0.5004
APT	Adenine phphoribyltransferase	0.4921
LSM7	U6 snRNA-associated Sm-like protein LSm7	0.4921
EIF3G	Eukaryotic translation initiation factor 3 subunit G	0.4921
PCCB	Propionyl-CoA carboxylase beta chain, mitochondrial	0.4921
EMID1	EMI domain-containing protein 1	0.4921
IRAK4	Interleukin-1 receptor-associated kinase 4	0.4921
MAP9	Microtubule-associated protein 9	0.4921
CHD7	Chromodomain-helicase-DNA-binding protein 7	0.4921
WASF3	Wiskott-Aldrich syndrome protein family member 3	0.4916
HINT1	Histidine triad nucleotide-binding protein 1	0.4897
IF4A1	Eukaryotic initiation factor 4A-I	0.4888
CLH1	Clathrin heavy chain 1	0.4762

TCPH	T-complex protein 1 subunit eta	0.4762
H11	Histone H1.1	0.4762
PTN6	Tyrine-protein phphatase non-receptor type 6	0.4762
TCPD	T-complex protein 1 subunit delta	0.4762
EIF3B	Eukaryotic translation initiation factor 3 subunit B	0.4762
DCPS	m7GpppX diphphatase	0.4762
NUCL	Nucleolin	0.4625
HMGB1	High mobility group protein B1	0.4619
RLA0	60S acidic ribomal protein P0	0.4619
ALDOC	Fructe-bisphphate aldolase C	0.4599
ACTB	Actin, cytoplasmic 1	0.4503
ACTG	Actin, cytoplasmic 2	0.4503
ACTC	Actin, alpha cardiac muscle 1	0.4482
RANG	Ran-specific GTPase-activating protein	0.4466
LYZ2	Lysozyme C-2	0.4456
PSA5	Proteasome subunit alpha type-5	0.4423
1433Z	14-3-3 protein zeta/delta	0.4400
NSF1C	NSFL1 cofactor p47	0.4365
ACLY	ATP-citrate synthase	0.4365
UPP2	Uridine phphorylase 2	0.4365
RL22	60S ribomal protein L22	0.4365
CSN3	COP9 signalome complex subunit 3	0.4365
DX39B	Spliceome RNA helicase Ddx39b	0.4330
PRDX1	Peroxiredoxin-1	0.4318
CHRD1	Cysteine and histidine-rich domain-containing protein 1	0.4288
TR150	Thyroid hormone receptor-associated protein 3	0.4288
LKHA4	Leukotriene A-4 hydrolase	0.4288
MINP1	Multiple initol polyphphate phphatase 1	0.4288
UFM1	Ubiquitin-fold modifier 1	0.4288
GALT7	N-acetylgalactaminyltransferase 7	0.4288
PPM1G	Protein phphatase 1G	0.4288
RALY	RNA-binding protein Raly	0.4288
LSM5	U6 snRNA-associated Sm-like protein LSm5	0.4288
NAA50	N-alpha-acetyltransferase 50	0.4288
RN219	RING finger protein 219	0.4288
UBXN1	UBX domain-containing protein 1	0.4288
ELOC	Transcription elongation factor B polypeptide 1	0.4288
RL26	60S ribomal protein L26	0.4288
BPNT1	3'(2'),5'-bisphphate nucleotidase 1	0.4288
LRC47	Leucine-rich repeat-containing protein 47	0.4288
MP2K1	Dual specificity mitogen-activated protein kinase kinase 1	0.4288
ADK	Adenine kinase	0.4288
PIANP	PILR alpha-associated neural protein	0.4288
CSF2R	Granulocyte-macrophage colony-stimulating factor receptor subunit alpha	0.4288

CSN5	COP9 signalome complex subunit 5	0.4288
NLTP	Non-specific lipid-transfer protein	0.4288
SF3A3	Splicing factor 3A subunit 3	0.4288
MTA3	Metastasis-associated protein MTA3	0.4288
KBTB3	Kelch repeat and BTB domain-containing protein 3	0.4288
TKTL2	Transketolase-like protein 2	0.4288
SPT2	Protein SPT2 homolog	0.4288
STOX2	Storkhead-box protein 2	0.4288
CO4A4	Collagen alpha-4(IV) chain	0.4288
1433E	14-3-3 protein epsilon	0.4264
WDR1	WD repeat-containing protein 1	0.4242
FKBP3	Peptidyl-prolyl cis-trans isomerase FKBP3	0.4226
SRSF2	Serine/arginine-rich splicing factor 2	0.4226
UBC9	SUMO-conjugating enzyme UBC9	0.4217
MIF	Macrophage migration inhibitory factor	0.4207
GELS	Gelsolin	0.4177
PGAM1	Phphoglycerate mutase 1	0.4170
KIF2C	Kinesin-like protein KIF2C	0.3914
VAS1	V-type proton ATPase subunit S1	0.3885
GNAO	Guanine nucleotide-binding protein G(o) subunit alpha	0.3848
IMB1	Importin subunit beta-1	0.3826
HSP7C	Heat shock cognate 71 kDa protein	0.3787
LYZ1	Lysozyme C-1	0.3765
PPGB	Lysomal protective protein	0.3758
OL141	Olfactory receptor 141	0.3733
EIF2A	Eukaryotic translation initiation factor 2A	0.3733
SRP19	Signal recognition particle 19 kDa protein	0.3733
TCPB	T-complex protein 1 subunit beta	0.3728
SDCB1	Syntenin-1	0.3699
VINC	Vinculin	0.3675
APLP2	Amyloid-like protein 2	0.3638
EIF3I	Eukaryotic translation initiation factor 3 subunit I	0.3638
PDIA1	Protein disulfide-isomerase	0.3615
1433F	14-3-3 protein eta	0.3585
TLN1	Talin-1	0.3581
1433T	14-3-3 protein theta	0.3530
CAPR1	Caprin-1	0.3467
CLIC1	Chloride intracellular channel protein 1	0.3396
IF5	Eukaryotic translation initiation factor 5	0.3379
SYNJ2	Synaptojanin-2	0.3336
PSB3	Proteasome subunit beta type-3	0.3299
LASP1	LIM and SH3 domain protein 1	0.3288
LIRB4	Leukocyte immunoglobulin-like receptor subfamily B member 4	0.3218
UBP14	Ubiquitin carboxyl-terminal hydrolase 14	0.3164
SERB	Phpherine phphatase	0.3127

HSP13	Heat shock 70 kDa protein 13	0.3094
PRS10	26S protease regulatory subunit 10B	0.3094
BGLR	Beta-glucuronidase	0.3094
RSMB	Small nuclear ribonucleoprotein-associated protein B	0.3094
PGM2	Phphoglucomutase-2	0.3094
NUDC	Nuclear migration protein nudC	0.3094
MA2B1	Lysomal alpha-mannidase	0.3094
CDC37	Hsp90 co-chaperone Cdc37	0.3094
RD23B	UV excision repair protein RAD23 homolog B	0.3094
CATL1	Cathepsin L1	0.3061
PFD2	Prefoldin subunit 2	0.3050
PDIA4	Protein disulfide-isomerase A4	0.3011
RL12	60S ribomal protein L12	0.2958
CATZ	Cathepsin Z	0.2934
LEG3	Galectin-3	0.2887
ARC1B	Actin-related protein 2/3 complex subunit 1B	0.2874
THOC4	THO complex subunit 4	0.2869
CATS	Cathepsin S	0.2827
EMIL2	EMILIN-2	0.2802
FABP5	Fatty acid-binding protein, epidermal	0.2741
RENR	Renin receptor	0.2734
NUCKS	Nuclear ubiquitous casein and cyclin-dependent kinase substrate 1	0.2729
TPM3	Tropomyin alpha-3 chain	0.2661
CAPG	Macrophage-capping protein	0.2647
NDKA	Nucleide diphphate kinase A	0.2646
IDI1	Isopentenyl-diphphate Delta-isomerase 1	0.2645
PUR4	Phphoribylformylglycinamidine synthase	0.2595
ASM3A	Acid sphingomyelinase-like phphodiesterase 3a	0.2595
EF1D	Elongation factor 1-delta	0.2595
ADAM8	Disintegrin and metalloproteinase domain-containing protein 8	0.2595
CATB	Cathepsin B	0.2594
SAP3	Gangliide GM2 activator	0.2564
HYAL1	Hyaluronidase-1	0.2440
DPYL2	Dihydropyrimidinase-related protein 2	0.2440
NIT2	Omega-amidase NIT2	0.2440
PRXD1	Prolyl-tRNA synthetase associated domain-containing protein 1	0.2440
UBE4B	Ubiquitin conjugation factor E4 B	0.2440
LSM2	U6 snRNA-associated Sm-like protein LSm2	0.2440
NLGN3	Neuroligin-3	0.2440
CRIP1	Cysteine-rich protein 1	0.2440
CD63	CD63 antigen	0.2440
METK2	S-adenylmethionine synthase isoform type-2	0.2440
TBCB	Tubulin-folding cofactor B	0.2440

TOIP1	Torsin-1A-interacting protein 1	0.2440
RAGP1	Ran GTPase-activating protein 1	0.2440
A16A1	Aldehyde dehydrogenase family 16 member A1	0.2440
FABP4	Fatty acid-binding protein, adipocyte	0.2440
RL19	60S ribomal protein L19	0.2440
EIF3H	Eukaryotic translation initiation factor 3 subunit H	0.2440
TEX11	Testis-expressed sequence 11 protein	0.2440
DNJA4	DnaJ homolog subfamily A member 4	0.2440
PIN1	Peptidyl-prolyl cis-trans isomerase NIMA-interacting 1	0.2440
VP26A	Vacuolar protein sorting-associated protein 26A	0.2440
ARSA	Arylsulfatase A	0.2440
VPS35	Vacuolar protein sorting-associated protein 35	0.2440
BACH	Cytolic acyl coenzyme A thioester hydrolase	0.2440
UBC12	NEDD8-conjugating enzyme Ubc12	0.2440
DAG1	Dystroglycan	0.2440
HNRPK	Heterogeneous nuclear ribonucleoprotein K	0.2440
PSA6	Proteasome subunit alpha type-6	0.2437
ERH	Enhancer of rudimentary homolog	0.2405
SET	Protein SET	0.2400
EMAL4	Echinoderm microtubule-associated protein-like 4	0.2365
NAMPT	Nicotinamide phphoribyltransferase	0.2362
LEG1	Galectin-1	0.2336
DNS2A	Deoxyribonuclease-2-alpha	0.2223
GBLP	Guanine nucleotide-binding protein subunit beta-2-like 1	0.2222
HMGB2	High mobility group protein B2	0.2221
ENOA	Alpha-enolase	0.2140
PSB8	Proteasome subunit beta type-8	0.2084
IF4B	Eukaryotic translation initiation factor 4B	0.2083
HCLS1	Hematopoietic lineage cell-specific protein	0.2083
PA1B2	Platelet-activating factor acetylhydrolase IB subunit beta	0.2083
SYYC	Tyrine--tRNA ligase, cytoplasmic	0.2083
MARE1	Microtubule-associated protein RP/EB family member 1	0.2014
NMU	Neuromedin-U	0.2014
NOE1	Noelin	0.2014
SYAC	Alanine--tRNA ligase, cytoplasmic	0.2012
BROX	BRO1 domain-containing protein BROX	0.2012
SYTC	Threonine--tRNA ligase, cytoplasmic	0.2012
DNLI1	DNA ligase 1	0.2012
NUMBL	Numb-like protein	0.1956
ERF1	Eukaryotic peptide chain release factor subunit 1	0.1953
EF1B	Elongation factor 1-beta	0.1913
SH3L1	SH3 domain-binding glutamic acid-rich-like protein	0.1907
DDX21	Nucleolar RNA helicase 2	0.1868
OSTA	Organic solute transporter subunit alpha	0.1856
PCNA	Proliferating cell nuclear antigen	0.1827

NASP	Nuclear autoantigenic sperm protein	0.1802
TCEA1	Transcription elongation factor A protein 1	0.1704
2AAA	Serine/threonine-protein phphatase 2A 65 kDa regulatory subunit A alpha isoform	0.1704
PFD3	Prefoldin subunit 3	0.1704
PTMA	Prothymin alpha	0.1674
TCPE	T-complex protein 1 subunit epsilon	0.1635
H4	Histone H4	0.1614
CLD13	Claudin-13	0.1547
SYNE1	Nesprin-1	0.1538
STMN1	Stathmin	0.1512
NONO	Non-POU domain-containing octamer-binding protein	0.1480
PPID	Peptidyl-prolyl cis-trans isomerase D	0.1476
PP14B	Protein phphatase 1 regulatory subunit 14B	0.1467
ARPC3	Actin-related protein 2/3 complex subunit 3	0.1409
HMGN2	Non-histone chromomal protein HMG-17	0.1398
TBB5	Tubulin beta-5 chain	0.1397
SEP11	Septin-11	0.1387
API5	Apoptis inhibitor 5	0.1387
GLOD4	Glyoxalase domain-containing protein 4	0.1387
LAP2B	Lamina-associated polypeptide 2, isoforms beta/delta/epsilon/gamma	0.1371
HNRPD	Heterogeneous nuclear ribonucleoprotein D0	0.1345
BLVRB	Flavin reductase (NADPH)	0.1333
DHPR	Dihydropteridine reductase	0.1333
TCOF	Treacle protein	0.1321
CSF1R	Macrophage colony-stimulating factor 1 receptor	0.1306
RBM8A	RNA-binding protein 8A	0.1301
AMPN	Aminopeptidase N	0.1225
BGAL	Beta-galactidase	0.1212
EIF3E	Eukaryotic translation initiation factor 3 subunit E	0.1212
B3GN2	N-acetyllactaminide beta-1,3-N-acetylglucaminyltransferase 2	0.1181
PRDX6	Peroxiredoxin-6	0.1170
SRSF1	Serine/arginine-rich splicing factor 1	0.1127
EF1G	Elongation factor 1-gamma	0.1114
HEXB	Beta-hexaminidase subunit beta	0.1096
SFPQ	Splicing factor, proline- and glutamine-rich	0.1091
ISOC1	Isochorismatase domain-containing protein 1	0.1091
DYHC1	Cytoplasmic dynein 1 heavy chain 1	0.1091
PRS6B	26S protease regulatory subunit 6B	0.1091
ARPC4	Actin-related protein 2/3 complex subunit 4	0.1091
CD9	CD9 antigen	0.1091
ARSB	Arylsulfatase B	0.1091
IF2G	Eukaryotic translation initiation factor 2 subunit 3, X-linked	0.1091
AMPB	Aminopeptidase B	0.1091

CLU	Clustered mitochondria protein homolog	0.1091
MCM2	DNA replication licensing factor MCM2	0.1091
EIF3C	Eukaryotic translation initiation factor 3 subunit C	0.1091
MTAP	S-methyl-5'-thioadenine phphorylase	0.1091
PSMD9	26S proteasome non-ATPase regulatory subunit 9	0.1091
ASAH1	Acid ceramidase	0.1091
SYSC	Serine--tRNA ligase, cytoplasmic	0.1091
PSA1	Proteasome subunit alpha type-1	0.1030
PDIA6	Protein disulfide-isomerase A6	0.1006
GLRX3	Glutaredoxin-3	0.1006
TCPG	T-complex protein 1 subunit gamma	0.1006
MESH1	Guanine-3',5'-bis(diphphate) 3'-pyrophphohydrolase MESH1	0.1006
DPP2	Dipeptidyl peptidase 2	0.1006
SYHC	Histidine--tRNA ligase, cytoplasmic	0.1006
PFD5	Prefoldin subunit 5	0.1006
COIA1	Collagen alpha-1(XVIII) chain	0.1006
NQO2	Ribyldihydronicotinamide dehydrogenase [quinone]	0.1006
CYBP	Calcyclin-binding protein	0.0985
PARK7	Protein DJ-1	0.0984
CBX3	Chromobox protein homolog 3	0.0981
PLTP	Phpholipid transfer protein	0.0893
LMNB2	Lamin-B2	0.0893
SENP7	Sentrin-specific protease 7	0.0893
RBBP7	Histone-binding protein RBBP7	0.0893
RBBP4	Histone-binding protein RBBP4	0.0893
INO1	Initol-3-phphate synthase 1	0.0886
RS12	40S ribomal protein S12	0.0874
CAB45	45 kDa calcium-binding protein	0.0862
ACTN1	Alpha-actinin-1	0.0818
PDXK	Pyridoxal kinase	0.0788
SIL1	Nucleotide exchange factor SIL1	0.0761
COL12	Collectin-12	0.0749
NUCB1	Nucleobindin-1	0.0749
STB5L	Syntaxin-binding protein 5-like	0.0610
GDIR1	Rho GDP-dissociation inhibitor 1	0.0601
XIRP2	Xin actin-binding repeat-containing protein 2	0.0536
ACTN4	Alpha-actinin-4	0.0513
B2MG	Beta-2-microglobulin	0.0493
TRI26	Tripartite motif-containing protein 26	0.0492
PPT1	Palmitoyl-protein thioesterase 1	0.0490
LDHA	L-lactate dehydrogenase A chain	0.0484
HIC2	Hypermethylated in cancer 2 protein	0.0427
PSB1	Proteasome subunit beta type-1	0.0425
METRL	Meteorin-like protein	0.0424
NPM3	Nucleoplasmin-3	0.0409

IGHG1	Ig gamma-1 chain C region secreted form	0.0302
CAP1	Adenylyl cyclase-associated protein 1	0.0256
PABP2	Polyadenylate-binding protein 2	0.0222
PDIA3	Protein disulfide-isomerase A3	0.0000
IGSF8	Immunoglobulin superfamily member 8	0.0000
LICH	Lysomal acid lipase/cholesteryl ester hydrolase	0.0000
6PGL	6-phphogluconolactonase	0.0000
CATC	Dipeptidyl peptidase 1	0.0000
APEX1	DNA-(apurinic or apyrimidinic site) lyase	0.0000
GLU2B	Glucidase 2 subunit beta	0.0000
PDC6I	Programmed cell death 6-interacting protein	0.0000
LIPL	Lipoprotein lipase	0.0000
IF4A3	Eukaryotic initiation factor 4A-III	0.0000
NAGAB	Alpha-N-acetylgalactaminidase	0.0000
FRIH	Ferritin heavy chain	0.0000
TNFL9	Tumor necris factor ligand superfamily member 9	0.0000
PRP19	Pre-mRNA-processing factor 19	0.0000
ARLY	Argininuccinate lyase	0.0000
STX7	Syntaxin-7	0.0000
DYR	Dihydrofolate reductase	0.0000
DDB1	DNA damage-binding protein 1	0.0000
HNRPQ	Heterogeneous nuclear ribonucleoprotein Q	0.0000
IF2B	Eukaryotic translation initiation factor 2 subunit 2	0.0000
SEPT7	Septin-7	0.0000
S10AA	Protein S100-A10	0.0000
TIM8B	Mitochondrial import inner membrane translocase subunit Tim8 B	0.0000
COPD	Coatomer subunit delta	0.0000
ATOX1	Copper transport protein ATOX1	0.0000
DNMT1	DNA (cytine-5)-methyltransferase 1	0.0000
IPO9	Importin-9	0.0000
ALD2	Alde reductase-related protein 2	0.0000
HMGN1	Non-histone chromomal protein HMG-14	0.0000
OTUB1	Ubiquitin thioesterase OTUB1	0.0000
TRXR1	Thioredoxin reductase 1, cytoplasmic	0.0000
IDE	Insulin-degrading enzyme	0.0000
EMAL2	Echinoderm microtubule-associated protein-like 2	0.0000
ARP3	Actin-related protein 3	0.0000
AATM	Aspartate aminotransferase, mitochondrial	0.0000
TPD52	Tumor protein D52	0.0000
CSN4	COP9 signalome complex subunit 4	0.0000
KI21A	Kinesin-like protein KIF21A	0.0000
GGH	Gamma-glutamyl hydrolase	0.0000
VATG1	V-type proton ATPase subunit G 1	0.0000
SYFA	Phenylalanine--tRNA ligase alpha subunit	0.0000

ITB1	Integrin beta-1	0.0000
SAFB1	Scaffold attachment factor B1	0.0000
HMGA2	High mobility group protein HMGI-C	0.0000
TSN	Translin	0.0000
ANGI	Angiogenin	0.0000
PSB7	Proteasome subunit beta type-7	0.0000
SYCC	Cysteine--tRNA ligase, cytoplasmic	0.0000
TPP2	Tripeptidyl-peptidase 2	0.0000
PLBL2	Putative phpholipase B-like 2	0.0000
VASP	Vasodilator-stimulated phphoprotein	0.0000
MYOF	Myoferlin	0.0000
ITA4	Integrin alpha-4	0.0000
PTGR1	Prtaglandin reductase 1	0.0000
SP16H	FACT complex subunit SPT16	0.0000
TCAF2	TRPM8 channel-associated factor 2	0.0000
SCLY	Selenocysteine lyase	0.0000
CREL2	Cysteine-rich with EGF-like domain protein 2	0.0000
BZW1	Basic leucine zipper and W2 domain-containing protein 1	0.0000
LC7L2	Putative RNA-binding protein Luc7-like 2	0.0000
CAR10	Caspase recruitment domain-containing protein 10	0.0000
CHD4	Chromodomain-helicase-DNA-binding protein 4	0.0000
PIPNA	Phphatidylinitol transfer protein alpha isoform	0.0000
AMPD2	AMP deaminase 2	0.0000
RTN4	Reticulon-4	0.0000
LIN7C	Protein lin-7 homolog C	0.0000
SCOT1	Succinyl-CoA:3-ketoacid coenzyme A transferase 1, mitochondrial	0.0000
AGAL	Alpha-galactidase A	0.0000
ARCH	Protein archease	0.0000
CSN1	COP9 signalome complex subunit 1	0.0000
CATA	Catalase	0.0000
SEPT2	Septin-2	0.0000
DDX1	ATP-dependent RNA helicase DDX1	0.0000
LTOR5	Ragulator complex protein LAMTOR5	0.0000
TOM1	Target of Myb protein 1	0.0000
BOLA2	BolA-like protein 2	0.0000
CBR1	Carbonyl reductase [NADPH] 1	0.0000
RL11	60S ribomal protein L11	0.0000
COR1B	Coronin-1B	0.0000
CLM5	CMRF35-like molecule 5	0.0000
OTUD3	OTU domain-containing protein 3	0.0000
WDR5	WD repeat-containing protein 5	0.0000
CNPY2	Protein canopy homolog 2	0.0000
SC23B	Protein transport protein Sec23B	0.0000
AS3MT	Arsenite methyltransferase	0.0000

H2AY	Core histone macro-H2A.1	0.0000
RSH6A	Radial spoke head protein 6 homolog A	0.0000
SYNC	Asparagine--tRNA ligase, cytoplasmic	0.0000
BASP1	Brain acid soluble protein 1	0.0000
WDHD1	WD repeat and HMG-box DNA-binding protein 1	0.0000
GALM	Alde 1-epimerase	0.0000
CCD96	Coiled-coil domain-containing protein 96	0.0000
NHLC2	NHL repeat-containing protein 2	0.0000
HIRP3	HIRA-interacting protein 3	0.0000
NOP58	Nucleolar protein 58	0.0000
SF3B1	Splicing factor 3B subunit 1	0.0000
NEUR1	Sialidase-1	0.0000
VATA	V-type proton ATPase catalytic subunit A	0.0000
PHAX	Phphorylated adapter RNA export protein	0.0000
ITB2	Integrin beta-2	0.0000
EXOS2	Exome complex component RRP4	0.0000
TRNT1	CCA tRNA nucleotidyltransferase 1, mitochondrial	0.0000
MYH7B	Myin-7B	0.0000
B4GT5	Beta-1,4-galactyltransferase 5	0.0000
ERP44	Endoplasmic reticulum resident protein 44	0.0000
DC1L1	Cytoplasmic dynein 1 light intermediate chain 1	0.0000
PPCE	Prolyl endopeptidase	0.0000
HAT1	Histone acetyltransferase type B catalytic subunit	0.0000
IFG15	Torsin-1A-interacting protein 2, isoform IFRG15	0.0000
SDF2L	Stromal cell-derived factor 2-like protein 1	0.0000
RUVB1	RuvB-like 1	0.0000
PHRF1	PHD and RING finger domain-containing protein 1	0.0000
SMRC1	SWI/SNF complex subunit SMARCC1	0.0000
SYEP	Bifunctional glutamate/proline--tRNA ligase	0.0000
NPTN	Neuroplastin	0.0000
DGKZ	Diacylglycerol kinase zeta	0.0000
TIF1B	Transcription intermediary factor 1-beta	0.0000
RTCB	tRNA-splicing ligase RtcB homolog	0.0000
LSM12	Protein LSM12 homolog	0.0000
C1RA	Complement C1r-A subcomponent	0.0000
SNUT2	U4/U6.U5 tri-snRNP-associated protein 2	0.0000
SMAP1	Stromal membrane-associated protein 1	0.0000
HAP28	28 kDa heat- and acid-stable phphoprotein	0.0000
RBBP6	E3 ubiquitin-protein ligase RBBP6	0.0000
GMFB	Glia maturation factor beta	0.0000
FKBP2	Peptidyl-prolyl cis-trans isomerase FKBP2	0.0000
LARP7	La-related protein 7	0.0000
PVRL1	Poliovirus receptor-related protein 1	0.0000
IFM3	Interferon-induced transmembrane protein 3	0.0000
SPB6	Serpin B6	0.0000

NAGK	N-acetyl-D-glucamine kinase	0.0000
S39AA	Zinc transporter ZIP10	0.0000
PHP14	14 kDa phphohistidine phphatase	0.0000
PNO1	RNA-binding protein PNO1	0.0000
FUCO2	Plasma alpha-L-fucidase	0.0000
PGM5	Phphoglucomutase-like protein 5	0.0000
CATF	Cathepsin F	0.0000
TXD12	Thioredoxin domain-containing protein 12	0.0000
PPT2	Lysomal thioesterase PPT2	0.0000
SIA8D	CMP-N-acetylneuraminate-poly-alpha-2,8-sialyltransferase	0.0000
TBX2	T-box transcription factor TBX2	0.0000
RB11B	Ras-related protein Rab-11B	0.0000
MACF1	Microtubule-actin crs-linking factor 1	0.0000
PGP	Phphoglycolate phphatase	0.0000
SEPT9	Septin-9	0.0000
DYL1	Dynein light chain 1, cytoplasmic	0.0000
VATB2	V-type proton ATPase subunit B, brain isoform	0.0000
RS18	40S ribomal protein S18	0.0000
PTG3L	Putative protein PTGES3L	0.0000
PP1G	Serine/threonine-protein phphatase PP1-gamma catalytic subunit	0.0000
SERF2	Small EDRK-rich factor 2	0.0000
HDGR2	Hepatoma-derived growth factor-related protein 2	0.0000
S10A6	Protein S100-A6	0.0000
SZRD1	SUZ domain-containing protein 1	0.0000
LSM4	U6 snRNA-associated Sm-like protein LSm4	0.0000
CISD1	CDGSH iron-sulfur domain-containing protein 1	0.0000
PTMS	Parathymin	0.0000
SAP18	Histone deacetylase complex subunit SAP18	0.0000
CK098	Uncharacterized protein C11orf98 homolog	0.0000
RL13	60S ribomal protein L13	0.0000
ACOT2	Acyl-coenzyme A thioesterase 2, mitochondrial	0.0000
NH2L1	NHP2-like protein 1	0.0000
RUXG	Small nuclear ribonucleoprotein G	0.0000
LTOR3	Ragulator complex protein LAMTOR3	0.0000
RPAB3	DNA-directed RNA polymerases I, II, and III subunit RPABC3	0.0000
ADHX	Alcohol dehydrogenase class-3	0.0000
RAB14	Ras-related protein Rab-14	0.0000
RAB7A	Ras-related protein Rab-7a	0.0000
PRPS1	Ribe-phphate pyrophphokinase 1	0.0000
TIGAR	Fructe-2,6-bisphphatase TIGAR	0.0000
MTNA	Methylthioribe-1-phphate isomerase	0.0000
RS10	40S ribomal protein S10	0.0000
ATIF1	ATPase inhibitor, mitochondrial	0.0000
CRYL1	Lambda-crystallin homolog	0.0000

UBE2K	Ubiquitin-conjugating enzyme E2 K	0.0000
IL2RG	Cytokine receptor common subunit gamma	0.0000
WDR61	WD repeat-containing protein 61	0.0000
ECI1	Enoyl-CoA delta isomerase 1, mitochondrial	0.0000
LARP1	La-related protein 1	0.0000
DNJC7	DnaJ homolog subfamily C member 7	0.0000
MTNB	Methylthioribule-1-phphate dehydratase	0.0000
DJB11	DnaJ homolog subfamily B member 11	0.0000
HYI	Putative hydroxypyruvate isomerase	0.0000
TSNAX	Translin-associated protein X	0.0000
DIAC	Di-N-acetylchitobiase	0.0000
PTN18	Tyrine-protein phphatase non-receptor type 18	0.0000
AIMP1	Aminoacyl tRNA synthase complex-interacting multifunctional protein 1	0.0000
MEPCE	7SK snRNA methylphphate capping enzyme	0.0000
NUF2	Kinetochore protein Nuf2	0.0000
PCBP2	Poly(rC)-binding protein 2	0.0000
PP2AB	Serine/threonine-protein phphatase 2A catalytic subunit beta isoform	0.0000
LSP1	Lymphocyte-specific protein 1	0.0000
EHD4	EH domain-containing protein 4	0.0000
VRK1	Serine/threonine-protein kinase VRK1	0.0000
PININ	Pinin	0.0000
KIF22	Kinesin-like protein KIF22	0.0000
CSTN1	Calsyntenin-1	0.0000
DNPEP	Aspartyl aminopeptidase	0.0000
SRRM1	Serine/arginine repetitive matrix protein 1	0.0000
GALNS	N-acetylgalactamine-6-sulfatase	0.0000
BAG1	BAG family molecular chaperone regulator 1	0.0000
CPZIP	CapZ-interacting protein	0.0000
SNX2	Sorting nexin-2	0.0000
COPB2	Coatomer subunit beta'	0.0000
BIN2	Bridging integrator 2	0.0000
THIC	Acetyl-CoA acetyltransferase, cytolic	0.0000
SHLB2	Endophilin-B2	0.0000
ODO2	Dihydrolipoyllysine-residue succinyltransferase component of 2-oxoglutarate dehydrogenase complex, mitochondrial	0.0000
GUAD	Guanine deaminase	0.0000
T2FA	General transcription factor IIF subunit 1	0.0000
PLRG1	Pleiotropic regulator 1	0.0000
PAK2	Serine/threonine-protein kinase PAK 2	0.0000
SAE2	SUMO-activating enzyme subunit 2	0.0000
RSRC1	Serine/Arginine-related protein 53	0.0000
CCD22	Coiled-coil domain-containing protein 22	0.0000
IMA3	Importin subunit alpha-3	0.0000
GUAA	GMP synthase [glutamine-hydrolyzing]	0.0000

AP2A1	AP-2 complex subunit alpha-1	0.0000
SYFB	Phenylalanine--tRNA ligase beta subunit	0.0000
TTL10	Protein polyglycylase TTLL10	0.0000
AFAP1	Actin filament-associated protein 1	0.0000
CF222	Uncharacterized protein C6orf222 homolog	0.0000
TCHP	Trichoplein keratin filament-binding protein	0.0000
MRC1	Macrophage manne receptor 1	0.0000
HGS	Hepatocyte growth factor-regulated tyrine kinase substrate	0.0000
TRDN	Triadin	0.0000
PARP1	Poly [ADP-ribe] polymerase 1	0.0000
FNBP4	Formin-binding protein 4	0.0000
NRDC	Nardilysin	0.0000
COPA	Coatomer subunit alpha	0.0000
CBPD	Carboxypeptidase D	0.0000
PDE3B	cGMP-inhibited 3',5'-cyclic phphodiesterase B	0.0000
F16A1	Protein FAM160A1	0.0000
TARA	TRIO and F-actin-binding protein	0.0000
USP9X	Probable ubiquitin carboxyl-terminal hydrolase FAF-X	0.0000
DYHC2	Cytoplasmic dynein 2 heavy chain 1	0.0000
CATD	Cathepsin D	-0.0030
H2A1H	Histone H2A type 1-H	-0.0128
H2A2C	Histone H2A type 2-C	-0.0128
NDKB	Nucleide diphphate kinase B	-0.0162
GRN	Granulins	-0.0163
ENV1	MLV-related proviral Env polyprotein	-0.0344
NPM	Nucleophmin	-0.0420
SAHH	Adenylhomocysteinase	-0.0432
PNPH	Purine nucleide phphorylase	-0.0490
GLYC	Serine hydroxymethyltransferase, cytolic	-0.0523
CD166	CD166 antigen	-0.0559
S10AB	Protein S100-A11	-0.0563
TADBP	TAR DNA-binding protein 43	-0.0582
6PGD	6-phphogluconate dehydrogenase, decarboxylating	-0.0649
QSOX1	Sulfhydryl oxidase 1	-0.0661
SYWC	Tryptophan--tRNA ligase, cytoplasmic	-0.0717
LGMN	Legumain	-0.0729
PSME1	Proteasome activator complex subunit 1	-0.0761
UROK	Urokinase-type plasminogen activator	-0.0781
RS28	40S ribomal protein S28	-0.0788
NAA38	N-alpha-acetyltransferase 38, NatC auxiliary subunit	-0.0788
IL1RA	Interleukin-1 receptor antagonist protein	-0.0841
AF1L1	Actin filament-associated protein 1-like 1	-0.0852
SUMO1	Small ubiquitin-related modifier 1	-0.0852
ACON	Aconitate hydratase, mitochondrial	-0.0852
LGUL	Lactoylglutathione lyase	-0.0852

ROAA	Heterogeneous nuclear ribonucleoprotein A/B	-0.0879
NRP2	Neuropilin-2	-0.0893
EF1A1	Elongation factor 1-alpha 1	-0.0897
HNRPF	Heterogeneous nuclear ribonucleoprotein F	-0.0926
DPEP2	Dipeptidase 2	-0.0985
UBA1	Ubiquitin-like modifier-activating enzyme 1	-0.0985
CAPZB	F-actin-capping protein subunit beta	-0.0985
PSD11	26S proteasome non-ATPase regulatory subunit 11	-0.1006
CERU	Ceruloplasmin	-0.1006
OTU6B	OTU domain-containing protein 6B	-0.1006
GRHPR	Glyoxylate reductase/hydroxypyruvate reductase	-0.1006
SWP70	Switch-associated protein 70	-0.1006
COR1C	Coronin-1C	-0.1006
GLCM	Glucylceramidase	-0.1006
UAP1L	UDP-N-acetylhexamine pyrophphorylase-like protein 1	-0.1091
FLNA	Filamin-A	-0.1110
RAC1	Ras-related C3 botulinum toxin substrate 1	-0.1127
H13	Histone H1.3	-0.1132
PEBP1	Phphatidylethanolamine-binding protein 1	-0.1134
RLA2	60S acidic ribomal protein P2	-0.1163
BIEA	Biliverdin reductase A	-0.1212
H15	Histone H1.5	-0.1256
PRDX2	Peroxiredoxin-2	-0.1277
HDGF	Hepatoma-derived growth factor	-0.1293
CAH2	Carbonic anhydrase 2	-0.1341
H2AZ	Histone H2A.Z	-0.1378
RSSA	40S ribomal protein SA	-0.1387
ROA2	Heterogeneous nuclear ribonucleoproteins A2/B1	-0.1387
STIP1	Stress-induced-phphoprotein 1	-0.1387
H14	Histone H1.4	-0.1387
LAMC1	Laminin subunit gamma-1	-0.1387
CLC5A	C-type lectin domain family 5 member A	-0.1387
GNS	N-acetylglucamine-6-sulfatase	-0.1393
PPIB	Peptidyl-prolyl cis-trans isomerase B	-0.1401
TREM2	Triggering receptor expressed on myeloid cells 2	-0.1480
SAP	Sulfated glycoprotein 1	-0.1508
CH60	60 kDa heat shock protein, mitochondrial	-0.1523
AL9A1	4-trimethylaminobutyraldehyde dehydrogenase	-0.1523
SRSF3	Serine/arginine-rich splicing factor 3	-0.1523
TYB10	Thymin beta-10	-0.1567
FPPS	Farnesyl pyrophphate synthase	-0.1597
RBM3	Putative RNA-binding protein 3	-0.1605
MDHC	Malate dehydrogenase, cytoplasmic	-0.1622
YBOX3	Y-box-binding protein 3	-0.1635
UBB	Polyubiquitin-B	-0.1653

TBB4B	Tubulin beta-4B chain	-0.1667
CCD12	Coiled-coil domain-containing protein 12	-0.1704
NAPSA	Napsin-A	-0.1704
COTL1	Coactin-like protein	-0.1704
ECM1	Extracellular matrix protein 1	-0.1719
ALDOA	Fructe-bisphphate aldolase A	-0.1753
HMGA1	High mobility group protein HMG-I/HMG-Y	-0.1754
UB2L3	Ubiquitin-conjugating enzyme E2 L3	-0.1755
CCL9	C-C motif chemokine 9	-0.1776
FUMH	Fumarate hydratase, mitochondrial	-0.1786
IMPA1	Initol monophphatase 1	-0.1790
GLDN	Gliomedin	-0.1801
PLD4	Phpholipase D4	-0.1850
AN32B	Acidic leucine-rich nuclear phphoprotein 32 family member B	-0.1871
HA12	H-2 class I histocompatibility antigen, D-D alpha chain	-0.1880
G3BP1	Ras GTPase-activating protein-binding protein 1	-0.1886
IDHC	Isocitrate dehydrogenase [NADP] cytoplasmic	-0.1958
CD44	CD44 antigen	-0.1958
GANAB	Neutral alpha-glucidase AB	-0.1970
5NT3A	Cytolic 5'-nucleotidase 3A	-0.2012
FLNB	Filamin-B	-0.2012
TCO2	Transcobalamin-2	-0.2012
UBP5	Ubiquitin carboxyl-terminal hydrolase 5	-0.2012
DPP3	Dipeptidyl peptidase 3	-0.2012
EDF1	Endothelial differentiation-related factor 1	-0.2012
LY86	Lymphocyte antigen 86	-0.2023
PSA2	Proteasome subunit alpha type-2	-0.2026
KPYM	Pyruvate kinase PKM	-0.2028
ABRAL	Ctars family protein ABRACL	-0.2056
P5CR3	Pyrroline-5-carboxylate reductase 3	-0.2083
MA2B2	Epididymis-specific alpha-mannidase	-0.2083
PFD1	Prefoldin subunit 1	-0.2083
TXND5	Thioredoxin domain-containing protein 5	-0.2083
SND1	Staphylococcal nuclease domain-containing protein 1	-0.2083
ADAM9	Disintegrin and metalloproteinase domain-containing protein 9	-0.2083
SEM6B	Semaphorin-6B	-0.2083
LSM3	U6 snRNA-associated Sm-like protein LSm3	-0.2083
MTND	1,2-dihydroxy-3-keto-5-methylthiopentene dioxygenase	-0.2083
ACTZ	Alpha-centractin	-0.2083
VS10L	V-set and immunoglobulin domain-containing protein 10-like	-0.2083
BOLA1	BolA-like protein 1	-0.2083
XCT	Cystine/glutamate transporter	-0.2083
HP1B3	Heterochromatin protein 1-binding protein 3	-0.2083
SRSF5	Serine/arginine-rich splicing factor 5	-0.2083
IFT80	Intraflagellar transport protein 80 homolog	-0.2083

STRAP	Serine-threonine kinase receptor-associated protein	-0.2083
MVD1	Diphphomevalonate decarboxylase	-0.2083
FKB15	FK506-binding protein 15	-0.2083
SF3A1	Splicing factor 3A subunit 1	-0.2083
CAN10	Calpain-10	-0.2083
UGGG1	UDP-gluce:glycoprotein glucyltransferase 1	-0.2083
ELAV1	ELAV-like protein 1	-0.2083
DBNL	Drebrin-like protein	-0.2083
ANFY1	Ankyrin repeat and FYVE domain-containing protein 1	-0.2083
SYN1	Synapsin-1	-0.2083
DCTN2	Dynactin subunit 2	-0.2083
CUTA	Protein CutA	-0.2083
SGTA	Small glutamine-rich tetratricopeptide repeat-containing protein alpha	-0.2083
SYDC	Aspartate--tRNA ligase, cytoplasmic	-0.2083
EI2BA	Translation initiation factor eIF-2B subunit alpha	-0.2083
NMRL1	NmrA-like family domain-containing protein 1	-0.2083
CD36	Platelet glycoprotein 4	-0.2083
IGF1	Insulin-like growth factor I	-0.2083
TWF2	Twinfilin-2	-0.2083
PRS6A	26S protease regulatory subunit 6A	-0.2083
TNC18	Trinucleotide repeat-containing gene 18 protein	-0.2083
SC31B	Protein transport protein Sec31B	-0.2083
TMM42	Transmembrane protein 42	-0.2083
GRDN	Girdin	-0.2083
RGF1B	Ras-GEF domain-containing family member 1B	-0.2083
RIMKA	N-acetylaspartylglutamate synthase A	-0.2083
PIM3	Serine/threonine-protein kinase pim-3	-0.2083
PMM2	Phphomannomutase 2	-0.2083
MPRI	Cation-independent manne-6-phphate receptor	-0.2083
NU188	Nucleoporin NUP188 homolog	-0.2083
MYCN	N-myc proto-oncogene protein	-0.2083
T2FB	General transcription factor IIF subunit 2	-0.2083
KLC1	Kinesin light chain 1	-0.2083
SEM3C	Semaphorin-3C	-0.2083
CENPJ	Centromere protein J	-0.2083
CSN8	COP9 signalome complex subunit 8	-0.2083
IPO7	Importin-7	-0.2083
DHX15	Putative pre-mRNA-splicing factor ATP-dependent RNA helicase DHX15	-0.2083
ENOPH	Enolase-phphatase E1	-0.2083
MANBA	Beta-mannidase	-0.2083
IMA7	Importin subunit alpha-7	-0.2083
ICAM1	Intercellular adhesion molecule 1	-0.2083
AP2B1	AP-2 complex subunit beta	-0.2083

ACOC	Cytoplasmic aconitate hydratase	-0.2083
ORN	Oligoribonuclease, mitochondrial	-0.2083
GNPI1	Glucamine-6-phphate isomerase 1	-0.2083
RPIA	Ribe-5-phphate isomerase	-0.2083
RNAS4	Ribonuclease 4	-0.2083
STC2	Stanniocalcin-2	-0.2083
MEP50	Methylome protein 50	-0.2083
ADA	Adenine deaminase	-0.2083
KAD2	Adenylate kinase 2, mitochondrial	-0.2083
HEM3	Porphobilinogen deaminase	-0.2083
DNPH1	2'-deoxynucleide 5'-phphate N-hydrolase 1	-0.2083
AIFM1	Apoptis-inducing factor 1, mitochondrial	-0.2083
IBP4	Insulin-like growth factor-binding protein 4	-0.2083
CDC42	Cell division control protein 42 homolog	-0.2083
RL24	60S ribomal protein L24	-0.2083
FUCM	Fuce mutarotase	-0.2083
GSHR	Glutathione reductase, mitochondrial	-0.2083
TPK1	Thiamin pyrophphokinase 1	-0.2083
LRC59	Leucine-rich repeat-containing protein 59	-0.2083
SMD2	Small nuclear ribonucleoprotein Sm D2	-0.2083
EFHD2	EF-hand domain-containing protein D2	-0.2083
RRBP1	Ribome-binding protein 1	-0.2083
CCD58	Coiled-coil domain-containing protein 58	-0.2083
TTC1	Tetratricopeptide repeat protein 1	-0.2083
HEM2	Delta-aminolevulinic acid dehydratase	-0.2083
CPPED	Calcineurin-like phphoesterase domain-containing protein 1	-0.2083
SPB8	Serpin B8	-0.2083
GTPC1	Putative GTP cyclohydrolase 1 type 2 Nif3l1	-0.2083
CAB39	Calcium-binding protein 39	-0.2083
UCP2	Mitochondrial uncoupling protein 2	-0.2083
ANXA3	Annexin A3	-0.2083
GBP2	Interferon-induced guanylate-binding protein 2	-0.2083
SMN	Survival motor neuron protein	-0.2083
FUBP2	Far upstream element-binding protein 2	-0.2083
LYRIC	Protein LYRIC	-0.2083
CSTF2	Cleavage stimulation factor subunit 2	-0.2083
MATR3	Matrin-3	-0.2083
ABI2	Abl interactor 2	-0.2083
INAR2	Interferon alpha/beta receptor 2	-0.2083
URP2	Fermitin family homolog 3	-0.2083
SP1	Transcription factor Sp1	-0.2083
FUS	RNA-binding protein FUS	-0.2083
AP2A2	AP-2 complex subunit alpha-2	-0.2083
MBB1A	Myb-binding protein 1A	-0.2083
ILF3	Interleukin enhancer-binding factor 3	-0.2083

DPOLA	DNA polymerase alpha catalytic subunit	-0.2083
EFCB5	EF-hand calcium-binding domain-containing protein 5	-0.2083
CBP	CREB-binding protein	-0.2083
ALBU	Serum albumin	-0.2106
RMXL1	RNA binding motif protein, X-linked-like-1	-0.2113
G6PD1	Gluce-6-phphate 1-dehydrogenase X	-0.2189
HEXA	Beta-hexaminidase subunit alpha	-0.2219
U2AF2	Splicing factor U2AF 65 kDa subunit	-0.2309
GDIB	Rab GDP dissociation inhibitor beta	-0.2312
TCTP	Translationally-controlled tumor protein	-0.2392
PLSL	Plastin-2	-0.2420
TALDO	Transaldolase	-0.2496
HA1D	H-2 class I histocompatibility antigen, K-D alpha chain	-0.2498
ANXA5	Annexin A5	-0.2529
PROF1	Profilin-1	-0.2535
HS3S5	Heparan sulfate glucamine 3-O-sulfotransferase 5	-0.2564
SRRM2	Serine/arginine repetitive matrix protein 2	-0.2564
TCAF3	TRPM8 channel-associated factor 3	-0.2564
PCP	Lysomal Pro-X carboxypeptidase	-0.2564
XRN1	5'-3' exoribonuclease 1	-0.2564
TM11L	Transmembrane protease serine 11B-like protein	-0.2564
NHSL1	NHS-like protein 1	-0.2564
MAP7	Ensconsin	-0.2564
TCP4	Activated RNA polymerase II transcriptional coactivator p15	-0.2564
MERL	Merlin	-0.2564
CYTB	Cystatin-B	-0.2595
NEXN	Nexilin	-0.2595
BLMH	Bleomycin hydrolase	-0.2595
TBA1C	Tubulin alpha-1C chain	-0.2630
YBOX1	Nuclease-sensitive element-binding protein 1	-0.2690
VAPA	Vesicle-associated membrane protein-associated protein A	-0.2759
PPRC1	Peroxisome proliferator-activated receptor gamma coactivator-related protein 1	-0.2778
IGJ	Immunoglobulin J chain	-0.2778
ANGL6	Angiopoietin-related protein 6	-0.2778
CQ074	Uncharacterized protein C17orf74 homolog	-0.2778
FUT8	Alpha-(1,6)-fucyltransferase	-0.2778
CP2DB	Cytochrome P450 2D11	-0.2778
GRIA2	Glutamate receptor 2	-0.2778
SHRM2	Protein Shroom2	-0.2778
DHX30	Putative ATP-dependent RNA helicase DHX30	-0.2778
RBM28	RNA-binding protein 28	-0.2778
PSB6	Proteasome subunit beta type-6	-0.2807
CALR	Calreticulin	-0.2891
PLCH1	1-phphatidylinitol 4,5-bisphphate phphodiesterase eta-1	-0.2899

SYNRG	Synergin gamma	-0.2899
TLR4	Toll-like receptor 4	-0.2899
PSB2	Proteasome subunit beta type-2	-0.2910
ENOB	Beta-enolase	-0.2929
OPA1	Dynamin-like 120 kDa protein, mitochondrial	-0.2976
IKZF4	Zinc finger protein E	-0.3030
KRI1	Protein KRI1 homolog	-0.3030
DET1	DET1 homolog	-0.3030
SGCE	Epsilon-sarcoglycan	-0.3070
PTBP1	Polypyrimidine tract-binding protein 1	-0.3094
CALU	Calumenin	-0.3094
SEM4B	Semaphorin-4B	-0.3094
CCD43	Coiled-coil domain-containing protein 43	-0.3125
OSTP	teopontin	-0.3130
CAZA1	F-actin-capping protein subunit alpha-1	-0.3148
NT5C	5'(3')-deoxyribonucleotidase, cytolic type	-0.3151
ANXA1	Annexin A1	-0.3151
PEAK1	Pseudopodium-enriched atypical kinase 1	-0.3205
BAZ1A	Bromodomain adjacent to zinc finger domain protein 1A	-0.3220
MID51	Mitochondrial dynamics protein MID51	-0.3220
MATN1	Cartilage matrix protein	-0.3241
SBNO2	Protein strawberry notch homolog 2	-0.3268
BAX	Apoptis regulator BAX	-0.3270
MKRN1	E3 ubiquitin-protein ligase makorin-1	-0.3274
COQ6	Ubiquinone biynthesis monooxygenase COQ6	-0.3289
CIB3	Calcium and integrin-binding family member 3	-0.3300
ADO	Aldehyde oxidase	-0.3301
DLGP5	Disks large-associated protein 5	-0.3303
COOA1	Collagen alpha-1(XXIV) chain	-0.3318
NEDD8	NEDD8	-0.3333
DPY30	Protein dpy-30 homolog	-0.3347
GPNMB	Transmembrane glycoprotein NMB	-0.3353
COF1	Cofilin-1	-0.3375
CAZA2	F-actin-capping protein subunit alpha-2	-0.3405
FUCO	Tissue alpha-L-fucidase	-0.3467
PAIRB	Plasminogen activator inhibitor 1 RNA-binding protein	-0.3467
PSMD4	26S proteasome non-ATPase regulatory subunit 4	-0.3467
DYL2	Dynein light chain 2, cytoplasmic	-0.3467
IMDH2	Inine-5'-monophphate dehydrogenase 2	-0.3467
NOP56	Nucleolar protein 56	-0.3467
PROS	Vitamin K-dependent protein S	-0.3467
EWS	RNA-binding protein EWS	-0.3467
IF4G1	Eukaryotic translation initiation factor 4 gamma 1	-0.3467
SKP1	S-phase kinase-associated protein 1	-0.3467
LYAG	Lysomal alpha-glucidase	-0.3467

ADA17	Disintegrin and metalloproteinase domain-containing protein 17	-0.3467
PTN21	Tyrine-protein phphatase non-receptor type 21	-0.3467
GSHB	Glutathione synthetase	-0.3467
MCTS1	Malignant T-cell-amplified sequence 1	-0.3467
SODM	Superoxide dismutase [Mn], mitochondrial	-0.3467
CFDP1	Craniofacial development protein 1	-0.3467
PSME3	Proteasome activator complex subunit 3	-0.3467
RPB4	DNA-directed RNA polymerase II subunit RPB4	-0.3467
TBC24	TBC1 domain family member 24	-0.3467
LACB2	Beta-lactamase-like protein 2	-0.3467
UGPA	UTP--gluce-1-phphate uridylyltransferase	-0.3467
PSD12	26S proteasome non-ATPase regulatory subunit 12	-0.3467
RS19	40S ribomal protein S19	-0.3467
MAP4	Microtubule-associated protein 4	-0.3467
PSB10	Proteasome subunit beta type-10	-0.3467
APEH	Acylamino-acid-releasing enzyme	-0.3467
UTP11	Probable U3 small nucleolar RNA-associated protein 11	-0.3467
IPYR	Inorganic pyrophphatase	-0.3467
GAS6	Growth arrest-specific protein 6	-0.3467
ARHL2	Poly(ADP-ribe) glycohydrolase ARH3	-0.3467
MIA40	Mitochondrial intermembrane space import and assembly protein 40	-0.3467
LMAN2	Vesicular integral-membrane protein VIP36	-0.3467
PCBP1	Poly(rC)-binding protein 1	-0.3467
BTF3	Transcription factor BTF3	-0.3467
SPS1	Selenide, water dikinase 1	-0.3467
PP4C	Serine/threonine-protein phphatase 4 catalytic subunit	-0.3467
GBB1	Guanine nucleotide-binding protein G(I)/G(S)/G(T) subunit beta-1	-0.3467
KAP2	cAMP-dependent protein kinase type II-alpha regulatory subunit	-0.3467
NMT1	Glycylpeptide N-tetradecanoyltransferase 1	-0.3467
FA50A	Protein FAM50A	-0.3467
MAP2	Methionine aminopeptidase 2	-0.3467
SLAP1	Src-like-adapter	-0.3467
CELF2	CUGBP Elav-like family member 2	-0.3467
HXK1	Hexokinase-1	-0.3467
PSB4	Proteasome subunit beta type-4	-0.3467
EI3JA	Eukaryotic translation initiation factor 3 subunit J-A	-0.3467
MVP	Major vault protein	-0.3534
FKBP4	Peptidyl-prolyl cis-trans isomerase FKBP4	-0.3573
MYG1	UPF0160 protein MYG1, mitochondrial	-0.3573
PLOD1	Procollagen-lysine,2-oxoglutarate 5-dioxygenase 1	-0.3573
PUR8	Adenyluccinate lyase	-0.3581
SH3L3	SH3 domain-binding glutamic acid-rich-like protein 3	-0.3652

RADI	Radixin	-0.3675
EZRI	Ezrin	-0.3675
IQGA1	Ras GTPase-activating-like protein IQGAP1	-0.3675
PIMT	Protein-L-isoaspartate(D-aspartate) O-methyltransferase	-0.3675
K1C24	Keratin, type I cytkeletal 24	-0.3675
SMAP	Small acidic protein	-0.3675
IF6	Eukaryotic translation initiation factor 6	-0.3675
GILT	Gamma-interferon-inducible lysomal thiol reductase	-0.3675
LDB1	LIM domain-binding protein 1	-0.3675
GRP78	78 kDa gluce-regulated protein	-0.3745
ERP29	Endoplasmic reticulum resident protein 29	-0.3772
S10A4	Protein S100-A4	-0.3787
TPM4	Tropomyin alpha-4 chain	-0.3841
AN32A	Acidic leucine-rich nuclear phphoprotein 32 family member A	-0.3886
SODC	Superoxide dismutase [Cu-Zn]	-0.3922
PPIA	Peptidyl-prolyl cis-trans isomerase A	-0.4032
FKB1A	Peptidyl-prolyl cis-trans isomerase FKBP1A	-0.4061
SYVC	Valine--tRNA ligase	-0.4088
SMHD1	Structural maintenance of chromomes flexible hinge domain-containing protein 1	-0.4108
DAPLE	Protein Daple	-0.4108
PCNP	PEST proteolytic signal-containing nuclear protein	-0.4108
COX17	Cytochrome c oxidase copper chaperone	-0.4108
ARG28	Rho guanine nucleotide exchange factor 28	-0.4108
MANF	Mesencephalic astrocyte-derived neurotrophic factor	-0.4176
SMD1	Small nuclear ribonucleoprotein Sm D1	-0.4203
XPO2	Exportin-2	-0.4251
CCL2	C-C motif chemokine 2	-0.4308
ACADV	Very long-chain specific acyl-CoA dehydrogenase, mitochondrial	-0.4378
C1QBP	Complement component 1 Q subcomponent-binding protein, mitochondrial	-0.4378
RYR3	Ryanodine receptor 3	-0.4410
MOES	Moesin	-0.4432
SUMO2	Small ubiquitin-related modifier 2	-0.4455
CH10	10 kDa heat shock protein, mitochondrial	-0.4526
HSP74	Heat shock 70 kDa protein 4	-0.4547
CYC	Cytochrome c, somatic	-0.4567
CCL3	C-C motif chemokine 3	-0.4577
PTGR2	Prtaglandin reductase 2	-0.4577
GCSH	Glycine cleavage system H protein, mitochondrial	-0.4577
MINT	Msx2-interacting protein	-0.4609
IPO5	Importin-5	-0.4652
G3P	Glyceraldehyde-3-phphate dehydrogenase	-0.4679
HMGN5	High mobility group nucleome-binding domain-containing protein 5	-0.4715

ACBP	Acyl-CoA-binding protein	-0.4715
PABP1	Polyadenylate-binding protein 1	-0.4762
CALX	Calnexin	-0.4762
VMA5A	von Willebrand factor A domain-containing protein 5A	-0.4762
HN1	Hematological and neurological expressed 1 protein	-0.4762
PEPD	Xaa-Pro dipeptidase	-0.4762
SEM4D	Semaphorin-4D	-0.4762
AMPL	Cytol aminopeptidase	-0.4762
ITM2B	Integral membrane protein 2B	-0.4762
SF01	Splicing factor 1	-0.4762
PKHO2	Pleckstrin homology domain-containing family O member 2	-0.4762
RL4	60S ribomal protein L4	-0.4762
GSTM1	Glutathione S-transferase Mu 1	-0.4762
SPRE	Sepiapterin reductase	-0.4762
PFD6	Prefoldin subunit 6	-0.4762
AP4A	Bis(5'-nucleyl)-tetraphphatase [asymmetrical]	-0.4762
HMOX1	Heme oxygenase 1	-0.4762
RS25	40S ribomal protein S25	-0.4762
CISY	Citrate synthase, mitochondrial	-0.4762
SMD3	Small nuclear ribonucleoprotein Sm D3	-0.4762
BCAT1	Branched-chain-amino-acid aminotransferase, cytolic	-0.4762
TFR1	Transferrin receptor protein 1	-0.4762
PSA3	Proteasome subunit alpha type-3	-0.4767
F10A1	Hsc70-interacting protein	-0.4767
SUMO3	Small ubiquitin-related modifier 3	-0.4789
FA49B	Protein FAM49B	-0.4797
LA	Lupus La protein homolog	-0.4797
ANXA2	Annexin A2	-0.4797
HCDH	Hydroxyacyl-coenzyme A dehydrogenase, mitochondrial	-0.4797
GLO2	Hydroxyacylglutathione hydrolase, mitochondrial	-0.4797
PSA	Puromycin-sensitive aminopeptidase	-0.4797
CDV3	Protein CDV3	-0.4880
LDLR	Low-density lipoprotein receptor	-0.4888
NTF2	Nuclear transport factor 2	-0.5000
AATC	Aspartate aminotransferase, cytoplasmic	-0.5052
ARP19	cAMP-regulated phphoprotein 19	-0.5058
ALDH2	Aldehyde dehydrogenase, mitochondrial	-0.5119
IDUA	Alpha-L-iduronidase	-0.5135
SPEE	Spermidine synthase	-0.5135
NKTR	NK-tumor recognition protein	-0.5135
OAT	Ornithine aminotransferase, mitochondrial	-0.5135
CS010	UPF0556 protein C19orf10 homolog	-0.5135
CALM	Calmodulin	-0.5176
RNT2	Ribonuclease T2	-0.5190
KCY	UMP-CMP kinase	-0.5330

CYTC	Cystatin-C	-0.5434
PGM1	Phphoglucomutase-1	-0.5456
CD14	Monocyte differentiation antigen CD14	-0.5547
RL17	60S ribomal protein L17	-0.5548
TAGL2	Transgelin-2	-0.5564
TXD17	Thioredoxin domain-containing protein 17	-0.5614
PPIC	Peptidyl-prolyl cis-trans isomerase C	-0.5683
ERAP1	Endoplasmic reticulum aminopeptidase 1	-0.5683
PLST	Plastin-3	-0.5766
TBCA	Tubulin-specific chaperone A	-0.5965
GRB2	Growth factor receptor-bound protein 2	-0.5996
SNX5	Sorting nexin-5	-0.6091
HYOU1	Hypoxia up-regulated protein 1	-0.6113
TIMP2	Metalloproteinase inhibitor 2	-0.6113
EIF1	Eukaryotic translation initiation factor 1	-0.6113
CANT1	Soluble calcium-activated nucleotidase 1	-0.6113
IF4E	Eukaryotic translation initiation factor 4E	-0.6113
RHOA	Transforming protein RhoA	-0.6113
IF2A	Eukaryotic translation initiation factor 2 subunit 1	-0.6113
IGHM	Ig mu chain C region	-0.6144
SARNP	SAP domain-containing ribonucleoprotein	-0.6150
ROA3	Heterogeneous nuclear ribonucleoprotein A3	-0.6254
TERA	Transitional endoplasmic reticulum ATPase	-0.6279
RISC	Retinoid-inducible serine carboxypeptidase	-0.6316
MEMO1	Protein MEMO1	-0.6601
PA2G4	Proliferation-associated protein 2G4	-0.6619
GDIR2	Rho GDP-dissociation inhibitor 2	-0.6681
MDHM	Malate dehydrogenase, mitochondrial	-0.6808
DMP4	Extracellular serine/threonine protein kinase FAM20C	-0.7088
PURA2	Adenyluccinate synthetase isozyme 2	-0.7527
PP1R7	Protein phphatase 1 regulatory subunit 7	-0.7641
THOP1	Thimet oligopeptidase	-0.7785
PIN4	Peptidyl-prolyl cis-trans isomerase NIMA-interacting 4	-0.8541
HPRT	Hypoxanthine-guanine phphoribyltransferase	-0.8819
RS21	40S ribomal protein S21	-0.8974
Z385A	Zinc finger protein 385A	-0.9313
SHPS1	Tyrine-protein phphatase non-receptor type substrate 1	-0.9381
GSTO1	Glutathione S-transferase omega-1	-1.0334
PP4R2	Serine/threonine-protein phphatase 4 regulatory subunit 2	-2.5000

Annex 2 Ranked list of proteins present in anti-Sema4D treated macrophage conditioned media with respect to the IgG treatment. Proteins obtained in the proteomic analysis of the conditioned media are listed according to their ratio, calculated as the difference of expression between anti-Sema4D and IgG treatments. Divergence amount between treatments is shown by a color scale from red (upregulated in Sema4D condition), passing through white (no differences), to green (downregulated in Sema4D condition). Only proteins that were present 2 or 3 times in each conditioned media triplicate were included in the analysis. Statistical significance is calculated by Mann-Whitney test. Values of p.value < 0.05 are depicted in red.

Protein symbol	***Protein name***	***p. value***	***Ratio***
HVM12	Ig heavy chain V region MOPC 104E	0.0006	7.0318
EPIPL	Epiplakin	0.0802	6.4510
KV3AD	Ig kappa chain V-III region PC 7043	0.0011	4.9704
PTMA	Prothymosin alpha	0.0373	3.7841
ENPL	Endoplasmin	0.0004	3.7433
PTN6	Tyrosine-protein phosphatase non-receptor type 6	0.0002	3.5840
VAS1	V-type proton ATPase subunit S1	0.0082	3.5525
KCRB	Creatine kinase B-type	0.0582	3.5231
OSTF1	Osteoclast-stimulating factor 1	0.2671	3.2975
WDR1	WD repeat-containing protein 1	0.1979	3.0848
TCOF	Treacle protein	0.2315	2.9507
PGAM1	Phosphoglycerate mutase 1	0.0175	2.9206
H32	Histone H3.2	0.0014	2.9183
H3C	Histone H3.3C	0.0014	2.9183
B2MG	Beta-2-microglobulin	0.0057	2.8589
AMPN	Aminopeptidase N	0.0078	2.8089
HS90B	Heat shock protein HSP 90-beta	0.0004	2.7935
RAN	GTP-binding nuclear protein Ran	0.0738	2.7797
SYNJ2	Synaptojanin-2	0.5428	2.5956
ELOB	Elongin-B	0.0019	2.5290
G6PI	Glucose-6-phosphate isomerase	0.0155	2.5021
RENR	Renin receptor	0.0019	2.3811
MTPN	Myotrophin	0.1117	2.2855
HS90A	Heat shock protein HSP 90-alpha	0.0093	2.2473
ROA1	Heterogeneous nuclear ribonucleoprotein A1	0.1502	2.2328
IF4A1	Eukaryotic initiation factor 4A-I	0.1197	2.1462
IF5A1	Eukaryotic translation initiation factor 5A-1	0.0726	2.1307
RL12	60S ribosomal protein L12	0.0218	2.1262
EMIL2	EMILIN-2	0.0281	1.9579
ACTB	Actin. cytoplasmic 1	0.0218	1.9282
ACTG	Actin. cytoplasmic 2	0.0218	1.9282
GANAB	Neutral alpha-glucosidase AB	0.0652	1.9149
ATNG	Sodium/potassium-transporting ATPase subunit gamma	0.2377	1.9077
ENV1	MLV-related proviral Env polyprotein	0.0146	1.8976
ACTC	Actin. alpha cardiac muscle 1	0.0335	1.8414
EF1D	Elongation factor 1-delta	0.0114	1.8104

CATZ	Cathepsin Z	0.0285	1.7900
SERC	Phosphoserine aminotransferase	0.0600	1.7495
SFPQ	Splicing factor. proline- and glutamine-rich	0.1374	1.7174
PROP	Properdin	0.0001	1.7048
LMNB1	Lamin-B1	0.0119	1.7013
TCPZ	T-complex protein 1 subunit zeta	0.2205	1.6665
ARPC5	Actin-related protein 2/3 complex subunit 5	0.1935	1.6503
RANG	Ran-specific GTPase-activating protein	0.0572	1.6395
ALDR	Aldose reductase	0.0276	1.6369
RCC2	Protein RCC2	0.0102	1.6323
TKT	Transketolase	0.0139	1.6224
CATD	Cathepsin D	0.0285	1.5837
COR1A	Coronin-1A	0.0309	1.5836
SYEP	Bifunctional glutamate/proline--tRNA ligase	0.2459	1.5778
RBBP7	Histone-binding protein RBBP7	0.1601	1.5665
TPIS	Triosephosphate isomerase	0.0359	1.5499
RBBP4	Histone-binding protein RBBP4	0.1866	1.4881
TCPE	T-complex protein 1 subunit epsilon	0.0664	1.4384
CATL1	Cathepsin L1	0.0058	1.4371
H4	Histone H4	0.0524	1.4156
HEXB	Beta-hexosaminidase subunit beta	0.0022	1.4023
H2A1H	Histone H2A type 1-H	0.1614	1.3868
H2A2C	Histone H2A type 2-C	0.1614	1.3868
EF2	Elongation factor 2	0.0234	1.3785
NASP	Nuclear autoantigenic sperm protein	0.0583	1.3449
PPGB	Lysosomal protective protein	0.0271	1.3408
LIPL	Lipoprotein lipase	0.2445	1.3321
LGMN	Legumain	0.1153	1.3110
CATS	Cathepsin S	0.1015	1.3048
TXNL1	Thioredoxin-like protein 1	0.2980	1.2430
ARP2	Actin-related protein 2	0.0317	1.2343
HA1L	H-2 class I histocompatibility antigen	0.0507	1.2317
SDCB1	Syntenin-1	0.4685	1.1721
LMNA	Prelamin-A/C	0.0114	1.1662
H2B1M	Histone H2B type 1-M	0.0058	1.1399
GLCM	Glucosylceramidase	0.0702	1.0886
CATB	Cathepsin B	0.0014	1.0854
SRSF2	Serine/arginine-rich splicing factor 2	0.0047	1.0659
NAGAB	Alpha-N-acetylgalactosaminidase	0.2390	1.0452
RS12	40S ribosomal protein S12	0.2682	1.0387
MIF	Macrophage migration inhibitory factor	0.2486	1.0348
1433E	14-3-3 protein epsilon	0.0511	1.0214
PFD2	Prefoldin subunit 2	0.0711	1.0158
1433B	14-3-3 protein beta/alpha	0.0152	0.9995
FLNB	Filamin-B (FLN-B)	0.5010	0.9891
PSB8	Proteasome subunit beta type-8	0.3255	0.9854
1433G	14-3-3 protein gamma	0.0120	0.9625

ARPC2	Actin-related protein 2/3 complex subunit 2	0.0187	0.9355
OLA1	Obg-like ATPase 1	0.3878	0.9163
PSA4	Proteasome subunit alpha type-4	0.0155	0.8985
ERH	Enhancer of rudimentary homolog	0.0366	0.8735
ROA2	Heterogeneous nuclear ribonucleoproteins A2/B1	0.3060	0.8711
NUCL	Nucleolin	0.0124	0.8440
PDIA3	Protein disulfide-isomerase A3	0.0350	0.8273
ENOPH	Enolase-phosphatase E1	0.6350	0.8111
TCPQ	T-complex protein 1 subunit theta	0.4286	0.8073
RINI	Ribonuclease inhibitor	0.1803	0.7944
EF1G	Elongation factor 1-gamma	0.1044	0.7897
COL12	Collectin-12	0.1201	0.7848
DNJC8	DnaJ homolog subfamily C member 8	0.0231	0.7790
IMB1	Importin subunit beta-1	0.2807	0.7788
MA2B1	Lysosomal alpha-mannosidase	0.0616	0.7411
HSP7C	Heat shock cognate 71 kDa protein	0.1684	0.7409
UAP1L	UDP-N-acetylhexosamine pyrophosphorylase-like protein 1	0.1216	0.7392
NRP2	Neuropilin-2	0.2647	0.7099
PLEC	Plectin	0.0787	0.7053
PSME2	Proteasome activator complex subunit 2	0.2916	0.7013
NSF1C	NSFL1 cofactor p47	0.0989	0.6954
PPT1	Palmitoyl-protein thioesterase 1	0.1952	0.6823
CNDP2	Cytosolic non-specific dipeptidase	0.2011	0.6645
HA12	H-2 class I histocompatibility antigen. D-D alpha chain	0.4972	0.6368
PSB3	Proteasome subunit beta type-3	0.5247	0.6241
1433F	14-3-3 protein eta	0.0916	0.6231
PLD4	Phospholipase D4	0.0769	0.6168
HNRPC	Heterogeneous nuclear ribonucleoproteins C1/C2	0.4116	0.6151
PDCD5	Programmed cell death protein 5	0.2496	0.6142
HYOU1	Hypoxia up-regulated protein 1	0.0927	0.6078
PGK1	Phosphoglycerate kinase 1	0.3225	0.6066
NUCB1	Nucleobindin-1	0.0195	0.6027
PDIA1	Protein disulfide-isomerase	0.2694	0.5970
1433T	14-3-3 protein theta	0.1298	0.5904
PPAC	Low molecular weight phosphotyrosine protein phosphatase	0.1181	0.5890
BGAL	Beta-galactosidase	0.1090	0.5873
HEXA	Beta-hexosaminidase subunit alpha	0.1329	0.5306
HNRPU	Heterogeneous nuclear ribonucleoprotein U	0.1928	0.5270
RD23B	UV excision repair protein RAD23 homolog B	0.4722	0.5248
LSM8	U6 snRNA-associated Sm-like protein LSm8	0.5566	0.5039
DNS2A	Deoxyribonuclease-2-alpha	0.1074	0.4999
GARS	Glycine--tRNA ligase	0.2913	0.4891
1433Z	14-3-3 protein zeta/delta	0.0944	0.4763
LYZ2	Lysozyme C-2	0.1197	0.4640
NUCKS	Nuclear ubiquitous casein and cyclin-dependent kinase substrate 1	0.4302	0.4530

PABP2	Polyadenylate-binding protein 2	0.8213	0.4525
PSA7	Proteasome subunit alpha type-7	0.1793	0.4510
UB2V2	Ubiquitin-conjugating enzyme E2 variant 2	0.2569	0.4409
GLU2B	Glucosidase 2 subunit beta	0.0280	0.4326
ESTD	S-formylglutathione hydrolase	0.3942	0.4251
COIA1	Collagen alpha-1(XVIII) chain	0.1993	0.4207
CAB45	45 kDa calcium-binding protein	0.3584	0.4184
EIF3B	Eukaryotic translation initiation factor 3 subunit B	0.4979	0.3933
CAPR1	Caprin-1	0.3410	0.3819
THOC4	THO complex subunit 4	0.3549	0.3693
NQO2	Ribosyldihydronicotinamide dehydrogenase	0.5504	0.3569
APEX1	DNA-(apurinic or apyrimidinic site) lyase	0.2418	0.3545
HMGB1	High mobility group protein B1	0.3885	0.3463
CDC37	Hsp90 co-chaperone Cdc37	0.4754	0.3407
LYZ1	Lysozyme C-1	0.3090	0.3356
API5	Apoptosis inhibitor 5	0.1583	0.3338
SYYC	Tyrosine--tRNA ligase. cytoplasmic	0.3787	0.3270
PDC6I	Programmed cell death 6-interacting protein	0.2406	0.3210
PURA2	Adenylosuccinate synthetase isozyme 2	0.3995	0.3182
GPNMB	Transmembrane glycoprotein NMB	0.3769	0.3148
TNFL9	Tumor necrosis factor ligand superfamily member 9	0.6030	0.2976
PDIA4	Protein disulfide-isomerase A4	0.3886	0.2747
OSTP	Osteopontin	0.3989	0.2683
FLNA	Filamin-A	0.6509	0.2487
CSF1R	Macrophage colony-stimulating factor 1 receptor	0.5093	0.2446
ARC1B	Actin-related protein 2/3 complex subunit 1B	0.4328	0.2387
MYH9	Myosin-9	0.5561	0.2263
IL1RA	Interleukin-1 receptor antagonist protein	0.5886	0.2254
SYRC	Arginine--tRNA ligase. cytoplasmic	0.8248	0.2242
PP14B	Protein phosphatase 1 regulatory subunit 14B	0.7840	0.2156
RSSA	40S ribosomal protein SA	0.4624	0.2132
HNRPK	Heterogeneous nuclear ribonucleoprotein K	0.6991	0.2035
RBM3	RNA-binding protein 3	0.4865	0.1977
VIME	Vimentin	0.5744	0.1957
PLOD1	Procollagen-lysine.2-oxoglutarate 5-dioxygenase 1	0.7953	0.1705
UBP14	Ubiquitin carboxyl-terminal hydrolase 14	0.8136	0.1436
PSA5	Proteasome subunit alpha type-5	0.6292	0.1425
ERF1	Eukaryotic peptide chain release factor subunit 1	0.8964	0.1273
IGSF8	Immunoglobulin superfamily member 8	0.6783	0.1243
PNPH	Purine nucleoside phosphorylase	0.8748	0.1229
RMXL1	RNA binding motif protein. X-linked-like-1	0.9233	0.1212
GELS	Gelsolin	0.8897	0.1203
HMGN2	Non-histone chromosomal protein HMG-17	0.8852	0.1171
NUDC	Nuclear migration protein nudC	0.5523	0.1165
CD44	CD44 antigen	0.8854	0.1035
PA1B2	Platelet-activating factor acetylhydrolase IB subunit beta	0.8037	0.0818

THIO	Thioredoxin	0.8194	0.0636
NACA	Nascent polypeptide-associated complex subunit alpha	0.9019	0.0575
ALDOC	Fructose-bisphosphate aldolase C	0.8551	0.0455
TCEA1	Transcription elongation factor A protein 1	0.9231	0.0389
IMPA1	Inositol monophosphatase 1	0.9279	0.0380
IF4B	Eukaryotic translation initiation factor 4B	0.8931	0.0300
PRDX1	Peroxiredoxin-1	0.9351	0.0264
DDX21	Nucleolar RNA helicase 2	0.9507	0.0238
HNRPD	Heterogeneous nuclear ribonucleoprotein D0	0.9752	0.0191
TLN1	Talin-1	0.9710	0.0143
PCNA	Proliferating cell nuclear antigen	0.9873	0.0102
NPM	Nucleophosmin	0.9997	0.0001
ARPC3	Actin-related protein 2/3 complex subunit 3	0.9987	-0.0006
LEG1	Galectin-1	0.9902	-0.0112
BIEA	Biliverdin reductase A	0.9781	-0.0117
HMGB2	High mobility group protein B2	0.9595	-0.0189
HMGA1	High mobility group protein HMG-I/HMG-Y	0.9095	-0.0294
LGUL	Lactoylglutathione lyase	0.8201	-0.0567
VAPA	Vesicle-associated membrane protein-associated protein A	0.9005	-0.0697
ASAH1	Acid ceramidase	0.7339	-0.0773
ENOA	Alpha-enolase	0.7944	-0.0925
PDIA6	Protein disulfide-isomerase A6	0.7427	-0.1047
UBC9	SUMO-conjugating enzyme UBC9	0.8321	-0.1055
PSA1	Proteasome subunit alpha type-1	0.8082	-0.1246
ITPA	Inosine triphosphate pyrophosphatase	0.6337	-0.1323
LDHA	L-lactate dehydrogenase A chain	0.5253	-0.1335
ACTN4	Alpha-actinin-4	0.7172	-0.1372
CAPG	Macrophage-capping protein	0.6628	-0.1476
FKBP3	Peptidyl-prolyl cis-trans isomerase FKBP3	0.6964	-0.1482
NDKA	Nucleoside diphosphate kinase A	0.7940	-0.1607
PROF1	Profilin-1	0.5170	-0.1943
GDIR1	Rho GDP-dissociation inhibitor 1	0.5838	-0.2070
PUR4	Phosphoribosylformylglycinamidine synthase	0.7386	-0.2090
HNRPQ	Heterogeneous nuclear ribonucleoprotein Q	0.4637	-0.2104
UROK	Urokinase-type plasminogen activator	0.6282	-0.2150
SRSF1	Serine/arginine-rich splicing factor 1	0.7800	-0.2159
PA2G4	Proliferation-associated protein 2G4	0.4771	-0.2249
SAHH	Adenosylhomocysteinase	0.6614	-0.2255
ARLY	Argininosuccinate lyase	0.7480	-0.2282
LASP1	LIM and SH3 domain protein 1	0.7810	-0.2654
IGKC	Immunoglobulin kappa constant	0.4509	-0.2657
PSA6	Proteasome subunit alpha type-6	0.4592	-0.2699
HSP74	Heat shock 70 kDa protein 4	0.4095	-0.2706
H2AZ	Histone H2A.Z	0.8410	-0.2788
PARK7	Protein/nucleic acid deglycase DJ-1	0.3395	-0.2789

SYNE1	Nesprin-1	0.9015	-0.2884
PRDX6	Peroxiredoxin-6	0.7779	-0.2906
DNMT1	DNA (cytosine-5)-methyltransferase 1	0.2581	-0.2925
CAH2	Carbonic anhydrase 2	0.6850	-0.3127
6PGD	6-phosphogluconate dehydrogenase	0.3094	-0.3198
SEP11	Septin-11	0.3785	-0.3223
HCLS1	Hematopoietic lineage cell-specific protein	0.0944	-0.3224
DHPR	Dihydropteridine reductase	0.7575	-0.3278
AN32A	Acidic leucine-rich nuclear phosphoprotein 32 family member A	0.7384	-0.3335
SET	Protein SET	0.0859	-0.3343
PPID	Peptidyl-prolyl cis-trans isomerase D	0.6481	-0.3355
CAP1	Adenylyl cyclase-associated protein 1	0.5423	-0.3394
PRDX5	Peroxiredoxin-5. mitochondrial	0.3899	-0.3436
PSB7	Proteasome subunit beta type-7	0.2570	-0.3468
TPM3	Tropomyosin alpha-3 chain	0.5713	-0.3612
TCTP	Translationally-controlled tumor protein	0.3401	-0.3615
PFD5	Prefoldin subunit 5	0.1855	-0.3623
NTF2	Nuclear transport factor 2	0.6318	-0.3632
DAG1	Dystroglycan	0.5301	-0.3649
ACTN1	Alpha-actinin-1	0.3107	-0.3652
GNS	N-acetylglucosamine-6-sulfatase	0.7008	-0.3657
NDKB	Nucleoside diphosphate kinase B	0.3132	-0.3811
PSB1	Proteasome subunit beta type-1	0.5323	-0.3888
PGM2	Phosphoglucomutase-2	0.6186	-0.4033
NEDD8	NEDD8	0.3112	-0.4063
JUPI2	Jupiter microtubule associated homolog 2	0.1083	-0.4088
H13	Histone H1.3	0.2437	-0.4176
ALDOA	Fructose-bisphosphate aldolase A	0.0914	-0.4225
PSME1	Proteasome activator complex subunit 1	0.6794	-0.4241
SH3L1	SH3 domain-binding glutamic acid-rich-like protein	0.4980	-0.4264
G3BP1	Ras GTPase-activating protein-binding protein 1	0.1435	-0.4544
HIC2	Hypermethylated in cancer 2 protein	0.5531	-0.4574
S10AB	Protein S100-A11	0.2803	-0.4662
DYR	Dihydrofolate reductase	0.3411	-0.4748
HMGN1	Non-histone chromosomal protein HMG-14	0.5104	-0.4774
EF1A1	Elongation factor 1-alpha 1	0.3758	-0.4942
DPEP2	Dipeptidase 2	0.2985	-0.5019
TIM8B	Mitochondrial import inner membrane translocase subunit Tim8 B	0.2738	-0.5048
PPIA	Peptidyl-prolyl cis-trans isomerase A	0.0333	-0.5154
EF1B	Elongation factor 1-beta	0.3412	-0.5197
PPIB	Peptidyl-prolyl cis-trans isomerase B	0.1101	-0.5247
AATC	Aspartate aminotransferase. cytoplasmic	0.0429	-0.5270
LG3BP	Galectin-3-binding protein	0.3995	-0.5287
MESH1	Guanosine-3'.5'-bis(diphosphate) 3'-pyrophosphohydrolase MESH1	0.4064	-0.5389
OTU6B	Deubiquitinase OTUD6B	0.0674	-0.5542

KCY	UMP-CMP kinase	0.1879	-0.5594
EZRI	Ezrin	0.2269	-0.5628
RADI	Radixin	0.2269	-0.5628
CALR	Calreticulin	0.4128	-0.5632
CBX3	Chromobox protein homolog 3	0.1907	-0.5670
PSB4	Proteasome subunit beta type-4	0.0914	-0.5680
ROAA	Heterogeneous nuclear ribonucleoprotein A/B	0.2942	-0.5696
BAX	Apoptosis regulator BAX	0.4517	-0.5711
BIP	Endoplasmic reticulum chaperone BiP	0.2259	-0.5881
SYSC	Serine--tRNA ligase. cytoplasmic	0.1552	-0.5884
CYTC	Cystatin-C	0.2519	-0.5988
FUMH	Fumarate hydratase	0.5685	-0.6000
MYG1	UPF0160 protein MYG1	0.4884	-0.6052
COTL1	Coactosin-like protein	0.1658	-0.6279
VINC	Vinculin	0.2517	-0.6339
CAZA1	F-actin-capping protein subunit alpha-1	0.0816	-0.6350
NONO	Non-POU domain-containing octamer-binding protein	0.7905	-0.6471
FABP5	Fatty acid-binding protein	0.2622	-0.6577
MDHC	Malate dehydrogenase	0.0791	-0.6726
GLOD4	Glyoxalase domain-containing protein 4	0.0456	-0.6741
IF2B	Eukaryotic translation initiation factor 2 subunit 2	0.3376	-0.6834
CYTB	Cystatin-B	0.1170	-0.6881
RLA2	60S acidic ribosomal protein P2	0.0875	-0.6983
IDHC	Isocitrate dehydrogenase	0.3067	-0.6990
PABP1	Polyadenylate-binding protein 1	0.0635	-0.7134
DPP3	Dipeptidyl peptidase 3	0.5275	-0.7161
LY86	Lymphocyte antigen 86	0.5694	-0.7178
FPPS	Farnesyl pyrophosphate synthase (FPP synthase)	0.0806	-0.7218
PSB2	Proteasome subunit beta type-2	0.3218	-0.7219
UBB	Polyubiquitin-B	0.1548	-0.7230
HNRPF	Heterogeneous nuclear ribonucleoprotein F	0.6753	-0.7236
FKBP4	Peptidyl-prolyl cis-trans isomerase FKBP4	0.2496	-0.7250
TERA	Transitional endoplasmic reticulum ATPase	0.1050	-0.7340
IGHG1	Ig gamma-1 chain C region secreted form	0.0166	-0.7365
LAP2B	Lamina-associated polypeptide 2	0.4812	-0.7494
MOES	Moesin	0.1260	-0.7651
RAC1	Ras-related C3 botulinum toxin substrate 1	0.4249	-0.7788
AATM	Aspartate aminotransferase	0.3547	-0.7851
TPM4	Tropomyosin alpha-4 chain	0.1392	-0.7871
PSB6	Proteasome subunit beta type-6	0.0667	-0.8109
IQGA1	Ras GTPase-activating-like protein IQGAP1	0.2341	-0.8113
FKB1A	Peptidyl-prolyl cis-trans isomerase FKBP1A	0.4297	-0.8246
ENOB	Beta-enolase	0.3489	-0.8268
CDV3	Protein CDV3	0.1428	-0.8289
ACBP	Acyl-CoA-binding protein	0.0984	-0.8357
H14	Histone H1.4	0.0251	-0.8393
COF1	Cofilin-1	0.1336	-0.8507

PSA3	Proteasome subunit alpha type-3	0.0417	-0.8514
CLC5A	C-type lectin domain family 5 member A	0.0372	-0.8581
KPYM	Pyruvate kinase PKM	0.0690	-0.8585
TALDO	Transaldolase	0.1547	-0.8640
SAP	Prosaposin	0.5357	-0.8650
STIP1	Stress-induced-phosphoprotein 1	0.1554	-0.8684
EMAL4	Echinoderm microtubule-associated protein-like 4	0.0015	-0.8702
BLMH	Bleomycin hydrolase	0.1300	-0.8722
RISC	Retinoid-inducible serine carboxypeptidase	0.2724	-0.8736
PRDX2	Peroxiredoxin-2	0.1233	-0.9049
PEBP1	Phosphatidylethanolamine-binding protein 1	0.1369	-0.9325
CD14	Monocyte differentiation antigen CD14	0.0749	-0.9514
DDB1	DNA damage-binding protein 1	0.2002	-0.9558
PGM1	Phosphoglucomutase-1	0.0522	-0.9603
PLSL	Plastin-2	0.0386	-1.0028
SUMO2	Small ubiquitin-related modifier 2	0.0553	-1.0490
EI3JA	Eukaryotic translation initiation factor 3 subunit J-A	0.0218	-1.0522
SYVC	Valine--tRNA ligase	0.0943	-1.0693
CAPZB	F-actin-capping protein subunit beta	0.0903	-1.0855
LAMC1	Laminin subunit gamma-1	0.0205	-1.0903
PSA2	Proteasome subunit alpha type-2	0.1005	-1.1125
FA49B	Protein FAM49B	0.0771	-1.1179
MAP4	Microtubule-associated protein 4	0.0458	-1.1180
STMN1	Stathmin	0.3546	-1.1274
HDGF	Hepatoma-derived growth factor	0.2971	-1.1331
GMFB	Glia maturation factor beta	0.0992	-1.1342
ANXA5	Annexin A5	0.0425	-1.1759
GDIB	Rab GDP dissociation inhibitor beta	0.0939	-1.1776
ERP29	Endoplasmic reticulum resident protein 29	0.0809	-1.2448
YBOX3	Y-box-binding protein 3	0.0274	-1.2632
TAGL2	Transgelin-2	0.0060	-1.2735
HA1D	H-2 class I histocompatibility antigen. K-D alpha chain	0.0458	-1.2765
IDI1	Isopentenyl-diphosphate Delta-isomerase 1	0.5938	-1.2791
TPP2	Tripeptidyl-peptidase 2	0.2199	-1.2872
S10A4	Protein S100-A4	0.5345	-1.3059
PP1R7	Protein phosphatase 1 regulatory subunit 7	0.0116	-1.3097
THOP1	Thimet oligopeptidase	0.2317	-1.3141
U2AF2	Splicing factor U2AF 65 kDa subunit	0.1475	-1.3180
G6PD1	Glucose-6-phosphate 1-dehydrogenase X	0.1714	-1.3315
SPB6	Serpin B6	0.2446	-1.3426
CCL9	C-C motif chemokine 9	0.2260	-1.3462
SNX5	Sorting nexin-5	0.0868	-1.3745
SUMO3	Small ubiquitin-related modifier 3	0.1006	-1.3851
QSOX1	Sulfhydryl oxidase 1	0.4801	-1.3980
UB2L3	Ubiquitin-conjugating enzyme E2 L3	0.0137	-1.4257
CCD12	Coiled-coil domain-containing protein 12	0.1335	-1.4436
CH60	60 kDa heat shock protein. mitochondrial	0.0950	-1.5029

ABRAL	Costars family protein ABRACL	0.1473	-1.5580
GSTO1	Glutathione S-transferase omega-1	0.1830	-1.5971
RS28	40S ribosomal protein S28	0.0061	-1.6120
YBOX1	Nuclease-sensitive element-binding protein 1	0.1810	-1.6154
F10A1	Hsc70-interacting protein	0.2668	-1.6417
GDIR2	Rho GDP-dissociation inhibitor 2	0.0131	-1.6537
INO1	Inositol-3-phosphate synthase 1	0.0154	-1.6567
SYWC	Tryptophan--tRNA ligase. cytoplasmic	0.1833	-1.6592
PPIC	Peptidyl-prolyl cis-trans isomerase C	0.0516	-1.6665
RS21	40S ribosomal protein S21	0.0161	-1.7110
TBCA	Tubulin-specific chaperone A	0.0098	-1.7247
SODC	Superoxide dismutase	0.0290	-1.8001
CAZA2	F-actin-capping protein subunit alpha-2	0.0349	-1.8146
ANXA1	Annexin A1	0.4548	-1.8234
IF4G1	Eukaryotic translation initiation factor 4 gamma 1	0.1795	-1.8863
TREM2	Triggering receptor expressed on myeloid cells 2	0.0179	-1.8925
G3P	Glyceraldehyde-3-phosphate dehydrogenase	0.0537	-1.9986
LDLR	Low-density lipoprotein receptor	0.0149	-2.0273
HAP28	28 kDa heat- and acid-stable phosphoprotein	0.1535	-2.0683
PIMT	Protein-L-isoaspartate(D-aspartate) O-methyltransferase	0.0808	-2.0731
CALM1	Calmodulin-1	0.0135	-2.1710
BASP1	Brain acid soluble protein 1	0.2831	-2.1831
PAIRB	Plasminogen activator inhibitor 1 RNA-binding protein	0.0260	-2.1866
MDHM	Malate dehydrogenase. mitochondrial	0.0711	-2.2088
IPO5	Importin-5	0.0191	-2.2370
ALBU	Serum albumin	0.1972	-2.2439
SH3L3	SH3 domain-binding glutamic acid-rich-like protein 3	0.0654	-2.2836
HPRT	Hypoxanthine-guanine phosphoribosyltransferase	0.0339	-2.3180
SPEE	Spermidine synthase	0.0274	-2.5622
GRB2	Growth factor receptor-bound protein 2	0.0176	-2.8638
MYDGF	Myeloid-derived growth factor	0.0023	-2.9862
PLST	Plastin-3	0.0014	-3.0792
TXD17	Thioredoxin domain-containing protein 17	0.0030	-3.2514

Annex 3 **Ranked list of secreted proteins of present in anti-Sema4D treated macrophage conditioned media with respect to the IgG treatment.** Secreted proteins obtained in the proteomic analysis of the conditioned media are listed according to their ratio, calculated as the difference of expression between anti-Sema4D and IgG treatments. Divergence amount between treatments is shown by a color scale from red (upregulated in Sema4D condition), passing through white (no differences), to green (downregulated in Sema4D condition). Only proteins that were present 2 or 3 times in each conditioned media triplicate were included in the analysis. Statistical significance is calculated by Mann-Whitney test. Values of p.value < 0.05 are depicted in red.

Protein symbol	***Protein name***	***p. value***	***Ratio***
B2MG	Beta-2-microglobulin	0.0057	2.8589
HS90B	Heat shock protein HSP 90-beta	0.0004	2.7935
G6PI	Glucose-6-phosphate isomerase	0.0155	2.5021
EMIL2	EMILIN-2	0.0281	1.9579
PROP	Properdin	0.0001	1.7048
CATD	Cathepsin D	0.0285	1.5837
LIPL	Lipoprotein lipase	0.2445	1.3321
SDCB1	Syntenin-1	0.4685	1.1721
CATB	Cathepsin B	0.0014	1.0854
MIF	Macrophage migration inhibitory factor	0.2486	1.0348
ROA2	Heterogeneous nuclear ribonucleoproteins A2/B1	0.3060	0.8711
PPT1	Palmitoyl-protein thioesterase 1	0.1952	0.6823
NUCB1	Nucleobindin-1	0.0195	0.6027
PDIA1	Protein disulfide-isomerase	0.2694	0.5970
GARS	Glycine--tRNA ligase	0.2913	0.4891
LYZ2	Lysozyme C-2	0.1197	0.4640
COIA1	Collagen alpha-1(XVIII) chain	0.1993	0.4207
HMGB1	High mobility group protein B1	0.3885	0.3463
LYZ1	Lysozyme C-1	0.3090	0.3356
PDC6I	Programmed cell death 6-interacting protein	0.2406	0.3210
OSTP	Osteopontin	0.3989	0.2683
IL1RA	Interleukin-1 receptor antagonist protein	0.5886	0.2254
GELS	Gelsolin	0.8897	0.1203
THIO	Thioredoxin	0.8194	0.0636
LEG1	Galectin-1	0.9902	-0.0112
HMGB2	High mobility group protein B2	0.9595	-0.0189
CAPG	Macrophage-capping protein	0.6628	-0.1476
UROK	Urokinase-type plasminogen activator	0.6282	-0.2150
DAG1	Dystroglycan	0.5301	-0.3649
PPIA	Peptidyl-prolyl cis-trans isomerase A	0.0333	-0.5154
LG3BP	Galectin-3-binding protein	0.3995	-0.5287
CYTC	Cystatin-C	0.2519	-0.5988
LY86	Lymphocyte antigen 86	0.5694	-0.7178
IGHG1	Ig gamma-1 chain C	0.0166	-0.7365
SAP	Prosaposin	0.5357	-0.8650
RISC	Retinoid-inducible serine carboxypeptidase	0.2724	-0.8736
CD14	Monocyte differentiation antigen CD14	0.0749	-0.9514
LAMC1	Laminin subunit gamma-1	0.0205	-1.0903

CCL9	C-C motif chemokine 9	0.2260	-1.3462
QSOX1	Sulfhydryl oxidase 1	0.4801	-1.3980
YBOX1	Nuclease-sensitive element-binding protein 1	0.1810	-1.6154
ANXA1	Annexin A1	0.4548	-1.8234
TREM2	Triggering receptor expressed on myeloid cells 2	0.0179	-1.8925
ALBU	Serum albumin	0.1972	-2.2439
MYDGF	Myeloid-derived growth factor	0.0023	-2.9862

Annex 4 **Ranked list of proteins in anti-Sema4D treated macrophage conditioned media with respected to the IgG treatment.** Proteins in the mouse cytokine array analysis of the conditioned media are listed according to their ratio, calculated as the difference of expression between anti-Sema4D and IgG treatments. Expression of both treatments was previously normalized as explained in the Materias & Methods section. Divergence amount between treatments is shown by a color scale from red (upregulated in Sema4D condition), passing through white (no differences), to green (downregulated in Sema4D condition). Statistical significance is calculated by Mann-Whitney test. Values of p.value < 0.06 are depicted in red, and p.value < 0.05 are highlighted in red.

Protein	***p. value***	***Ratio***
IL12 p40/70	0.7000	1.6200
M-CSF	**0.0571**	0.5233
IL6	1.0000	0.5230
MIG	0.1143	0.4580
VCAM1	0.4000	0.4150
TIMP1	0.4000	0.4033
TARC	0.2286	0.3583
MCP5	0.2286	0.3567
TPO	0.1143	0.3317
CRG2	0.6286	0.3258
Ltn/XCL1	0.1536	0.3200
CXCL12	**0.0498**	0.3150
IGF2	0.4000	0.3070
MIP3 beta	0.2286	0.3067
P selectin	**0.0571**	0.2925
TECK	0.2286	0.2850
IFN gamma	0.6286	0.2397
MIP3 alpha	0.2286	0.2375
CX3CL1	0.4000	0.2250
TCA3	0.2286	0.2213
PF4	0.4000	0.1933
SCF	0.8571	0.1808
Fas ligand	0.7213	0.1683
sTNFRII	0.8584	0.1550
BLC	1.0000	0.1467
L selectin	0.8571	0.1375
IL10	0.8571	0.1350
IGFBP5	0.6000	0.1133
Axl	0.8571	0.0817
GITR	0.8571	0.0660
LIX	0.6286	0.0650
IL1 beta	0.8000	0.0633
RANTES	1.0000	0.0617

CD30L	1.0000	0.0350
IL13	0.8584	0.0300
CD40	1.0000	0.0283
KC	0.8571	0.0258
IL3 Rb	1.0000	0.0108
Leptin	1.0000	0.0092
IL3	1.0000	0.0067
IL2	1.0000	0.0058
CXCL16	0.8571	0.0050
CTACK	1.0000	-0.0117
GM-CSF	0.8571	-0.0142
MIP1 alpha	1.0000	-0.0217
IGFBP6	0.7213	-0.0283
CD30	1.0000	-0.0341
IL12 p70	0.8571	-0.0420
Leptin R	1.0000	-0.0525
IL1 alpha	0.7213	-0.0583
MIP1 gamma	1.0000	-0.0730
IGFBP3	0.5926	-0.0758
IL5	1.0000	-0.0800
sTNFRI	0.6286	-0.0845
VEGFR1	0.8571	-0.0940
VEGFR3	0.4000	-0.1080
Flt3 ligand	1.0000	-0.1130
VEGF	0.8571	-0.1150
IL17	0.4000	-0.1378
MMP2	0.8571	-0.1390
MCP1	0.4000	-0.1540
IL9	1.0000	-0.1545
OPG	0.6286	-0.1570
eotaxin1	1.0000	-0.1708
TSLP	0.6286	-0.1945
IL15	0.4000	-0.2100
CD26	0.6286	-0.2105
eotaxin 2	0.6286	-0.2200
Lungkine	0.6286	-0.2300
DtK	0.5926	-0.2525
E selectin	0.6286	-0.2600
TCK1	0.4000	-0.2770
TRANCE	0.4000	-0.2800
ICAM1	0.4000	-0.2820
Resistin	0.4000	-0.2905
ITAC	0.4000	-0.2940
TIMP2	0.6286	-0.2950
MDC	0.6286	-0.2970

IGF1	0.2845	-0.3080
IL4	0.4000	-0.3145
IL17B R	0.4000	-0.3145
OPN	0.1143	-0.3420
Shh-N	0.1143	-0.3480
IGFBP2	0.2286	-0.3480
VEGFR2	**0.0571**	-0.3500
bFGF	0.2286	-0.3530
TROY	0.2286	-0.3630
HGFR	0.2286	-0.3740
VEGF D	0.2118	-0.4445
Fc gamma RIIB	0.2286	-0.4450
MMP3	0.2286	-0.4505
Pro-MMP9	**0.0571**	-0.4830
MIP2	**0.0571**	-0.5770
GCSF	0.1333	-3.2672

Annex 5 **List of genes included in the Microenvironment Cell Population-counter (MCP) method to specifically differentiate subpopulations of stromal and immune cells.** The list includes genes that allow to differentiate among T cells, CD8 T cells, cytotoxic lymphocytes, B lineage, NK cells, monocytic lineage, myeloid lineage, neutrophils, endothelial cells and fibroblasts. Data were obtained from Becht et al., 2016.

Tcells	CD8T cells	Cytotoxic lymphocytes	B lineage	NK cells	Monocytic lineage	Myeloid lineage	Neutrophils	Endothelial cells	Fibroblasts
CD28	CD8B	CD8A	BANK1	CD160	ADAP2	CD1A	CA4	ACVRL1	COL1A1
CD3D		EOMES	CD19	KIR2DL1	CSF1R	CD1B	CEACAM3	APLN	COL3A1
CD3G		FGFBP2	CD22	KIR2DL3	FPR3	CD1E	CXCR1	BCL6B	COL6A1
CD5		GNLY	CD79A	KIR2DL4	KYNU	CLEC10A	CXCR2	BMP6	COL6A2
CD6		KLRC3	CR2	KIR3DL1	PLA2G7	CLIC2	CYP4F3	BMX	DCN
CHRM3-AS2		KLRC4	FCRL2	KIR3DS1	RASSF4	WFDC21P	FCGR3B	CDH5	GREM1
CTLA4		KLRD1	IGKC	NCR1	TFEC		HAL	CLEC14A	PAMR1
FLT3LG			MS4A1	PTGDR			KCNJ15	CXorf36	TAGLN
ICOS			PAX5	SH2D1B			MEGF9	EDN1	
MAL							SLC25A37	ELTD1	
MGC40069							STEAP4	EMCN	
PBX4							TECPR2	ESAM	
SIRPG							TLE3	ESM1	
THEMIS							TNFRSF10C	FAM124B	
TNFRSF25							VNN3	HECW2	
TRAT1								HHIP	
								KDR	
								MMRN1	
								MMRN2	
								MYCT1	
								PALMD	
								PEAR1	
								PGF	
								PLXNA2	
								PTPRB	
								ROBO4	
								SDPR	
								SHANK3	
								SHE	
								TEK	
								TIE1	
								VEPH1	
								VWF	

Publications

Intellectual work is an act of creation.

Ramón y Cajal

Publications

- **Refereed Journals:**

Marta Pàez-Ribes*, **Iratxe Zuazo-Gaztelu***, Patricia Carrasco et al. Anti-tumor effects of Semaphorin 4D blockade unravel a novel pro-invasive mechanism of vascular targeting agents. *Research article*. In revision.

* Both authors contributed equally to this work.

Zuazo-Gaztelu I, Casanovas O. Unraveling the role of Angiogenesis in Cancer Ecosystems. Frontiers in Oncology. 2018 Jul;8:248. doi: 10.3389/fonc.2018.00248

Carrasco P, **Zuazo-Gaztelu I**, Casanovas O. Sprouting strategies and dead ends in anti-angiogenic targeting of NETs. J Mol Endocrinol. 2017 Jul;59(1):R77-R91. doi: 10.1530/JME-17-0029.

- **Book chapters:**

Zuazo-Gaztelu I., Casanovas O. (2016) Mechanisms of Tumor Angiogenesis. In: Marmé D. (eds) Tumor Angiogenesis. Springer, Cham

Contributed presentations

During the thesis period, this work was presented in three national congresses. More information in the *curriculum vitae* (attached).